GALACTIC X-RAY SOURCES AND THEIR RADIO COUNTERPARTS

by

MARCUS LESLIE DULDIG

submitted in fulfilment
of the requirements for the degree of
Doctor of Philosphy
UNIVERSITY OF TASMANIA
HOBART
July, 1981

Except as stated herein, this thesis contains no material which has been accepted for the award of any other degree or diploma in any university. To the best of my knowledge and belief, this thesis contains no copy or paraphrase of material previously published or written by another person, except when due reference is made in the text of the thesis.

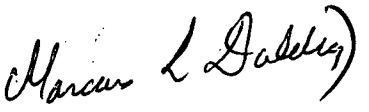

Marcus L. Duldig
10/7/81

ACKNOWLEDGEMENTS

The X-ray detector design and construction has involved many people. I wish to gratefully acknowledge all their contributions both large and small. Several people, however, deserve special thanks:

Dr. John Greenhill has supervised these studies. His constructive criticism and guidance through all stages of the project and in the preparation of this thesis have been of great benefit and it has been a pleasure to work with him.

During the time that Dr. Richard Thomas was a member of the X-ray group he was a source of inspiration and encouragement. His contribution through discussion and cooperative projects have been of great value and I am pleased to acknowledge his support.

The radio observations would not have been possible without the help of Dr. Ray Haynes. His assistance in all the radio observations and his keen eye for detail in the preparation of this thesis have been invaluable and I wish to express my sincere thanks for his contribution.

The staff of the Physics department workshops at the University of Tasmania as well as those of the Australian Balloon Launch Station and the CSIRO Parkes Observatory have also been of great assistance and I acknowledge their help.

Others who should be thanked include Mr. D.J. Watts, Dr. A.G. Fenton, Dr. K.B. Fenton, Mr. M.W. Emery, Mr. D. Dourneau and Dr. P.G. Murdin. Dr. Graham Giles assisted in proof reading the final manuscript and I am grateful to him for assisting with such an unenjoyable task.

Finally, I wish to express my sincere thanks to Miss Kerry Gorringe who competently undertook the task of typing this thesis. Her

pleasant nature and helpful suggestions regarding style and layout have been very much appreciated.

ABSTRACT

A 5200 cm^2, xenon-filled, multiwire proportional counter of 21 cm depth has been constructed for balloon-borne X-ray astronomy. The telescope is sensitive to photons in the energy range 10 - 100 keV and is surrounded on all sides, except the entrance window, by a Sn/Cu graded shield and anti-coincidence guard counters. The counter and 7° × 20° FWHM collimator were contained within an hermetically sealed aluminium pressure vessel of 1 metre diameter having expandable mylar ends.

Counter pulses were pulse-height-analysed into 20 channels and telemetered, together with count rate data (0.5 ms sample rate) and house keeping data.

The telescope was equatorially mounted on a magnetically referenced, reaction wheel servo-stabilized platform. Pointing under ground control to within 0°.5 of a specified source position was achieved during flights in December 1976 and November 1978.

On line, quick-look, analysis of the telemetered data with a PDP 11/10 computer enabled the observers to immediately assess the telescope performance and attempt to rectify any problems by radio command.

A complete description of the telescope system and the payload performance during balloon flights in December 1976 and November 1978 is presented. Problems encountered with outgassing of impurities and the subsequent loss of resolution and gain are considered. Temporal observations of VEL X-1, showing the ∿ 290s periodicity, and SCO X-1, indicating rapid intensity variations, and spectral analyses of SCO X-1 are presented. More recent improvements to the telescope system are also described.

Following the discovery of periodic radio flaring coincident with sharp X-ray cutoffs from CIR X-1 a radio survey of 98 well determined X-ray source positions at 14.7 GHz (λ=2cm) was undertaken using the Parkes 64 m radio-telescope. Twelve radio counterparts, eight of which are new, were detected and a further 81 upper limits were obtained. Searches for variable radio emission correlated with X-ray events from X-ray burst sources, as part of a world-wide 'Burst Watch', gave a null result but enabled upper limits to the radio burst flux to be established. Results from monitoring a complete flare of CIR X-1 showed a complex triple peaked structure at λ = 2 cm. Observations carried out at 5 GHz (λ=6cm) were combined with other published results to deduce a rate of decrease for the orbital period of CIR X-1.

The implications of these observations are discussed with particular reference to the recent eccentric orbit, luminosity-driven shock model for radio emission from CIR X-1. The significance of the other radio counterparts and selected upper limit results are also considered.

CONTENTS

CHAPTER 1

INTRODUCTION

1.1. X-RAY ASTRONOMY

1.1.1 SHORT HISTORY

Non-solar X-ray astronomy began in 1962 when Sco X-1 was discovered (Giacconi et al. 1962) during a rocket flight, ostensibly to observe fluorescence X-rays from the lunar surface. Atmospheric opacity to X-rays necessitated high altitude observations and by the end of the decade more than twenty X-ray sources had been discovered by rocket and, to a lesser extent, balloon-borne detectors.

The first X-ray satellite, UHURU, was launched in December 1970 and was used to carry out an all sky survey which increased the number of known X-ray sources to $\sim$ 340 (Forman et al. 1978). The early 70's saw the launching of a number of other X-ray satellites including the British Ariel V in 1974 and SAS-3, which was designed at MIT, in 1975.

The HEAO-1 satellite, launched in August 1977, produced X-ray source positions accurate to a few tenths of a minute of arc and by 1978 more than 500 X-ray sources had been discovered, $\sim$ 200 of them with positions known to a few arc minutes.

1.1.2 THE NEED FOR HIGH ENERGY OBSERVATIONS

Most of the X-ray sources had been observed only at energies < 20 keV. The energy spectra had therefore, only been determined over a narrow energy range (1-20 keV) and the need for hard X-ray observations became more important. It was clear that most sources had steep spectra and the resulting low flux levels at energies > 20 keV required large area detectors to observe the emission. Such large area detectors are,

by their very nature, heavy, so balloon-borne observations from the upper regions of the atmosphere are a cost effective method of making the observations.

High energy observations are necessary to characterize the spectra of the harder sources, differences in spectral form being more easily deduced when the energy range is extended. The presence of hard X-ray features in the spectra of some sources had been reported. Haymes et al. (1972) has observed a hard energy "tail" in the spectrum of Sco X-1 and Trumper et al. (1978) have reported a high energy cyclotron line in Her X-1. Further observations, searching for hard spectral "tails" or cyclotron lines in these and other X-ray sources would lead to a better understanding of possible source mechanisms.

A number of X-ray emitting active galaxies and quasars have relatively hard spectra. It is not clear in some cases whether the spectra are thermal or power law. Superposition of the emission from these objects has been proposed as a possible source of the diffuse X-ray background which is thermal with $kT = 40$ keV. Since this spectrum steepens at higher energies observations of such objects, above 20 keV, are required to determine if their spectra are compatible with the hypothesis that they are significant contributors to the diffuse X-ray background.

Observations of variability at high energies are also required. Reports of very short time-scale structure in CYG X-1 and Cir X-1 have been proposed as evidence for the possible presence of black holes in these sources. Searches for similar activity from other hard X-ray sources as well as further observations of these sources are therefore of great importance.

The energy dependence of pulse profiles from X-ray pulsars also requires further study. Models proposed to explain the pulsed emission will have to account for the form of this dependence.

1.1.3 X-RAY PROPORTIONAL COUNTERS

Two main types of detector are employed for hard X-ray observations, proportional counters and scintillation counters. Each have their inherent advantages and disadvantages.

The proportional counter is relatively simple in design and may be constructed at reasonably low cost. On the other hand they suffer from escape (see later in this section) and are only useful up to $\sim$ 100 keV. Scintillation counters do not suffer from escape problems to the same extent, but are very costly, have a greater weight penalty and are more complex than proportional counters. Proportional counters are also potentially capable of much better energy resolution than scintillation counters.

A proportional counter, as the name implies, produces a pulse with an amplitude proportional to the energy absorbed in the counter. For hard X-ray observations such counters are normally filled with a high atomic number gas such as xenon. The dominant mechanism of photon interaction is the photoelectric effect. Usually the X-ray photon will deposit all of its energy when interacting with the detection gas. These interactions produce photoelectrons which ionize the surrounding atoms.

The ejection of an electron leaves the atom in an excited state. De-excitation of the atom may involve a cascade of photons near the K-edge energy (fluorescence) or the ejection of a second electron at a similar energy (Auger effect). The probabilities of these de-excitations for xenon are 0.89 and 0.11 respectively.

Xenon is relatively transparent to its own fluorescence photons and the probability of fluorescent photon escape is therefore quite high, especially in smaller detectors. Should this occur, the energy deposited in the counter is then the energy of the incident photon less that of the fluorescent photon. For xenon the K edge is $\sim$ 30 keV. Thus the pulse height distribution emerging from the counter will include a peak at the incident photon energies, known as the *photopeak*, and another peak 30 keV lower in energy, called the *escape peak*. The probability that the Auger electron will escape the counter is negligible.

This picture is somewhat simplified as there are a number of possible transitions near the K edge. These are the K_α transitions at 29.7 keV ($K_{\alpha 1}$ and $K_{\alpha 2}$ separated by $\sim$ 0.4 keV) and the K_β transitions ($K_{\beta 1}$ and $K_{\beta 2}$) at 33.8 keV. The relative probabilities of these two transitions are 0.802 and 0.197 respectively. The K_α and K_β transitions are considered as the only two possible, for the purposes of analysis, as counters can not resolve the 0.4 keV differences within either transition.

The secondary electrons, resulting from the photoelectron ionization of the surrounding atoms, will drift toward the anode wires of the counter. An avalanche effect in the high field region close to the anode produces a pulse, proportional to the energy. The avalanche of electrons is a stochastic process which results in a finite counter resolution. In xenon, $\sim$ 47 electron-ion pairs are produced for each keV deposited in the counter. The actual number produced by an X-ray photon is distributed "normally". Therefore a monoenergetic beam of X-ray photons illuminating the counter will produce a gaussian pulse height distribution at the photon energy (together with a second gaussian

profile escape peak, 30 keV lower in energy if the initial photons have an energy in excess of the K edge of xenon).

The resolution is usually described by the profile width at half height, divided by the energy of the peak centre and expressed as percentage.

$$\text{i.e. Resolution} = \frac{\text{FWHM (keV)}}{\text{MAX (keV)}} \times 100\%$$

The resolution is expected to vary with energy as $E^{\frac{1}{2}}$. Doubling the incident photon energy doubles the number of ion-pairs produced in the counter and improves the resolution by a factor of $\sqrt{2}$ as long as statistical variations are the dominant contribution to the scatter.

1.1.4 THE UNIVERSITY OF TASMANIA X-RAY COUNTER

A large area proportional counter is superior to a collection of smaller modules because of its lighter construction and significantly reduced escape probability. The maximum energy observable by the counter is determined by the counter depth and the detection gas pressure.

The need for hard X-ray energy observations described in the previous section prompted the design and construction of a large area (5220 cm^2 - effective area), multiwire, Xe filled proportional counter by the X-ray astronomy group of the University of Tasmania. The choice of a proportional counter was based on the preceding arguments of low cost, light-weight construction together with good energy resolution ($\sim$10% at 60 keV) and large achievable sensitive area. The counter depth of 21 cm allowed observations up to about 85 keV and the detector geometry was selected, after Monte-Carlo simulations by

Dr. R.M. Thomas, to give the lowest escape probability.

The sensitivity of the telescope to weak sources is given by

$$N = S(E) \cdot \varepsilon(E,P)\sqrt{\frac{T.\Delta E.A}{2B(E)}}.$$

where N is the number of standard deviations of the signal above the background

A is the counter effective area (cm^2)

P is the residual atmospheric pressure

T is the time interval of the observation (sec)

E is the energy (keV)

ΔE is the energy bandwidth (keV)

B(E) is the counter background in the selected energy range per unit area (counts/keV-cm^2-sec)

S(E) is the source rate above the atmosphere (counts/keV-cm^2-sec)

and $\varepsilon(E,P)$ is the counter efficiency including atmospheric absorption.

Reduction of the counter background will improve the telescope sensitivity as effectively as increasing the counter effective area. Passive shielding of atmospheric X-rays and active background rejection of charged particles are therefore important. A passive graded shield of Sn and Cu was chosen using Monte Carlo techniques to optimize its effectiveness within the constraint of a fixed mass of shielding. Further reduction of the background was achieved by veto-

counter rejection of charged particle events within the counter. These methods of sensitivity improvement do not carry a great weight penalty allowing higher altitudes to be reached with the same lift. Higher altitudes also increase the efficiency $\varepsilon(E,P)$ resulting in further improvements to the sensitivity.

1.2 RADIO COUNTERPARTS TO X-RAY SOURCES

1.2.1 SHORT HISTORY

In 1968 Andrews and Purton (1968) discovered the radio counterpart to SCO X-1. Variability of the radio flux density was reported by Ables (1969) and this was followed by the discovery of the triple radio source structure (Hjellming and Wade 1971). By 1975 six compact X-ray sources had well established radio counterparts. These were SCO X-1, CYG X-1, GX 17 + 2, CYG X - 2 and CYG X - 3 (Hjellming 1974) and the X-ray nova A0620-00 (Davis et al. 1975, Craft 1975, Lequex 1975, Owen et al. 1976), which flared and then decayed to below detectable limits on a timescale of weeks.

In May 1976, as part of a 6 cm galactic plane survey, the Parkes radiotelescope was observing the region about Cir X-1. By chance, the position of Cir X-1 was in an overlay region between two maps. This resulted in observation of the Cir X-1 region on two successive evenings and it was found that the flux density of the candidate counterpart proposed by Clark et al. (1975) had increased from 0.3 to 1.4 Jy* (Whelan et al. 1979) in less than 29 hours. This unusual behaviour led to coordinated world-wide observations of the source and the development of a model to explain the emissions at all frequencies (see next section).

The continued improvement in the X-ray positional error

---

* 1 Jy = 10^{-26}W $m^{-2}Hz^{-1}$

boxes (1.1.1) and the detection of the unusual object Cir X-1 led the X-ray astronomy group at the University of Tasmania and the CSIRO Division of Radiophysics to jointly undertake (in 1977-1978) a systematic search for radio counterparts of X-ray sources. The survey was made at 2 cm wavelength (Chapter 7) because of the narrow beam size of the Parkes radiotelescope at this wavelength and the resulting reduction in source confusion. Variable radio emission from a candidate source is strong evidence of a physical association (Hjellming 1974) and a detailed study of possible variability from candidate sources was made (Chapter 8).

1.2.2 MODEL FOR CIR X-1

Murdin et al. (1980) proposed an eccentric orbit binary system to account for the X-ray emission from Cir X-1. The binary period is 16.8 day and the HLM model (Haynes, Lerche and Murdin 1980, Murdin et al. 1980) proposed an orbital eccentricity of 0.7 to 0.8. Observations of the optical counterpart to Cir X-1 showed the primary star to be an OB supergiant with a mass in the range 20 $M_\odot$ - 100 $M_\odot$ and a radius of $\sim 2 \times 10^{12}$ cm.

In the model the secondary star is assumed to be compact, having a mass of $\sim 1\ M_\odot$. The eccentricity of the system implies that the secondary star passes within 5 to 9×10^{12} cm of the primary at periastron passage. H_α and H_β observations have shown significant mass loss from the primary and mass accretion onto the compact object is certain. The X-ray intensity of Cir X-1 increases approaching periastron passage and then suddenly declines with a corresponding increase in the low energy X-ray cut—off. The slow intensity increase is attributed to the increasing accretion rate. Close to periastron passage, X-ray absorption becomes significant. The orbital orientation

with the line of sight is confined to within narrow limits by the shape of the X-ray light curve. The light curve has been observed to change slowly over the past eight years and precession of the eccentric orbit has been used to explain the gradual change.

Analysis of 6 cm radio observations show a "front porch" enhancement to the quiescent radio emission shortly after the X-ray decline. This effect is attributed to an enhancement of the radio emission resulting from the increasing accretion rate during the approach to periastron. Modelling the expected shape of this enhancement showed that the shape of the "front porch" could only be generated if the orbital eccentricity was 0.7, a value consistent with the X-ray data.

Following the "front porch" the radio source flares one or more times and these flares are observed initially at higher radio frequencies (>10 GHz) and subsequently at lower frequencies (down to about 400 MHz, several days later). The infalling matter at periastron passage can be shown to produce radiation fluxes close to and possibly exceeding the Eddington limit. Thus the infalling matter will be ejected through radiation pressure. This in turn produces a blast wave which propagates outward producing the radio flares. These flares then follow the behaviour of an adiabatically expanding cloud of relativistic electrons, producing synchrotron radiation at radio frequencies (Haynes, Lerche and Murdin 1980). Following the expansion of the blast front accretion may recommence and the process can repeat itself, up to 3 or 4 times during the periastron passage.

The HLM model for Cir X-1 predicts several observable effects (Haynes et al. 1979). The X-ray light curve should return to its earlier shape as the orbit precesses. The orbit of the compact object should circularize in about 500 years. This circularization

will manifest itself in two ways. Firstly the orbital period should decrease by about 0.05 day per year and secondly the radio flaring should decrease as the periastron passage increases. The radio emission during a "front porch" enhancement may show evidence of short timescale (minutes or seconds) structure due to uneven accretion whereas the flare emission should only show larger timescale features (hours/ days).

The observations of Cir X-1 presented in Chapter 7 and discussed in Chapter 8 were carried out to test some of these predictions. It was hoped that the survey of other X-ray source positions would result in the discovery of other similar systems.

1.3 REFERENCES

Ables J.G. (1969) Astrophys. J. (Lett) 155, L27

Andrews B.H. and Purton C.R. (1968) Nature 218, 855

Clark D.H., Parkinson J.H. and Caswell J.L. (1975) Nature 254, 674

Craft H.D. (1975) I.A.U. Circ. 2822

Davis, Edwards, Morrison and Spencer (1975) I.A.U. Circ 2822

Forman W., Jones C., Cominsky L., Julian P., Murray S., Peters G., Tananbaum H. and Giacconi R. (1978) Astrophys. J. Suppl. 38

Giacconi R., Gursky H., Paolini F.R. and Rossi B. (1962) Phys. Rev. Lett. 9, 439

Haymes R.C., Harnden F.R., Johnson W.N. and Prichard H.M. (1972) Astrophys. J. (Lett), 172, L47

Haynes R.F., Caswell J.L. and Simons L.W. (1976) IAUC 2977

Haynes R.F., Jauncey D.L., Lerche I. and Murdin P.G. (1979) Aust. J. Phys. 32, 43

Haynes R.F., Lerche I. and Murdin P. (1980) Astron. Astrophys. 87, 299

Hjellming R.M. and Wade C.M. (1971) Astrophys. J. (Lett). 168, L21

Hjellming R.M. (1974) "International Conference on X-rays in Space" p.211 ed. Venkatesan D., University of Calgary

Lequex J. (1975) I.A.U. Circ. 2822

Murdin P., Jauncey D.J., Haynes R.F., Lerche I., Nicholson G.D., Holt S.S. and Kaluzienski L.J. (1980) Astron. Astrophys. 87, 292

Owen F.N., Balonek T.J., Dickey J., Terzian Y. and Gottesman S.T. (1976) Astrophys. J. (Lett) 203, L15

Trumper J., Pietsh W., Reppin C., Voges W., Staubert R. and Kendziorra E. (1978) Astrophys. J. (Lett) 219, L105

Whelan J.E.J., Mayo S.K., Wickramasinghe D.T., Murdin P.G., Peterson B.A., Hawarden T.G., Longmore A.J., Haynes R.F., Goss W.M., Simons L.W., Caswell J.L., Little A.G. and McAdam W.B. (1977) Mon. Not. R. astr. Soc. 181, 259

CHAPTER 2

X-RAY TELESCOPE INSTRUMENTATION

2.1 INTRODUCTION

The X-ray astronomy payload was conceived as a cost-effective means of making high quality spectral and temporal observations of cosmic X-ray sources at hard X-ray energies (>15 keV). The counter, supporting instrumentation and gondola were designed to achieve a maximum sensitive area whilst minimizing the total payload weight and thus substantially saving on balloon and launch costs.

Although the detection efficiency of gas counters decreases more rapidly with increasing photon energy than do,for example,NaI scintillation counters, they possess superior energy resolution. With the larger achievable sensitive area and the known steep spectra of cosmic X-ray sources in the energy range 20-100 keV, a xenon counter compares very favourably with scintillation telescopes.

The author joined the research group shortly after the initial design stage and was involved with the construction of the telescope system and in most of the subsequent improvements which are described.

2.2 EQUIPMENT

2.2.1 OVERVIEW OF THE TELESCOPE SYSTEM

The 5200 cm^2, xenon-filled,multiwire,proportional counter is housed in an hermetically sealed aluminium pressure vessel of 1 metre diameter (Figure 2-3). This vessel is divided into two sections, the lower half containing the counter whilst the upper section houses the collimator. Shielding from atmospheric X-rays generated by cosmic rays interacting with the atmosphere, is achieved using a graded shield of Sn (in the form of pewter) and Cu.

The whole counter and collimator vessel was equatorially mounted on an aluminium frame (Figure 2-1). This frame, constructed from one inch aluminium tubing,also supported the batteries, telemetry encoder electronics, receiver and transmitter and the azimuth servo-stabilization circuitry.

Azimuthal stability was achieved by sensing the local geomagnetic field with two orthogonal, horizontally mounted fluxgate magnetometers and applying the resulting magnetometer error signal (derived from the offset of the payload azimuth from true north) to a reaction wheel system which was located at the top of the payload suspension rigging.

The support frame was designed so that it would absorb the impact of landing, through deformation and thus protect the X-ray counter from damage.

With the payload stabilized in azimuth the telescope could be pointed at particular source positions by ground commands. The stepping motor drive on the hour angle axis could be driven at slewing or tracking rates in either direction. Similarly the declination stepping motor could be activated by command from the ground station but only at a single slewing speed.

Counter pulses were fed through a 20 channel pulse height analyser to the telemetry encoder where these data and other house keeping data were arranged into the telemetry format and output serially to the transmitter.

The ground station consisted of a telemetry receiver and command transmitter, a bit synchronizer/conditioner from which the Non-Return to Zero (NRZ) bit stream was fed to the telemetry decoder and a PDP 11/10 computer and magnetic tape recorder system (Figure 2-2). The

Figure 2-1 The University of Tasmania X-ray telescope system. The reaction wheel and suspension system are shown together with the platform and equatorially mounted telescope. Parts of the styrofoam thermal insulation are also present.

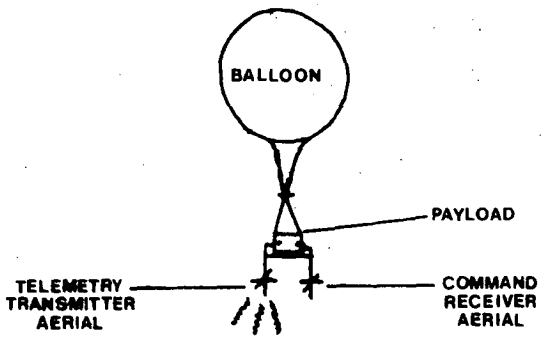

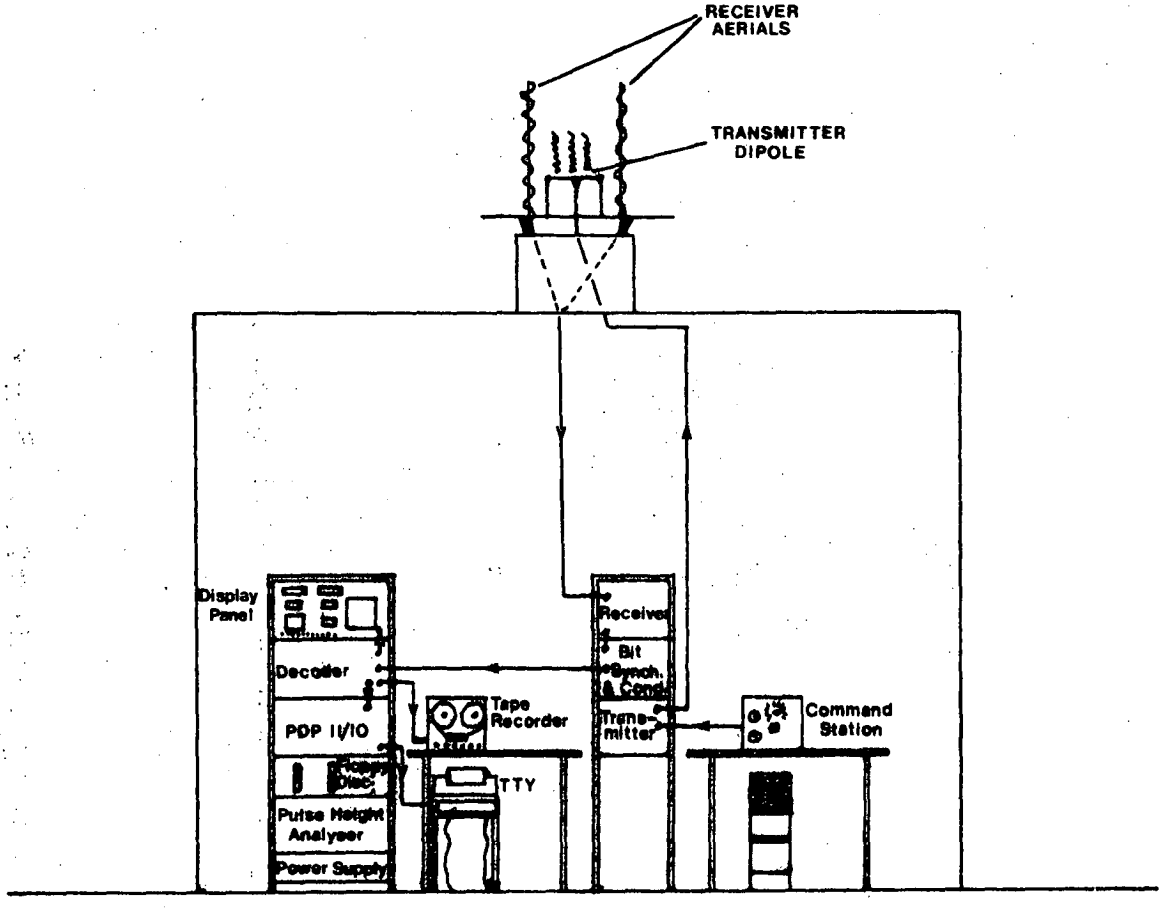

Figure 2-2. The ground station for data reception and command transmission.

telemetry decoder output included a generated clock signal and was recorded on a modified domestic tape recorder using a record head saturation technique as a complete permanent record of the flight for post flight analyses. The data were also passed as 16 bit parallel words to the computer where quick-look analyses were carried out and the results printed on a teletype (TTY). This quick look output enabled observers to monitor the payload performance at all times.

2.2.2 THE X-RAY COUNTER

The X-ray detector (Figure 2-3) is a multi-layer proportional counter of 5200 cm^2 effective area filled with a xenon-helium-methane gas mixture to slightly above atmospheric pressure. It comprises six octagonal trays stacked one above the other to give an octagonal cylinder with a sensitive region 95 cm along a diagonal and 21 cm deep.

The detector is of wall-less construction in which the sensitive region is surrounded on all sides except the entrance window by cathode wires rather than solid walls. Charged particles entering the detector are sensed by the veto counters, amplified and employed in analogue switching circuitry, thus rejecting the subsequent counter pulses. Shielding from atmospheric X-rays is provided by a graded shield of Sn (in the form of pewter) and Cu. The counter is housed in a lightweight hermetic chamber fabricated from aluminium and mylar.

The active volume of the counter (Figure 2-4) consists of five octagonal stacked trays, each with twenty one anodes. These anodes are connected together in groups of three called 'cells'. The thirty five cells each have their own preamplifiers attached to the counter support frame within the gas detection volume. The preamplifier outputs are fed through five convenient locations around the cylinder circumference where they are added together via gain matching resistors. These five

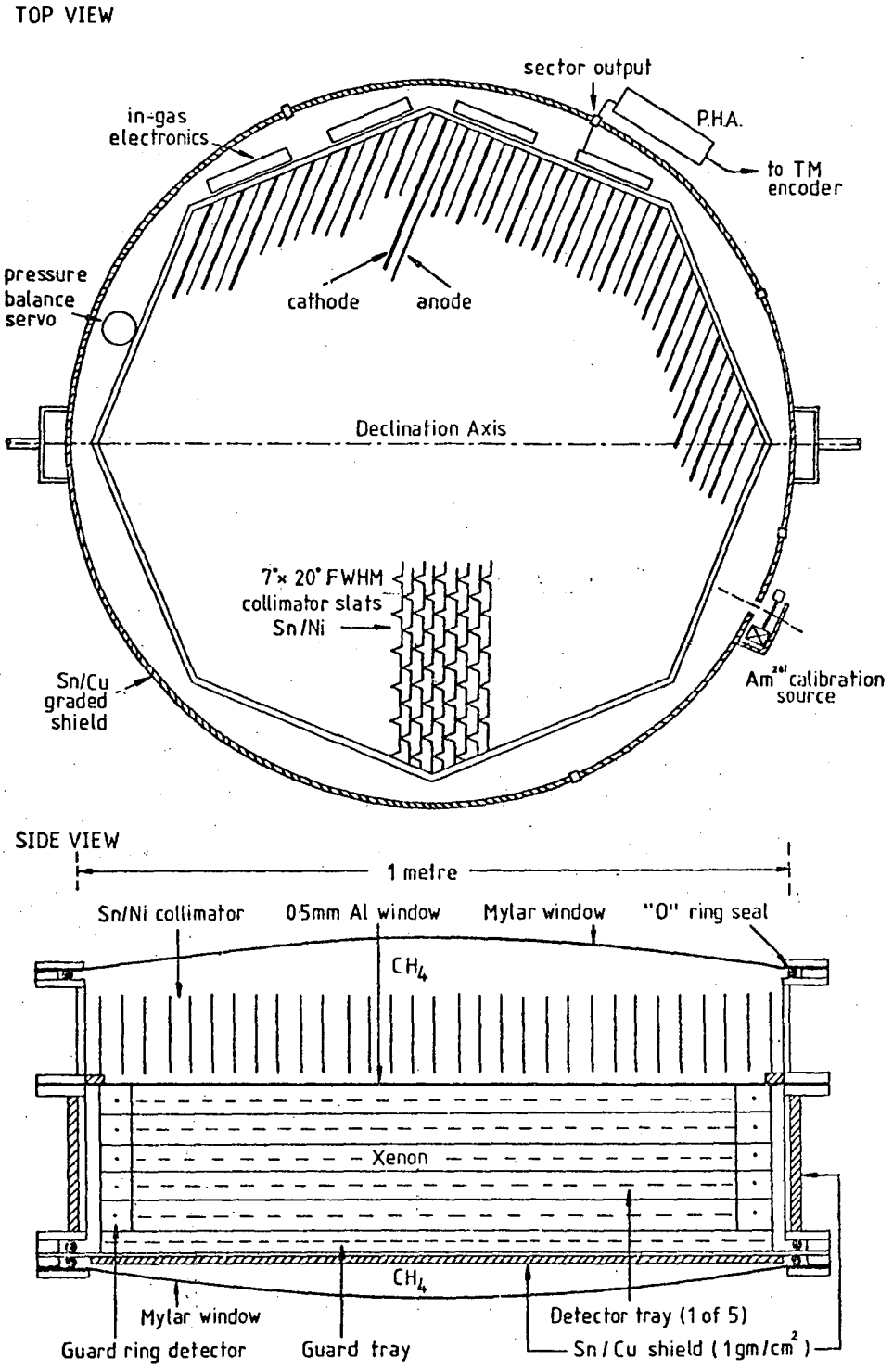

Figure 2-3. The University of Tasmania balloon-borne proportional counter.

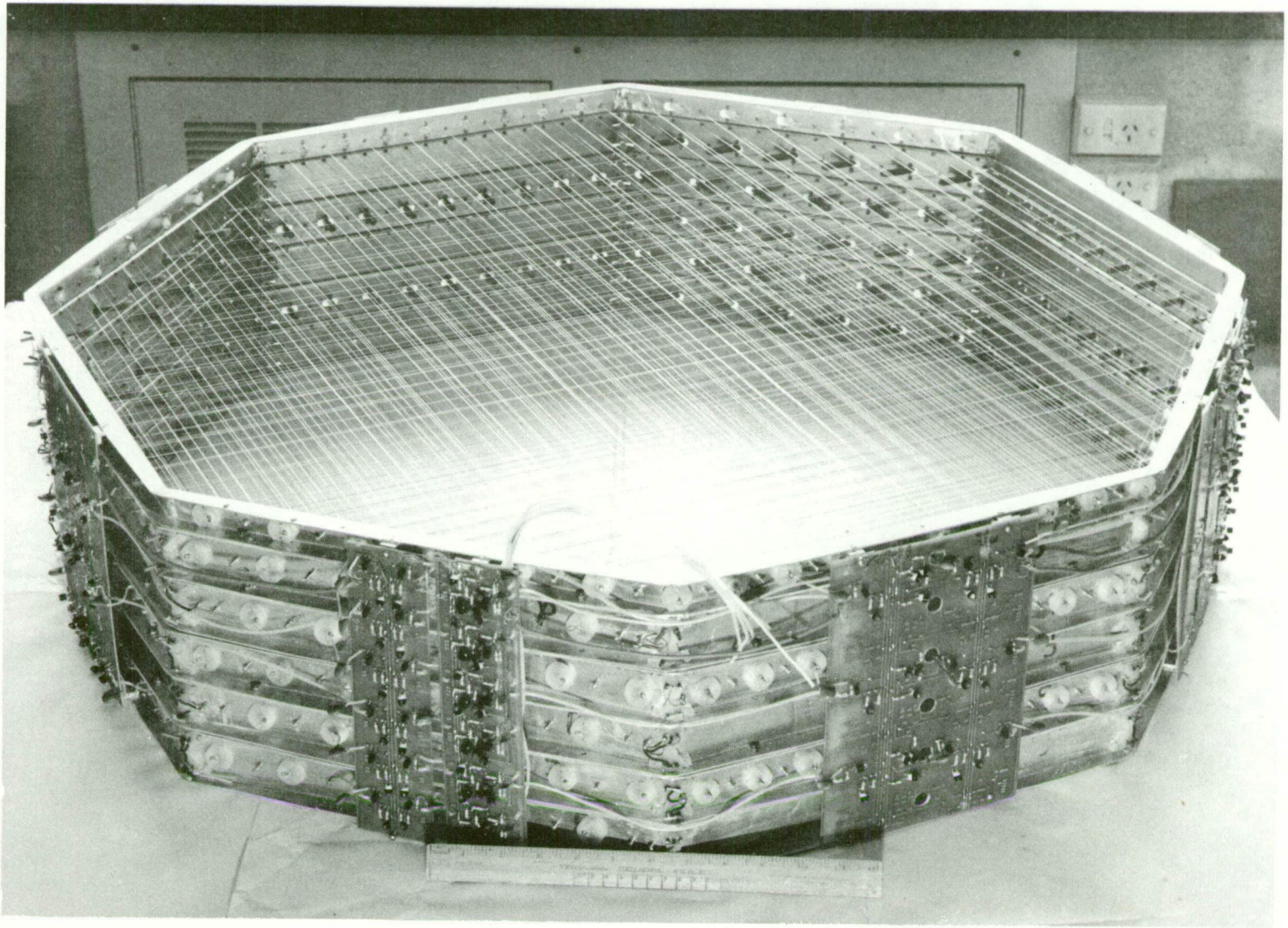

Figure 2-4 The X-ray detector showing the multiwire construction and preamplifiers.

added signals are referred to as 'sector' outputs. The five sector outputs are then fed to the pulse height analyser (PHA).

The PHA consists of veto logic circuits and a pulse stretcher combined with an analogue to digital converter. Figure 2-5 shows a schematic representation of the PHA system.

Amplified counter pulses were fed via the veto switching circuitry to the PHA/ADC and the lower level discriminator (LLD). All pulses above the LLD bias level produced a strobe pulse which switched the PHA/ADC to active. The PHA/ADC produced a square pulse of the same duration as the strobe pulse at one of its 19 outputs corresponding to the channel number in which a pulse of the detected height belonged. PHA channel 20 carried the veto counts. All pulses were summed for each channel at a later stage. The LLD and channel boundary pulse heights could be adjusted and a linear pulse height to channel number conversion was employed.

Collimation of the X-rays was achieved by a slat collimator having a field of view of $\sim 7° \times 20°$ FWHM constructed from nickel-plated pewter sheet modules stacked alongside one another above the xenon filled volume and separated from it by a 0.5 mm aluminium window. The collimator section of the telescope was filled with CH_4 or CO_2 and was also connected to a small end section below the counter.

Due to the flexible nature of the mylar ends of the hermetic chamber, variations in the ambient air pressure during ascent and descent of the balloon led to substantial pressure differentials ($\sim$ 50mb) between the counter and collimator sections of the vessel. Such a pressure differential would distort the aluminium entrance window and counter resolution would be adversely affected due to the intrusion of the 0.5 mm window into the sensitive region of the detector. To avoid this problem a differential pressure transducer was employed in a servo-system to valve

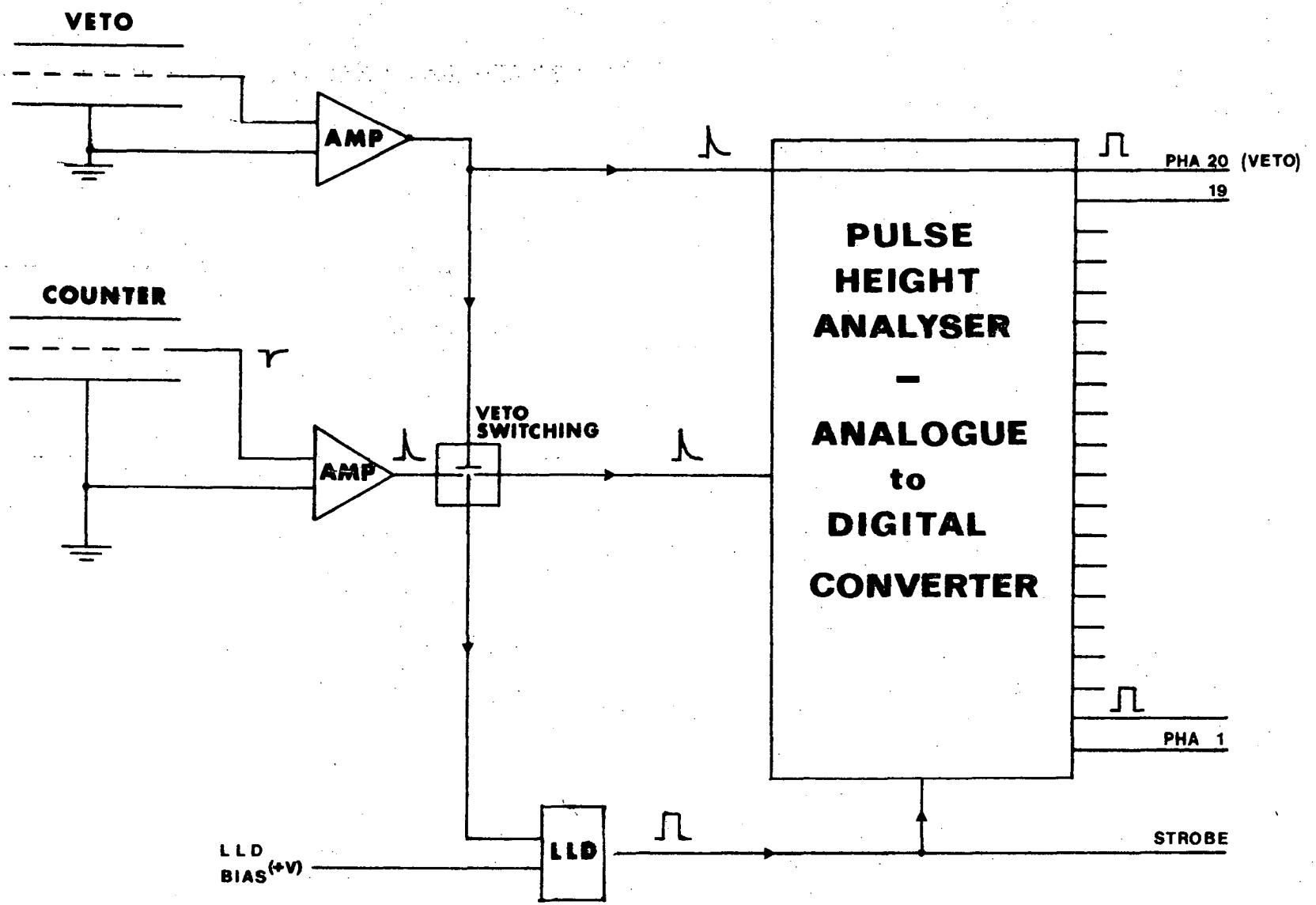

Figure 2-5. A schematic representation of the in flight Pulse Height Analyser system.

additional CH_4 into the collimator section during ascent and vent excess CH_4 from the collimator section during descent and thus maintain a zero pressure differential to within a few millibars across the aluminium entrance window.

2.2.3 THE GAS RECIRCULATION SYSTEM

Following the inaugural flight of the detector system in December 1976 it was found that outgassing,occurring within the xenon compartment, was degrading the gas gain and resolution on a timescale of hours. The counter response was similar to that shown in figure 2-12 but after two weeks the 25 keV fluorescent X-ray source placed at the entrance aperture of the telescope no longer produced a discernible peak in the counter response.

Initially, to overcome this problem, the counter was evacuated for a fortnight with periodic pumping to remove any outgassed components. The counter was then refilled but still showed signs of degradation over a period of hours, though not as severe as previously.

A gas circulation system was developed which pumped the xenon through a combination of molecular sieve, potassium and heated steel wool. This circulation system was run continually prior to and during subsequent flights and resulted in a dramatic initial improvement in gas gain and resolution over the first day or so followed by an almost constant response. No further gas deterioration was observed while the circulation system was operating but deterioration occurred as soon as the gas recirculation was stopped.

2.2.4 THE GONDOLA AND AZIMUTH STABILIZATION SYSTEM

The gondola platform was specially designed to be of light-weight construction and to absorb the energy of impact on landing, through deformation and thus protect the X-ray detector from damage. The telescope

was mounted equatorially on the platform (see figure 2-1).

Azimuthal stability of the platform was achieved by a reaction-wheel servo-system. Two orthogonal, horizontally mounted fluxgate magnetometers, one mounted in a north-south orientation and the other in an east-west orientation, were employed to sense the geomagnetic field. An error signal was derived from the offset from the minimum field condition in the E-W magnetometer, current amplified and fed to the reaction wheel turning the wheel in the direction of the azimuth error offset. This in turn caused the payload platform to rotate in the opposite sense cancelling the error signal and swinging the platform back into the correct azimuthal orientation.

Location of the magnetometers on the gondola platform was important. They were mounted as far as possible from any ferrous metal, current carrying cables or the transmitter to avoid erroneous readings and hence an incorrect azimuth angle of stabilization.

The major drawbacks of an equatorial system are: 1) variations in latitude as the balloon payload drifts are difficult to compensate for during the flight (the hour angle axis will no longer be aligned with the polar axis) and; 2) variations in latitude and longitude result in a change of the geomagnetic offset from true north (the magnetometers having been set for the fixed offset of the launch site). The second of these problems may be solved by an additional mechanical drive or an electrical offset applied to the magnetometer output. Both these criticisms have been overcome in a subsequent altitude-azimuth mounting system now employed and briefly described in section 5.3.

2.2.5 POINTING CONTROL

Telescope pointing was under ground control at all times. Commands sent from the ground station were processed within the telemetry

encoder electronics package (encoder) and actuated the hour angle and declination drives in either direction. The available commands for the telescope system are shown in table 2-1.

Table 2-1

1978 Balloon Flight Commands

Command Number	Function
1	H.A. stop/run
2	H.A. W/E
3	H.A. slew/track
4	Parachute Release
5	Ballast destruct
6	TERMINATE
7	Ballast on
8	Ballast off
9	Dec. stop/run
10	Dec. N/S
11	EHT on/off
12	Az. servo on/off

The observer was therefore able to check the quick look output from the computer and determine the direction required to drive the telescope for the next observation. The direction and speed commands were sent as required followed by the stop-run command. Once the telescope reached the desired position the stop-run command for the relevant drive would be re-transmitted stopping the drive. In the case of a tracking observation the drive rate would be changed under command.

The quick-look output from the computer displayed the current status of the drives (viz. direction, rate and on/off) as well as the shaft encoder angles in degrees. The shaft encoder outputs were converted from their two's complement gray code, to binary, through a lookup table within

the PDP 11/10. These binary numbers were then transformed to decimal degrees for comparison with tables of source positions.

2.2.6 TELEMETRY ENCODER ELECTRONICS PACKAGE

The encoder collated all incoming PHA data and house keeping data and ordered it for serial transmission by the transmitter. Figure 2-6 is a schematic representation of the functions performed by telescope signal processing system. The bulk of the processing was achieved within the encoder.

Power was derived from organic lithium batteries and fed into an inverter which produced a number of regulated and unregulated voltages which were fed to the encoder and then to the various circuits and transducers connected to the system.

Counter pulses were fed to the PHA (2.2.2) and then through to the encoder where they were summed in an 11 bit binary counter cycling modulo 2048. The count rate per PHA channel was sufficiently low that the PHA buffers never accumulated more than 2048 counts between successive transmissions (512ms). Pulses were also binned in 0.5ms count rate samples over a preselected PHA channel range (i.e. a fixed energy range) for transmission (see 2.2.7).

House keeping information was also stored for transmission. The status (open or closed) of the CH_4 inlet and vent valves, the shaft encoder outputs, magnetometer outputs, status of the drive limit switches, high altitude pressure transducer output and counter temperature were all fed into the encoder for storage and transmission. Internally the encoder temperature, motor status, EHT supply status, in flight calibrator status and azimuth servo system status as well as a low altitude pressure transducer reading were determined and stored for transmission.

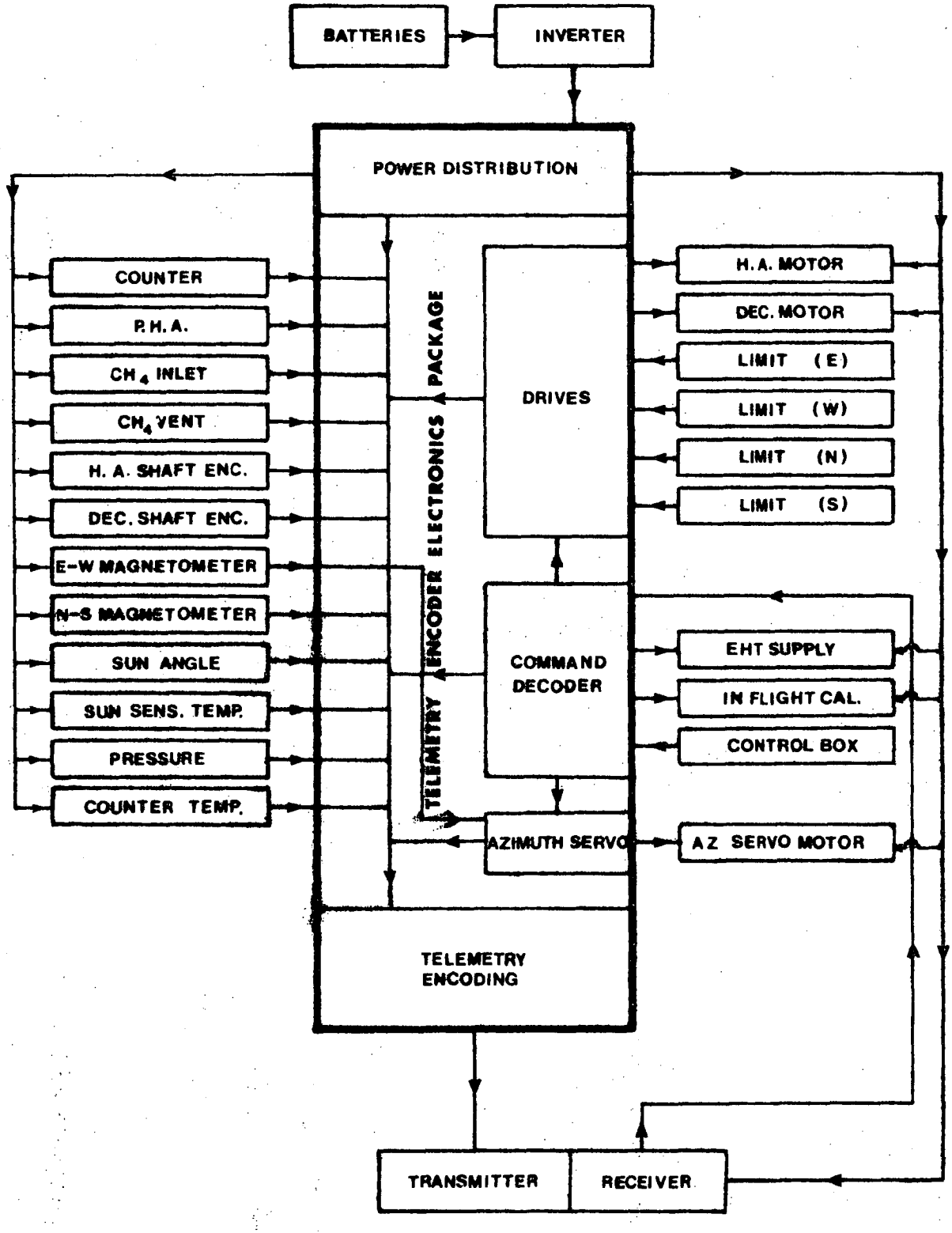

Figure 2-6. Block diagram of the telescope signal processing system.

The drive electronics section acted on signals decoded by the command decoder driving the motors at the required speed in the chosen direction. Limit switches were located on the platform and when actuated caused the drive electronics to reverse the relevant motor direction automatically.

The command decoder section, also decoded the azimuth servo on/off command and passed it to the servo electronics, as well as the on/off commands for the EHT and the in flight calibrator. The EHT power supply was located in the collimator section of the counter vessel and generated a high tension voltage linearly dependent on the applied input voltage. This input voltage was fixed before flight to give an EHT voltage of $\sim$ 2300 volts and the relevant input supply was switched on or off by command.

The control box was a directly connected series of push-button switches which allowed local manual operation of the commands for laboratory testing or pre-launch final checkouts. Light emitting diodes above each switch showed verification of the command acceptance.

The azimuth servo-system picked up the E-W magnetometer signal and drove the reaction wheel as described in 2.2.4. Within the encoder all these signals were stored and fed to the transmitter in serial form. Odd parity after every eight bits and format frame identification numbers were also added to facilitate decoding at the ground receiver station.

2.2.7 TELEMETRY FORMAT

The telemetry signal is formatted with two types of sixteen bit data words, the 'A' and 'B' words. Figure 2-7 shows the structure of a complete Subframe. The Subframe is built up from thirty two 'A' words, each one being followed by four 'B' words.

The 'A' words are made up of two parts: the five most

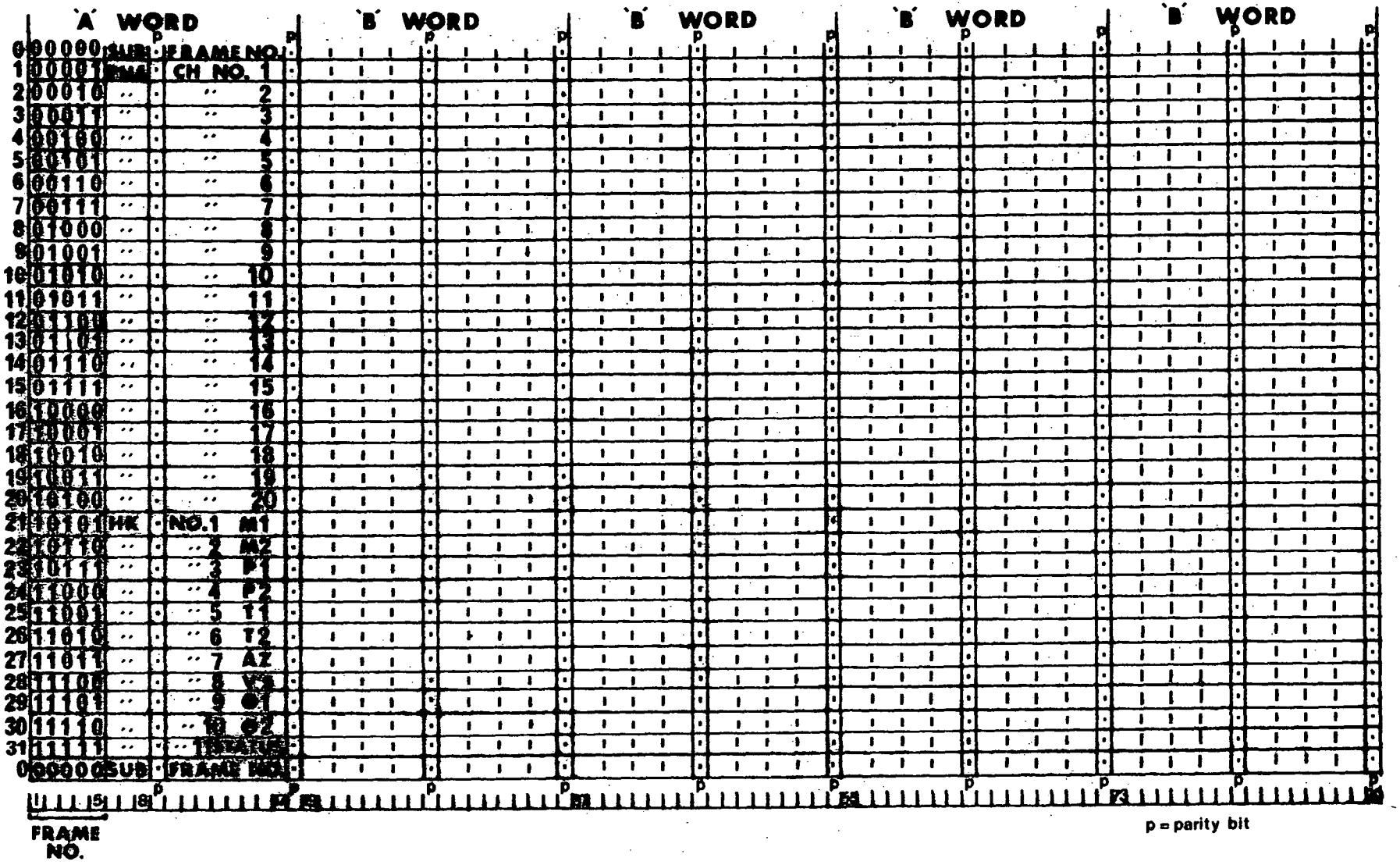

Figure 2-7. The telemetry format of a complete subframe. Bit numbers within each frame are shown at bottom.

significant bits are an identifier (ID) from zero to thirty one whilst the remaining eleven bits are PHA or House Keeping (HK) data. Frame '00000' is followed by a Subframe number of eleven bits (2047 maximum). Frames '00001' (1) to '10100' (20) are followed by the PHA totals and frames '10101' (21) to '11111' (31) are followed by the HK data. Table 2-2 shows the allocations of the HK channels for the 1976 flight. The output of frame '11100' (28) was subcommutated to give four voltages (battery, +12 volt regulated, EHT supply and +24 volt unregulated).

Table 2-2

House Keeping Channel Allocations for Flight 665

Frame No.	HK No.	Data Type	Function
21	1	11 bit binary	Magnetometer E-W
22	2	"	" N-S
23	3	"	Pressure transducer 1
24	4	"	" " 2
25	5	"	Electronics temperature
26	6	"	Counter "
27	7	"	Azimuth error voltage
28	8	"	Voltages, subcommutated
29	9	11 bit gracode	Hour Angle shaft encoder
30	10	"	Declination " "
31	11	11 bit (individual)	Status word

Frame '11111" (31), the status word, was broken up as shown in Table 2-3. The MX indicator was a two bit word indicating which of the four subcommutated voltages was last transmitted.

Table 2-3

ID 31 'A' Word Allocation of Status Bits

	on/off	open/closed			on/off	N/S	on/off	track/slew	W	on/off
1 1 1 1 1	×	×	×	× ×	×	×	×	×	×	×
Frame No. 31	cal	Inlet Vent		MX	AZ	Dec		HA		

The 'B' words were made up of eight, two bit count rate words, known as PSR words, each representing the number of pulses detected by the PHA in channels six to fourteen inclusive in 0.5 ms. The two bit output was usually zero but could also have values of one, two or greater than or equal to three.

Each word, 'A' or 'B', took 3.2 ms to be transmitted. Alternatively, the time to transmit a complete Subframe was 512 ms. During this time 128 'B' words or 1024 two bit, 0.5 ms count rate samples were transmitted (i.e. 512 ms of real time samples). Thus the 'A' word data had to be interwoven into the bit stream by compressing the 'B' words (to 410 ms) to allow real time transmission.

Before transmission a parity bit was added after every eighth bit. Thus 2880 bits were transmitted every Subframe (512 ms) corresponding to a bit rate of 5625 bits per second.

This telemetry bit stream was passed from the encoder to the transmitter in Non Return to Zero (NRZ) form.

2.2.8 TELEMETRY DECODER

A schematic diagram of the decoder is presented in figure 2-8. The bit synchronizer generated a data clock signal at the same frequency and in phase with the NRZ data signal. The voltage control oscillator (VCO) frequency was divided by three when locked to the data signal but was adjusted by varying the divisor to ÷4 or ÷2 if the data signal was

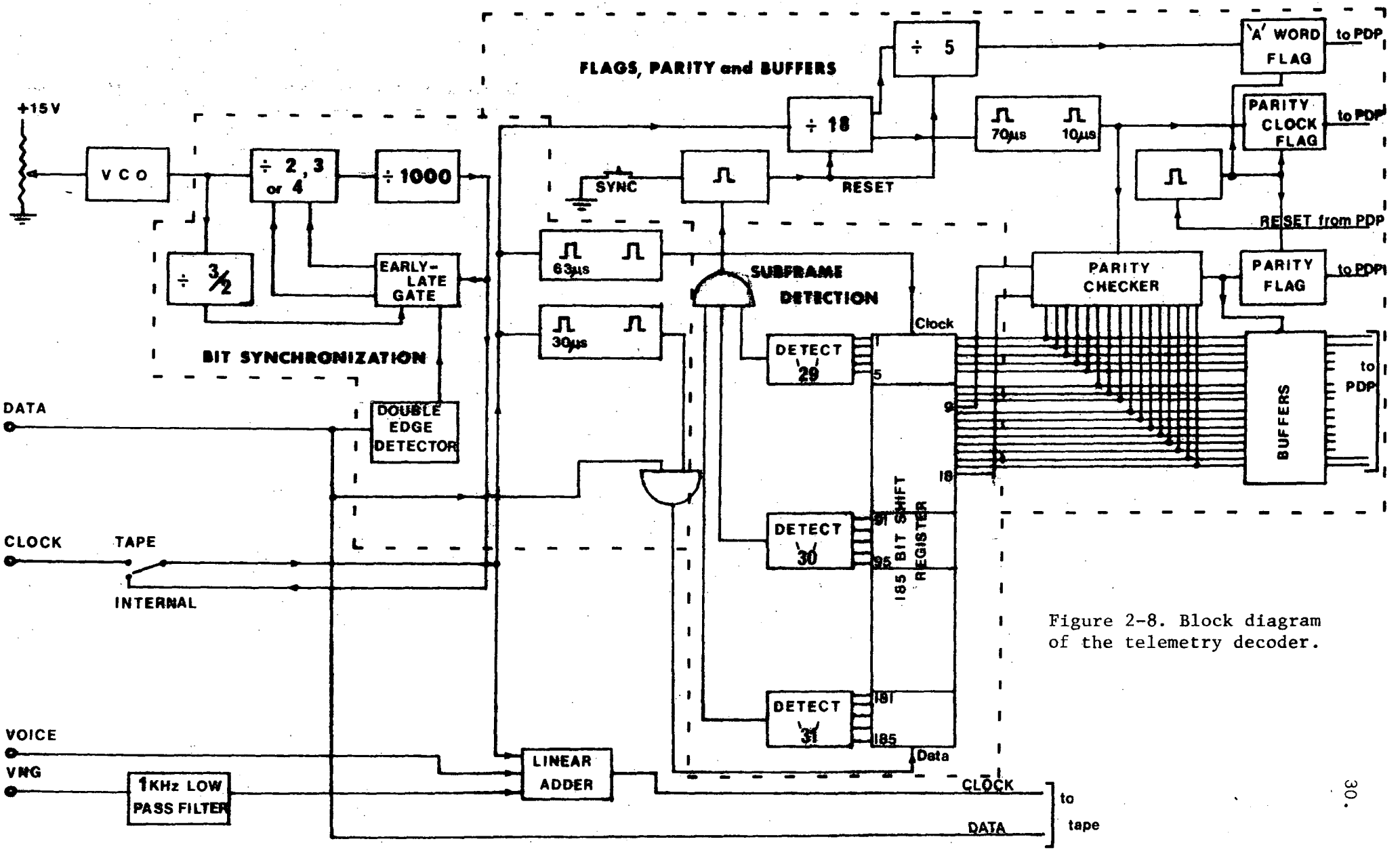

Figure 2-8. Block diagram of the telemetry decoder.

early or late. This technique was especially important when replaying the data tapes as tape stretch and dropouts could generally be coped with satisfactorily.

Subframe synchronization was achieved by detecting three frame numbers within each Subframe. The data were fed serially into a 185 bit shift register and the detection of '30', '31' and '0' in bits 1-5, 91-95 and 181-185 respectively generated a synchronizing pulse every 512 ms. This pulse was then used to reset the clock dividers for the various data type flags.

The parity clock flag was generated once every 18 bits. As two bits were used for parity and removed by the decoder, once synchronized this flag indicated that a new 16 bit data word was available in the buffers. The parity clock flag was therefore employed to generate interrupts to the PDP 11/10 processor.

The 'A' word flag was derived from the parity clock flag by a simple division by five. As can be seen from the telemetry format in figure 2-7 every fifth 16 bit word was an 'A' word and when synchronized this flag was passed to the computer to indicate the data word type (1 for an 'A' word, 0 otherwise).

Finally the parity flag was generated by the parity checker when each parity clock flag pulse appeared. Odd parity was used to avoid synchronization problems when long strings of zeros (or ones) were encountered in the NRZ bit stream (i.e. a data bit transition at least every 15 bits must occur thus enabling synchronization of the generated clock to the bit stream). Parity errors were passed to the computer using the parity flag.

All flags were reset by the computer on completion of the buffer read sequence.

Data recording is described in the following section, however

it should be noted that the clock signal was recorded after the VNG short wave radio standard time signal and a voice commentary had been added within the decoder at much lower levels than the clock signal.

2.2.9 DATA RECORDING

A TEAC A-3300SX domestic tape recorder was modified to allow the 5.625 KHz NRZ data bit stream to be recorded by a head saturation technique. This involved passing a fixed current through the record head and magnetically saturating the tape and reversing the current flow for a transition between zeros and ones.

For data recovery the playback head output was amplified and fed through a Schmidt trigger and the resulting TTL compatible signal was fed direclty to the PDP 11/10 computer via the decoder.

The clock signal modulated by VNG and a voice recording was recorded on the other track of the tape using frequency modulation and was recovered by passing the playback head output through a phase locked loop and filters to the decoder clock input.

2.2.10 QUICK-LOOK ANALYSIS

Machine code software for the PDP 11/10 computer was developed by the author to produce the quick look analysis. Figure 2-9 is a highly simplified flow diagram of the programme. Data interrupts occur every 3.2 ms and real time quick-look processing proved to be difficult. Output was produced every 2ls, this being the time required to complete each printout. The machine code was designed with time efficiency rather that 'core' (memory) efficiency in mind. A typical example is the conversion of the shaft encoder outputs. This was achieved by including a 2048 word lookup table within the programme. The encoder outputs were then treated as offsets from the start of the table and the resulting memory location contained the binary number equivalent to the graycode shaft encoder output. This involved only three machine instructions as opposed to more

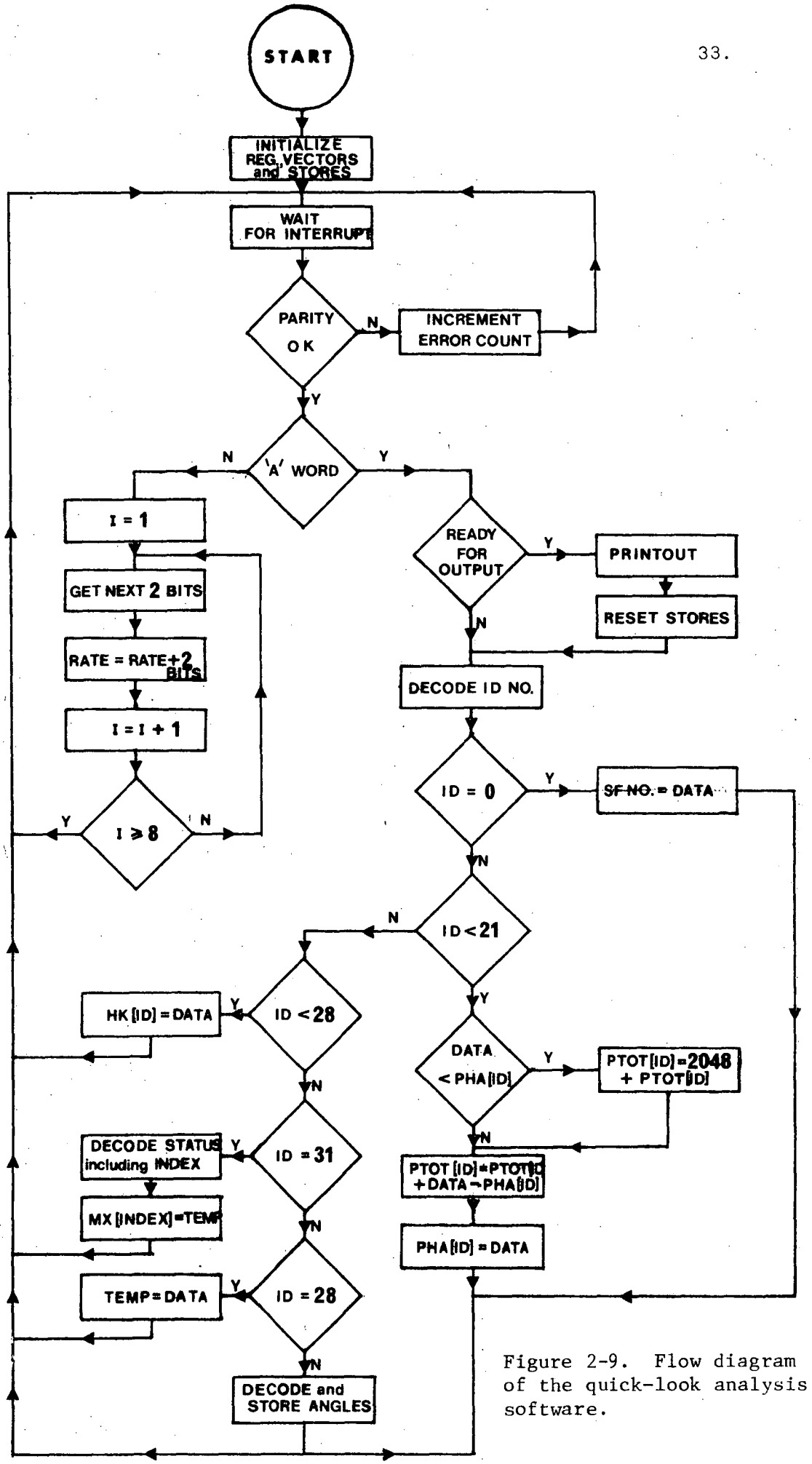

Figure 2-9. Flow diagram of the quick-look analysis software.

than twenty instructions for a conversion routine. Similarly the output table was prepared using a time efficient binary to decimal character conversion routine. The table was stored in memory in advance in character format so that minimum time, under interrupt, would be spent servicing the TTY printer and thus ensuring that all incoming data were analysed.

Figure 2-10 shows a sample of the quick-look output from flight 710, with the meaning of the various numbers. This hard copy was also an emergency backup facility in case of tape recorder failure.

2.2.11 DISPLAY PANEL

Obviously, reading this hard copy output during a flight is not easy and a display panel was constructed by the author which showed the telescope hour angle, declination, sidereal and solar times on seven segment LED displays as well as the eleven status bits on individual LED's. Also included was a thumbwheel switch and seven segment display to allow selection of any 'A' word frame number and display the value of the transmitted word. Thus any HK or PHA channel could be continuously monitored.

The display panel has since been dismantled and replaced by a micro-processor system (described briefly in 5.3.3) and no photographs of the panel are available. Figure 2-11 is a line drawing of the display panel as it was constructed and used. The pattern on the right represents the parity clock flag which was monitored on a CRO display mounted on the panel.

2.2.12 LABORATORY PULSE HEIGHT ANALYSIS

Ground based tests of the counter resolution and escape parameters and cell and sector gain matching (see 2.3.1) were undertaken with a pulse height analyser attached to the PDP 11/10 computer.

Each incoming counter pulse was pulse height analysed and the resulting channel number passed to the computer. Within the computer

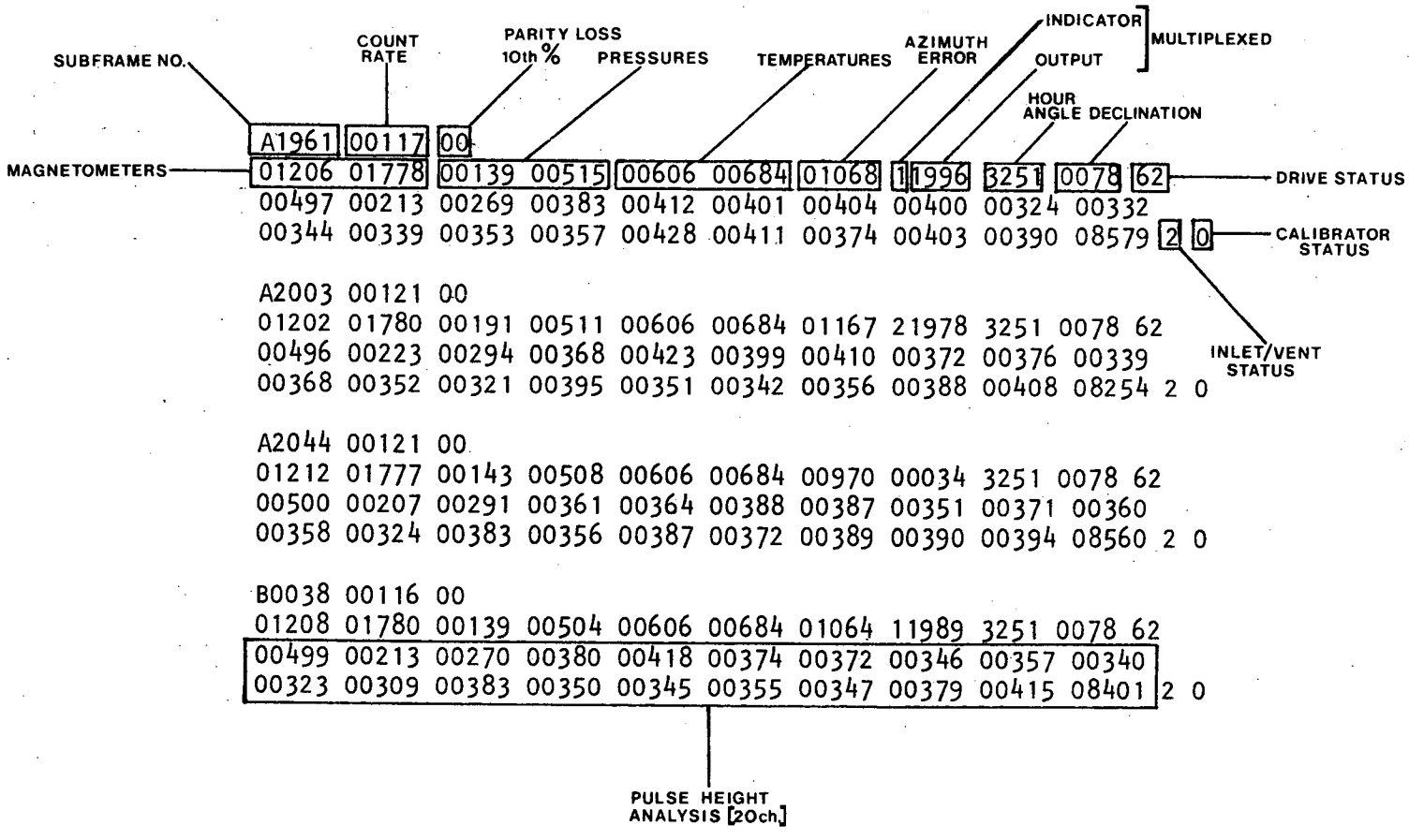

Figure 2-10 Sample output from the quick-look analysis of flight 710. Labels have been added to show the allocations of each number.

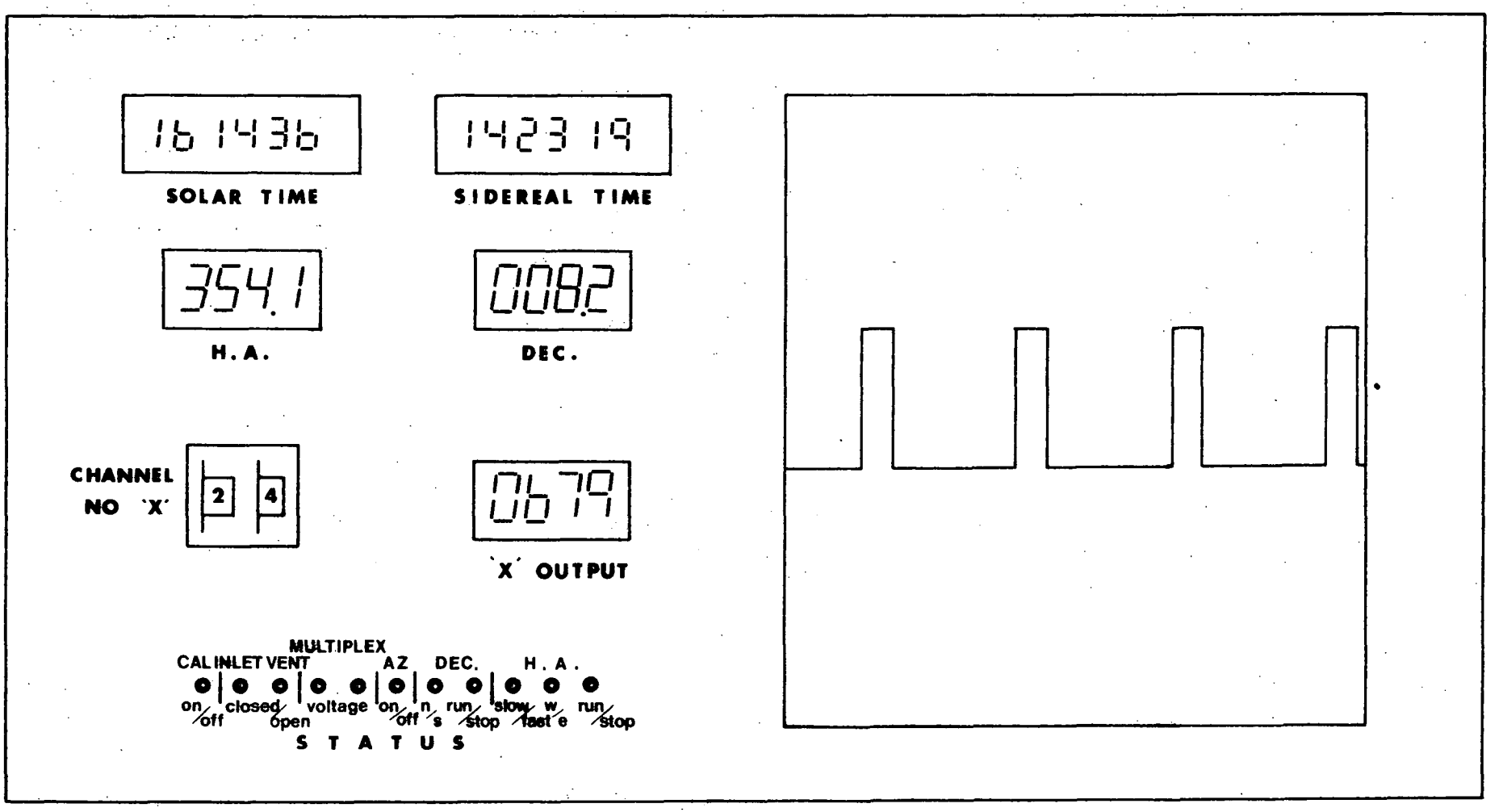

Figure 2-11. Line drawing of the display panel. The pattern at right represents the oscilloscope trace of the parity clock flag.

the received channel number storage location was incremented.

The computer also displayed the contents of all or any selected section of the pulse height distribution on a cathode ray oscilloscope display. Background subtraction was also incorporated. Pulse height analysis could be carried out with 128, 256, 512 or 1024 channels.

The author was responsible for the software development for this system.

2.3 SYSTEM CALIBRATIONS

2.3.1 COUNTER RESPONSE CALIBRATION

Prior to calibrating the counter energy response it is necessary to match the amplifier gains of all the 35 cells. The counter was illuminated by a 25 keV tin fluorescence X-ray source and each cell within one of the five sectors was pulse height analysed into 256 channels using the PHA associated with the PDP 11/10 computer (2.2.12). By varying the input resistor values on a simple adder circuit the gains of the individual cells within each sector were matched. The added outputs from each sector were then fed to the in flight PHA (2.2.2) which included further adjustable gain matching to equalize the sector gains. Comparison and gain adjustments of these five inputs was carried out, resulting in matching of the gain of all 35 cells. Figure 2-12 shows the results of this process for the 1978 pre-flight calibrations. The single sector curve (a) shows the best resolution achieved within an individual sector. Curve (b) shows the overall counter response and demonstrates the difficulties in perfect matching of all the anode gains.

Once the gains of all the cells had been matched the counter energy resolution and escape parameters were determined. Various X-ray calibration sources were employed to calibrate the linearity of the counter, the resolution variation with energy and the probability of Xe K edge

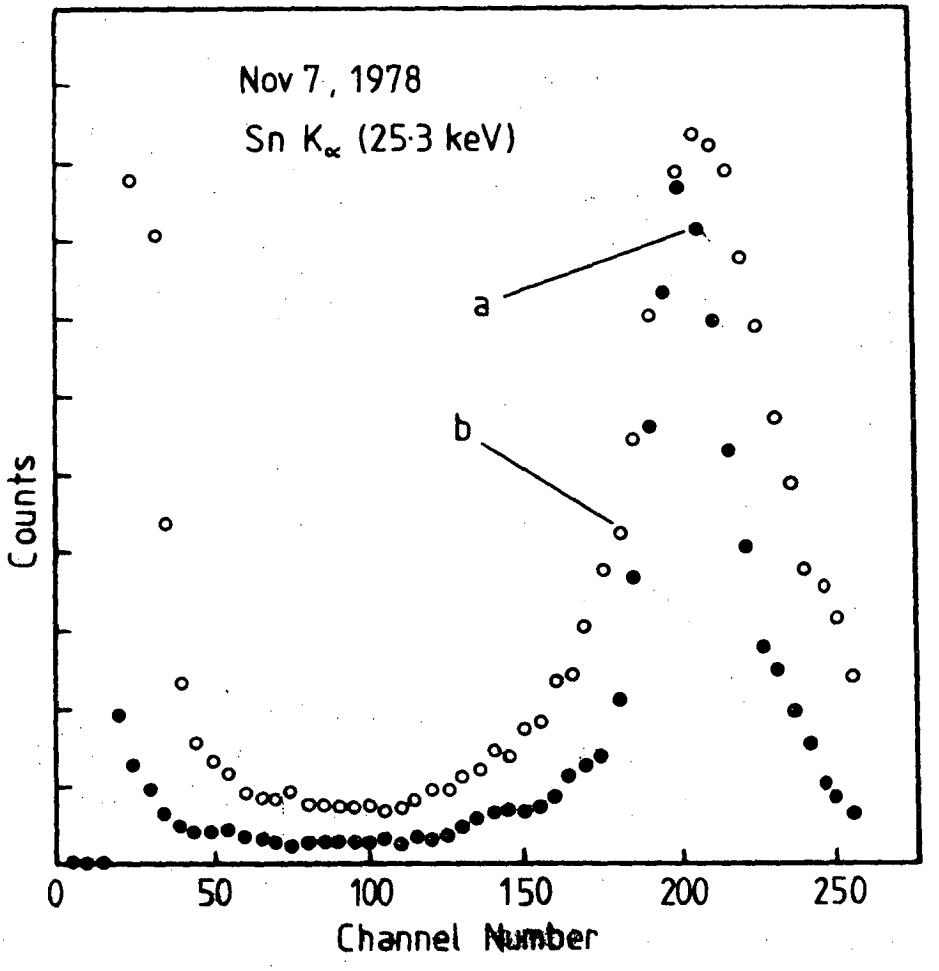

Figure 2-12. Laboratory pulse height distributions (Sn K_α) for (a) sector 5 only, comprising 4 cells and 12 anodes, and (b) all sectors added, i.e. 35 cells and 105 anodes. Resolutions are 15% and 25% FWHM respectively.

fluorescent photon escape. Figure 2-13 shows the results of some of these calibration checks using the in-flight PHA in December 1977. PHA channel 4 was inoperative due to a faulty buffer IC at this time. Other calibration curves are presented in Appendix B. The in-flight Am^{241}, 60 keV source was used to monitor variations in the counter response during flights, giving resolution, gain and escape parameters through the 20 channel PHA telemetered to the ground station (See chapter 3). Counter parameters for the flights are presented in chapter 4.

2.3.2 COLLIMATOR RESPONSE

Ideally,the collimator response should be measured with a calibration source at an infinite distance or at least effectively so. The one metre diameter telescope with a field of view of $\sim 7°$ FWHM would require a source to counter distance in excess of 50 m to achieve this, a difficult task for ground based measurements.

During pre-flight preparations in 1976 $\sim$ 5 mCi Am^{241} (60 keV) source was mounted on top of a radio transmitter tower resulting in a source to counter distance of 17 metres. By placing the source vertically above the counter it was also possible to set up the shaft encoders to give a zero readout at the zenith position. The calibration curves are presented in figure 2-14. Further hour angle and declination collimator response curves determined between 1976 and 1978 are included in Appendix B.

The true collimator response was expected to be triangular with slight rounding at base and apex due to imperfection in collimator cell alignment and could be derived from these calibration curves by two methods. Firstly the FWHM was found by extrapolating the linear part of the response curve after removing the background rate. This method resulted in determinations for collimator FWHM's of 7°.3 and 20°.0 for the

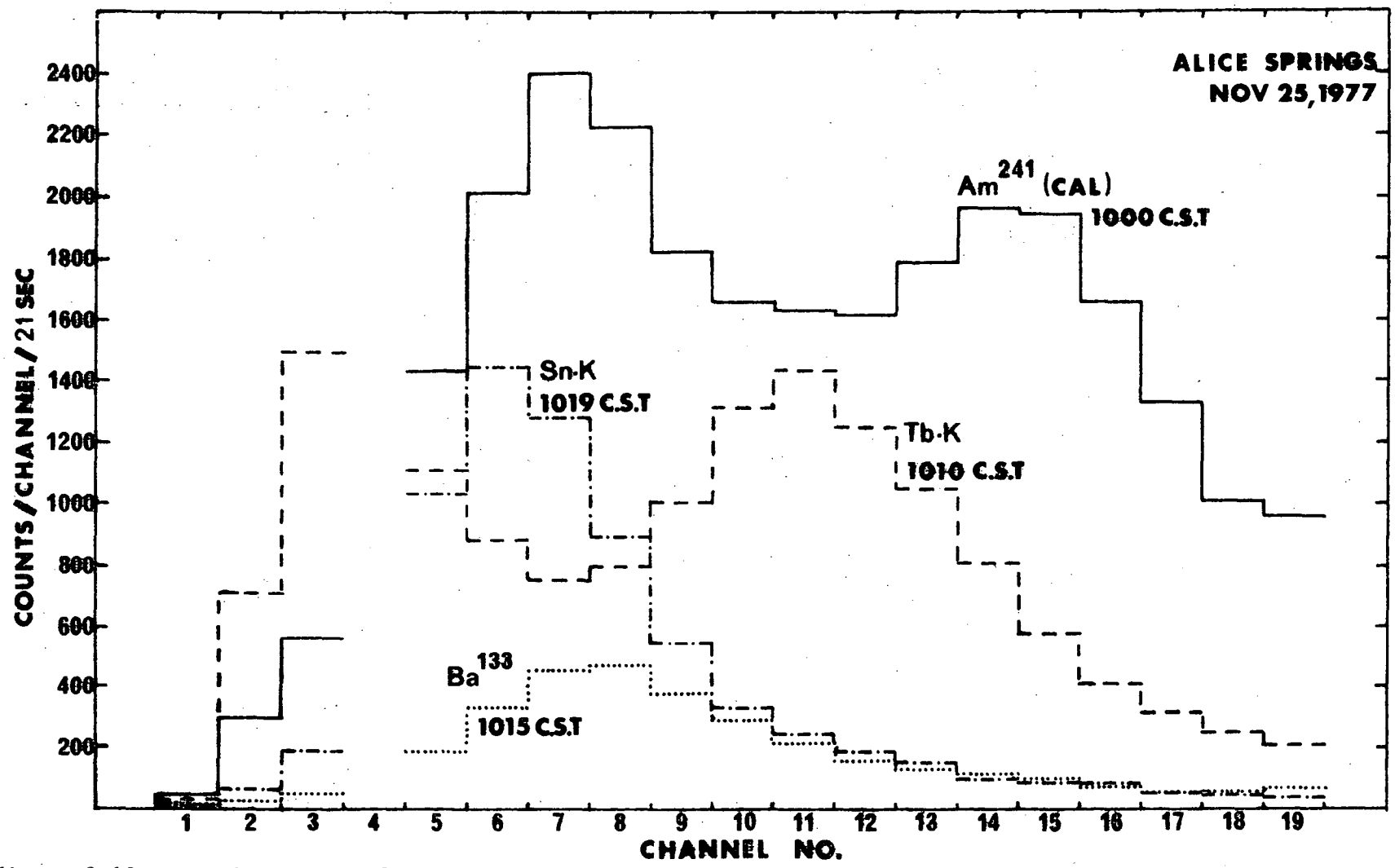

Figure 2-13. Calibration of the counter response to various X-ray line sources.

hour angle and declination respectively. The declination response curve in figure 2-14 has been fitted by this method. The second method of determination involved a least-squares fit of the observed response to a geometric model of the calibration arrangement. The FWHM and source rates were used as variables for this fit. Shown in figure 2-14 on the hour angle plot is the calculated best fit derived by R.M. Thomas using this technique. The result of this determination being $7^{\circ}.3 \pm 0^{\circ}.15$ FWHM for the hour angle collimator.

Final confirmation of the collimator response can be obtained by scanning the telescope across a galactic source of constant intensity during a balloon flight. Unfortunately no constant intensity sources were scanned during the two successful flights.

2.3.3 HOUSE KEEPING TRANSDUCER CALIBRATIONS

The house keeping transducers were calibrated prior to each flight. Temperature calibrations were achieved by recording the ambient equipment temperature as it varied from day to day during the pre-flight preparations and plotting the results against the telemetered output. Packing the equipment in ice also allowed calibration of the lower temperature region.

Pressure transducer calibrations were carried out in the large vacuum chamber used for filling the counter. The chamber was evacuated in stages and transducer readings were recorded at each stage down to $\sim$ 2mb. The resulting calibration curve was then rechecked during the chamber refilling. Several evacuations and refillings were conducted to confirm that the transducer outputs were not affected by pressure cycling.

Voltages monitored throughout the data processing system were also calibrated through the telemetry system. These calibrations are presented in Appendix B.

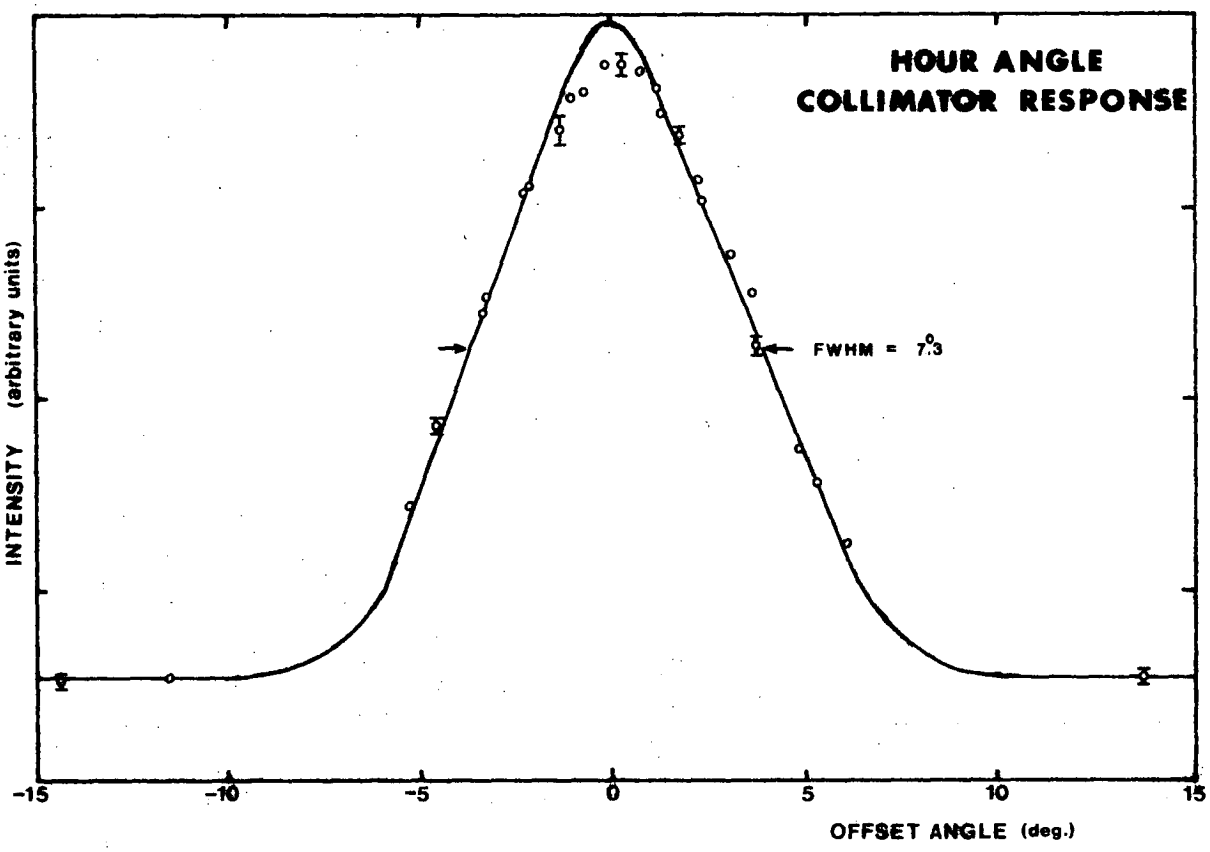

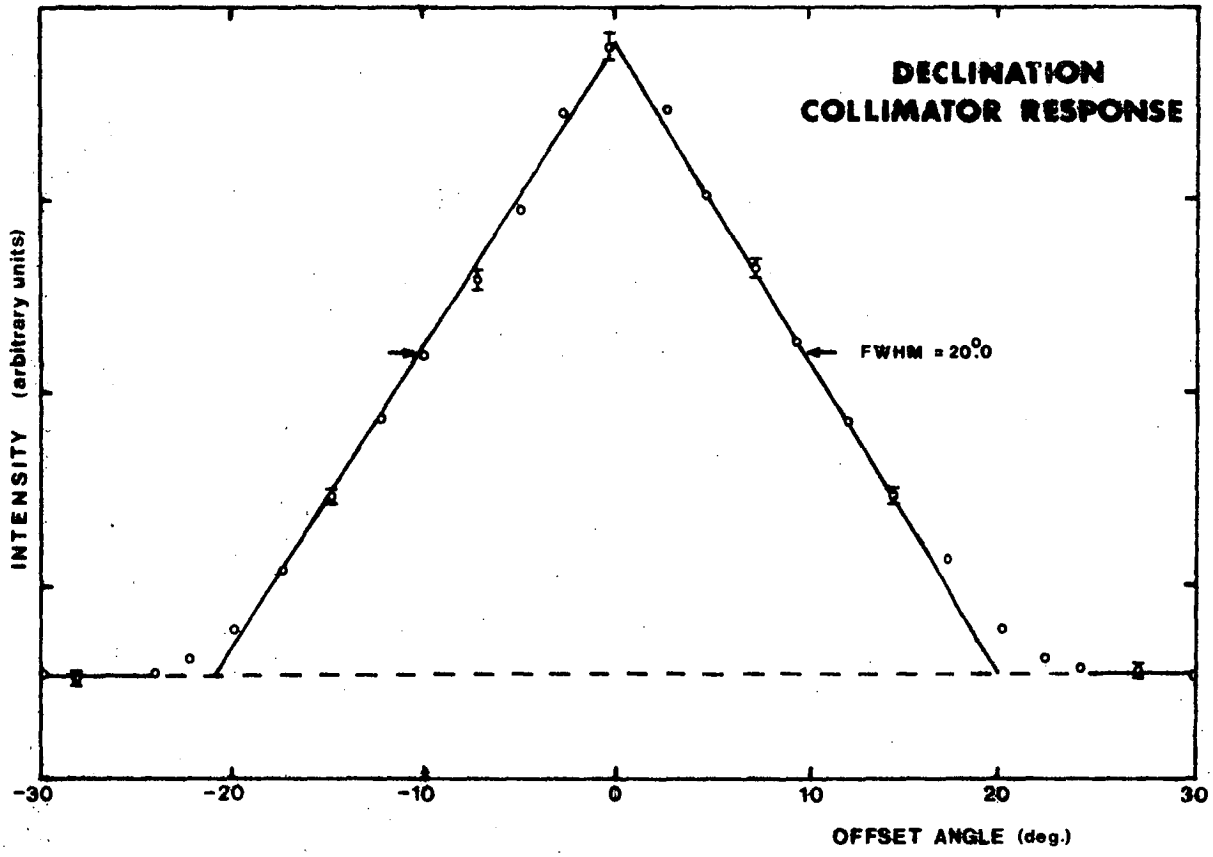

Figure 2-14. Collimator response curves determined in 1976. The error bars are ±1σ.

2.3.4 MAGNETOMETER CALIBRATIONS

The complete payload was mounted on a rotatable table well clear of all buildings. A true north-south line was determined from known local survey points and the magnetometer mounting was adjusted to produce a minimum response in the east-west magnetometer when the payload was oriented along the north-south line. A complete 360° sweep was then carried out and the magnetometer readings were calibrated against the offset angle from north allowing an unambiguous determination of the payload azimuth at all times. Figure 2-15 shows such a calibration.

2.3.5 AZIMUTH STABILIZATION ADJUSTMENTS

Having calibrated the magnetometer response it was then necessary to adjust the azimuth stabilization. The azimuth error signal was derived from the E-W magnetometer output. Variable gain, dependent on the input signal voltage, produced the non-linear error signal shown in figure 2-15. This response,when current-amplified and fed to the reaction wheel motor,produced a maximum restoration torque over most of the azimuth range. Near zero azimuth offset,the lower gain employed allowed locking to the correct orientation. 'Fine tuning' of this system was achieved by adjusting the feedback in this small offset region to give the best possible stability and damping of the servo system. Stability to better than 0°.5 was achieved in the two successful flights.

2.4 OBSERVING TECHNIQUE

2.4.1 TRACKING

The hour angle drive rate had been preset to allow accurate tracking of a source position across the sky. The telescope was driven to the desired declination and then the hour angle drive was slewed to the correct source position. Strong sources were easily seen entering

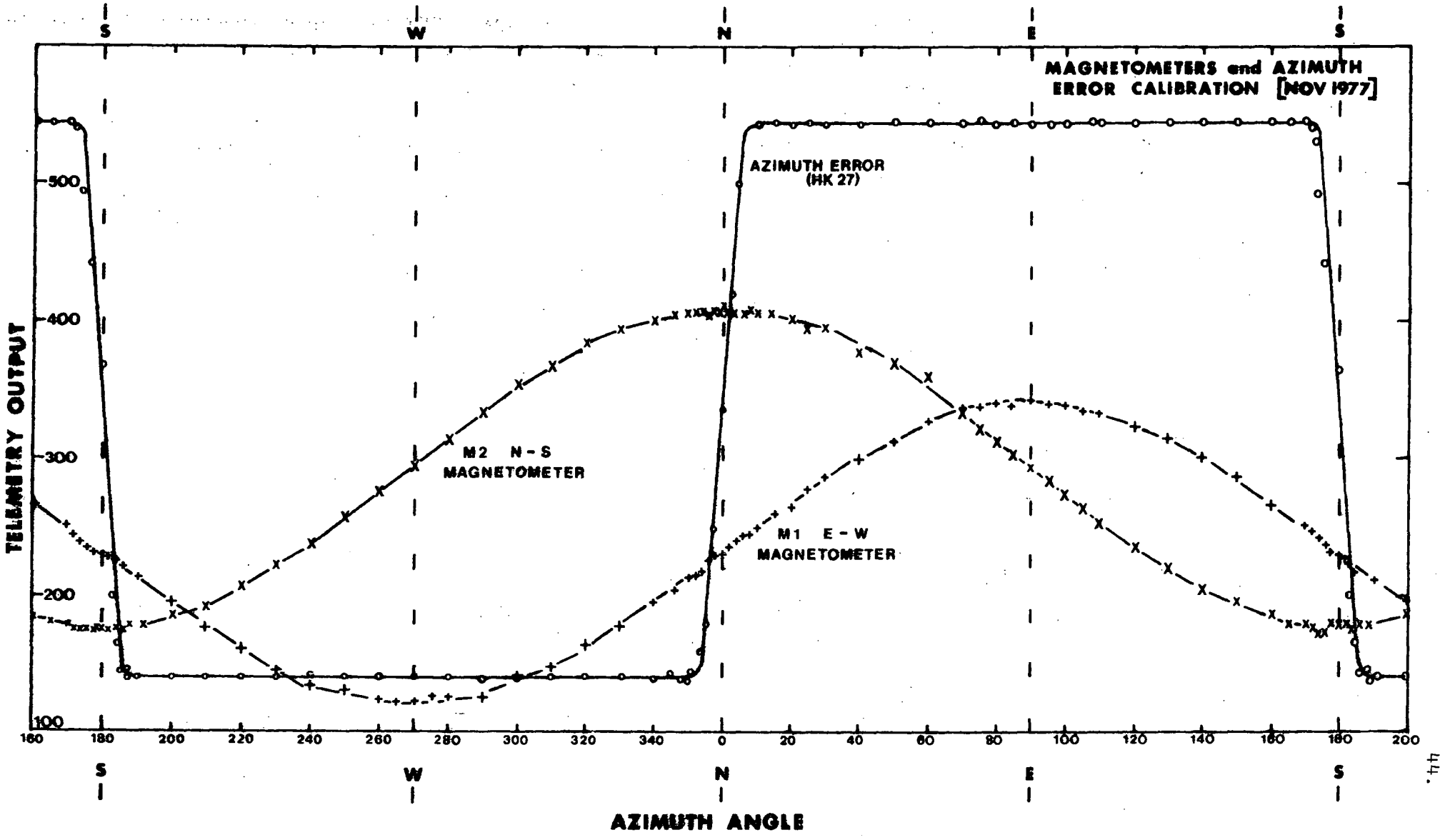

Figure 2-15. Magnetometer and Azimuth Error calibration curves from November 1977.

the narrower hour angle field of view. Once the telescope was positioned on the source the hour angle drive rate would be reduced from the slewing to tracking rates.

Observations of this type were employed to study temporal variations in X-ray sources, especially X-ray pulsars like VEL X-1 (4U0900-40). By driving off source until the collimator field of view excluded the X-ray source position a background rate estimate could be made. Care had to be taken to ensure that this background measurement was obtained from the same zenith angle as the observation because atmospheric absorption and rates of cosmic ray induced atmospheric X-rays showed a strong zenith angle dependance. In practice it was found that background observations, at constant zenith angles, on either side of the source were required to obtain satisfactory estimates of the background rate.

2.4.2 SCANNING

For X-ray source energy spectra determinations a simple method of source scanning was employed. The telescope was pointed to a position ahead (in time) of the X-ray source position. The X-ray source would then drift into the field of view, through the centre of the field and out again. In this way a background spectrum on either side of the source at constant zenith angle was measured and could be subtracted from the source spectrum after taking the triangular response of the collimator into account.

If sufficient time was available, such as in a three day flight, it would have been possible to combine these two observational techniques. The desired X-ray source would be allowed to drift into the centre of the field of view at which time tracking would be commenced. After the desired tracking period had elapsed the hour angle motor would be stopped and the source allowed to drift out of the field of view.

This would enable simple temporal and spectral data reduction from a single extended observation of the source. Unfortunately this optimal technique was not employed as no long duration flights of the telescope system were achieved and the required observation time was not available.

CHAPTER 3

X-RAY DATA REDUCTION

3.1 INTRODUCTIONS

Flight data recovery from magnetic tape was undertaken in several stages. The first stage of the data reduction process involved replaying the tapes and passing the data through the decoder (2.2.8) and then to the computer.

Within the computer the pressure altitude and the pulse height distributions (PHD) of the in flight calibrations were decoded and stored on floppy discs or RK05 disc cartridges allowing a determination of the counter parameters throughout the flight. The tapes were later replayed to recover the PHD's or count rate data of the observed sources for storage in a similar manner.

Count rate data were summed into sample bins of between 0.5 ms and $\sim$ 5 min. depending on the type of subsequent analysis. It was found that sample intervals shorter than $\sim$ 100 ms were of limited value due to the small signal to noise ratio. PHD data could also be binned with a variable sample interval ranging from 0.5 s to $\sim$ 5 min. but generally an interval of $\sim$ 20 s was employed.

3.2 ENERGY SPECTRAL ANALYSIS

3.2.1 General

Two methods of energy spectra determination were employed during analysis of the X-ray data. The minimum χ^2 reduction technique was used as the fundamental procedure for deducing the source spectrum incident at the top of the atmosphere from the flight PHD's. The χ^2 method has some shortcomings, the most important of which is the fitting of an arbitrarily preconceived spectrum with a non-unique solution rather

than an objective reduction. For this reason a more direct approach of spectral reduction, namely apodization, was also employed. (Dolan 1972, Watts and Thomas 1979)

The observed PHD could not be used by the spectral reduction programmes until the effects of the triangular collimator response and the background were removed. A straight line fit of the background count rate, for each pulse height channel, on either side of the source was made. Background subtraction was then undertaken employing these fits. Following the background removal the data for each pulse height channel were summed for the period during which the source was within the collimator field of view. The collimator response function was removed by reducing the total effective time of the observation; this being equivalent to rescaling the intensity of each sample in proportion to the collimator response.

An assumed input spectrum of a 60 keV line source was utilized to model the in-flight calibrations. The spectral reduction programmes, using this model, were applied to the in-flight 60 keV Am calibration PHD's to derive the counter resolution and escape peak to total ratio. These parameters along with the pressure-altitude, the zenith angle of the observation, the effective time of the observation and the background subtracted PHD data were stored for subsequent spectral reduction analysis.

3.2.2 SPECTRAL REDUCTION BY MINIMUM χ^2

The observed distribution as a function of pulse height $P(E')dE$ resulting from a source at the top of the earth's atmosphere and having a differential spectrum $N(E, \alpha, \beta)$ as a function energy E, and described by the parameters α and β can be written as (Stein

and Lewin 1967)

$$P(E')dE = \int_0^\infty N(E, \alpha, \beta).T_a.T_w.(1-T_g).[F_k R(E-E_k,E') + (1-F_k).R(E,E')]dE.dE'$$

$$= N(E, \alpha, \beta).Q(E,E')\ dEdE' \qquad \text{Eq.(3.1)}$$

where T_a, T_w and T_g are the energy dependent absorption functions due to line of sight residual atmosphere, counter window and detection gas respectively;

F_k is the K shell fluorescence escape probability per detected photon for energies greater than the K absorption edge of the detection gas (E_k); and

$$R(E,E') = \frac{1}{\sigma\sqrt{2\pi}} \exp\left[-\frac{(E-E')^2}{2\sigma^2}\right]$$

is the Gaussian function which describes the finite energy resolution of the dectector.

Q(E,E') may be regarded as the total instrument response function. Equation 3.1 has been simplified by treating K_α and K_β resonances together and ignoring L fluorescence escape. The resulting error from these assumptions is very small compared with the counter resolution effects for this experiment and may,therefore,be ignored.

A computer programme including equation 3.1 was employed to generate an expected PHD for a given input spectrum N(E, α, β) and observation time. The counter model (i.e. the non-linear function Q(E,E')) was calculated over an energy range of 10-130 keV to allow for the redistribution effects due to fluorescent photon escape and finite counter resolution.

The generated PHD was then compared with the observations P(E') and the initial estimate parameter values for α and β were adjusted through a least squares analysis. This iterative process continued until the χ^2_ν statistic

$$\chi^2_\nu = \frac{1}{m-k} \sum_{i=1}^{m} \frac{(P'_i - P_i)^2}{\sigma^2_i}$$ was minimized.

where m is the number of pulse height channels; k is the number of spectral parameters deduced, (usually two); and σ_i is the error in the i'th channel total.

The resulting spectral parameters were the *best fit* values for the chosen spectral type. That is not to say that the chosen spectral form was applicable for the source production mechanism. Furthermore the *best fit* solution may still be unacceptable and this would be reflected by the resulting minimum value of the χ^2_ν statistic.

Figure 3-1 is a schematic block diagram of the minimum χ^2 spectral reduction technique.

Three types of spectrum were employed when reducing the PHD data and they are given in table 3-1.

Table 3-1

Test Spectra Employed for Spectral Reduction

Spectral Type	Formula	Variables
Power Law	$I = AE^{-\alpha}$	A, α
Black Body	$I = AE\ /(e^{(\frac{E}{\beta})}-1)$	A, β
Thermal Bremsstrahlung	$I = Ae^{-(\frac{E}{\beta})}/(\beta E)^{\frac{1}{2}}$	A, β

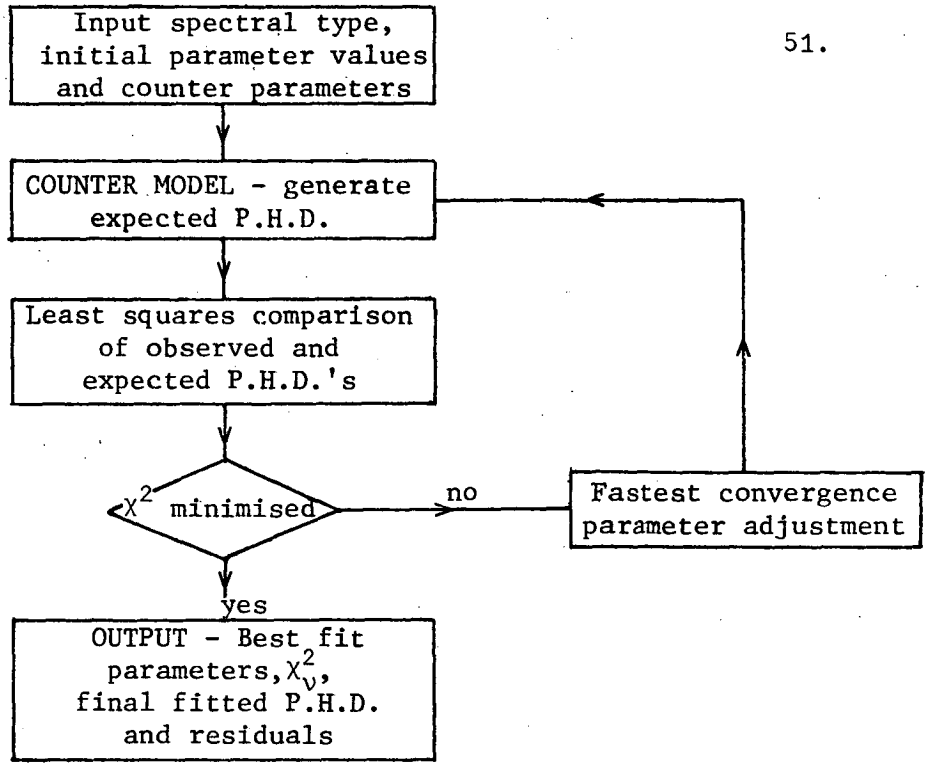

Figure 3-1. Schematic block diagram of the Minimum χ^2 Reduction Technique.

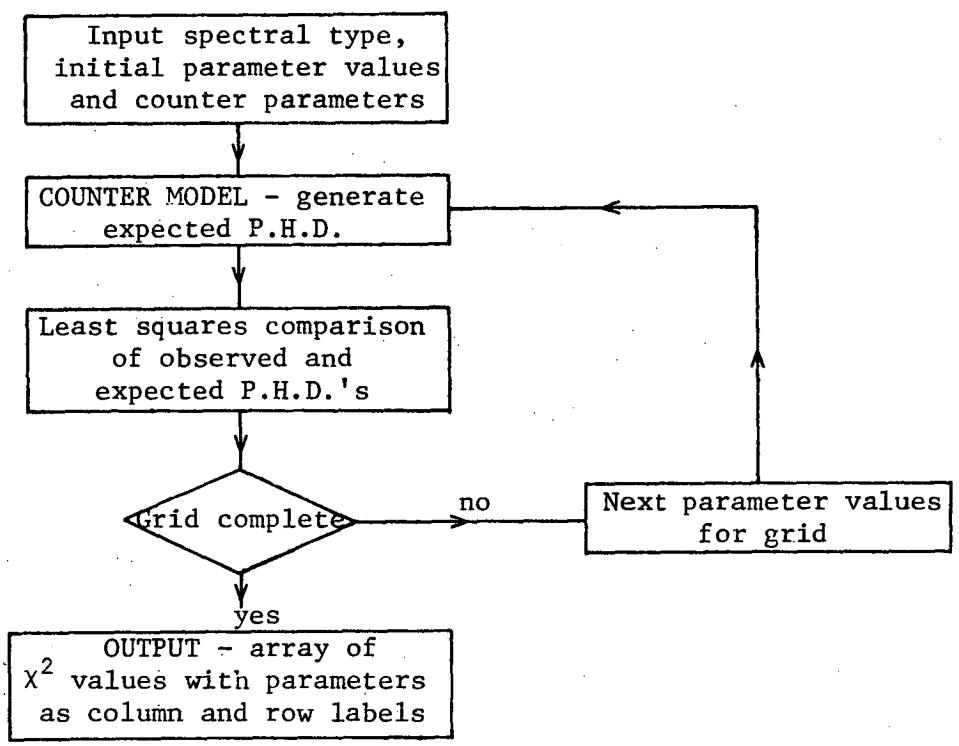

Figure 3-2. Schematic block diagram of the 90% χ^2 contour determination.

3.2.3 90% CONFIDENCE CONTOURS FOR χ^2

Once a minimum χ^2_ν had been determined for a given test spectrum an estimate of the best fit parameter errors was found by calculating the 90% confidence contours about the parameters. This process involved the determination of the χ^2_ν sum for a grid of spectral parameter values about the best fit solution. Figure 3-2 is a block diagram of this process. The parameter pairs which resulted in χ^2_ν sums corresponding to the 90% confidence level were then plotted.

This technique of error estimation was necessary because the counter response function was highly non-linear and similar PHD's could be generated by the counter model for quite different spectral parameters.

3.2.4 APODIZATION

Equation (3-1) may also be written in matrix form (Reigler 1969, Dolan 1972) thus

$$C = QN = RF_k(I-T_g)T_w.T_a.N \qquad \text{Eq. (3-2)}$$

where I is the unit matrix;

C is the column matrix form of the observed PHD; and

N is the matrix form of the incident differential spectrum.

The incident differential spectrum could be determined by a matrix inversion of equation (3-2).

viz. $$N = Q^{-1}C = T_a^{-1}.T_w^{-1}.(I-T_g)^{-1}.F_k^{-1}.R^{-1}.C \qquad \text{Eq. (3-3)}$$

The inverse matrices of the right hand side of equation (3-3) are easily determined with the exception of the R matrix which is effectively singular. Dolan (1972) proposed the use of the technique

known as apodization (Lloyd 1968) to obtain a numerical approximation for $R^{-1}C$. By letting $R^{-1}C = C'$, C' will have column elements

$$C'_i = C_i - s_i\left[\frac{1}{2}\,(C_{i+\ell} + C_{i-\ell}) - C_i\right] \qquad \text{Eq. (3-4)}$$

where ℓ is known as the apodization length in channels; and

s_i is an instrument factor given by

$s_i = (\sigma^2/\ell)$

Dolan recommends choosing $s_i \sim 1$ and tests carried out by Watts and Thomas (1979) showed $s_i = 1$ to be optimum.

A computer programme incorporating equations (3-3) and (3-4) was written by Watts and Thomas to determine the incident differential source spectrum and then to compare this reduced spectrum with the various model spectra presented in table 3-1. The technique proved to be extremely quick and inexpensive to run on the Burroughs B6700 computer. The errors involved in the reduced spectra were larger than the corresponding errors for the minimum χ^2 determinations (Watts and Thomas 1979) but the derived parameters were consistent. For this reason the apodization technique was utilized for the initial estimate parameter values which were then employed in the χ^2 determinations.

Another, more important, reason for employing the apodization technique was the direct generation of the source spectrum. The true incident spectrum could be determined and checked for unusual features (i.e. a two component spectrum or a line in the spectrum) before choosing the best test model for the χ^2 reduction analysis. This then allowed the χ^2 reduction technique to be employed without the problems of a preconceived spectral form affecting the interpretation.

3.3 TEMPORAL ANALYSIS

3.3.1 FAST FOURIER ANALYSIS

Searches for periodic behaviour in the X-ray count rate data were made using the fast Fourier transform (FFT) technique. The algorithm employed was that of Cooley and Tukey (1965). Searches for periods in the range 0.5 - 500s were made using the power spectrum formed from the FFT.

Individual power spectrum terms are characterized by standard deviations equal to the power terms (i.e. 100%) for all frequencies except zero and 1/2T, where T is the sample integration time. The zero and 1/2T terms have standard deviations $\sqrt{2}$ times larger (Welch 1967). These large errors must be reduced before the power spectrum is of any value.

One method of error reduction is to smooth the power spectrum. Such smoothing was achieved by averaging four individual power spectrum terms and thus reducing the standard deviations to half the power (or 50%) for each spectral point excluding the zero and 1/2T terms. This also reduces the number of points making up the spectrum by a factor of four and so increases the bandwidth of each averaged point by the same factor.

An alternative method of error reduction is discussed by Welch (1967). If the data sample is divided into N non-overlapping sections and the power spectrum determined for each section then the average of all the resulting power spectra will have standard deviations reduced by a factor of $\sqrt{N}$.

Consider four sections of data each consisting of 256 samples with a sample integration time of T. Using the method discussed by Welch a power spectrum of 128 points, covering the frequency range zero to 1/2T, with standard deviations of $1/\sqrt{4}$ times the power (i.e. 50%)

will result. These four sections may also be considered as a single data set of 1024 points. Performing the FFT analysis on this larger set produces a 512 point power spectrum over the same frequency range. The four point average of this spectrum is a 128 point power spectrum with standard deviations of 50%. Clearly,the two error reduction techniques are equivalent, the first method being a special application of the more general second method.

Power spectral analysis was carried out on the PDP 11/10 computer and limited memory storage required that Fourier transforms be limited to a maximum size of 1024 points. Both techniques of error reduction were therefore employed.

3.3.2 SUPERPOSED EPOCH ANALYSIS

When an X-ray source of known periodicity was observed (e.g. Vela X-1) superposed epoch analysis was applied to the count rate data. This simple technique involved folding the count rate data, modulo the known period, and summing the data into a number of bins (usually 10). The resulting count rate profile would thus enhance any periodic fluctuations at the source period and a pulse profile against periodic phase was produced. The fraction of the source flux responsible for the periodic variation could also be easily determined from the resulting profile if the off source background count rate were known.

3.4 REFERENCES

Cooley J.W. and Tukey J.W. (1965) Math. Computation 19, 297

Dolan J.F. (1972) Astrophys. Space Sci. 17, 472

Lloyd K.H. (1968) Am. J. Phys. 37, 329

Reigler G.R. (1969) NASA Report X-611-69-1, Goddard Space Flight Center, Greenbelt, Maryland

Stein J.A. and Lewin W.H.G. (1967) J. Geophys. Res. 72, 383

Watts D.J. and Thomas R.M. (1979) Astrophys. Space Sci. 64, 213

Welch P.D. (1967) IEEE Trans. Audio and Electroacoustics Vol AU-15, p70.

CHAPTER 4

X-RAY OBSERVATIONS

4.1. BALLOON FLIGHTS

4.1.1 GENERAL

The author was involved in three balloon flight expeditions in 1976, 1977 and 1978. The three flights were launched by the Australian Balloon Launch Station staff and will be referred to by their ABLS flight numbers: 665, 687 and 710 respectively.

4.1.2 FLIGHT 665

Payload preparations for flight 665 were undertaken in October and November 1976 at the ABLS, Mildura. The detector was filled to 1100 mbar ($\sim$1.1 atmospheres) with 406 mbar Xe, 563 mbar Ar, 63 mbar CH_4 and 68 mbar He. The balloon payload was transported to Parkes, central New South Wales, where the flight was launched at 5.25 a.m. Australian Eastern Summer Time on 2nd December 1976.

The payload achieved a float altitude of 4.7 mbar at 7.45 a.m. and drifted north and west. The telemetry signal was finally lost at 3.45 p.m. and the flight was terminated by payload cutdown at 4.20 p.m., landing near Cobar in Western New South Wales. The payload was recovered, with minor damage to the support frame, on the following day.

This inaugural flight of the complete telescope system had been planned, primarily as an engineering flight, testing the system under observational conditions. The system performance was excellent and some observations of scientific interest were made. (Duldig et al. 1977)

4.1.3 FLIGHT 687

Flight preparations of the payload were started in early November 1977 at the ABLS site at Alice Springs airport, Central

Australia. An attempted launch on 30th November was aborted when the balloon failed to lift the payload, dragging it across the airfield. The launch failure appeared to be due to a leak from the balloon, however this is not certain. High ground winds over the next week prevented any further opportunity for a launch in 1977.

4.1.4 FLIGHT 710

Preparations for a three day balloon flight were commenced in October 1978 in Alice Springs. The payload was launched at dawn on 20th November, attaining a float altitude of $\sim$ 3.5 mbar. The balloon and payload were maintained at this altitude by ballast drops until the early evening when the balloon began to descend. Failure of the ballast release valve forced a premature termination of the flight at approximately 9.00 a.m. Central Standard Time on 21st November.

The payload was recovered on the same day. The support frame was severely damaged by the impact, having rolled over when the parachute failed to release. The telescope, however, remained undamaged.

The counter had been filled with 710 mbar Xe and 304 mbar He. The He was necessary to increase the counter section pressure whilst maintaining an acceptable signal to noise ratio and operating with a comfortably low anode high voltage. Subsequent modifications to the detection electronics have allowed a pure Xe detection medium.

4.2 RESOLUTION, ESCAPE AND LINEARITY

4.2.1 FLIGHT 665

Counter resolution was determined by ground based measurements prior to launch as well as in-flight measurements of the calibration source. A resolution of 40% FWHM at 59.6 keV (Am^{241} line energy) was deduced for flight 665. (Greenhill et al. 1977). The same measurements yielded the escape peak to total absorption ratio, known as the escape

fraction, of 0.60. Using Monte Carlo techniques, Dr. R. Thomas predicted that, for a pure xenon detection medium the escape fraction would be 0.37 and for Flight 665 0.57. The higher value reflects the decreased absorption of the gas mixture employed.

The pulse height analyser (PHA) linearity was checked before the flight by illuminating the counter with a series of calibration sources in turn (figure 2-13 and section 2.3.1). All PHA channels were found to be 5 keV wide with the exception of the first channel where the LLD (figure 2-5 and section 2.2.2) was set to a pulse height equivalent to 5 keV. The range of the first channel was 5-7 keV. For this flight only, the last PHA channel (PHA 20) contained the counts detected above 97 keV, as opposed to the veto counter rate.

Figure 4-1 shows the preflight counter response to the 59.6 keV Am source. Curve (a) gives the pulse height distribution on 24th November, with a resolution of 38%, and curve (b) shows the distribution in its telemetry format five days later. The resolution in curve (b) is 40% and shows the extent of gas deterioration with only 406 mbar of Xe in the counter. A pure Xe counter would be even more sensitive to outgassing impurities and the need for the gas recirculation system described in section 2.2.3 is obvious.

4.2.2 FLIGHT 710

Prior to the launch the counter resolution was found to be 25% FWHM at 25 keV (figure 2-12) or $\sim$ 16% at 60 keV (Greenhill et al. 1979b). A fault in the pressure equalization servo system (section 2.2.2) resulted in severe distortion of the aluminium entrance window. This displacement increased the volume of the detector chamber which, in turn, reduced the Xe pressure within the detecting medium. The gas gain of this type of proportional counter is extremely sensitive to

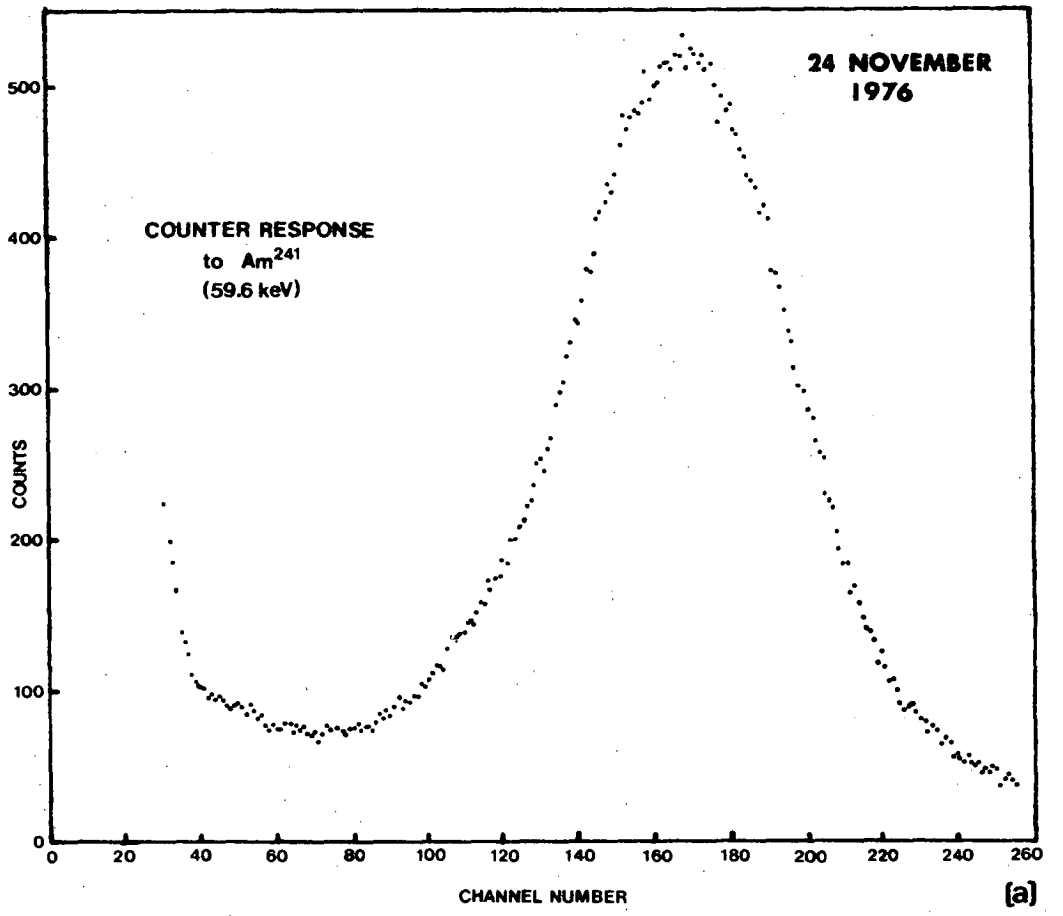

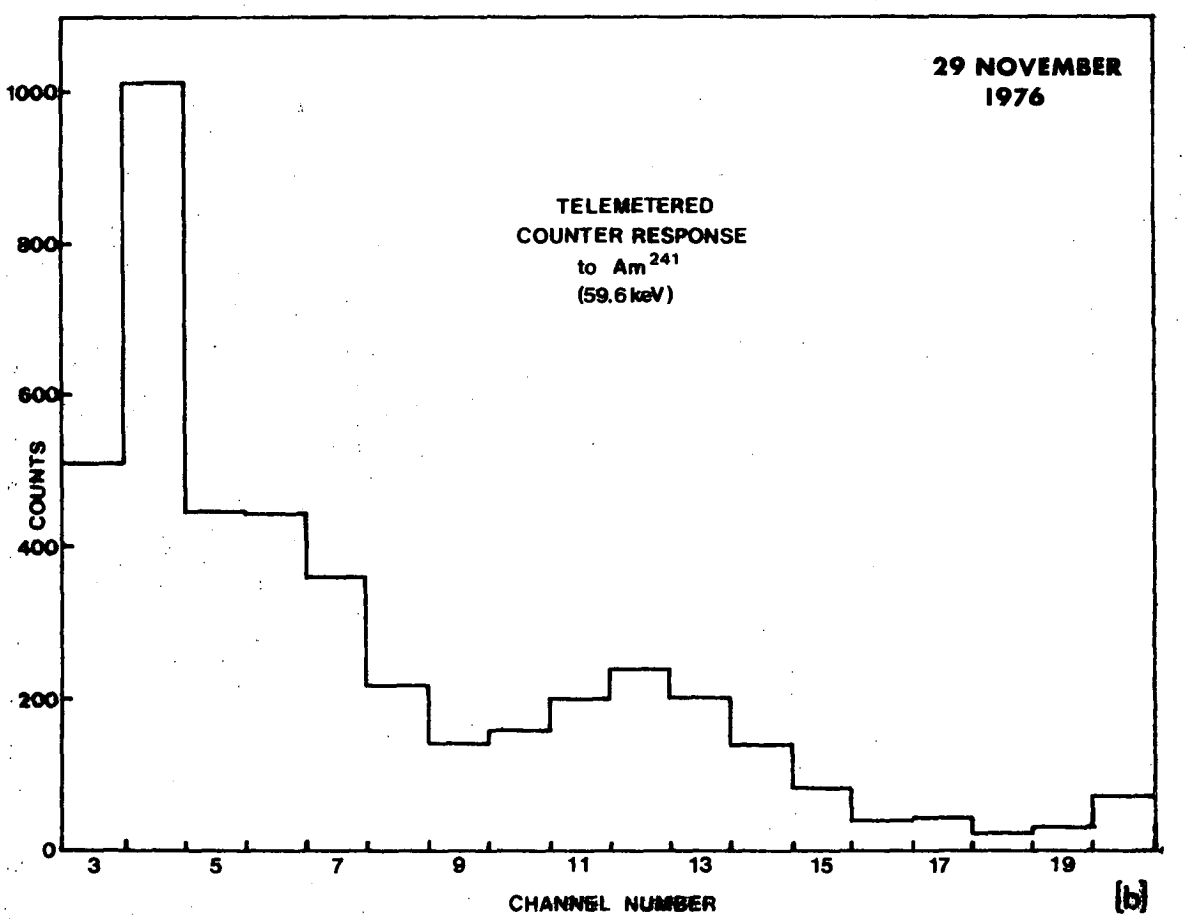

Figure 4-1 Preflight counter response. Curve (a) is from the ground based pulse height analyser and curve (b) is from the telemetry PHA.

changes in pressure and thus a large gain increase resulted.

In flight calibrations at the float altitude no longer showed the 59.6 keV Am^{241} peak which had shifted beyond the upper channel during ascent as a result of the gain increase described above. The escape peak at $\sim$ 30 keV was still visible. Assuming that zero energy X-rays would still give rise to zero height pulses it was possible to compare the pre-flight and in-flight positions of the 30 keV escape peak and determine the channel boundaries. Extrapolating the pre-flight energy linearity curve back to zero energy gave the fixed zero energy reference point from which the in-flight linearity curve could be determined, (figure 4-2). The resulting channel widths were found to be 2.75 keV with a minimum energy for the second PHA channel of 8.92 keV.

A further difficulty resulting from the window distortion was encountered. The window acted as a ground plane for the uppermost detection tray. Thus the resolution and gain of the top tray were significantly different from the remaining trays. X-rays from the in-flight calibration source, mounted on the counter chamber wall adjacent to the central tray, are usually absorbed before reaching the top tray and as such do not illuminate the top tray well. At the centre of the top tray < 3% of the X-rays will have penetrated. Thus the effects of observing through the entrance window and top tray (where $\sim$ 50% of the incoming X-rays will be detected) were poorly determined from the in-flight calibrations.

Energy resolution and escape parameters of the counter were derived by fitting the observed pulse height distribution to an input line spectrum after deconvolving the counter response function. The results are presented in Table 4-1.

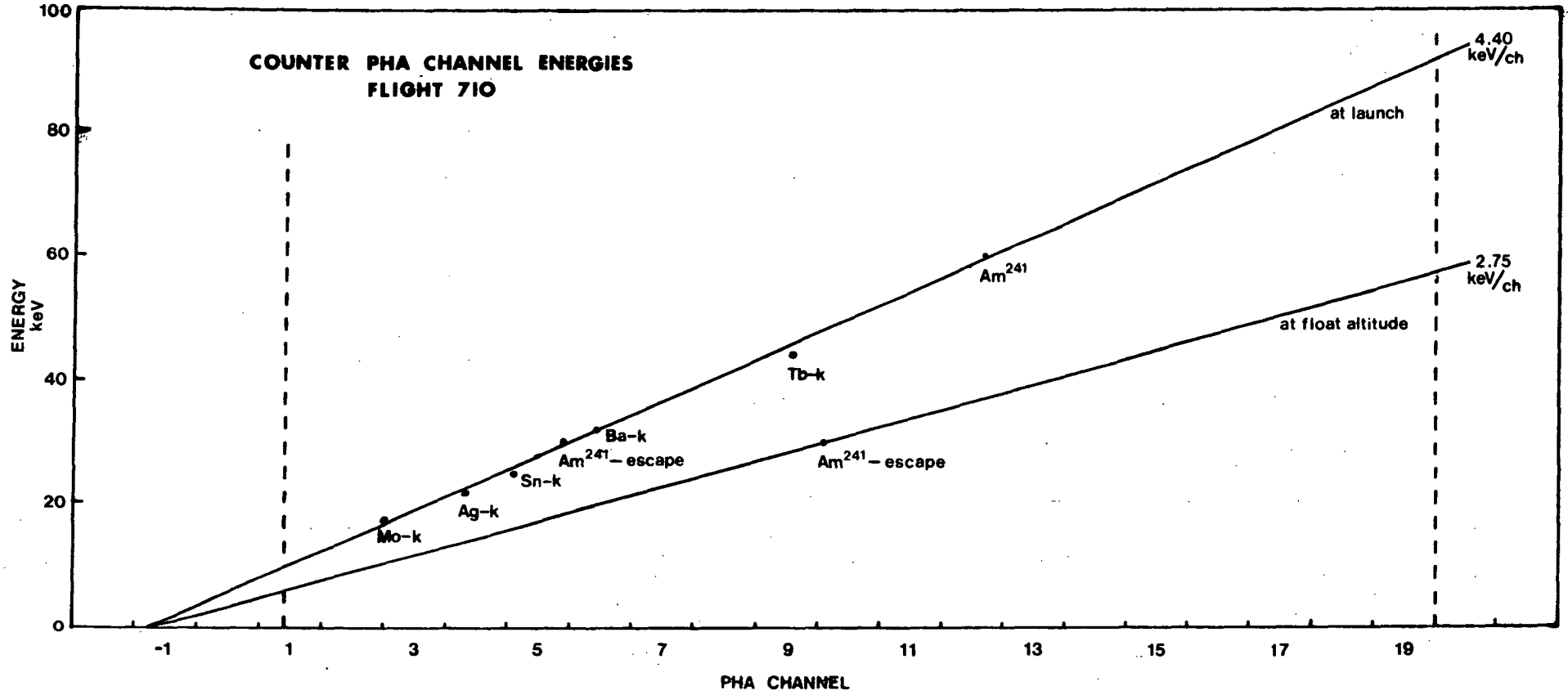

Figure 4-2 In-flight counter PHA energy linearity curve for flight 710.

Table 4-1

Calibration source determination of the counter parameters	
Minimum Energy of PHA2	8.92 keV
PHA Channel Width	2.75 keV
Resolution at 60 keV	50.6%
Escape fraction	0.455

By varying these counter parameters it was found that better fits to the spectral data from the two scans of SCO X-1 (4.4.3) were obtained with the counter parameters given in Table 4-2.

Table 4-2

Best Fit Counter Parameters for SCO X-1 Data	1st Scan	2nd Scan
Minimum Energy PHA2	8.92 keV	8.60 keV
PHA Channel Width	2.75 keV	2.68 keV
Resolution	40.1%	
Escape	0.455*	
Pressure Altitude (measured)	4.47	3.90

*See text

To justify using the counter parameters given in Table 4-2 simulated data were generated for various spectral forms using the counter model with known resolution and "escape" parameters. Noise was then added to these data which was then deconvolved assuming various resolution and "escape" parameters. Table 4-3 shows the results of this technique for a power law spectrum of the form

Table 4-3

Fits to generated power law with resolution of 40% and escape of 0.46

RESOLUTION \ ESCAPE		0.25	0.35	0.45	0.55	0.65
50%	χ^2_ν		0.504	0.775	1.232	
	I,α		4.3×10^{-4},4.96	4.7×10^{-4},4.74	5.1×10^{-4},4.54	
40%	χ^2_ν	0.152	0.093	0.144	0.403	
	I,α	4.1×10^{-4},4.96	4.6×10^{-4},4.72	5.1×10^{-4},4.46	5.5×10^{-4},4.2	
30%	χ^2_ν		0.590	0.265	0.159	0.477
	I,α		4.8×10^{-4},4.48	5.4×10^{-4},4.18	5.9×10^{-4},3.89	6.4×10^{-4},3.64
20%	χ^2_ν				0.724	0.683
	I,α				6.3×10^{-4},3.61	6.8×10^{-4},3.33

$$I = 5 \times 10^{-4}\left(\frac{E}{40}\right)^{-4.5}$$

with the resolution at 60 keV being 40% and "escape" being 0.46. As can be seen from the table the best fit results were obtained with the correct value for resolution. The "escape" variation produced results which were not as well behaved (i.e. true escape fraction did not produce the best fits). It was necessary to rely on the escape parameter determined from the in-flight calibrations. The escape fraction is purely a function of the mass of Xe present in the counter and should not have been affected by the Xe pressure changes. Thus the escape fraction derived from the in-flight calibrations is consistent with the amount of Xe employed for the flight. The conclusion reached, regarding Sco X-1 are not significantly dependent on the choice of the resolution parameter, however the spectral fits are improved.

4.3 RESULTS

4.3.1 VELA X-1 (3U0900-40)

During flight 665 the periodic X-ray source Vela X-1 was tracked for $\sim$ 45 minutes from 2115 hours U.T. on 1st December 1978 (Duldig et al. 1977). Figure 4-3 shows the pulse profile derived from superposed epoch analysis of the observation. For comparison the results of McClintock et al. (1976) have been included.

The background counting rate was poorly determined during this observation because the source was setting and reached the telescope drive limits. It was therefore impossible to deduce a modulation depth, relative to the steady source strength, (i.e. pulsed fraction) for this observation.

At the time of writing, it had not been possible to satisfactorily recover the data from the recording tapes which had been recorded

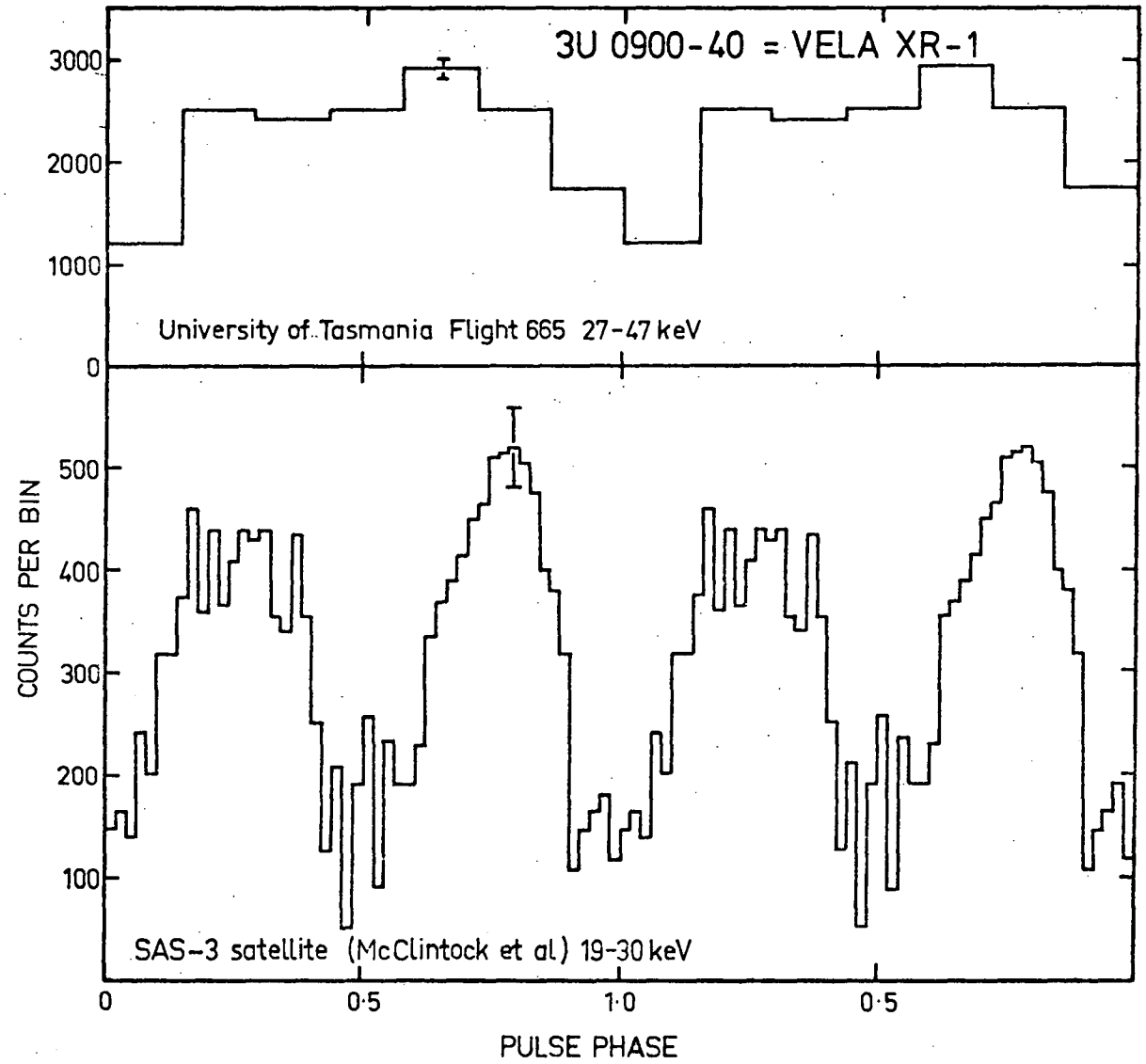

Figure 4-3 Derived pulse profile for Vela X-1.

with an older system than that described in 2.2.9. Thus no spectral analyses have been carried out for this flight.

4.3.2 GALACTIC CENTRE

The galactic centre region was also scanned during flight 665 and a number of sources were apparent. The large (7° × 20°) field of view of the telescope, and the resulting source confusion in the galactic centre region, made data analysis impossible. The galactic centre scan is presented in figure 4-4.

4.3.3 SCO X-1 SPECTRUM

Two scans of Sco X-1 were made during flight 710 and these are shown in figure 4-5 (Greenhill et al. 1979a and 1979b). Clearly Sco X-1 was in an active state, with significant intensity variations during both scans. The data were separated, by eye, into two "states", high and low, to determine whether the intensity variations showed any corresponding significant spectral changes. Spectral analyses were also carried out on the unseparated data from each scan.

The telescope was driven onto the position of Sco X-1 for the first scan to make sure that the source was visible. The source was then allowed to drift from the field of view while the telescope remained locked at a fixed position. The P.H.A. channel background determinations were derived from observations after Sco X-1 had drifted from the field of view and no other known hard X-ray sources were present. The background observations were therefore made at the same zenith and azimuth angles to avoid any possible directional dependence. A least squares, straight line fit to the background rate from each channel showed that the background within each channel was constant.

The telescope was driven ahead of Sco X-1 for the second scan and background observations were again carried out. In this case the background was observed before and after Sco X-1 was in the field of

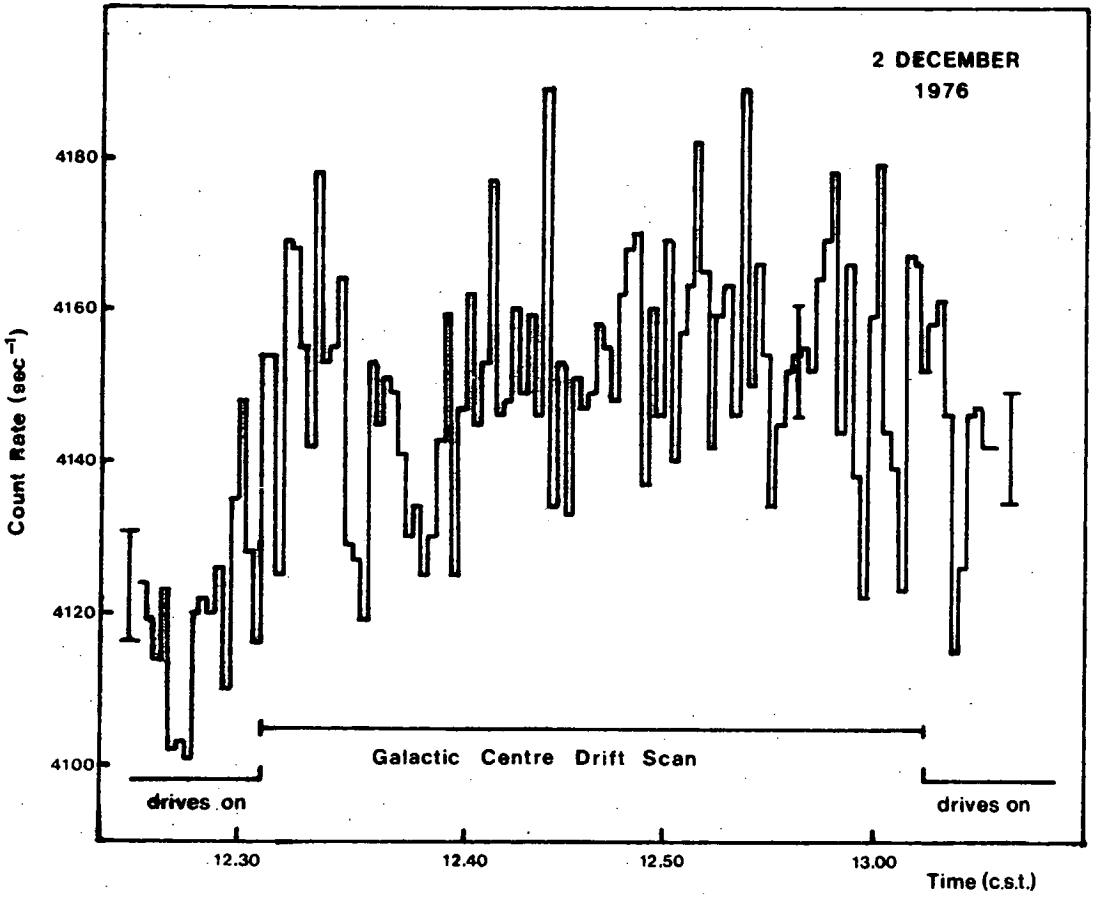

Figure 4-4 Galactic centre drift scan during flight 665.

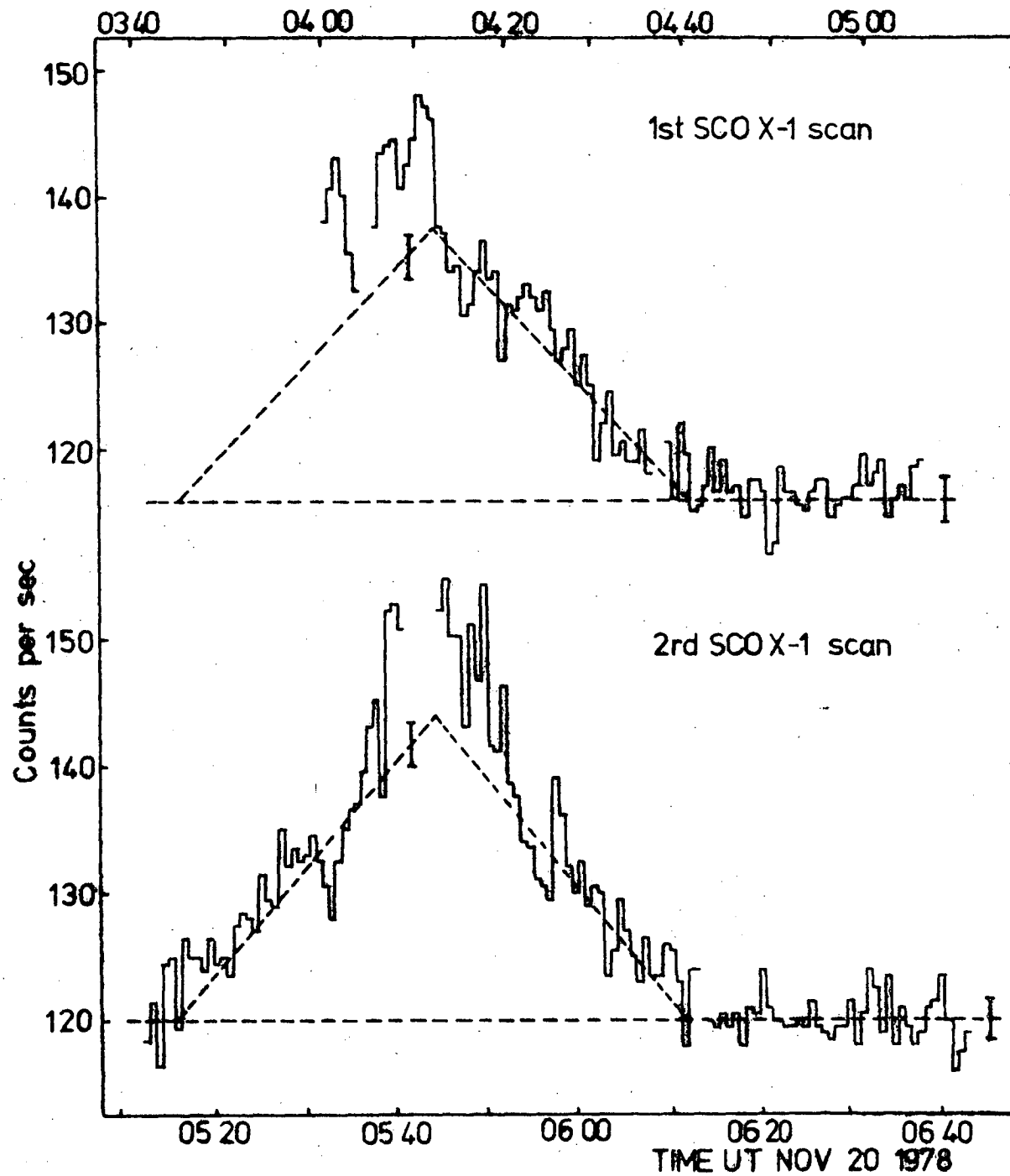

Figure 4-5 Counter response to SCO X-1 drift scan during flight 710. The energy interval over which the data were collected was 20-45 keV. The collimator triangular response is shown, centred on the expected source transit time.

view. The least squares fits to the background on both sides of the source for each PHA channel again resulted in a constant background.

The background for each channel was also plotted and inspected for any anomalies. No unusual features were found. Figure 4-6 shows the counter background during the second Sco X-1 scan. Clearly the calibration source is not sufficiently shielded from the counter and a computer model fitted to the background has been used to estimate the fraction of the background due to the calibration source. The results of this analysis showed that 13% of the background count rate was due to 59.6 keV X-rays from the calibration source and a further 21% was due to 25 keV fluorescent X-rays from the Sn shielding of the shutter between the calibration source and the X-ray telescope.

Gaps in the data presented in figure 4-5 are due to in-flight calibrations and the data at these times were rejected from the analysis.

The results of the spectral analyses are summarized in Tables 4-4 and 4-5 for the "Best fit" and "Calibration fit" counter parameters respectively.

The two tables show the value of χ^2 per degree of freedom (χ^2_ν), indicating the *goodness of the fit*, the normalized intensity (A) and the temperature (β) or spectral index (α). The temperature, β is expressed in keV and is equal to kT where k is Boltzmann's constant and T is the source temperature in °K (see 3.2.2). Two additional spectral forms were employed in the Sco X-1 analyses. A Thermal bremsstrahlung spectrum with an energy dependent gaunt factor of the form $(\frac{E}{\beta})^{-0.4}$ was used to more accurately model the source mechanism. As well as the inclusion of the gaunt factor, the final

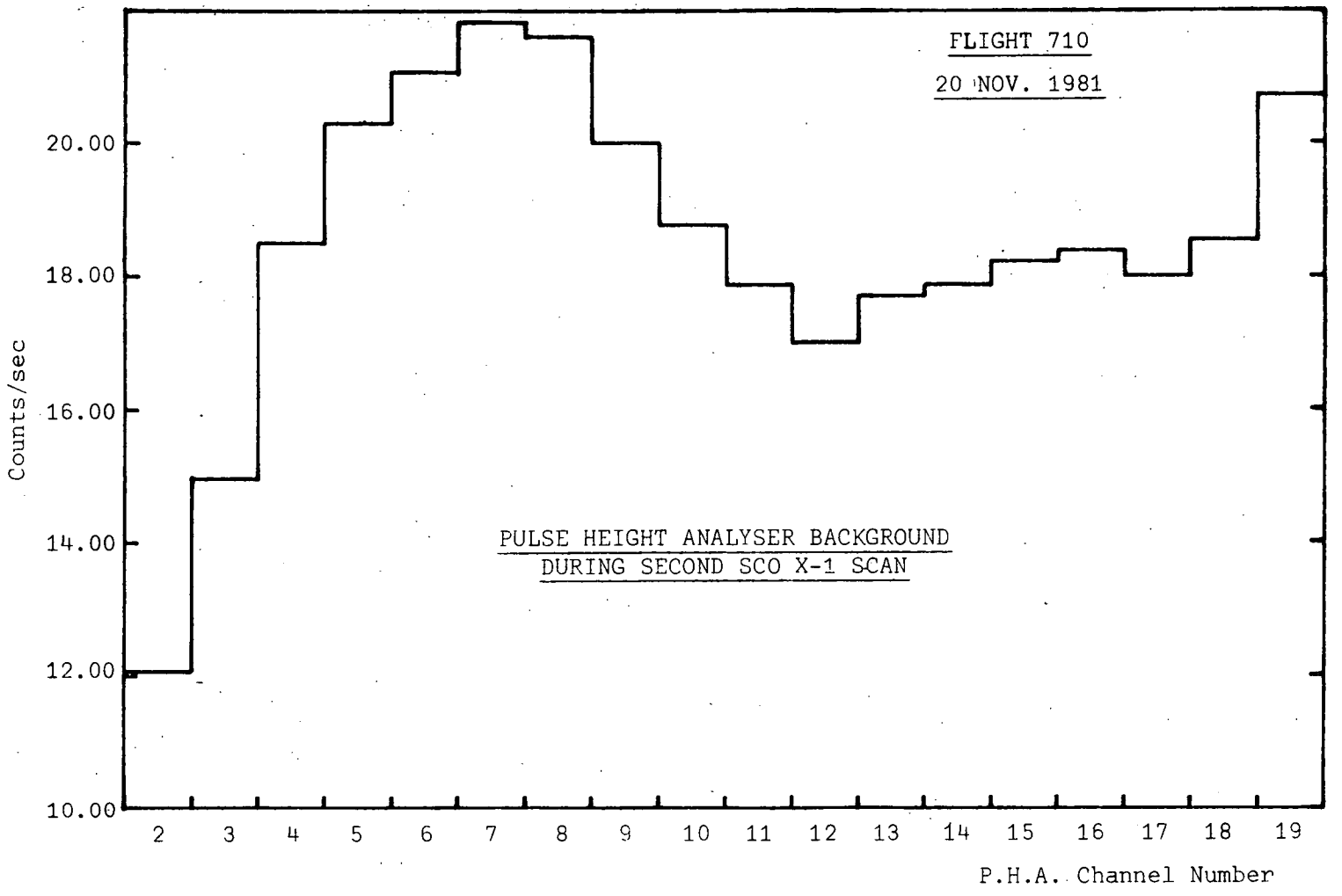

Figure 4-6 Counter pulse height analyser background for the second SCO X-1 scan of flight 710. The shape is due to insufficient shielding of the calibration source.

Table 4-4

Spectral Results Using "Best Fit" Counter Parameters

FIRST SCAN	POWER LAW	BLACK BODY	EXPONENTIAL	EXP & GAUNT	EXP, GAUNT & P.L.
COMBINED					
χ^2_ν	1.120	2.574	1.693	1.598	0.6290
A	6.300×10^{-4}	3.069×10^{-3}	8.846	9.687	25.95 2.183×10^{-4}
kT &/or α	4.537	4.372	8.226	9.316	6.530 1.007×10^{-7}
HIGH					
χ^2_ν	0.8451	1.578	1.085	1.036	0.6528
A	8.980×10^{-4}	2.228×10^{-3}	7.827	8.299	19.65 2.678×10^{-4}
kT &/or α	4.198	4.786	9.364	10.72	7.529 4.240×10^{-8}
LOW					
χ^2_ν	0.7181	1.683	1.077	1.022	0.5415
A	5.291×10^{-4}	5.626×10^{-3}	9.641	10.74	26.10 1.947×10^{-4}
kT &/or α	4.716	3.918	7.714	8.690	6.309 2.849×10^{-7}
SECOND SCAN					
COMBINED					
χ^2_ν	2.143	2.177	1.854	1.848	2.015
A	5.663×10^{-4}	2.488×10^{-3}	7.137	7.794	7.512 6.772×10^{-5}
kT &/or α	4.346	4.400	8.338	9.470	9.397 4.764×10^{-4}
HIGH					
χ^2_ν	2.149	1.918	1.766	1.778	1.915
A	6.148×10^{-4}	2.547×10^{-3}	7.392	7.971	7.890 5.490×10^{-5}
kT &/or α	4.296	4.431	8.425	9.590	9.493 5.207×10^{-3}
LOW					
χ^2_ν	0.4277	0.6959	0.5332	0.5155	0.4792
A	3.667×10^{-4}	2.488×10^{-3}	6.613	7.309	21.55 2.453×10^{-4}
kT &/or α	4.678	4.190	7.708	8.705	5.734 2.285

Table 4-5

Spectral Results Using "Calibration Fit" Counter Parameters

FIRST SCAN	POWER LAW	BLACK BODY	EXPONENTIAL	EXP & GAUNT	EXP, GAUNT & P.L.
COMBINED					
χ^2_ν	2.869	2.402	2.472	2.498	2.269
A	5.924×10^{-4}	5.602×10^{-3}	14.00	15.94	32.21 1.692×10^{-4}
kT &/or α	4.792	4.018	7.187	8.039	6.23 6.847×10^{-8}
HIGH					
χ^2_ν	2.099	1.680	1.797	1.824	1.766
A	8.560×10^{-4}	4.178×10^{-3}	11.83	12.98	25.39 2.186×10^{-4}
kT &/or α	4.424	4.355	8.176	9.249	7.154 1.173×10^{-7}
LOW					
χ^2_ν	1.635	1.422	1.440	1.450	2.050
A	4.898×10^{-4}	7.020×10^{-3}	15.95	18.53	9.165 7.852×10^{-7}
kT &/or α	5.000	3.825	6.700	7.453	9.281 2.075×10^{-4}
SECOND SCAN					
COMBINED					
χ^2_ν	5.893	3.854	4.628	4.761	5.469
A	6.010×10^{-4}	2.779×10^{-3}	7.537	8.157	7.993 1.603×10^{-7}
kT &/or α	4.242	4.346	8.263	9.388	9.497 1.043×10^{-8}
HIGH					
χ^2_ν	5.666	3.750	4.510	3.947	5.676
A	6.541×10^{-4}	2.795×10^{-3}	7.678	12.35	8.002 2.059×10^{-8}
kT &/or α	4.185	4.388	8.395	8.362	9.501 3.738×10^{-5}
LOW					
χ^2_ν	0.6583	0.5438	0.5651	0.5421	0.9941
A	3.875×10^{-4}	3.056×10^{-3}	7.589	13.31	5.757 4.272×10^{-10}
kT &/or α	4.612	4.089	7.459	7.319	9.914 5.614×10^{-3}

spectral form also contained an additional power law term. This power law term was incorporated in an attempt to improve the fit to the higher energy channels which generally contained excess counts.

Typical fits of the complete data from the first and second scans are presented in figures 4-7 and 4-8. Figure 4-9 shows the fits of two thermal spectra to the observed new data, before deconvolution of the counter response. Plots of all other Sco X-1 spectral fits are included in Appendix C, together with the results of the initial apodization analyses (3.2.4). It is clear from these plots that the lowest energy channel ($\sim$9-12 keV) was, in almost all cases, poorly fitted. The first channel had already been rejected, as the lower level discriminator cutoff energy was not known accurately and could therefore not be modelled. Fits were made for the data from each scan with this additional channel also removed. The detection efficiency is very low ($\sim$2%) (figure 4-10) for this channel and atmospheric absorption is also significant with less than 10^{-4}% transmittance and thus there is some justification for rejecting the channel. The resulting χ^2_ν were significantly improved, as can be seen from Table 4-6. More importantly, the spectral parameter values were not significantly different from the previous results, implying that this channel reduced the *goodness of fit* when included but did not affect the spectral parameters greatly. Therefore, the conclusions presented in the following chapter are derived from the complete eighteen channel spectral analyses. Two typical spectral fits of this type are presented in figures 4-11 and 4-12. The remaining fits also appear in Appendix C.

90% χ^2 confidence contours were determined for all two parameter fits (3.2.3) and typical examples are presented in figure 4-13. Further 90% confidence contours are included in Appendix D.

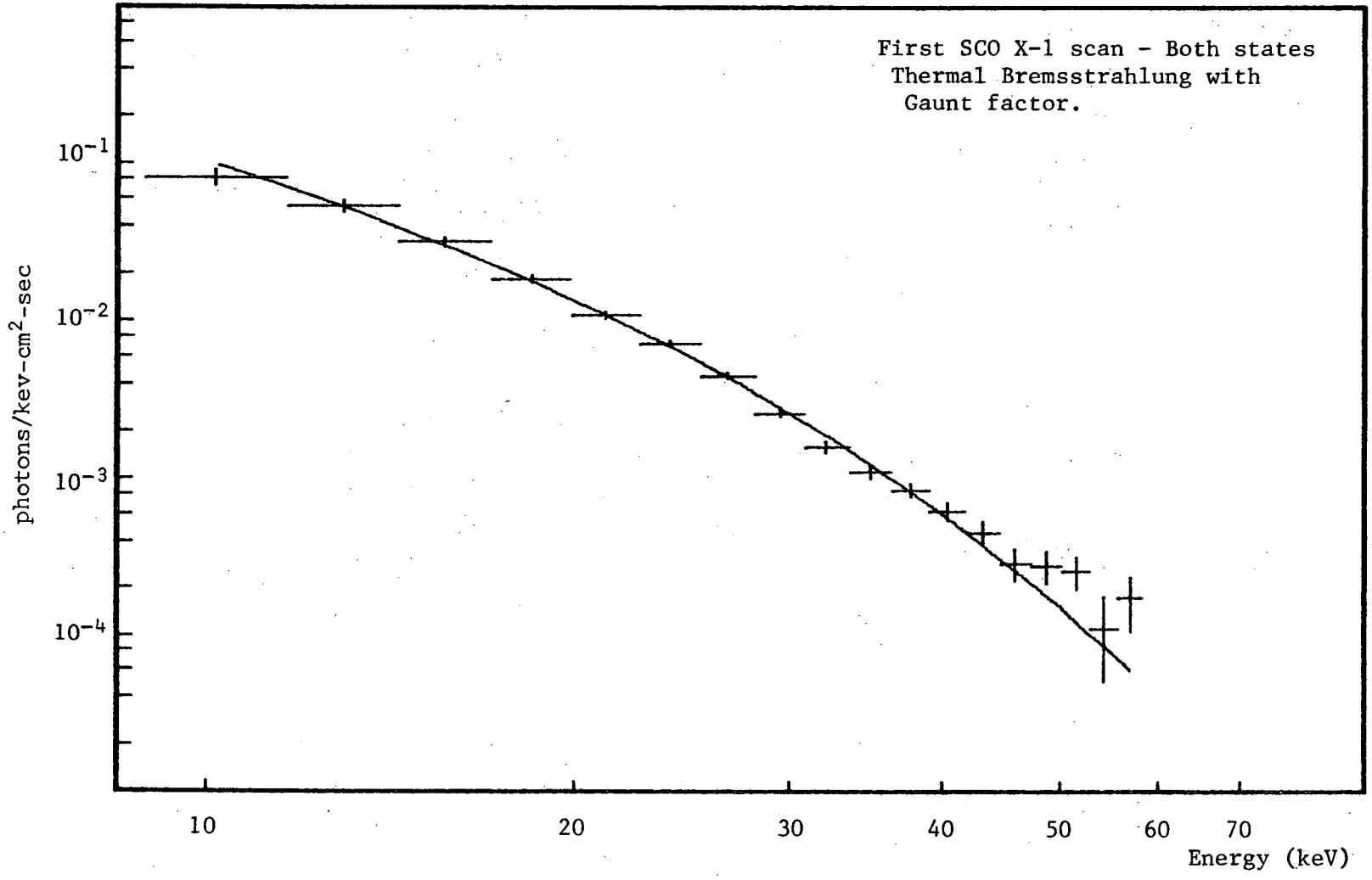

Figure 4-7 Spectral fit to the combined data of the first SCO X-1 scan.

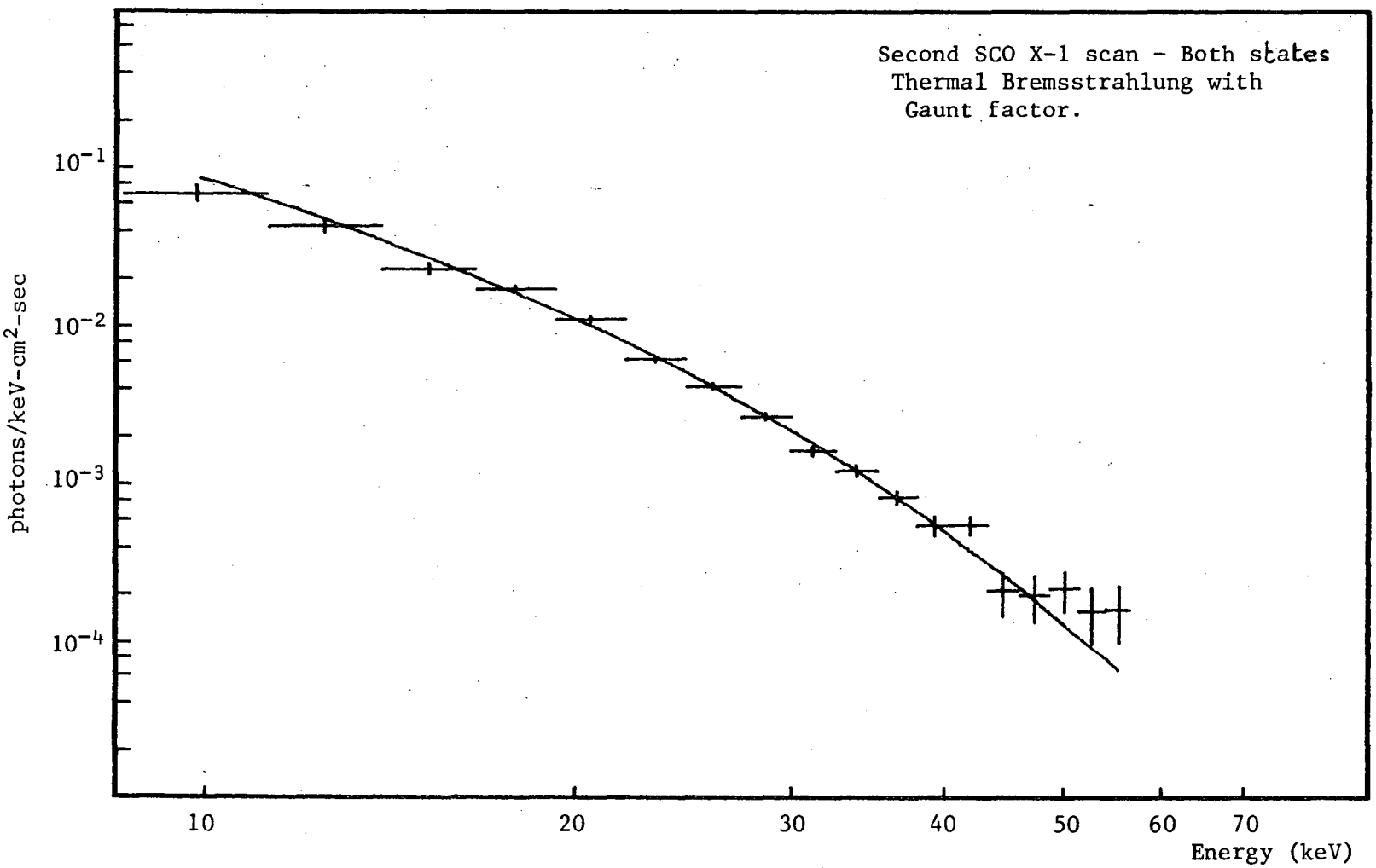

Figure 4-8 Spectral fit to the combined data of the second SCO X-1 scan.

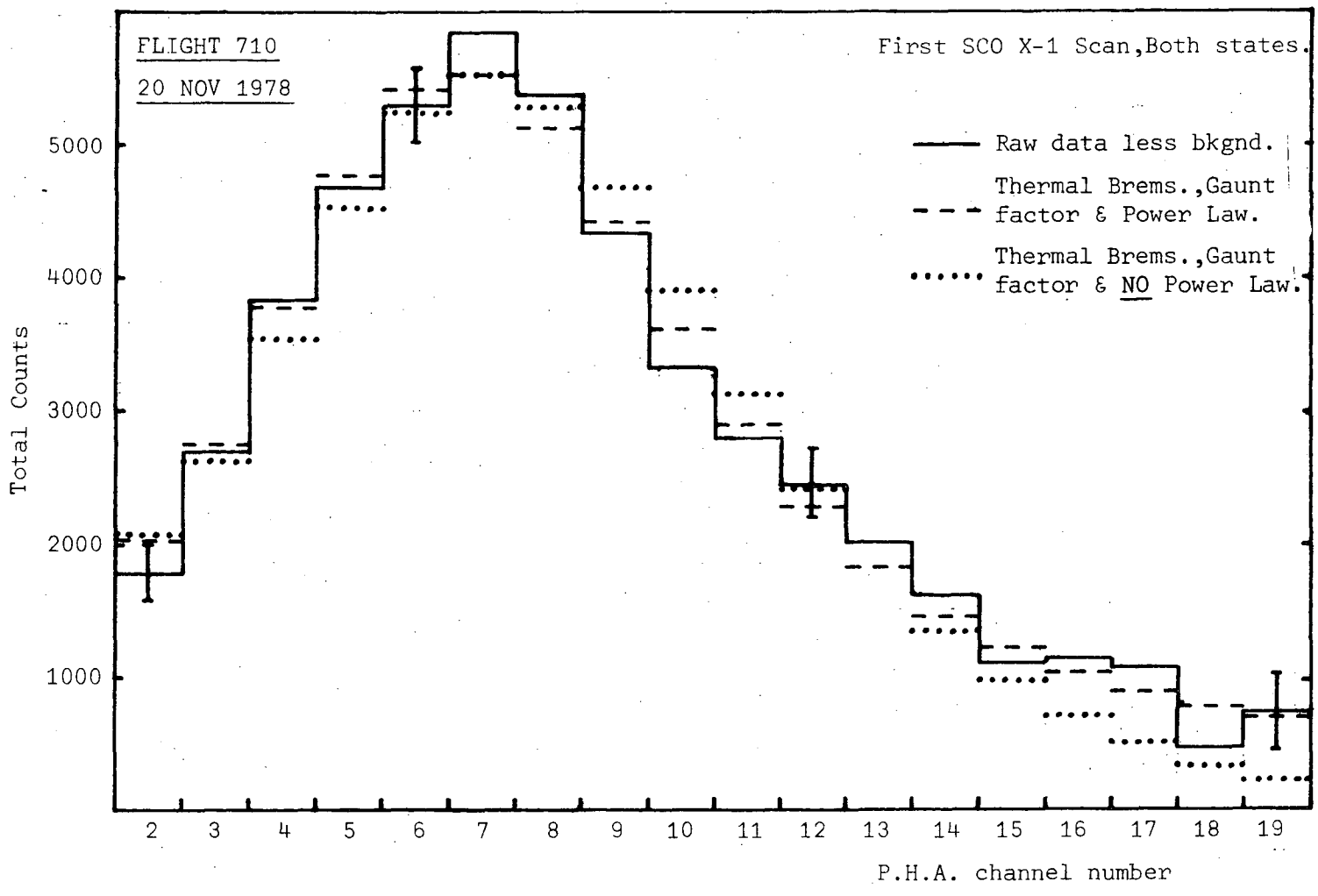

Figure 4-9 Thermal spectral fit to the combined raw data of the first SCO X-1 scan before deconvolution of the counter response function.

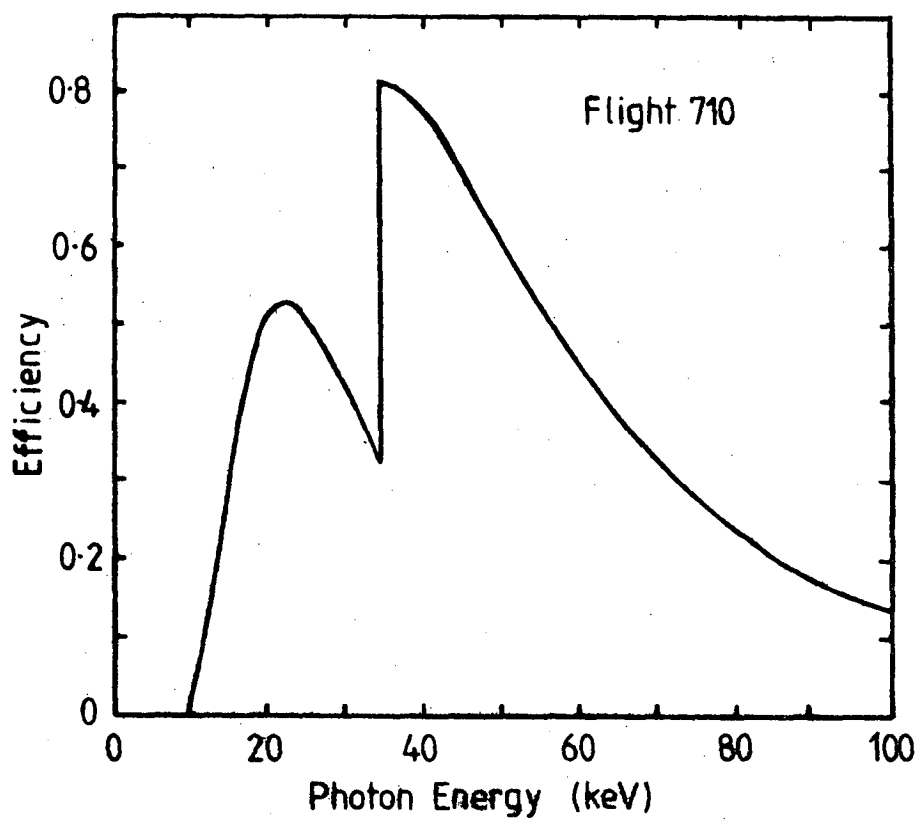

Figure 4-10 Counter detection efficiency (neglecting effects of resolution, K-escape and residual atmosphere) for flight 710. The discontinuity is the K-edge of Xe at 34.56 keV.

Table 4-6

Using "Best Fit"

17 Ch.

FIRST SCAN	P.L.	B.B.	EXP	E&G	E,G & P.L.
COMBINED					
χ^2_ν	0.8052	2.713	1.643	1.516	0.5742
A	6.486×10^{-4}	2.864×10^{-3}	8.307	8.994	25.45 2.211×10^{-4}
kT &/or α	4.486	4.423	8.425	9.580	6.567 1.197×10^{-7}
SECOND SCAN					
COMBINED					
χ^2_ν	1.693	2.241	1.704	1.662	1.567
A	5.831×10^{-4}	2.493×10^{-3}	6.700	7.207	11.18 1.289×10^{-4}
kT &/or α	4.300	4.403	8.557	9.749	8.028 7.861×10^{-7}

Using "Cal Fit"

17 Ch.

FIRST SCAN	P.L.	B.B.	EXP	E&G	E,G & P.L.
COMBINED					
χ^2_ν	1.698	2.039	1.782	1.758	1.431
A	6.113×10^{-4}	5.133×10^{-3}	12.67	14.25	33.58 1.729×10^{-4}
kT &/or α	4.766	4.079	7.455	8.371	6.289 7.570×10^{-8}
SECOND SCAN					
COMBINED					
χ^2_ν	3.906	2.843	3.149	3.212	3.652
A	5.860×10^{-4}	3.189×10^{-3}	8.475	9.302	9.973 3.962×10^{-5}
kT &/or α	4.409	4.277	8.025	9.076	8.760 3.015×10^{-14}

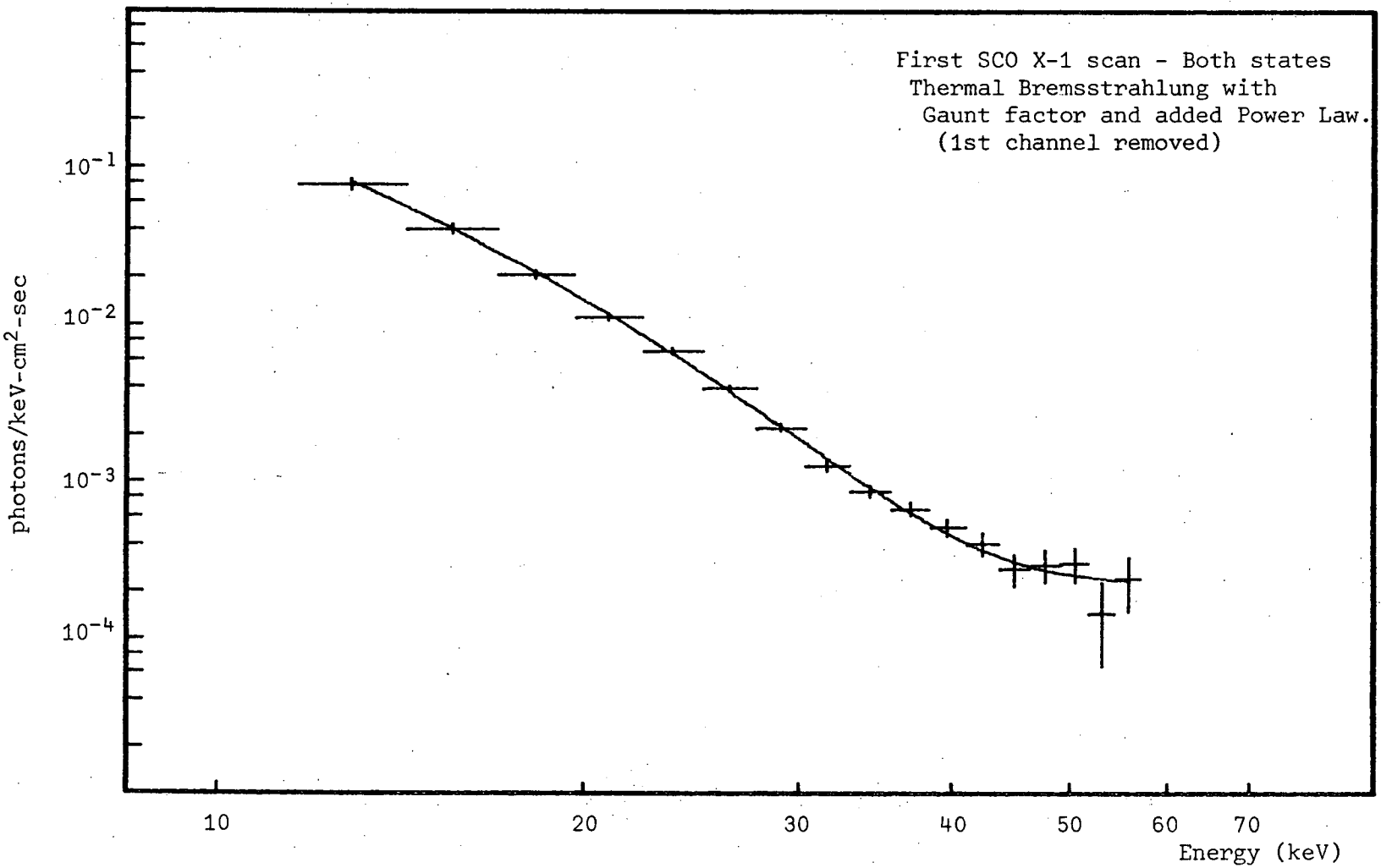

Figure 4-11 Spectral fit to the combined data of the first SCO X-1 scan rejecting the first channel.

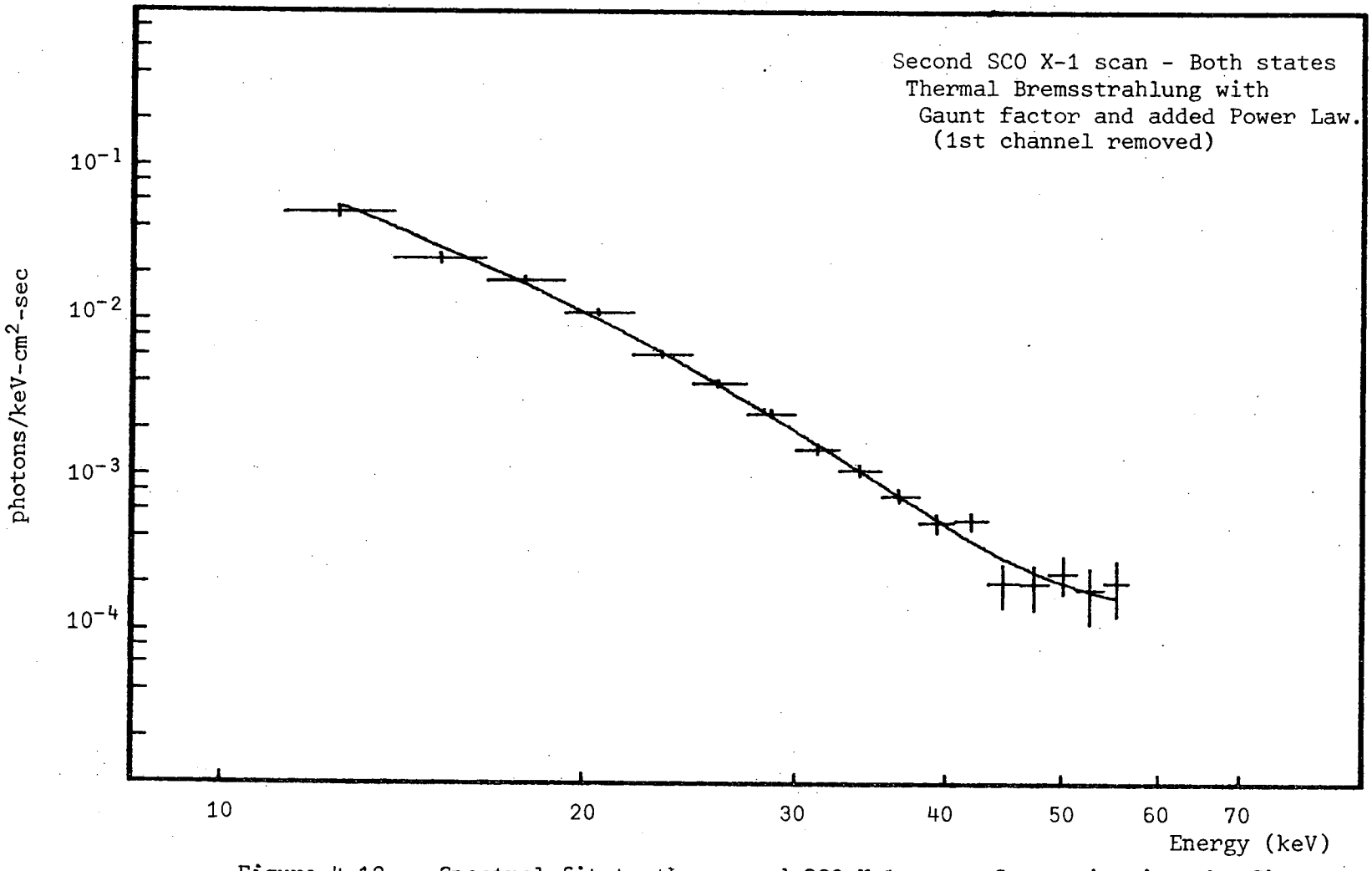

Figure 4-12 Spectral fit to the second SCO X-1 scan after rejecting the first channel.

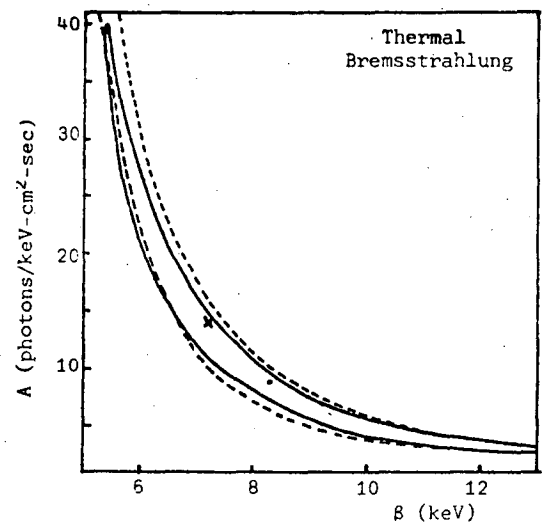

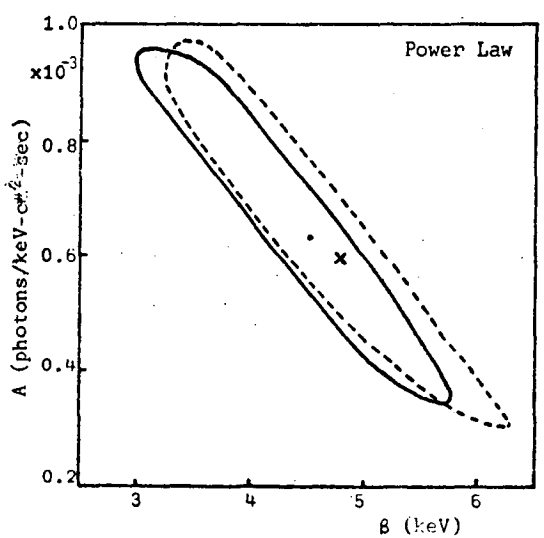

90% X^2 Confidence

Contours

First SCO X-1 Scan

Both States

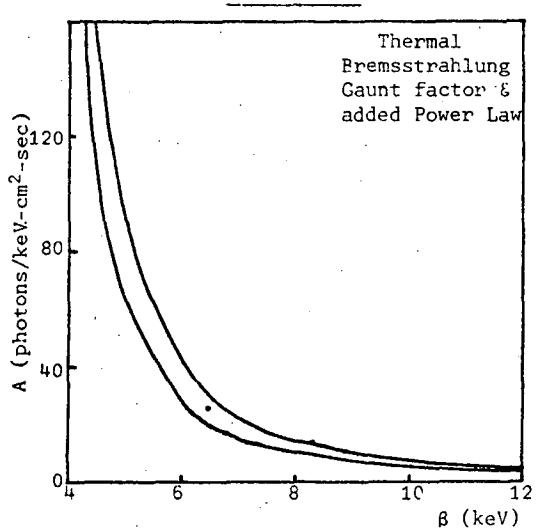

Figure 4-13

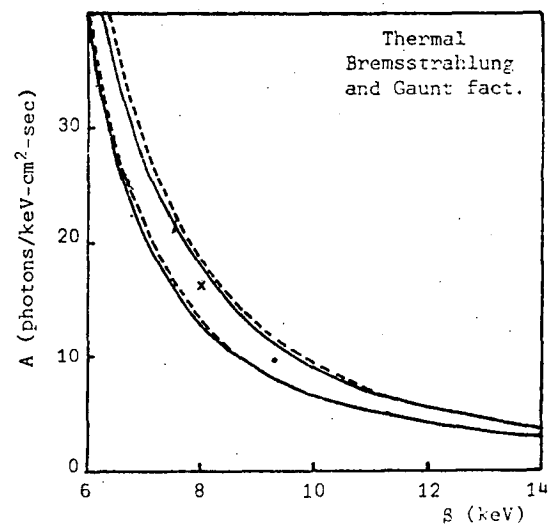

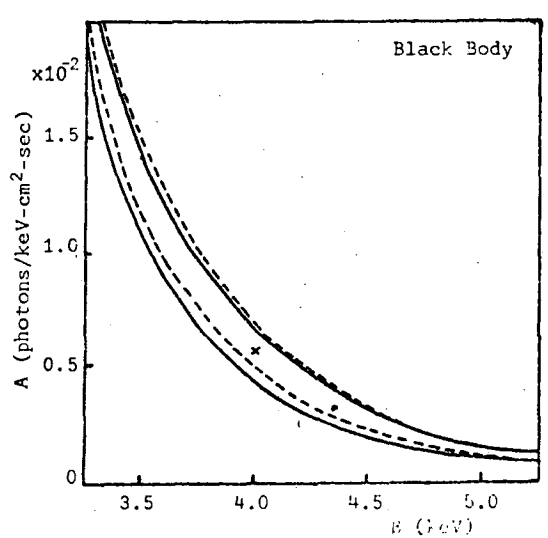

The solid curve is for "best" fit counter parameters and the dot is the fitted minimum X^2.
The broken curve is for "cal" fit counter parameters and the cross is the fitted minimum X^2.

4.3.4 SCO X-1 TEMPORAL ANALYSES

Figure 4-5 showed the variable nature of the X-ray emissions from Sco X-1. Fast fourier analyses of the count rate (20-45 keV) for Sco X-1 (3.3.1) were also carried out. A section of the data before analysis by this technique is shown in figure 4-14. The raw power spectrum derived from these data is given in figure 4-15 and the smoothed power spectrum is similarly shown in figure 4-16. The remaining power spectra are presented in Appendix E.

No significant periodic component is apparent from any of the power spectral analyses over the period range 0.5-500s.

4.4 REFERENCES

Duldig M.L., Emery M.W., Fenton A.G., Fenton K.B., Greenhill J.G. and Thomas R.M. (1977) Proc. A.S.A. Vol.3. No.2. p.117

Greenhill J.G., Duldig M.L., Emery M.W., Fenton A.G., Fenton K.B., Thomas R.M. and Watts D.J. (1979a) Proc. A.S.A. Vol.3. Nos.5 & 6. p.349

Greenhill J.G., Fenton A.G., Fenton K.B., Thomas R.M., Duldig M.L., Emery M.W., Cooke D.J., Phillips J., Watts D.J., Hudson R.M., Middleton E. and Salmon G.(1979b) Proc. 16th Int. Cosmic Ray Conf., Kyoto, Japan, Vol.11, T1-4., 8

McClintock J.E., Rappaport S., Joss P.C., Bradt H., Buff J., Clark G.W., Hearn D., Lewin W.H.G., Matilsky T., Mayer W. and Primine F. (1976) Astrophys. J. Lett. 206, L99

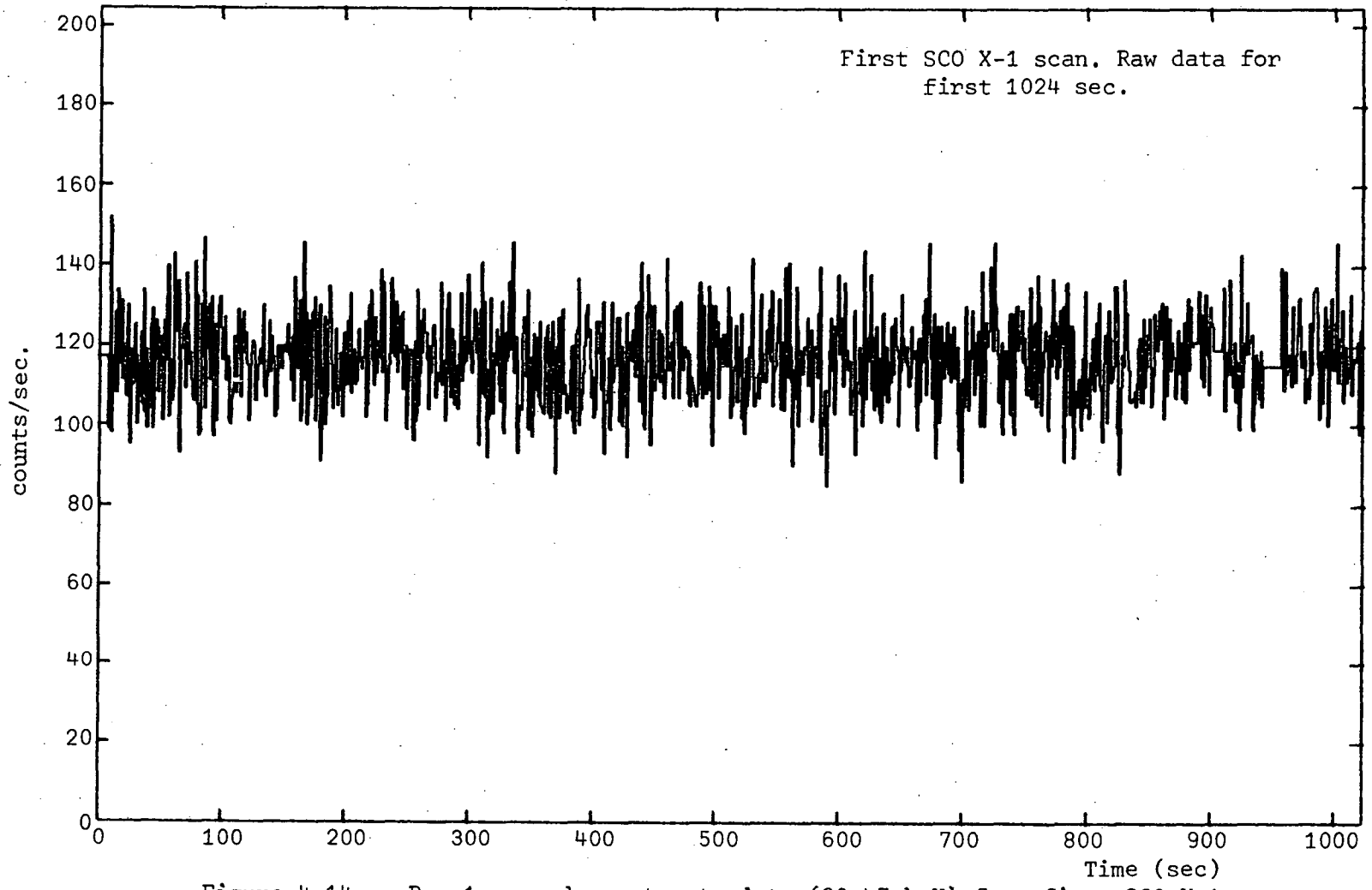

Figure 4-14 Raw 1 second count rate data (20-47 keV) from first SCO X-1 scan.

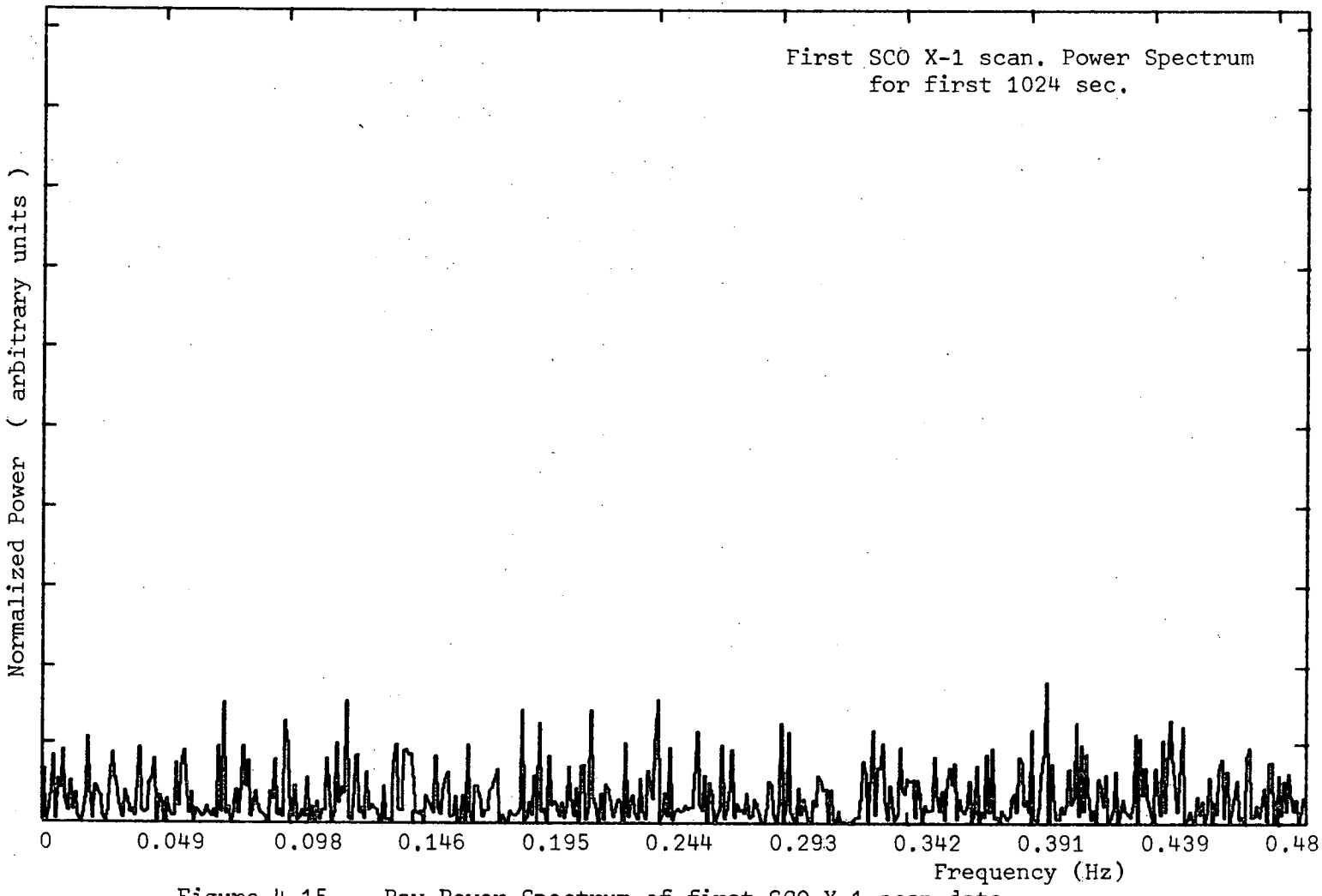

Figure 4-15 Raw Power Spectrum of first SCO X-1 scan data.

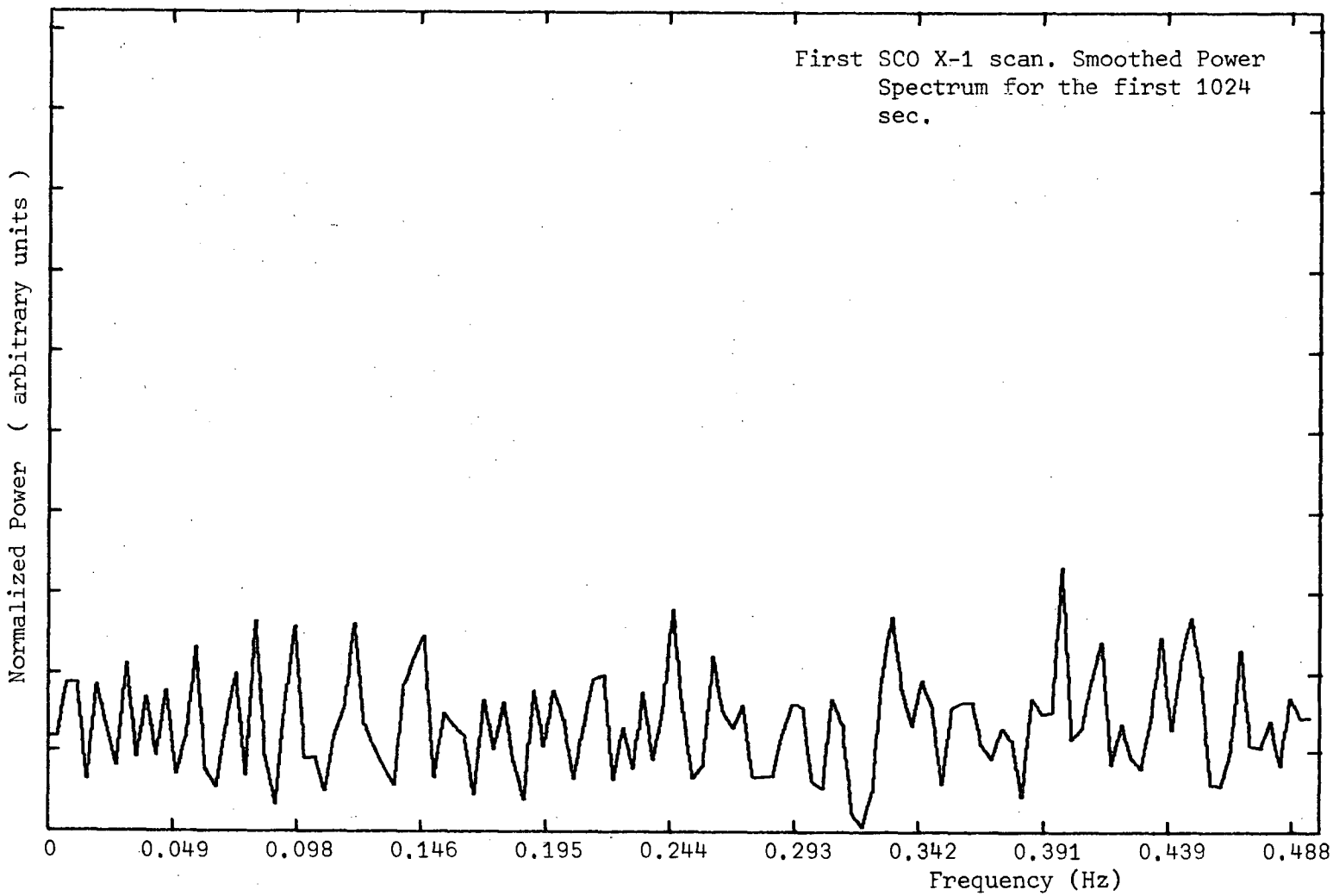

Figure 4-16 Smoothed Power Spectrum of the first SCO X-1 scan data.

CHAPTER 5

DISCUSSION OF X-RAY RESULTS

5.1 VELA X-1

5.1.1 PULSE PROFILE

The derived pulse profile shown in Figure 4-3 consisted of a single broad peak extending across the phase interval 0.1 to 0.8 for energies between 27 and 47 keV. Observations by McClintock et al. (1976), for the energy range 19-30 keV, indicated a double pulse structure consisting of a flat topped pulse from phase 0.1 to 0.4 and a second, more intense pulse, from phase 0.6 to 0.9. Staubert et al. (1980) have observed a similar double pulse profile in the 18-82 keV energy range. The modulation depth was found to decrease with energy in this latter observation, almost disappearing in the 66-82 keV energy range.

The results presented in this work are consistent with the observations of McClintock et al. (1976) and Staubert et al. (1980). The poor temporal resolution, resulting from the recorded data (4.3.1), has meant that only a coarse profile determination was possible. The very broad pulse profile is somewhat different in form from the observations of Staubert et al. (1980) although the period of 283 ± 0.5 sec. is the same within the accuracy of the observation.

Staubert et al. (1980) observed significant changes in the pulse to pulse shape but on all occasions a double pulse structure was present. The pulse profile derived here is made up from only four pulse periods but suggests that the pulse shape may be more variable than observed by Staubert et al. (1980).

The remaining half of the data and the absolute timing information have not yet been retrieved due to the tape recorder difficulties described earlier. (The quick look output for this flight

included only half the P.H.A. data). The time of phase zero is therefore poorly determined. If the timing data is recovered in the future, which appears quite likely, an estimation of $\dot{P}/P$ can be derived from comparison of the time of phase zero in these observations and the phase zero time derived from OSO-8 observations earlier in 1976 (Becker et al. 1978).

5.2 SCO X-1 ENERGY SPECTRUM

5.2.1 GENERAL

The spectral plots presented in the previous chapter and in Appendix C extend down to $\sim$ 9 keV. It is important to realize that atmospheric attenuation below $\sim$ 20 keV means that fewer than two percent of the source X-rays actually reach the detector. The plotted points are therefore an extrapolation of the source spectrum. They have been included because the observed counts at these lower energies are mostly due to escape photons from 50 keV and below. The spectral plots therefore give an indication of how well these escape photons have been modelled. The derived spectral fits therefore apply over the energy range 20 keV - 60 keV.

5.2.2 "HIGH" AND "LOW" STATES

The results presented in Tables 4-4 and 4-5 show that the "best fit" counter parameters give greatly improved spectral fits to the data. Although the quality of these "best fit" results is superior to those obtained using the calibration parameters, the 90% χ^2 confidence contours are generally similar for both sets of counter parameters. The similarity in the χ^2 contours is believed to be due to the poor values of resolution which have a severe smoothing effect.

Referring to Table 4-4, Figure 4-10 and Appendix D, it is clear that no significant difference was observed between the "high"

and "low" states during either scan. The results presented in Table 4-4 show a tendency toward harder spectra in the "high" state but the 90% χ^2 confidence contours have large regions of overlap indicating that the apparent differences are not significant (Appendix D).

Lewin et al. (1970) observed intensity variations in Sco X-1 of a factor of more than two on time scales of $\sim$ 30 minutes in the energy range 18-38 keV. They also found that the spectral form was independent of source intensity. At lower energies, between 2.5 and 7.5 keV, White et al. (1976) have observed strong correlation between intensity and spectral hardness. Miyamoto and Matsuoka (1977) in their review article on Sco X-1, concluded that during an X-ray flare, observations show that the apparent temperature increases to between 10 and 30 keV in the energy range $\sim$ 3-10 keV, while at higher energies (20 - 30 keV) the apparent temperature remains unchanged. The observations presented here are consistent with this statement.

5.2.3 SCO X-1 APPARENT TEMPERATURE

The best fit thermal bremsstrahlung spectra of both scans are consistent with an apparent temperature of $\sim$ 9 keV. The 90% χ^2 confidence contours suggest that kT was in the range 6-14 keV. During the first scan the residual atmosphere depth increased linearly from 4.03 mbar to 4.73 mbar. This means that the atmospheric absorption early in the scan is slightly over estimated. However the change to the fitted spectral parameter is not significant.

The second scan was made shortly after a ballast drop and had a constant residual atmospheric depth of 3.9 mbar.

Inclusion of a hard energy "tail", discussed in the following section, reduced the effective temperature for the first scan to $\sim$ 6.5 keV. Miyamoto and Matsuoka (1977) state that in the energy range

20-40 keV the source temperature is generally 4-6 keV although several observers (e.g. Toor et al. 1970, Agrawal et al. 1969) have reported higher temperatures. The results presented here show a harder spectrum than often reported but still well within the range previously observed (see e.g. Figure 8 in Miyamoto and Matsuoka). The apparent temperature of Sco X-1 seems to be variable ranging between at least 3 keV and 20 keV in the energy range of interest ($\sim$10-60 keV). Lamb and Sanford (1979) attempt to explain variations of the Sco X-1 spectrum as being due to variations in electron scattering optical depth due to changing accretion rates. They show that Compton scattering together with a constant electron temperature can be employed to produce spectra which fit the observations more closely than other spectral forms and result in lower source temperatures.

The Lamb and Sanford model is unsatisfactory for energies greater than $\sim$ 100 keV in Sco X-1. Analyses of the first Sco X-1 scan low state using the model of Lamb and Sanford produced a χ^2_ν value of 1.10, poorer than for all other spectral forms except a black body spectrum. Similarly, analysis of the second Sco X-1 scan high state by this method resulted in a χ^2_ν value of 2.55, much worse than the values obtained using simpler spectral models.

It seems therefore that Compton scattering effects cannot be employed to explain the Sco X-1 spectrum between 10 keV and 60 keV at the time of these observations.

5.2.4 SCO X-1 HARD SPECTRAL TAIL

The addition of a power law to the thermal spectrum resulted in significant improvements to the spectral fits to the observations during the first scan. The added power law for the first scan was virtually flat with a spectral index $\alpha \sim 10^{-7}$. The best fit temperature

was also reduced to $\sim$ 6.5 keV, much closer to the more commonly reported value of 5 ± 2 keV. The 90% χ^2 confidence contours were derived by fixing the power law parameters at their best fit values and varying the thermal bremsstrahlung parameters. The resulting 90% confidence range of kT being 4-12 keV.

Incorporation of a power law term to the second scan fits had little effect, increasing the minimum χ^2_ν value slightly. The spectral fit plots (Appendix D) show that a less pronounced high energy excess was still present during the second scan and thus the high energy component during this scan was not well represented by a power law. It would be valuable to fit a thermal component or high energy line to this feature for both scans, however time has not permitted such an analysis in this thesis.

An error in the background estimation of the high energy channels could give rise to an apparent hard tail in the spectrum. For these observations an error of $\sim$ 3.5% in the background for the highest three channels could give rise to such an effect. The background error derived from the observations is 0.6% per channel at the 1σ level. It seems unlikely that the background could have been incorrectly estimated by such a large factor (6σ) in each of the last four channels for both scans.

The change in residual atmospheric depth during the first scan has no significant effect at these energies. It can therefore be concluded that during these observations a hard energy tail in the spectrum of Sco X-1 is present and probably variable in nature. It must be emphasised that this conclusion is unchanged if the "calibration" fit rather than "best" fit counter parameters are used.

The existence of a hard component in the spectrum of Sco X-1 is a strongly debated issue. Haymes et al. (1972), determined a high energy excess (34-300 keV) which could be fitted by a power law of index 1.8 or thermal spectrum with kT = 190 keV equally well. Greenhill et al. (1979) reported an excess in Ariel 5 data which was fitted by a thermal spectrum with kT = 35 ± 5 keV. The "tail" described here lies between these observations. Matsuoka (1972) and Riegler et al. (1970) have also reported a similar feature in their observations of Sco X-1. Conversely Johnson et al. (1980), Coe et al. (1980) and Lewin et al. (1970) all failed to detect a "tail" in their spectra. In each case the flux observed here is $\sim$ 3 times the upper limits. The results described here would imply that a "tail" in the spectrum is real and possibly variable on time scales as short as 30 minutes. To the author's knowledge these observations are the second observations of possible variability in the hard component of the spectrum (the first being Matsuoka et al. 1972) although such variability has been suspected for some time (Coe et al. 1980, Johnson et al. 1980).

Coe et al. (1980) have suggested that when the "tail" *is present* it may show periodic structure reflecting the orbital position of the compact object. They suggest that the hard X-ray emission probably arises from a different region within the source than does the soft X-ray emission, evidence for this being the much greater variability of hard X-ray emission.

Figure 5-1 represents observations when a hard energy component was reported in the spectrum from Sco X-1. The intensity observed at 50 keV has been plotted against phase of Sco X-1 using the ephemeris of Gottlieb et al. (1975). No definite trend is apparent but more data are required before the possibility of a periodic component in the hard X-ray region could be ruled out.

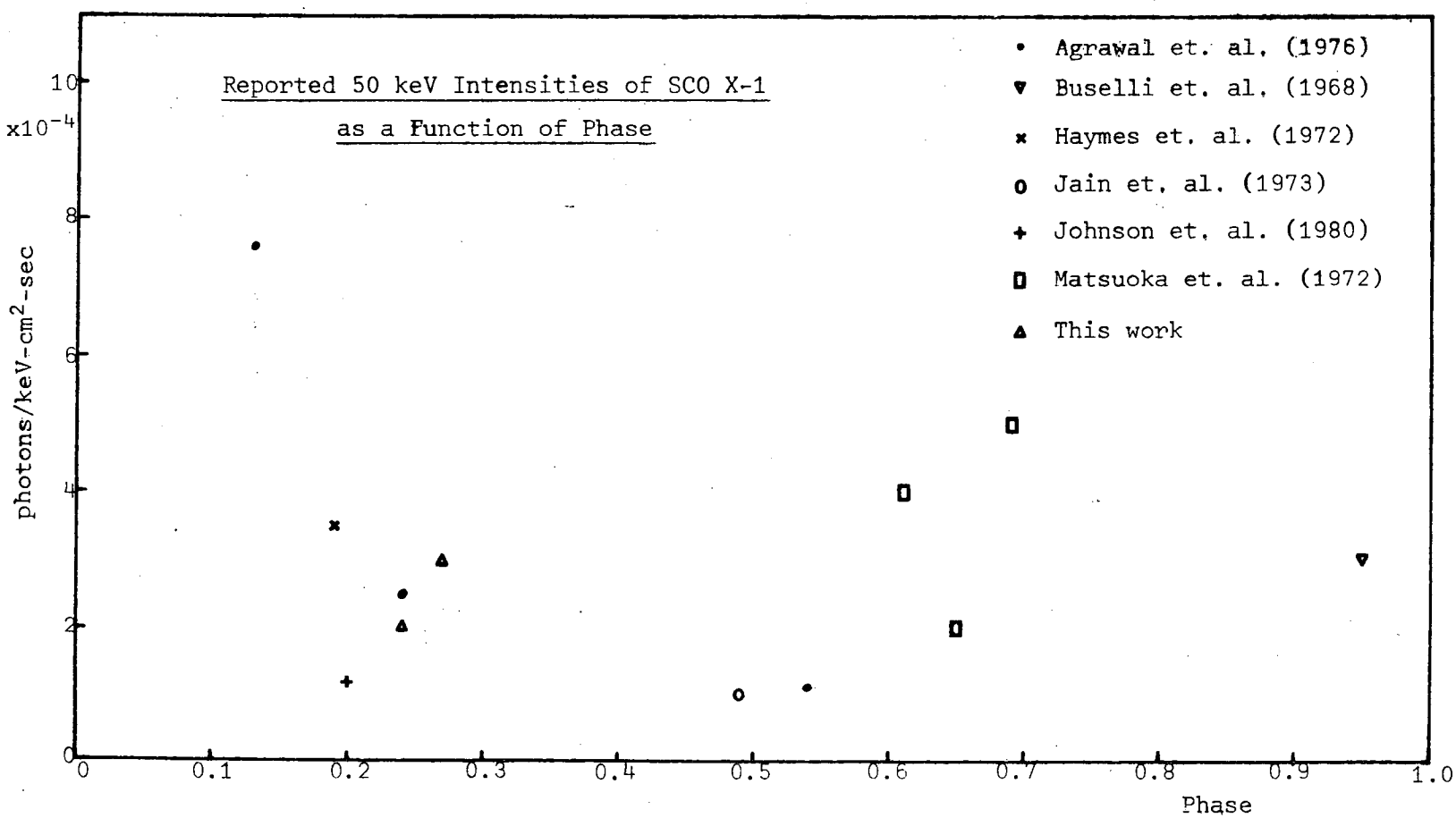

Figure 5-1 50 keV intensities of SCO X-1 as a function of orbital phase.

5.2.5 SCO X-1 POWER SPECTRA

Power spectral analyses resulted in no significant periodicities in the range 0.5-500 sec.

Terrell and Olsen (1970) describe a technique for deducing shot noise parameters of a variable source signal. Pulses of zero risetime and exponential decay are assumed. Terrell(1972) carried out such an analyses on data from observations of CYG X-1 and concluded that the pulsations present in the data could be attributed to many, overlapping, short duration random pulses (i.e. shot noise). The important relations derived by Terrell are

$$\lambda = \langle L \rangle^2 / S(0+)$$

$$T_e = S(0+)/\sigma^2(L)$$

$$n \equiv \lambda T_e = \langle L \rangle^2 / \sigma^2(L)$$

where T_e is the effective pulse length

λ is the pulse rate

n is the average number of pulses overlapping at one time

$\langle L \rangle$ is the average signal

$\sigma^2(L)$ is the variance of the signal L

and $S(0+)$ is limit approached by the power spectrum as $f \to 0$ but not the actual value at $f = 0$.

If shot noise were present in the data, with effective pulse lengths in the period range covered by the power spectrum, then there would be a significant power in the low frequencies. For the power spectra derived for Sco X-1 no such low frequency power was evident. Therefore the variations in the source intensity are not a result of shot noise for effective pulse lengths of 0.5-500 sec. Derivation of

shot noise parameters using the autocorrelation function have been made for Sco X-1 (Holt et al. 1976) for the energy range 3-6 keV. Their results indicated that the X-ray emission of Sco X-1 may be characterized by $\sim$ 200 flares per day each having a duration of $\sim$ 1/3 day. Any similar activity above 20 keV would not be resolved by the current observations. The greater variability of Sco X-1 at higher energies (Miyamoto and Matsuoku 1977, Coe et al. 1980) could possibly be due to shorter flares or a decreased flare rate. These observations rule out flares of less than 500 sec duration. Clearly there is a need for observations over several days with temporal resolution of $\sim$ 5 min to test for shots in the remaining temporal window.

5.3 TELESCOPE IMPROVEMENTS SINCE FLIGHT 710

5.3.1 GENERAL

The improvements described briefly below have not been undertaken by the author but are included as a basis for the suggestions of section 5.4.

5.3.2 TOP TRAY GROUND PLANE

The detection chamber depth has been increased and a wire ground plane added above the top detection tray. Thus the top tray ground plane is independant of the thin aluminium window separating the counter and collimator sections of the telescopes. Should the pressure equalization system fail the gas gain will still be affected but the energy resolution of the telescope should remain constant for all five trays and the problem encountered in flight 710 should not recur.

5.3.3. PULSE DETECTION CIRCUITRY

The counter pulse detection circuitry has been redesigned since the 1978 flight. The new system incorporates lower noise pre-amplifiers and peak detection circuits. These peak detectors sense the presence of any counter pulses. When counter pulses are present the

peak detector output switches on an analogue gate connecting the counter pulses to the adding amplifier. Thus, when no pulses are present from a given cell, the signal from that cell is not included in the added signal. This in turn significantly reduces the noise added into the counter output. In addition pulses detected simultaneously in more than three trays are also rejected, further reducing the background.

5.3.4 TELESCOPE MOUNTING

With the development of microprocessor (μP) systems it has been possible to convert the telescope mounting system to an Altitude-azimuth system with pointing under μP control. At the same time a rocking mechanism to alternatively drive the telescope on and off source was developed. This enables better background determination.

5.3.5 COLLIMATOR

A new narrower angle collimator has been added with field of view of $\sim 2°$ FWHM. The platform stabilization servo system has also been modified with the reaction wheel located at the base of the platform and a small motor above the payload. Addition of velocity feedback to the servo system has significantly improved the azimuthal stability and fluctuations in azimuth are now less than $\sim 0.1°$.

5.3.6 SHIELDING

The passive graded shielding around the counter has recently been modified. It now consists of 0.5 mm Pb, 2 mm Sn and 0.25 mm Cu, almost twice the thickness of the former shielding and should significantly reduce the background count rate, especially above 50 keV.

5.3.7. GROUND BASED IMPROVEMENTS

The telemetry rate has been reduced to 1440 bits per second to allow greater flexibility in real time ground based analyses. A

μP controlled quick look video display has replaced the display panel. A second μP is used to display the telescope field of view on another video display together with Right Ascension and Declination grids. A star field camera system is being developed which will continously transmit a star field picture. The star field picture will then be overlaid onto the telescope field of view display.

5.4 SUGGESTED FURTHER IMPROVEMENTS

5.4.1 CALIBRATION

Clearly many of the problems encountered in the data reduction of flight 710 could have been avoided if the calibration source had been mounted in front of the collimator. Such a calibration system is highly desirable for all future flights.

Furthermore a second calibration source at $\sim$ 40 keV should be included. This would produce peaks at 60 keV and 40 keV as well as escape peaks at 30 keV and 10 keV which covers most of the range of the detector.

5.4.2 PULSE HEIGHT ANALYSES

If the counter performance continues to improve and resolutions of better than 20% FWHM can be achieved it will be worthwhile to add several P.H.A. channels. Thirty two channels would allow each channel to be $\sim$ 2 keV wide. Thus, the Am^{241} calibration source will be seen in five channels and the escape peak will be present in four. Fewer channels will make in flight calibration modelling more difficult and less accurate.

5.4.3. GAS DETERIORATION

It is most important that detailed studies of the gas deterioration within the counter are undertaken. Design modifications to avoid outgassing should certainly be attempted. More importantly,

the nature of the contaminants MUST be determined so that an effective technique for their removal can be employed.

5.4.4 TELEMETRY FORMAT

Although difficult to incorporate into the present telescope system a modular telemetry format should be considered for the future. The present telemetry format is cumbersome and extremely difficult to modify when adding new equipment modules. The telemetry format is also incompatible with fast computer decoding, thus preventing real time energy or power spectral analyses.

5.5 REFERENCES

Agrawal P.C., Biswas S., Gokhale G.S., Iyengar V.S., Kunte P.K., Manchanda R.K. and Sreekantan B.V. (1976) Nature 224, 51

Becker R.H., Rothschild R.E., Boldt E.A., Holt S.S., Pravdo S.H., Serlemitsos P.J. and Swank J.H. (1978) Astrophys. J. 221, 912

Buselli G., Clancey M.C., Davison P.J.N., Edwards P.J., McCracken K.G. and Thomas R.M. (1968) Nature 219, 1124

Coe M.J., Dennis B.R., Dolan J.F., Crannel C.J., Maurer G.S., Frost K.J., Orwig L.E., Graf W. and Price K.M. (1980) Astrophys. J. 237,148

Gottlieb E.W., Wright E.L. and Liller W. (1975) Astrophys. J. (Lett) 195,L33

Greenhill J.G., Coe M.J., Burnell S.J., Strong K.T. and Carpenter G.F. (1979) Mon. Not. R. astr. Soc. 189, 563

Haymes R.C., Harnden F.R., Johnson W.N. and Prichard H.M. (1972) Astrophys. J. (Lett) 172, L47

Jain A.K., Jayanthi V.B., Kasturirangan K. and Rao U.R. (1973) Astrophys. Space Sci. 21, 107

Johnson W.N., Kurfess J.D., Maurer G.S. and Strickman M.S. (1980) Astrophys. J. 238, 982

Lamb P. and Sanford P.W. (1979) Mon. Not. R. astr. Soc. 188, 555

Lewin W.H.G., McClintock I.E., Ryckman S.G., Glass I.S. and Smith W.B. (1970) Astrophys. J. (Lett) 162, L109

McClintock J.E., Rappaport S., Joss P.C., Bradt H., Buff J.,

Clark G.W., Hearn D., Lewin W.H.G., Matilsky T., Mayer W. and Primine F. (1976) Astrophys. J. (Lett) 206, L99

Matsuoka M., Fujii M., Miyamoto S., Nishimura J., Oda M., Ogawara Y., Hayakawa S., Kasahara I., Makino F., Tanaka Y., Agrawal P.C. and Sreekantan B.V. (1972) Astrophys. Space Sci. 18, 472

Miyamoto S. and Matsuoka M. (1977) Space Sci. Rev. 20, 687

Reigler G.R., Boldt E.A. and Serlemitsos P.J. (1970) Nature 226, 1041

Staubert R., Kendziona E., Pietsch W., Reppin C., Trumper J. and Voges W. (1980) preprint.

Terrell J. and Olsen K.H. (1970) Astrophys. J. 161, 399.

Terrell N.J. (1972) Astrophys. J. (Lett) 174, L35

White N.E., Mason K.O. and Sanford P.W. (1976) Mon. Not. R. astr. Soc. 176, 91

CHAPTER 6

RADIO OBSERVATIONS - EQUIPMENT AND TECHNIQUES

6.1 INTRODUCTION

Prior to the present work approximately ten radio counterparts to binary X-ray sources were known. Included in these were CYG X-1, CYG X-3, SCO X-1, GX17+2, GX5-1, A0620-00 and CIR X-1. These identifications had been achieved where a good position estimate was available, sometimes provided by the optical counterpart if one was known, together with correlated variability at radio and X-ray wavelengths. Most of the radio observations had been carried out at declinations north of -40°, principally by groups at Westerbork (Braes and Miley 1973) and NRAO, Virginia (Hjellming 1974). Observations of SCO X-1 (Ables 1969) and CIR X-1 (Haynes 1977 priv. comm.) had been made at ANRAO, Parkes.

With improvements in the X-ray source position determinations by satellites it became feasible to carry out a radio survey in the directions of a large number of the smaller (< 2'arc) X-ray error boxes. Such a survey was undertaken using the Parkes 64 m radiotelescope at λ = 2 and 6 cm wavelength.

6.2 EQUIPMENT

6.2.1 GENERAL

The Parkes radiotelescope near Parkes, central New South Wales, is operated by the CSIRO Division of Radiophysics. The telescope is an altitude-azimuth mounted,64 m parabolic reflector dish,with the receivers located in the receiver cabin at the prime focus (Fig 6-1). Telescope pointing is maintained by an independently mounted equatorial telescope known as the Master Equatorial (ME). A beam of light is projected from the base of the radio dish onto the plane mirror within the ME and

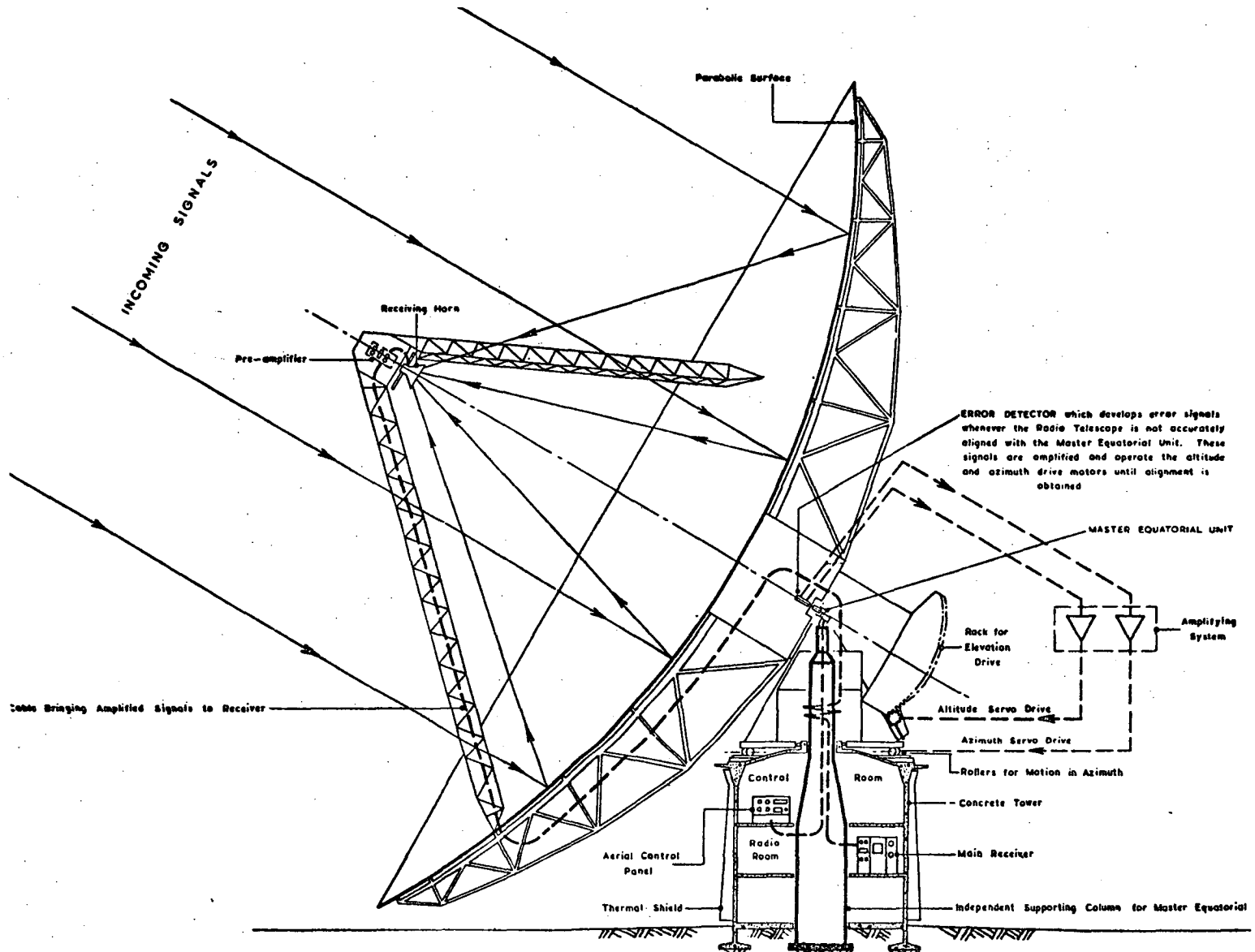

FIG 6-1 SIMPLIFIED REPRESENTATION OF THE RADIO TELESCOPE

reflected back to error sensors. A servo-system is employed to lock the radio dish to the ME.

The reflector dish has three distinct surfaces enabling observations over a large range of wavelengths. The central 16.7 m zone is constructed from solid aluminium panels allowing observations at mm wavelengths (Yabsley 1977). The zone between 16.7 m and 37 m is constructed from perforated aluminium panels thus enabling observations at cm wavelengths. (Yabsley 1975, Johston et al. 1972). The outer zone, constructed from 1 cm aluminium mesh is used for observations at longer wavelengths ($\gtrsim$ 5 cm).

Observations may be made at any azimuth angle but the telescope cannot be driven to zenith angles less than $\sim 3°$ or greater than 60°.

Telescope tracking and positioning is controlled by an on-line PDP 11/40 computer and positions in all usual celestial co-ordinate systems may be used. Receiver sampling and data analysis are controlled by a PDP 9 computer.

6.2.2 THE 2 CM RECEIVER

This receiver consisted of three cryogenically cooled parametric amplifiers each having a gain of $\sim$ 10db. These amplifiers were cascaded to give an overall gain of $\sim$ 30db. The receiver frequency was tuned to 14.7 GHz for the 1977 observations and to 14.4 GHz for the 1978 observations. The receiver bandwidth was 500 MHz on both occasions and with the selected feed, as described in section 6.2.5, the system noise temperature was $\sim$ 90K.

The receiver was,unfortunately,damaged during maintenance by the CSIRO staff in 1979 and was therefore unavailable for the planned observing session later that year or for the 1980 observing sessions.

6.2.3 THE 6 CM RECEIVER

The 6 cm receiver consisted of two cryogenically cooled parametric amplifiers cascaded to give a gain of 20db. The receiver was tuned to 5.0 GHz for both observing sessions in 1980 and had a bandwidth of $\sim$ 400-500 MHz and a system noise temperature of 100K with the selected feed arrangement (6.2.5).

Both the 2 cm and 6 cm receiver outputs underwent further amplification in the IF stages before transmission to the main receiver package located in the radio room of the tower. Block diagrams of both receivers are presented in figure 6-2.

6.2.4 CALIBRATION

Receiver calibration was checked periodically against a signal from a gas discharge tube fed into the receiver front end. The magnitude of this calibration signal was initially determined by comparisons with a standard calibration source, in this case Hydra A (PKS 0915-11) or Virgo A (PKS 1228+12). The receiver gain was then monitored against the fixed output from the discharge tube for the duration of the observing session with daily checks of the output of the discharge tube against the calibration sources.

6.2.5 THE FEED SYSTEM

Variable atmospheric effects can be highly disruptive at λ = 2 cm and to a lesser extent at λ = 6 cm. Figure 6-3a and b show the atmospheric absorption and emission against frequency (Walters 1976). Figure 6-4 presents the absorption by condensed water vapour against frequency (Crane 1976) and clearly shows the increased importance of water vapour absorption at the shorter wavelength. Variable rainfall rates (solid lines) or cloud densities (dashed lines) can result in significant variation in the attenuation of the incoming signal. To overcome these

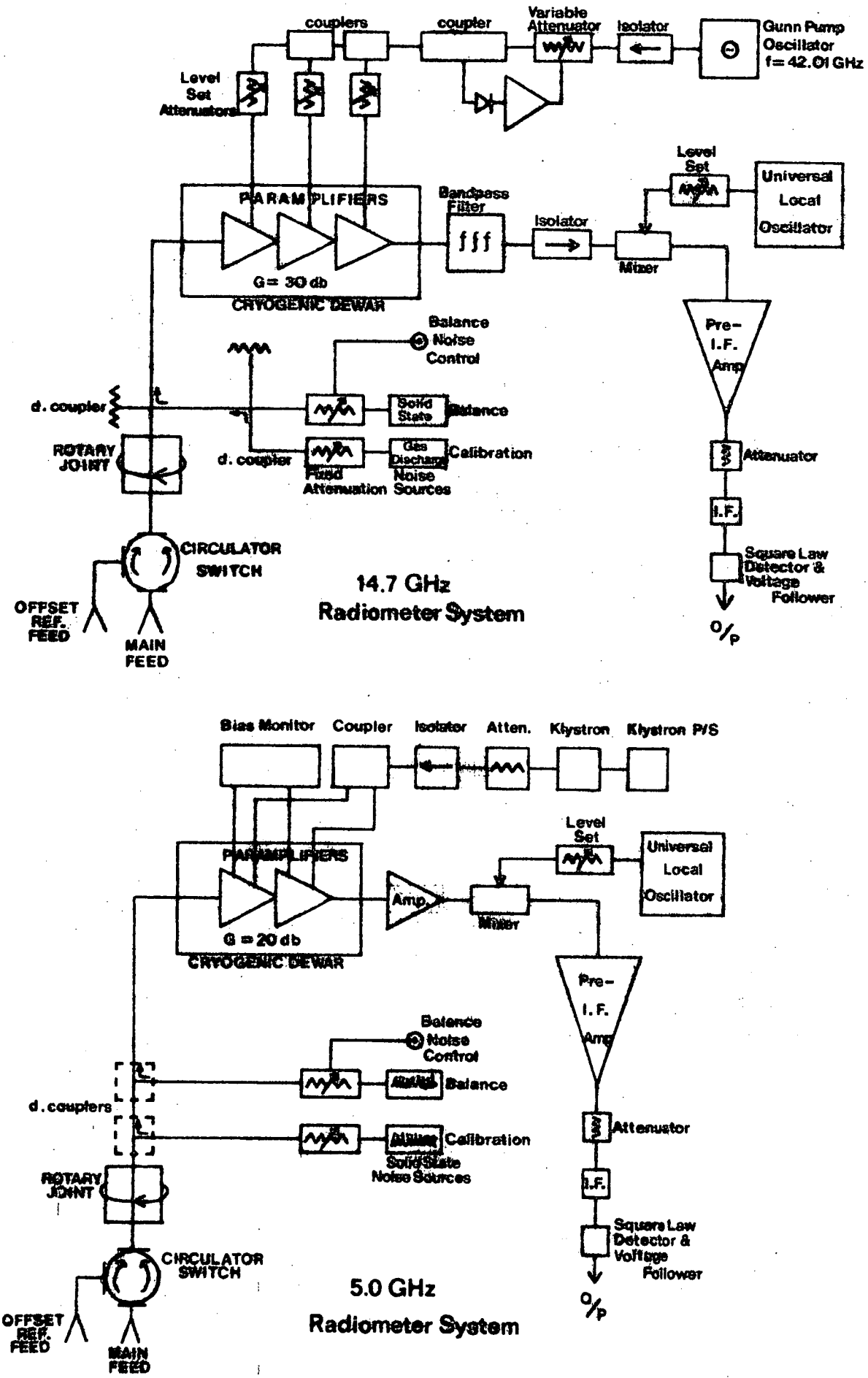

Figure 6-2. Block Diagrams of the Receivers.

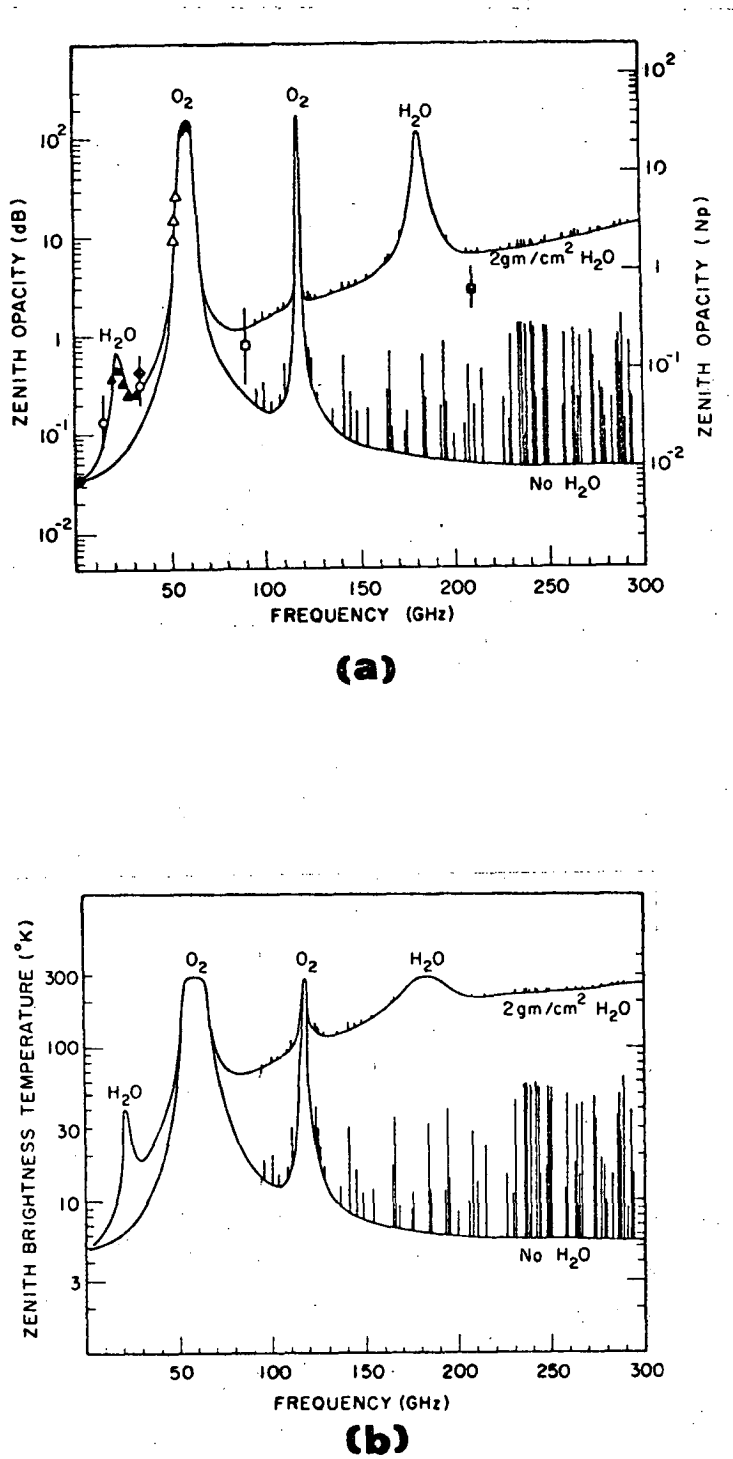

Figure 6-3 Atmospheric absorption (a) and emission (b) versus frequency, viewing at the zenith from sea level. (from Walters 1976)

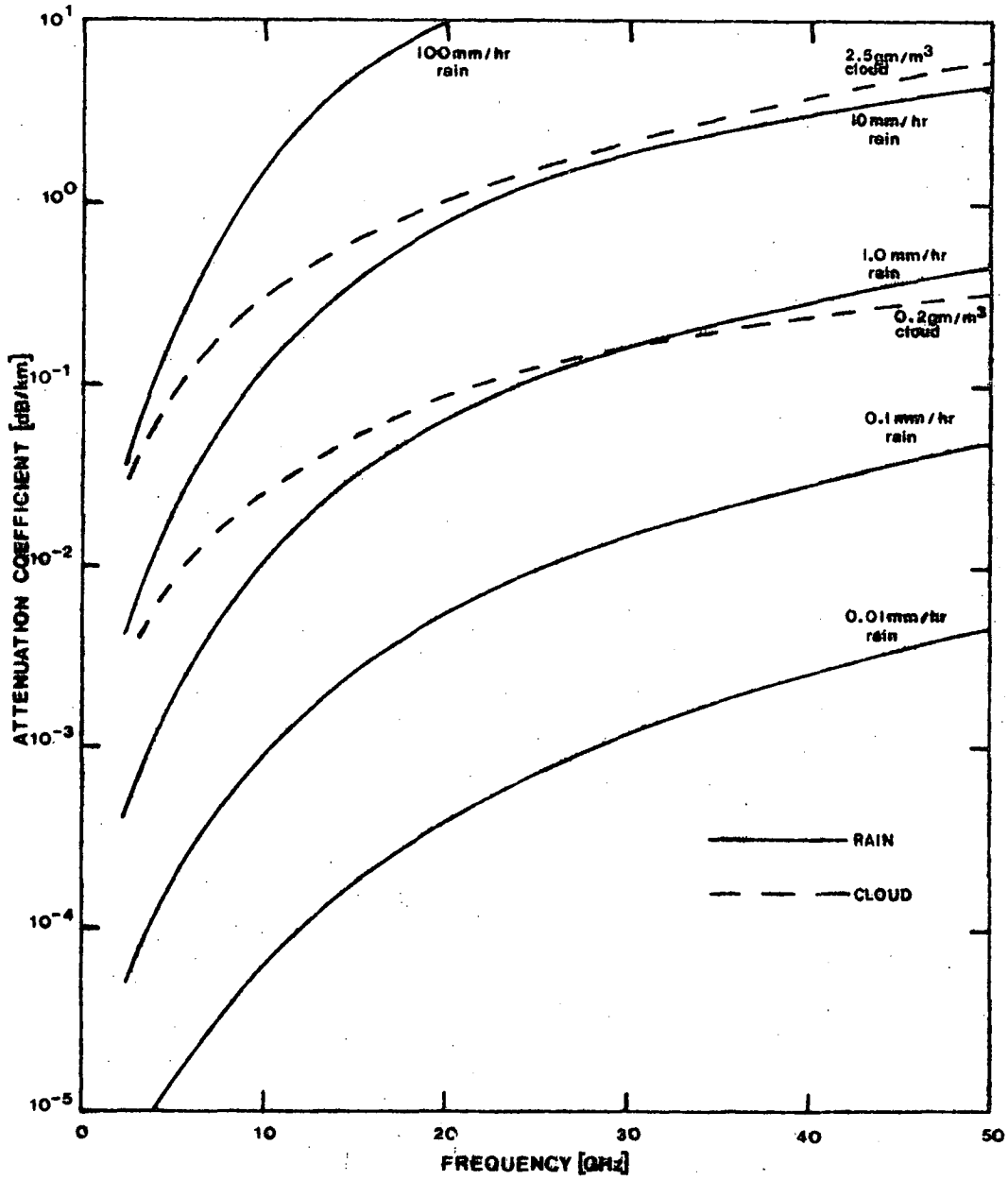

Figure 6-4. Condensed water vapour absorption curves from Crane(1976).

variable absorption effects a dual beam feed arrangement was chosen.

The receiver front end was Dicke switched at a rate of 78 Hz between the on-axis feed (main beam) and a feed displaced from the optimum focus. The displaced feed produced a beam response offset from the main beam by 6.2'arc at λ = 2 cm and 10.2'arc at λ = 6 cm. Half power beam widths were 2.2'arc and 4.3'arc at λ = 2 cm and λ = 6 cm respectively.

By sampling the signal difference between the two beams these atmospheric effects were removed in all but the most severe weather conditions.

The beam widths of the main and offset beams and their separation was determined by scanning both beams through one or other of the calibration sources and measuring the responses (Fig.6-5). Both beams were compared to confirm that they had similar responses.

The offset feed could be rotated about the on-axis feed thus enabling an observation to be made with the two feeds at a constant position angle on the sky and ensuring that the background (offset beam) was always determined from a fixed point with respect to the main beam.

6.2.6 POINTING CORRECTIONS AND GAIN CURVE

The 64 m dish shape varies with zenith angle and these deformations result in variations in both the overall system gain and pointing direction.

Gain corrections for zenith angle dependence are determined, as is the system gain, by observing the calibration sources over the full range of zenith angles. The gain corrections are then calculated from the observed flux and the assumed flux and plotted as in Fig. 6-6.

Pointing corrections are found by observing extra-galactic pointing calibration sources (Bolton and Wright priv. comm.) at various zenith and azimuth angles and fitting the observed minus true positions to a mathematical model describing the pointing variability of the telescope.

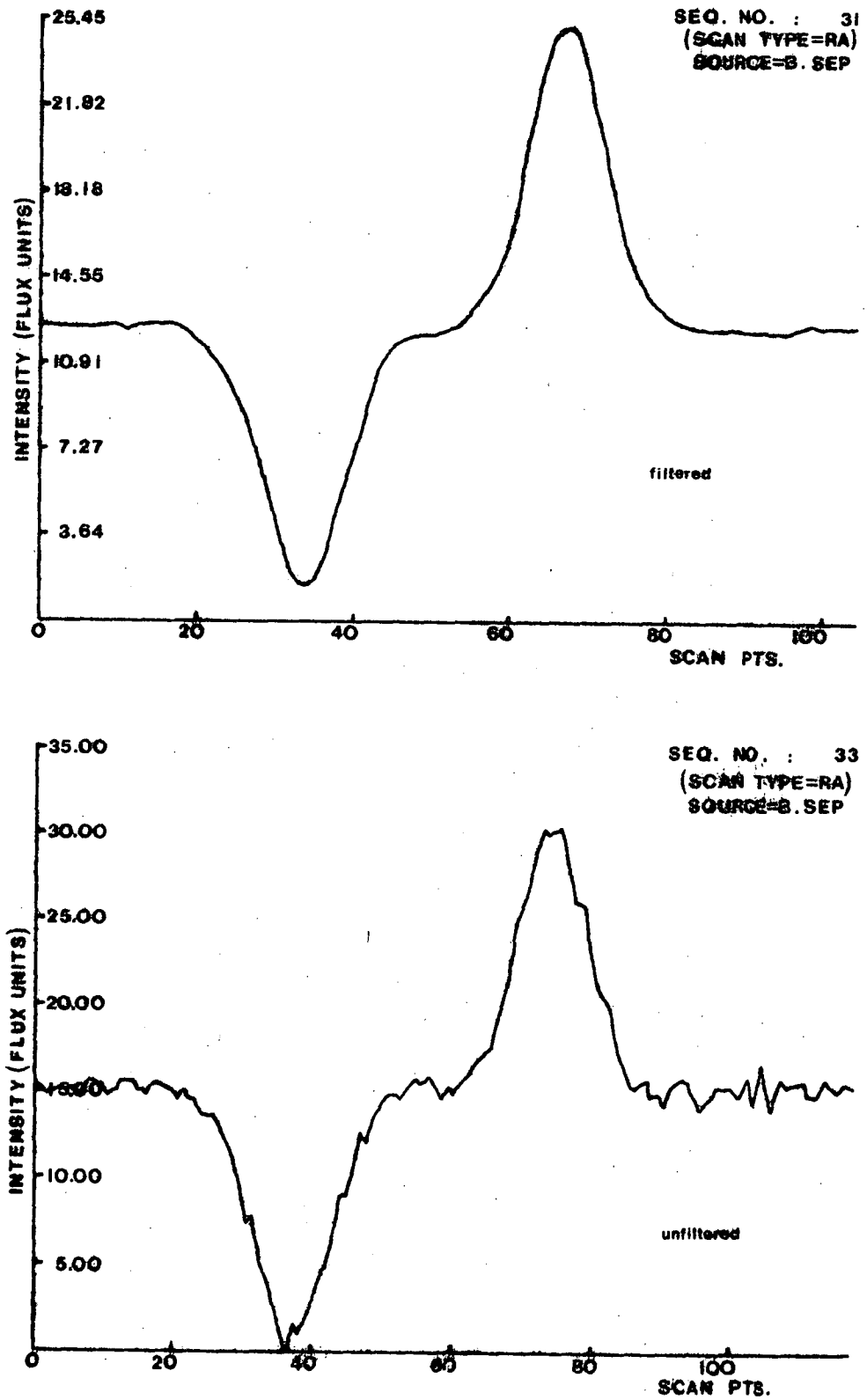

Figure 6-5. Typical 2cm scans showing both beams passing through the source.

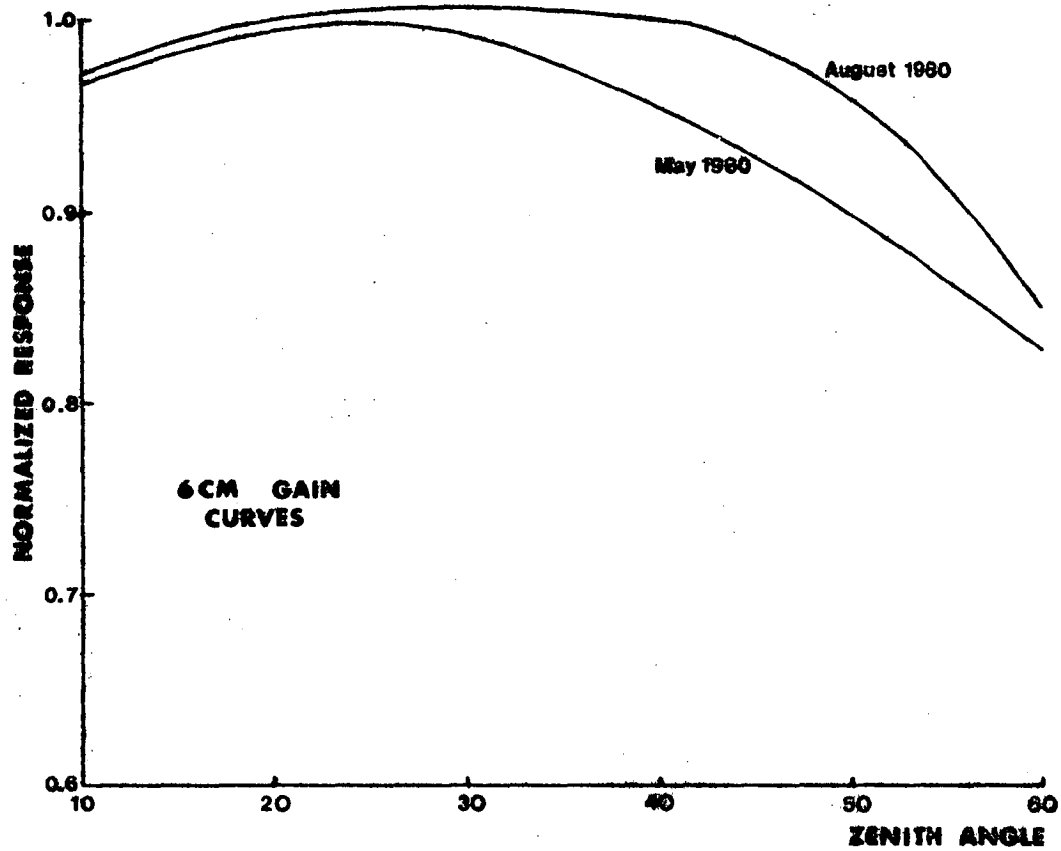

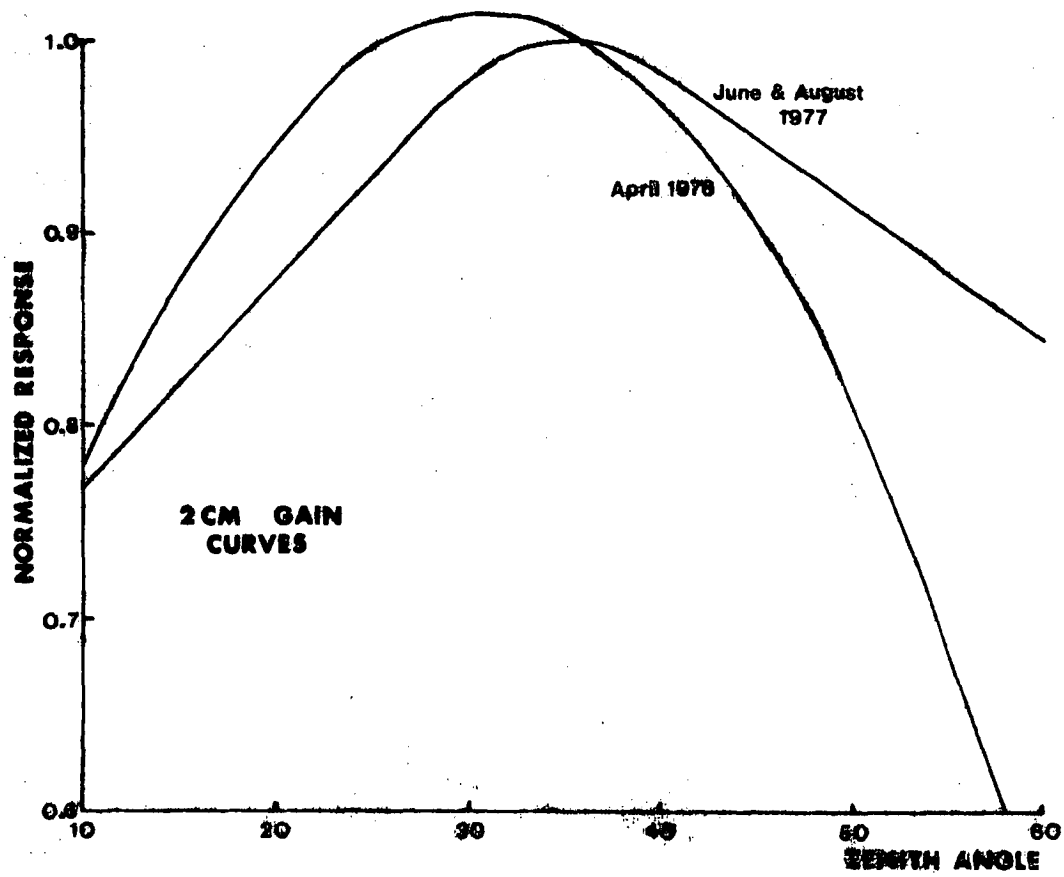

Figure 6-6. System gain curves.

Once the pointing correction coefficients have been determined and entered into the PDP 11 computer,the pointing corrections are automatically carried out each time the telescope is positioned. Typically,the pointing accuracy achieved for the full zenith angle range was ±15"arc rms and for zenith angles in the range 20° to 40° ±10"arc rms.

6.3 OBSERVING TECHNIQUES

6.3.1 SCANNING

The automatic scanning program STAKFL was employed for all scanning observations. The integration time could be chosen as desired but for unknown source fields a minimum integration time of 1000s was used. A calibration check of the receiver was carried out prior to each source observation.

Scans20'arc in length were made through the optimum source position in both right ascension and declination.

Output from the on-line data reduction included the peak flux of any detected source on the scan, integrated flux and source centroid position. These results were determined by fitting the Gaussian beam shape to the integrated scans after digital filtering. The telescope could be repositioned onto the determined centroid of the source position for each set of scans.

If no source was present it was necessary to reposition the telescope manually to centre the scan on the best X-ray source position estimate.

When using the STAKFL program care must be taken to ensure that the offset beam does not scan through the source. Source confusion can also be a problem and the offset beam has to be positioned so that no nearby confusion source passes through it. This often involves checking points around the central search positions and setting the feed angle accordingly.

6.3.2 NODDING

Observations using the "nodding" technique were carried out through the NODDY program. Integration times of 1000s or more were used to reduce the noise level in the absence of sources to approximately 5mJy. In essence,the "Nodding" technique involved driving the telescope until the offset beam was set on the search position and making a calibration check (Fig.6-7). Source sampling continued for 10s and the main beam was then driven to the search position where integration resumed and another calibration was made. Finally,the offset beam was repositioned on the search position and the first stage was repeated.

The telescope could be "nodded" (in zenith angle) or "wagged" (in azimuth angle) and the feed angle had to be set to 0° or 90° for "nodding" or "wagging" respectively. Generally "wagging" was used to avoid the necessity for corrections due to the zenith angle dependence of the telescope gain and subsequent variations in the background level. "Nodding" was sometimes used when the zenith angle was near 30° as telescope gain varied very slowly with zenith angle at this optimum position (Fig.6-6). Nodding was also employed if a confusion source was present in the "wagging" measurement.

No positional information was determined by the NODDY program and so the telescope had to be positioned accurately on the search position prior to the commencement of the observation. The "nodding" technique is inherently more sensitive than the scanning method when searching for weak radio sources because all of the integration time is spent on the search position. This technique was therefore used extensively during the survey.

Output data, after the specified number of "wags",included the mean peak flux of a detected source, the rms deviation between the series of "wags" and the standard error of the observation.

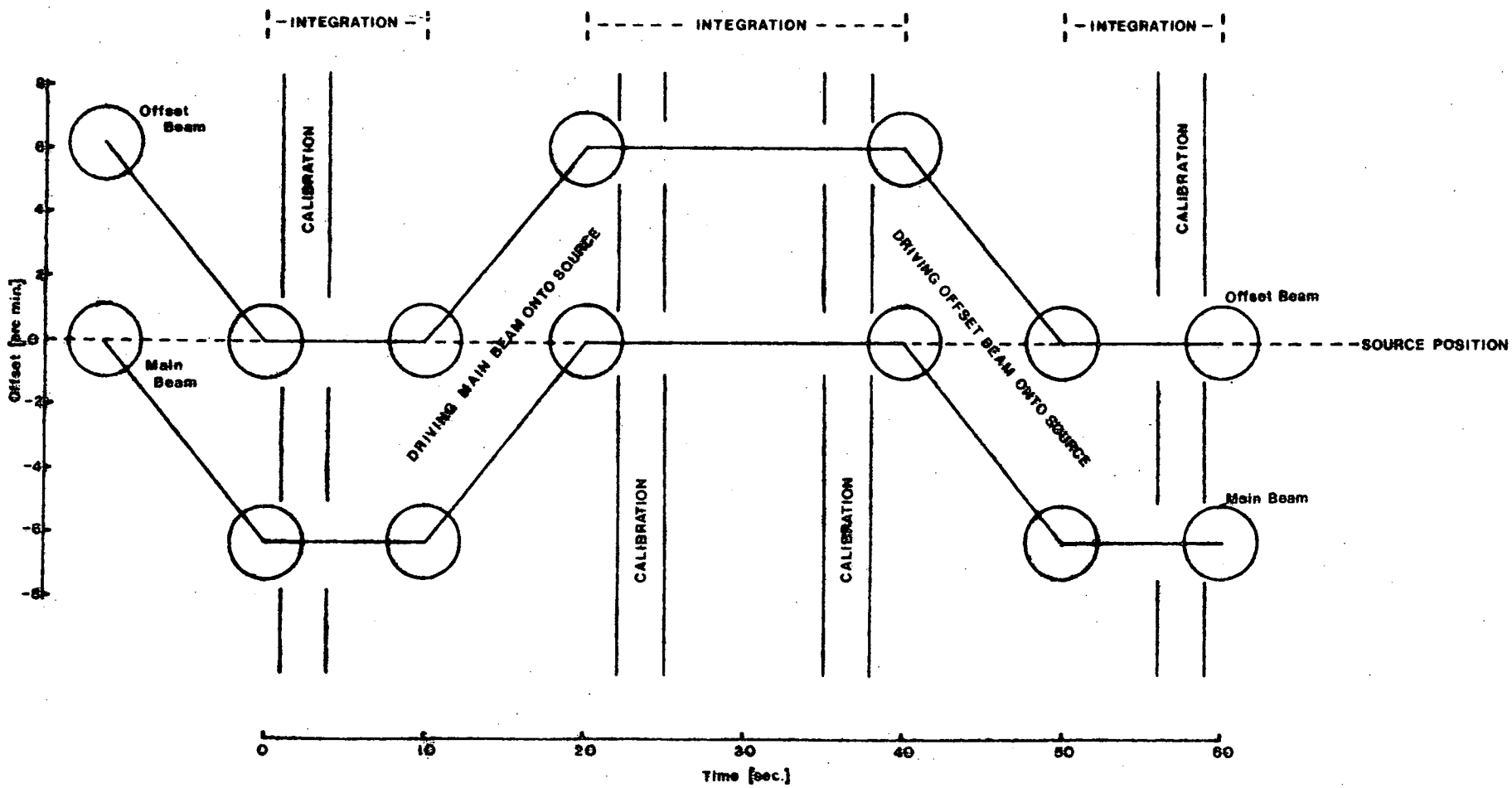

Figure 6-7. The beam sizes (circles) and the beam separation are for the 2cm receiver system.

6.3.3 FAST TIME RESOLUTION OBSERVATIONS

Searches for short time scale,variable,radio emission from several X-ray burst source positions were made in conjunction with simultaneous satellite and other ground-based observations. During such observations the telescope was used to track the source and the sampled integrations, usually of 0.02s each,were digitally stored on magnetic tape together with the starting time of each sample. Plots were produced on the on-line plotter every 1000 integration periods (20s). Data were not sampled during the plotting which lasted approximately 5s. Receiver calibration checks were automatically carried out every few minutes.

The position angle of the feeds was not crucial for these observations but had to be kept constant throughout any observation. To enable comparison of one day's observations with another,the position angle for each burst observation of a given source position was always set to the same value.

As the telescope position was only corrected for pointing errors at the start of each observation, the telescope not being driven during an observation, it was necessary to reposition the telescope manually every 15 minutes to update the pointing corrections.

6.4 GALACTIC PLANE CONFUSION

The problem of source confusion in the galactic plane is compounded by using a dual beam system.

Confusing sources may exist in both the main and offset beams. Because of the signal differencing technique, resolved confusing sources in the offset beam may be immediately discarded as they produce a negative receiver response.

A statistical test of the observing method was carried out by making "nodding" (or "wagging") observations at 103 random positions along

the galactic plane at which there was no *a priori* evidence from the Parkes 6 cm survey (Haynes et al. 1978) for the existence of any radio source. The test was to determine the probability of finding any significant positive or negative signals by chance. As a source separated by the beam separation on *either* side of the nominal observation position would produce a negative response, effectively, 309 galactic plane positions were sampled. Six significant signals (3σ) in excess of 14mJy were recorded, this being the intensity of the weakest source discovered (7.6.4). As expected, twice as many of these were negative.

In the survey 86 galactic plane or Large Magellanic Cloud positions were searched. Twelve other high galactic latitude positions were not expected to have confusion problems. One would therefore expect to observe two or at most three chance sources during the survey on the basis of the above test. This expectation was supported by the observational results (7.3).

Further confusion tests were made for all those sources for which there was a positive detection. The source positions were scanned in right ascension and declination using the STAKFL program (6.3.1) and a series of eight nodding measurements (6.3.2) were made around each source at an offset of half of the half power beam width. In the absence of confusion the point source intensity should drop to half the value observed at the correct on source position.

These tests comprehensively determined the confusion level around the detected sources.

6.5 REFERENCES

Ables J.G.(1969) Astrophys.J.Lett. 155, L27

Braes L.L.E. and Miley G.K.(1973) I.A.U. Symposium #55,"X and γ Ray Astronomy", ed. Bradt H. and Giacconi R., D. Reidel, Dordrecht, Holland. pp 86-97.

Crane R.K. (1976) "Methods of Experimental Physics" ed. Meeks M.L., Acad. Press, Vol 12, part B pp 177-182

Haynes R.F., Caswell J.L. and Simons L.W.J. (1978) Aust. J. Phys. Astrophys. Suppl. No.45

Hjellming R.M. (1974) "International Conference on X-rays in Space" ed. Venkatesan D., University of Calgary, p 211

Johnston K.J., Robinson B.J., Caswell J.L. and Batchelor R.A. (1972) Astrophys. Lett. 10, 93

Walters J.W. (1976) "Methods of Experimental Physics" ed. Meeks M.L., Acad.Press, Vol 12, part B pp 173-174

Yabsley D.E. (1975) "IREE Convention Digest, International Electronics Convention '75' (IREE Aust., Sydney)" p 203

Yabsley D.E. (1977) Proc. A.S.A. 3, 113

CHAPTER 7

RADIO OBSERVATIONS - RESULTS

7.1 INTRODUCTION

Initially, observations were carried out at λ = 2 cm in three separate observing sessions (Duldig et al. 1979a and 1979b): (1) 1977 June 13-18, (2) 1977 August 18-20, (3) 1978 April 19-28. During these three sessions 98 X-ray source positions were surveyed, 81 of which resulted in upper limits to any detected source flux. Six search positions proved to be highly confused and no meaningful observations could be made in these regions. The remaining eleven positions gave a positive detection (3σ) on at least one occasion. Searches for bursting radio behaviour from known X-ray burst sources were also carried out as part of a world-wide observation programme. (Thomas et al. 1979)

Two additional observing sessions were undertaken at λ = 6 cm: (4) 1980 May 9-16, (5) 1980 July 31 - August 5, at which time SCO X-1 was observed at a significant level.

During all sessions the X-ray/radio flaring source CIR X-1 was monitored (Thomas et al. 1978a). Fast time resolution observations (6.3.3) of CIR X-1 were carried out in the λ = 6 cm observing sessions. Also , further observations of X-ray burst sources were made as part of a second world-wide observation programme.

Searches for radio emission from the recurrent X-ray transient source A0538-66 were undertaken throughout an expected X-ray flare during the final observing session.

7.2 UPPER LIMITS

7.2.1 GENERAL

Table 7-1 shows the λ = 2 cm upper limit results for 69 X-ray

(1) X-ray source	(2) Other names	(3) X-ray position (1950.0) R.A. h m s	(4) Dec. ° ′ ″	(5) Flux dens. upper limit (1 σ r.m.s.) (mJy)	(6) Remarks and refs.*
2S 0050-727	SMC X-3	00 50 21.2	-72 42 01	<8	
2S 0052-739	SMC X-2	00 52 54.5	-73 56 58	<7	
3U 0115-73	SMC X-1/Sk160	01 16 06	-73 39 06	<6	(3)
2S 0512-400	MX 0513-40/ NGC 1851	05 12 28.7	-40 05 53	<7	
+3U 0521-72	LMC X-2	05 21 19	-72 00 07	<4	HEAO-1 position (5)
ZA 0526-328		05 26 27.5	-32 32 46	<5	4 possible HEAO-1 positions (6)
		05 26 22.9	-32 54 47	<5	
		05 27 37.2	-32 53 34	<7	
		05 27 41.6	-32 32 24	<5	
2S 0532-664	LMC X-4	05 32 54	-66 24 10	<5	
HDE 245770	A 0535+26	05 35 48	+26 17 18	<6	X-ray flare preceded this observation by ~15 days (7)
3U 0538-64	LMC X-3	05 38 38.1	-64 06 20	<5	HEAO-1 position (5)
MX 0656-07		06 56 01	-07 11 42	<5	X-ray nova
HD 77581	3U 0900-40/ Vela XR-1	09 00 13.2	-40 21 25.2	<6	
2S 0918-549	4U 0919-54	09 18 55.6	-54 59 33	<6	
2S 0921-630		09 21 25.4	-63 04 27	<5	(5)
ZA 0922-317		09 22 10.5	-31 29 06	<3	HEAO-1 position (6)
2S 0945-307	MCG-5-23-16	09 45 28.7	-30 42 24	<11	(8)
Krzeminski star	Cen X-3	11 19 01.3	-60 20 59	<3	
Henize 715	2S 1145-619	11 45 35.6	-61 55 44	<7	Confusing source ~2' arc north
Wray 977	2S 1223-624	12 23 49.6	-62 29 40	<40	Confusing source 4' arc south
2S 1239-599	A 1239-59	12 39 07.5	-59 55 39	<5	
A 1246-58		12 46 39	-58 51 00	<4	
2S 1254-690	3U 1254-69	12 54 19.7	-69 01 03	<6	
2S 1333-340	MCG-6-30-15	13 33 00.7	-34 02 26	<8	(9)
2S 1524-617	A 1524-61/ Tr A X-1	15 24 06.9	-61 42 41	<4	
2S 1538-522		15 38 40.2	-52 13 38	<6	
2S 1543-624	A 1543-62	15 43 33.9	-62 24 56	<6	
3U 1543-47	A 1543-47	15 43 50	-47 33 36	<5	<10 mJy at 5000 MHz (4)
2S 1553-542	MX 1553-54	15 53 55.6	-54 16 15	<4	
2S 1556-605	3U 1556-60	15 56 47.2	-60 35 47	<5	
2S 1608-522	4U 1608-52	16 08 51.2	-52 18 02	<4	
Sco X-1	3U 1617-15	16 17 01.7	-15 32 17	<2	Each position belongs to a member of the known triple radio source (1)
		16 17 04.5	-15 31 16	<3	
		16 17 06.8	-15 30 14	<5	
2S 1624-490		16 24 19.6	-49 05 07	<50	Within extended 2 cm source
2S 1627-673	3U 1626-67	16 27 13.6	-67 21 23	<4	
A 1630-47	3U 1630-47	16 30 16.5	-47 16 51	<9	
A 1633-64	3U 1632-64	16 33 12	-64 04 48	<10	
2S 1636-536	MXB 1636-53	16 36 57.6	-53 39 21	<5	
2S 1642-455		16 42 09.9	-45 31 10	<50	Within extended 2 cm source
A 1659-48	3U 1658-48/ GX 339-4	16 59 02	-48 42 25	<6	Ariel-5 position (12)
HD 153919	3U 1700-37	17 00 32.7	-37 46 27	<6	
2S 1702-363	GX 349+2	17 02 23.3	-36 21 23	<5	Like Sco X-1; <5 mJy at 2695, 8085 MHz (1); also (17)
2S 1702-429	A 1702-42?	17 02 40.4	-42 57 58	<7	
Nova Oph 1977	H 1705-25	17 05 10.4	-25 01 38	<6	(13)
2S 1715-321	MX 1716-31	17 15 31.9	-32 07 15	<6	
2S 1728-337	MXB 1728-34	17 28 39.6	-33 47 52	<12	Confused by strong source to north
2S 1728-247	3U 1728-24	17 28 57.4	-24 42 42	<5	<15 mJy, 5000 MHz (4)
MXB 1730-335		17 30 07.2	-33 20 36	<6	HEAO-1 position (10)
H 1743-32		17 43 01	-32 12 42	<6	2 possible positions from HEAO-1 (11)
		17 41 47	-32 12 12	<8	
2S 1744-265	GX 3+1	17 44 49	-26 32 51	<5	11±4 mJy at 1415 MHz (2); <5 mJy at 1415, 2695 MHz (1)
A 1744-36	GX 354-5	17 44 52	-36 06 30	<7	
2S 1746-370	3U 1746-37/ NGC 6441	17 46 48.7	-37 02 17	<4	
2S 1755-338		17 55 22.1	-33 48 25	<6	
2S 1758-250	GX 5-1	17 58 33	-25 04 39	<50	Confused at 2 cm by extended source to west; 10 mJy at 1415 MHz (15)
2S 1758-205	GX 9+1	17 58 33.3	-20 31 40	<7	8 mJy, 2695 MHz (1)
2S 1803-245	MX 1803-24	18 03 45.8	-24 35 38	<6	
2S 1811-171	GX 13+1	18 11 37.2	-17 10 16	<6	<15 mJy, 1415 MHz (1)
A 1812-12		18 12 23.5	-12 04 52	<7	
2S 1813-140	GX 17+2	18 13 11.2	-14 03 10	<10	Like Sco X-1; 11 mJy at 1415 MHz; 22 mJy at 2695 MHz (1); 3 mJy at 5000 MHz (14)
NGC 6624	3U 1820-30	18 20 29.6	-30 23 40	<5	
2S 1822-099		18 22 48.5	-00 02 24	<6	
ZA 1822-371		18 22 22.3	-37 07 34	<4	HEAO-1 position (6)
A 1835-08		18 35 45	-08 21 14	<4	Ariel-5 position (12)
2S 1837+049	Ser X-1	18 37 29.8	+04 59 23	<7	
A 1850+01		18 50 18	+01 15 36	<5	(12)
2S 1850-087	A 1850-08	18 50 21.6	-08 45 36	<7	
A 1856+08		18 56 40	+08 10 59	<5	(12)
2S 1905+000	MXB 1905+00	19 05 54.9	+00 05 37	<3	
A 1907+09		19 07 48	+09 31 48	<4	
2S 1908+005	Aql X-1	19 08 42.9	+00 30 05	<5	Optical candidate position (16)
2S 1916-053	A 1915-05	19 16 08.5	-05 19 51	<3	
2S 1957+115	A 1956+11	19 57 02.9	+11 34 14	<4	

*(1) Braes & Miley (1973); (2) Miley, private communication in Janes *et al.* (1973); (3) McGee, Newton & Brooks (1974); (4) A. E. Wright (1978, private communication); (5) H. Bradt (1978, private communication); (6) R. Griffiths (1978, private communication); (7) Clark & Chartres (1978); (8) Pineda & Schnopper (1978); (9) Davis *et al.* (1978); (10) Doxsey *et al.* (1977a); (11) Gursky *et al.* (1977); (12) G. Carpenter (1977, 1978, private communications); (13) Griffiths *et al.* (1978); (14) Hjellming (1978); (15) Braes *et al.* (1972); (16) Thorstenson, Charles & Bowyer (1977); (17) Zuiderwijk (1978); Glass & Feast (1978).

Table 7-1: λ = 2 cm Upper Limit Results

sources with well determined positions. Column (1) contains the X-ray source catalogue name or the name of the known optical counterpart, column (2) includes the more common X-ray source name, columns (3) and (4) show the X-ray position used in the survey in 1950.0 epoch equatorial coordinates, the 1σ r.m.s. lowest upper limit observed appears in column (5) in mJy and column (6) contains remarks and references. Table 7-2 shows the upper limits determined for eleven X-ray sources of high galactic latitude which had larger X-ray position error boxes.

Table 7-2

λ = 2 cm Observations of X-ray Sources with Galactic Latitude >10°

Source	Position (1950) R.A. h m s	Dec. ° ' "	Flux dens. upper limit (1 σ r.m.s.) (mJy)	X-ray error box size (90% conf.) (deg^2)
2A 0039-096	00 39 46	-09 37 48	<7	0.075
2A 0120-353	01 20 55	-35 19 12	<3	0.053
2A 0235-526	02 35 05	-52 32 24	<4	0.078
2A 0311-227	03 11 38	-22 46 48	<2	0.056
2A 1246-410	12 46 17	-41 03 00	<10	0.094
2A 1631-644	16 31 29	-64 24 36	<6	0.072
2A 2009-569	20 09 07	-56 57 00	<6	0.072
2A 2127+120	21 27 22	+12 00 00	<5	0.035
2A 2251-178	22 51 25.4	-17 50 40	<2	4×10^{-4}*
2A 2302-088	23 02 12	-08 53 24	<8	0.080
2A 2315-428	23 15 19	-42 48 36	<4	0.067

*Error box is 40"arc radius.

Several of these sources deserve further comment.

7.2.2 A0535+26

This X-ray source is known to have flared to 0.4 times the Crab nebula intensity by 1978 April 12, 12^h UT (Clark and Chartres 1978).

A search for λ = 2 cm radio emission on April 25 detected no signal to an upper limit (1σ) of 7mJy (Thomas et al. 1978b).

7.2.3 2S1145-619 (≡HEN715)

Scans through the X-ray source position show that a λ = 2 cm source of flux density about 40mJy peaks $\sim$ 2' arc north of the well established optical counterpart Henize 715 (Bradt et al. 1977). The Parkes 6 cm survey (Haynes et al. 1978a) shows a large extended source $\sim$ 10' arc to the east (Fig. 7-1) with which the λ = 2 cm observation is probably associated. There is no evidence to suggest any physical association between the radio and X-ray objects. No point radio source is observed to an upper limit (1σ) of 7mJy.

7.2.4 2S1223-624 (≡GX301-2, ≡WRA977)

Seaquist (1977) suggested the identification of this X-ray source with an extended radio source, possibly an HII region, of about 1Jy flux density at λ = 6 cm and λ = 3.5 cm wavelengths. The Parkes 6 cm survey (Fig. 7-2) shows a peak flux density of $\sim$ 650mJy near the X-ray source position. The λ = 2 cm source position is in good agreement with the 6 cm survey position and is $\sim$ 4' arc south of the confirmed optical counterpart WRA977 (Bradt et al. 1977). There is no evidence to suggest that this radio feature is associated with the X-ray source.

The estimated λ = 2 cm flux density upper limit (1σ) of 40mJy for a point source at the WRA977 position may be somewhat high due to the nearby, extended confusing source.

7.2.5 2S1608-523

This X-ray source underwent an X-ray outburst prior to the 1977 August observing session. The X-ray intensity in the 3-6 keV range was still 0.45 times that of the Crab at the time of our observations on 1977 August 20, $08^h\ 45^m$ UT (Kaluzienski and Holt, private comm.). No

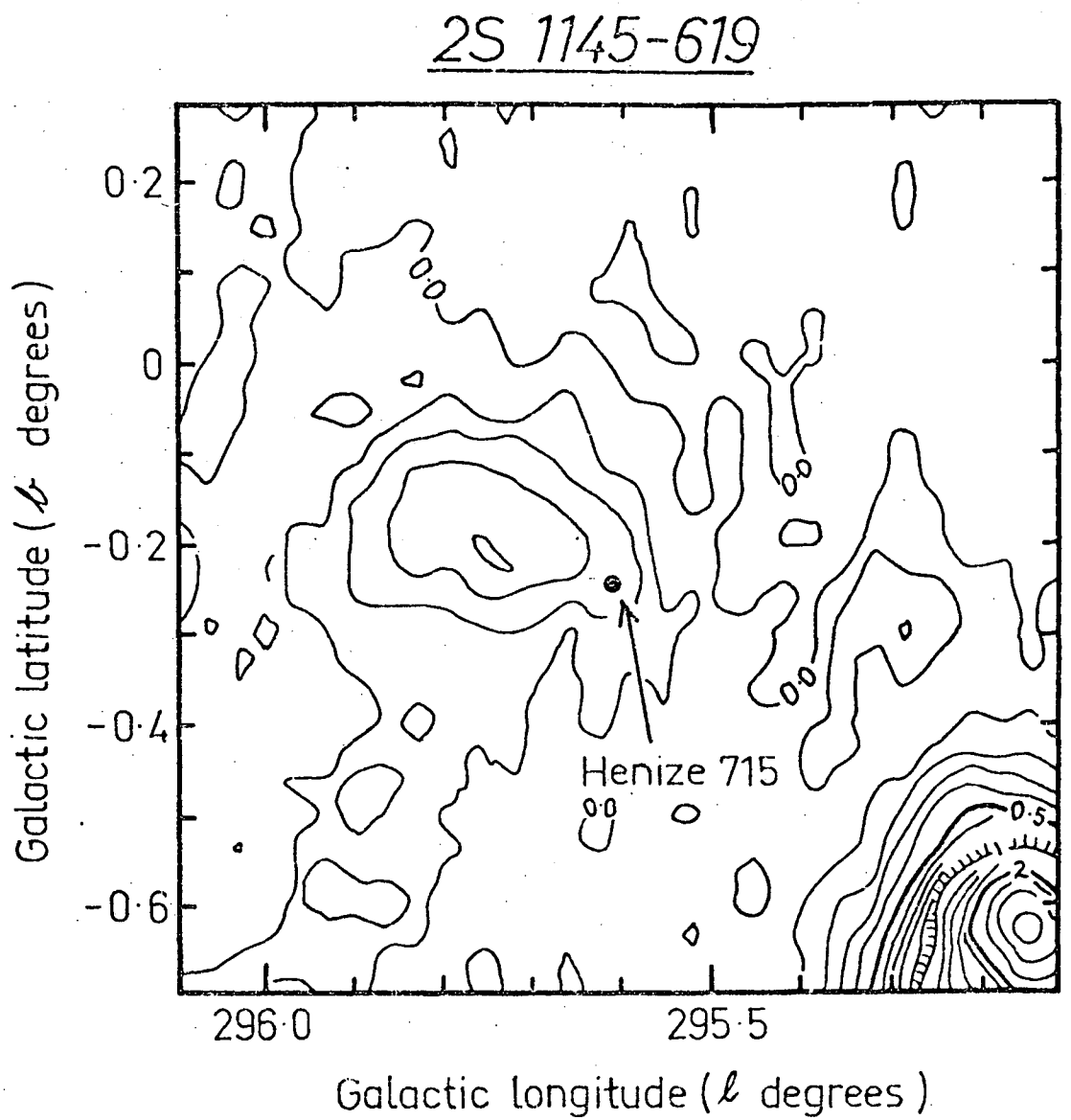

Figure 7-1. Parkes 6cm survey map of the region surrounding 2S1145-619 with the position of the optical counterpart HEN715.

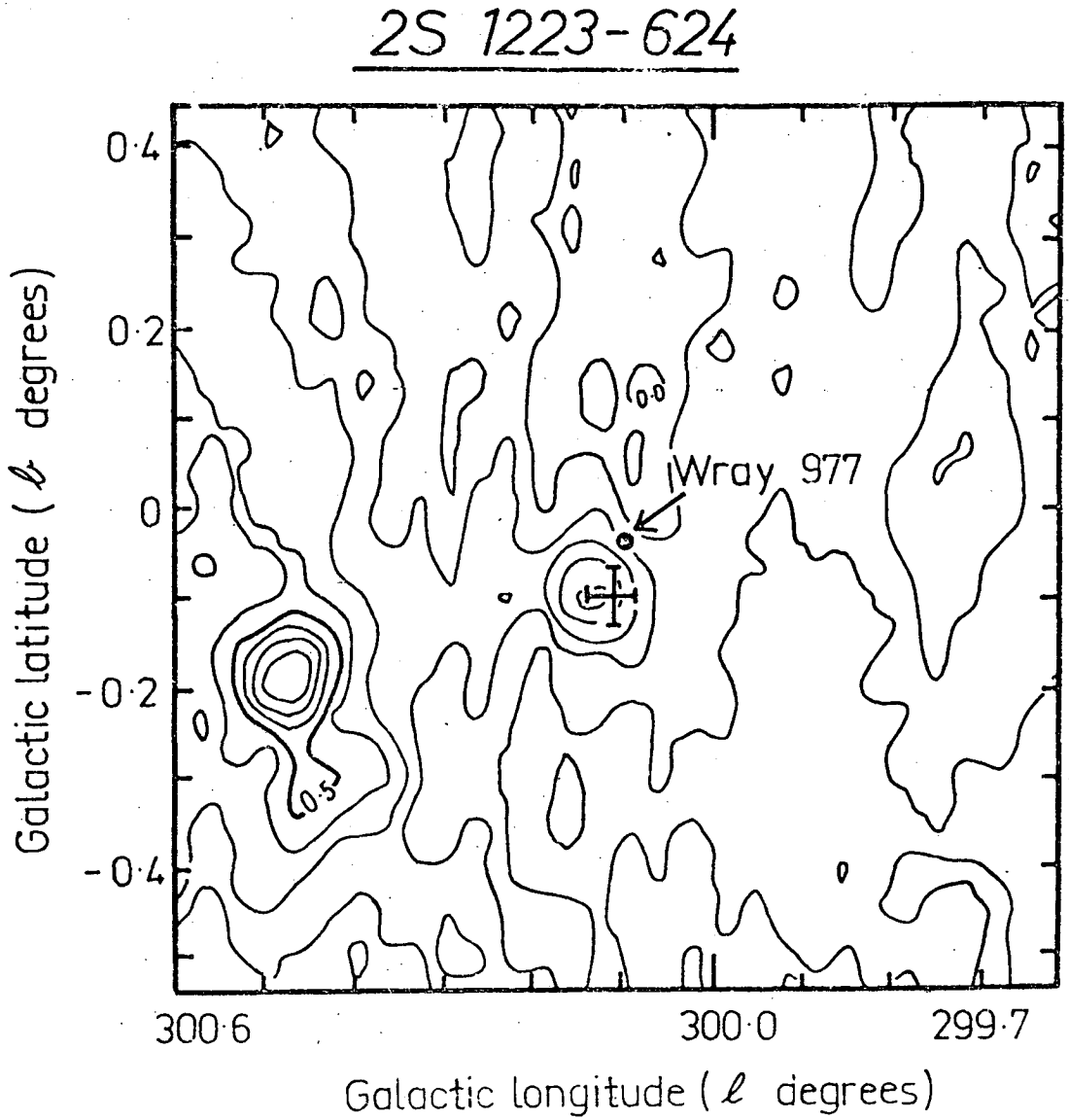

Figure 7-2. Parkes 6cm survey map of the region surrounding 2S1223-624 with the position of the optical counterpart WRA977. The 2cm radio source position is shown (the cross with ±1' arc error bars).

radio source down to an upper limit (1σ) of 8mJy was detected (Duldig et al. 1977).

7.2.6 2S1624-490

Sanduleak and Dolan (1974) drew attention to the close positional coincidence between this X-ray source and the 11 cm Parkes survey radio source G334.9-0.3 (Thomas and Day 1969). The Parkes 6 cm survey shows an elongated object (∿30×12' arc), probably an HII region, in the direction of the X-ray source (Fig. 7-3). The radio source is perhaps associated with the galactic cluster NGC6134. Figure 7-3 shows that the X-ray source is located at one end of this extended object. λ = 2 cm observations indicate that the X-ray source position is very near the central ridge of the radio emission. However, no coincident λ = 2 cm point radio source was found to an estimated upper limit (1σ) of 50mJy.

7.2.7 2S1642-455 (≡GX340+0, ≡Ara X-1)

Sanduleak and Dolan (1974) also suggested a possible association between this X-ray source and a weak Parkes 11 cm survey source. Seaquist (1977) reported that a small HII region with an observed flux density of about 3Jy at λ = 6 and 3.5 cm coincided with the X-ray source. The λ = 2 cm results show an extended source of ∿ 4' arc with a peak flux density of ∿ 700mJy offset from the X-ray position by ∿ 2' arc (Fig. 7-4b). This result is in reasonable agreement with the Parkes 6 cm survey map of the region which shows a peak flux of ∿ 2.6Jy (Fig. 7-4a). There is no sign of any point source down to an upper limit (1σ) of 50mJy.

Follow up observations were carried out by Dr. Ray Haynes using the Fleurs synthesis telescope (Haynes et al. 1979). This high resolution observation at 1415MHz (λ = 21 cm) also found no point radio

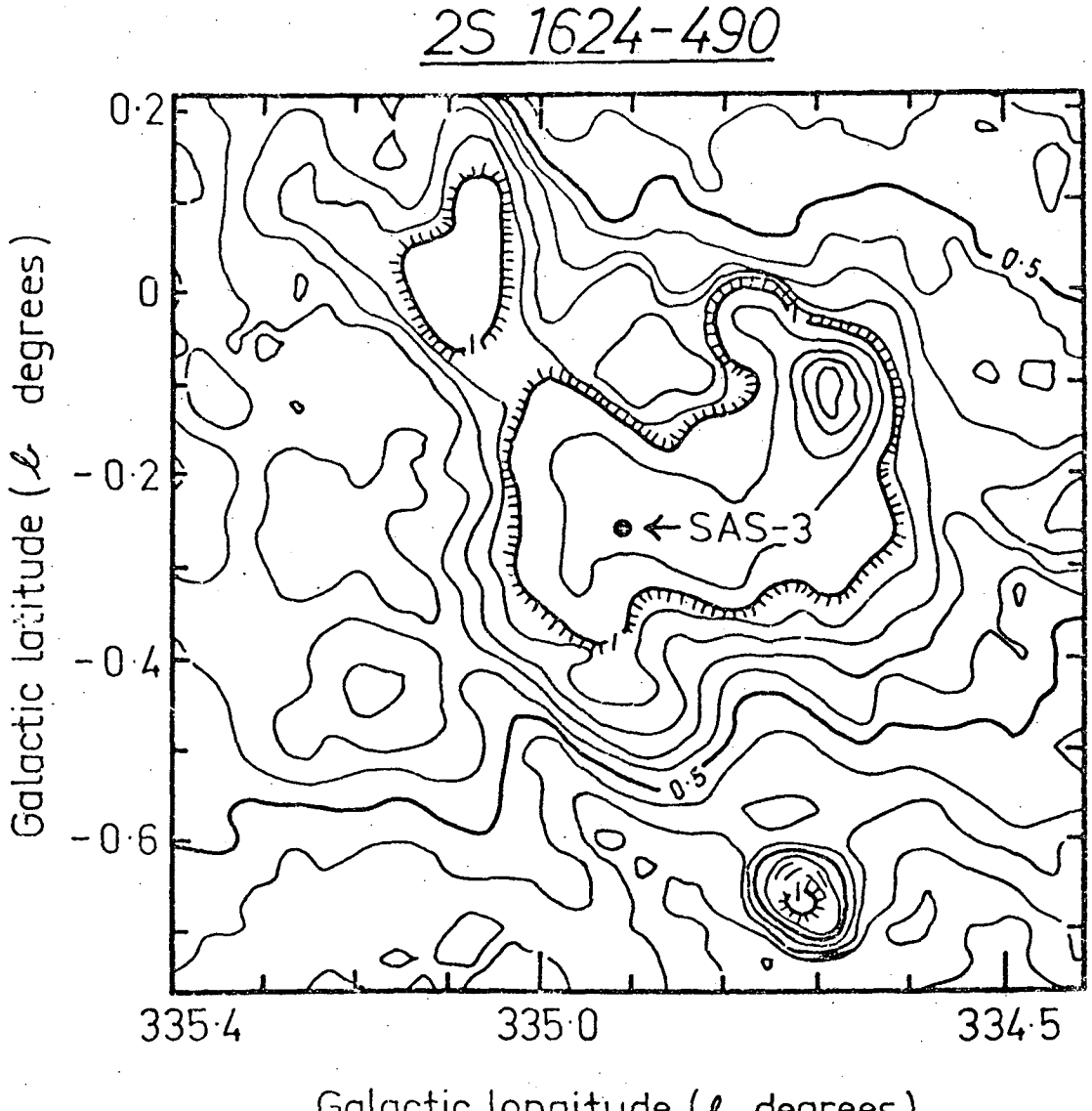

Figure 7-3. Parkes 6cm survey map of the region surrounding 2S1624-490 with the SAS-3 error circle (90% confidence) shown by the filled circle (Bradt 1978).

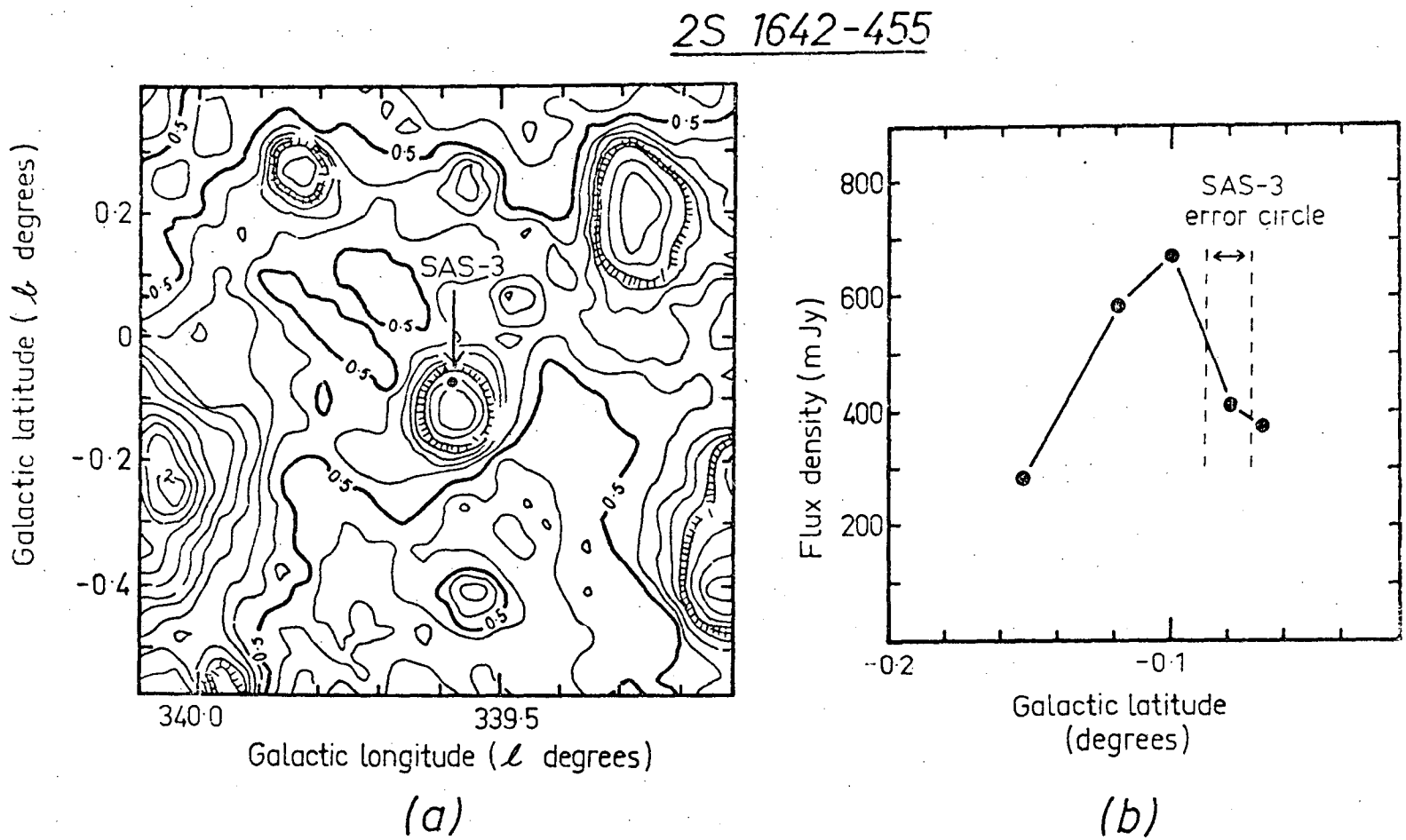

Figure 7-4. (a) Parkes 6cm survey map of the region surrounding 2S1642-455 with the SAS-3 error circle (90% confidence) shown by the filled circle (Bradt 1978).
(b) 2cm measurements made through the X-ray source position at constant galactic longitude.

source but further considerations showed that the two sources may be at about the same distance (see 8.4.1).

7.2.8 SCO X-1 AND SIMILAR SOURCES

SCO X-1 has a known triple radio counterpart (Braes and Miley 1973) with a radio flux density spectrum of $S_\nu \propto \nu^{-1}$. During 15% of the time large-scale radio flaring by up to a factor of 100 has been observed. As well,Miyamoto and Matsuoka (1977) have noted that for 20% of the time the radio components at 11 cm wavelength are weaker than 3mJy. It is therefore not surprising that the SCO X-1 components remained undetected at 2 cm wavelength in 1978 April.

The sources 2S1702-363, 2S1758-250 (GX5-1) and 2S1813-140 (GX17+2) are all similar to SCO X-1 at X-ray and/or optical wavelengths (Greenhill et al. 1979). 2S1758-250 and 2S1813-140 have previously been detected at a number of radio wavelengths (Braes et al. 1972, Braes and Miley 1973, Hjellming 1978) at flux density levels below our λ = 2 cm sensitivity limit. If the similarities between these three objects and SCO X-1 extend to the radio regime,it is not surprising that they also remained undetected at λ = 2 cm.

7.2.9 LMC X-1

The field surrounding the X-ray source LMC X-1 was mapped at λ = 2 cm (Duldig et al. 1980a). The map (Fig. 7-5) was formed from the weighted addition of two maps created from two independent sets of declination scans. Unlike earlier maps of MC76 and MC77 (McGee et al. 1974), Figure 7-5 incorporates pointing error corrections. Both radio sources are extended and may be composed, as the optical photograph suggests (Fig. 7-6), of a number of unresolved radio components (see comments by McGee et al. 1978). The position of LMC X-1 (Johnson et al. 1978, Epstein 1977) and the stellar candidate R148 (Rapley and Touhy 1974)

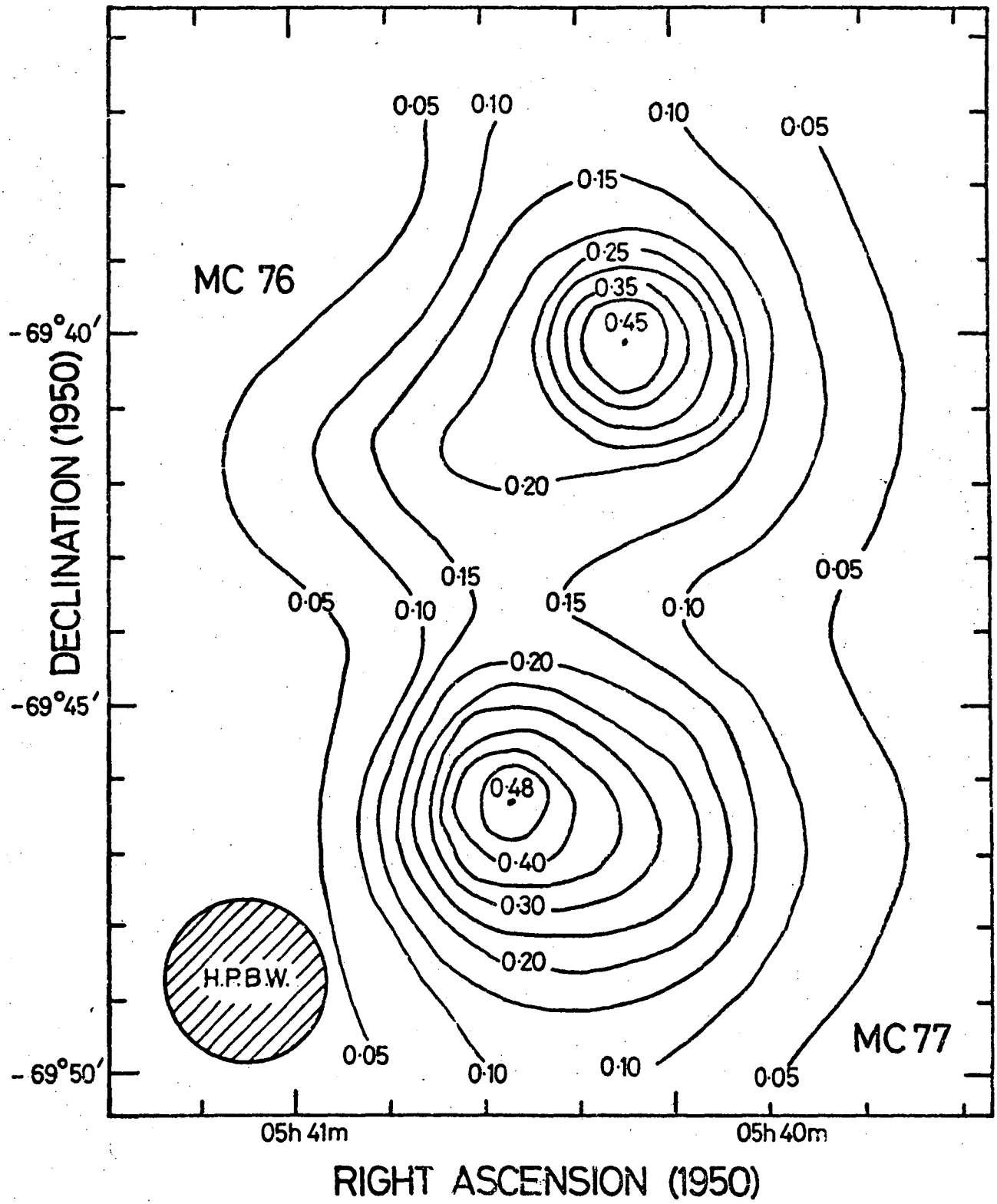

Figure 7-5. The 2cm map of the region near LMC X-1 showing MC76 and MC77. Pointing error corrections are included to give a positional uncertainty of < 15" arc.

are shown in figure 7-6 and are offset from the peak of MC77. MC77 is extended toward the HEAO-1 position for LMC X-1 and the existence of an unresolved point radio source associated with the X-ray object can not be ruled out. An upper limit of 200mJy (90% confidence) is set for any coincident point radio source.

7.3 CONFUSION

Six X-ray source positions, namely 2S1728-337 (MXB1728-34), A1742-289 (detected as a radio transient by Davies et al. 1976), A1742-294, A1743-28, 2S1758-250 (GX5-1) and 2S1845-024 could not be observed due to very high galactic plane confusion toward the galactic centre. The X-ray source GX5-1 has been detected at radio wavelengths by Braes, Miley and Schoenmaker (1972) using facilities with better angular resolution than that available to us.

As discussed in 6.4 a statistical test of the observing method was carried out. "Nodding" or "Wagging" observations were made at 103 random positions along the galactic plane. A significant positive or negative signal (3σ) in excess of 14mJy was observed at six of the 309 positions effectively sampled. Of these six significant signals, four were negative as would be expected. (Twice as many offset positions are searched on either side of the central position and because of the signal difference technique, produce a negative response.)

The expected number of positive detections, by chance, as indicated by this test would be two or at most three with twice this number of negative detections.

In the survey, 86 galactic plane or Large Magellanic Cloud positions were searched and on five occasions a significant negative response was recorded, in agreement with the expectation from the above test. Thus two or possibly three of the detected radio sources may be

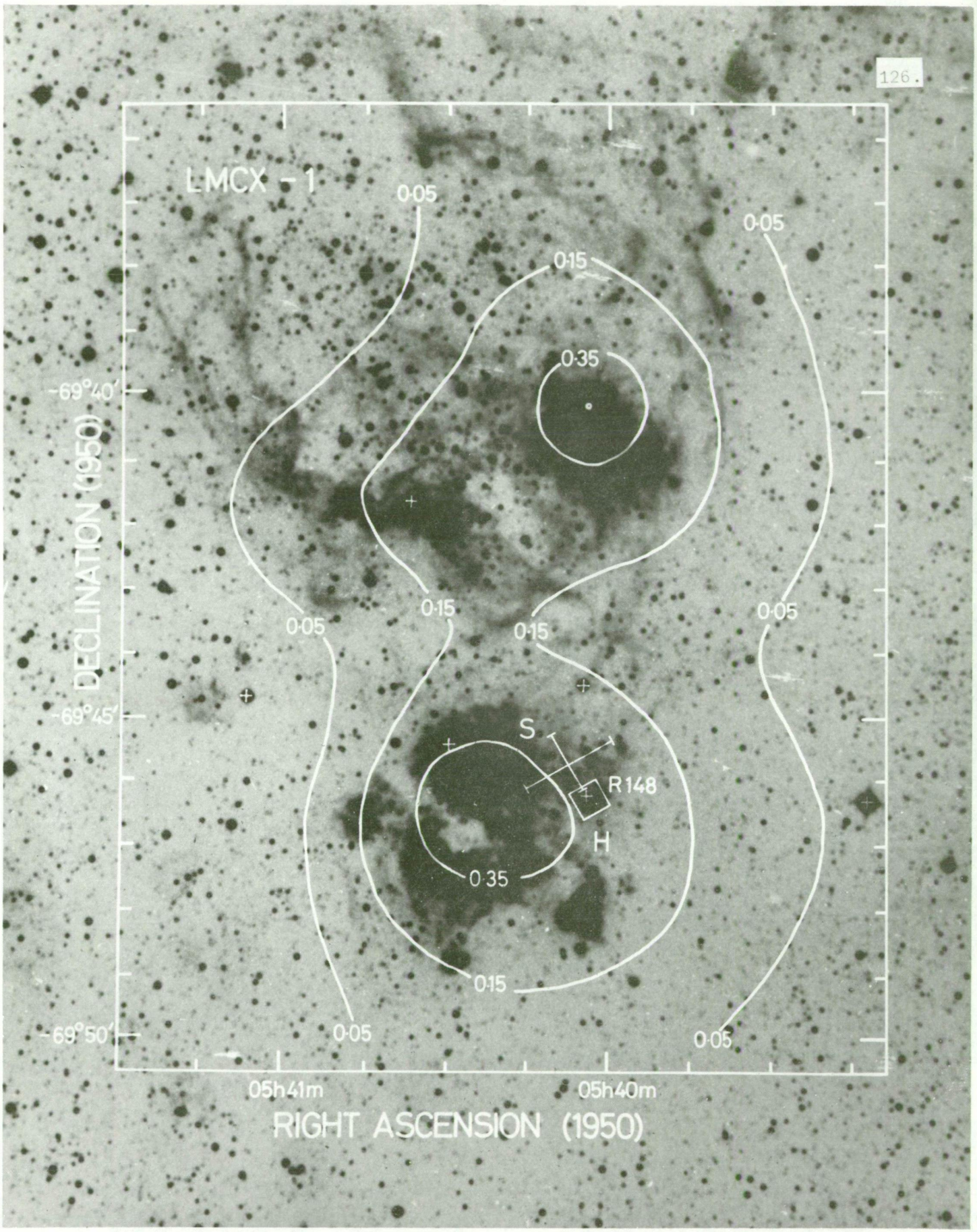

Figure 7-6. Simplified radio contours of the LMC X-1 region overlayed onto the optical field. The SAS-3 position (cross) and the HEAO position (box) are shown as well as the optical candidate R148.

spurious chance coincidences. The remaining twelve search positions were at high galactic latitude and as such were not expected to have confusion problems.

7.4 THE BURST WATCH OBSERVATIONS

Observations of the X-ray burst source MXB1636-53 (Hoffman, Lewin and Doty 1977) were carried out as part of a programme of world-wide coordinated observations of several X-ray burst sources organized by the SAS-3 satellite team (IAU Circular No. 3078). This burst source is identified with the steady X-ray source 2S1636-536 (4U1636-53) whose position is known to within 20" arc (90% confidence error radius - Jernigan et al. 1977). Radio observations were carried out on the night of 1977 June 17 to search for any radio activity correlated with X-ray bursts. Figure 7-7 shows the SAS-3 satellite and Parkes observing times. In one SAS-3 orbit of $\sim$ 94 minutes duration, approximately one hour of data was usually obtained on any given source, the remaining time being lost as a result of Earth occultation. Technical difficulties with the 2 cm receiver stability at Parkes were not overcome until $12^h\ 30^m$ UT prior to which time no useful data were obtained. A single burst was observed by SAS-3 commencing at $14^h\ 33^m\ 50^s$ UT. The burst lasted 6s at energies between 6 and 12 keV and slightly longer at lower energies.

In figure 7-8 the Parkes and SAS-3 results are summarized. The Parkes data comprise eleven point running means of the original 0.25s data, giving an effective integration time of 2.75s. The plotted sample interval is 0.5s and the quasi-periodic ($\sim$ 8s) modulation of the radio data is instrumental in origin. No significant radio enhancement above the rms noise level of $\sim$ 100mJy is apparent during the X-ray burst. In fact no radio event was observed during the complete Burst Watch. An upper limit (1σ) of 100mJy is found for any radio burst, either coincident with the X-ray burst or at any time during the radio observations.

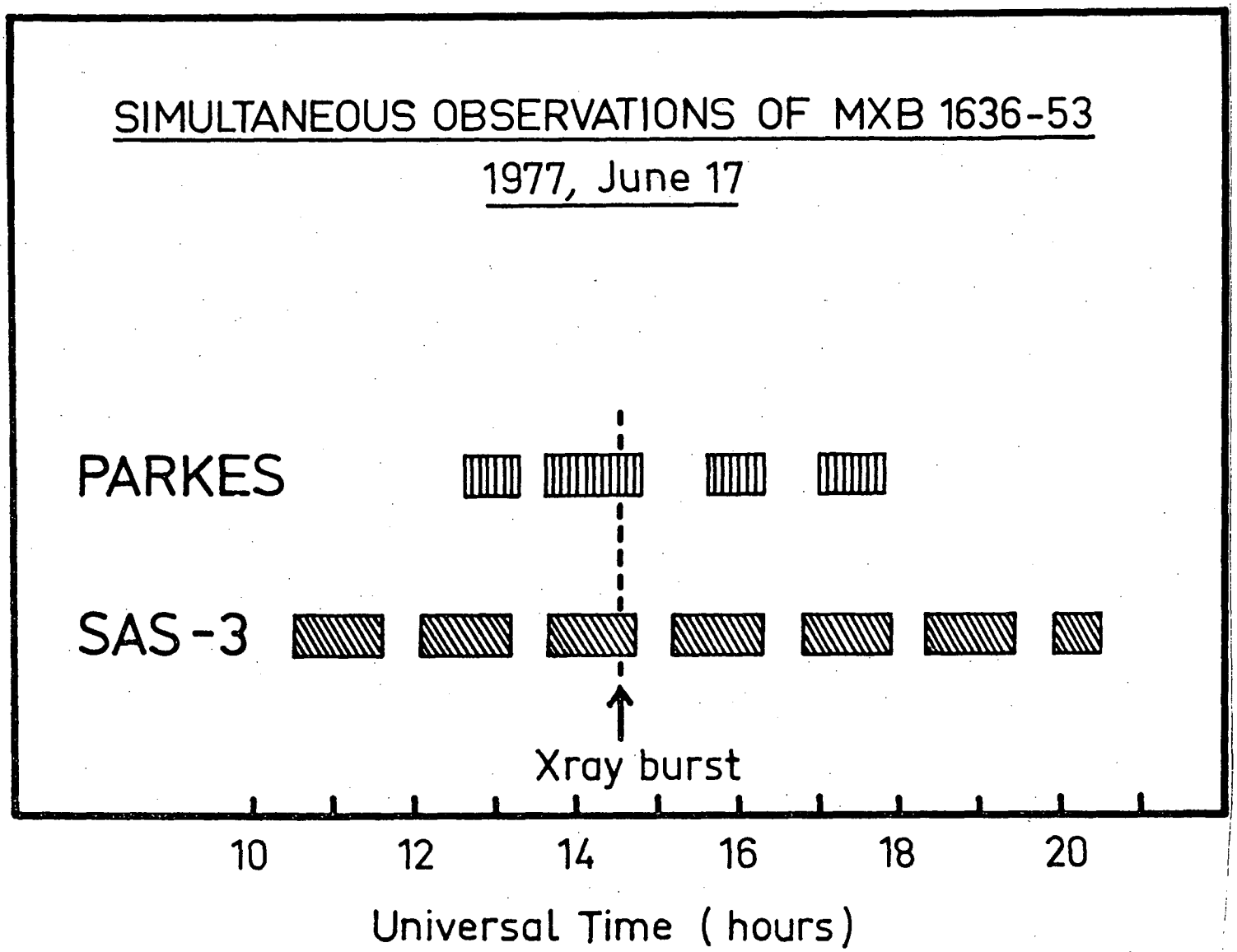

Figure 7-7. Summary of the Parkes 2cm and SAS-3 observing times. The single X-ray burst is shown.

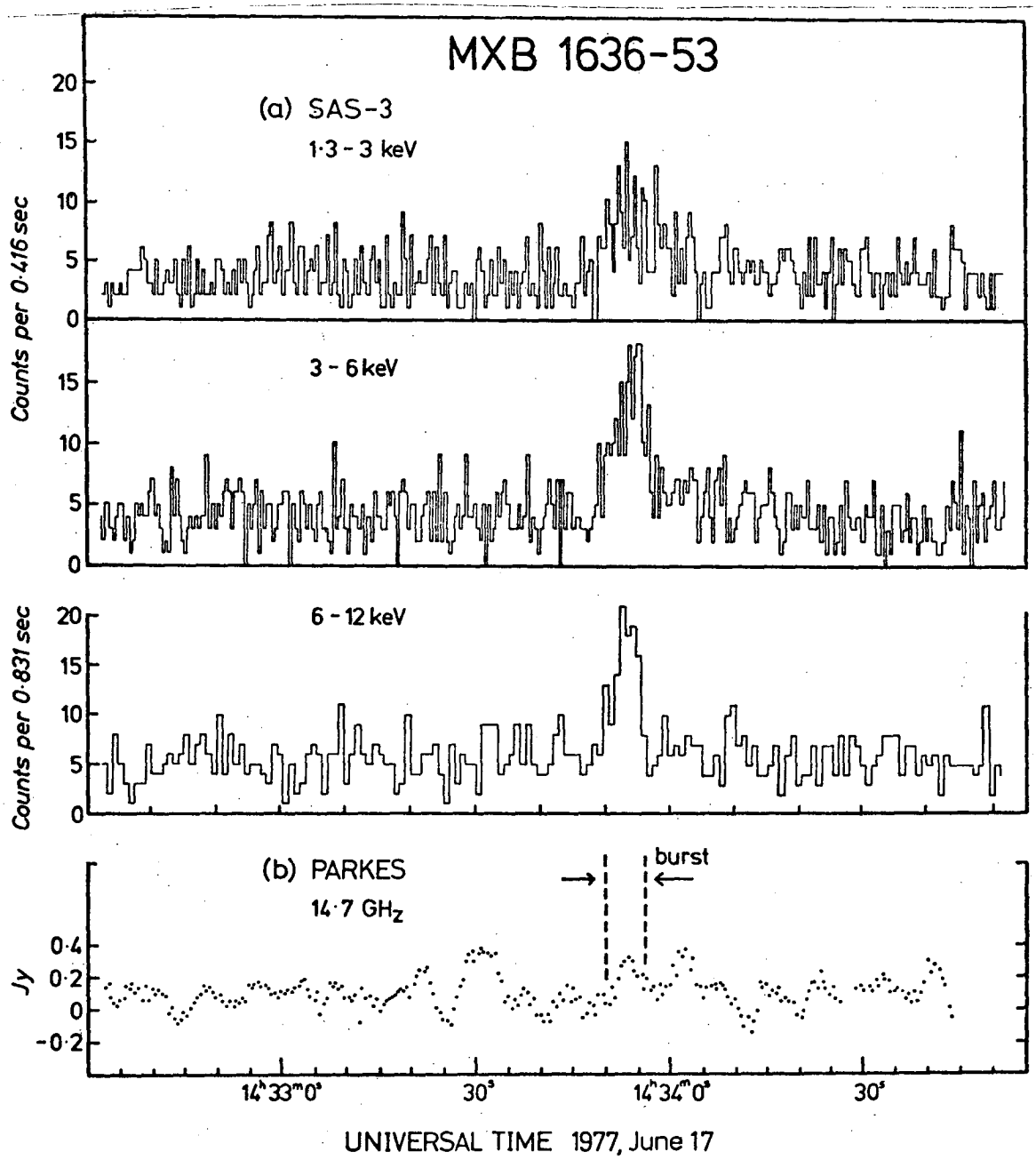

Figure 7-8. The X-ray burst event as recorded by the SAS-3 satellite and the simultaneous Parkes 2cm observations.

The burst source MXB1730-335 was monitored at λ = 6 cm during the 1980 July - August observing session. The source was monitored continuously during the period shown in Table 7-3 with a sample time of 0.02s.

Table 7-3

MXB1730-335 Observing Times in 1980 (UT)

July	31	$07^h\ 00^m$	- $10^h\ 55^m$
July	31	$11^h\ 14^m$	- $16^h\ 00^m$
August	1	$06^h\ 26^m$	- $10^h\ 48^m$
August	1	$11^h\ 47^m$	- $15^h\ 52^m$
August	2	$06^h\ 37^m$	- $10^h\ 41^m$
August	2	$11^h\ 27^m$	- $15^h\ 51^m$
August	3	$06^h\ 53^m$	- $07^h\ 46^m$
August	3	$08^h\ 30^m$	- $10^h\ 38^m$
August	3	$11^h\ 58^m$	- $15^h\ 00^m$
August	4	$08^h\ 33^m$	- $10^h\ 27^m$
August	4	$11^h\ 01^m$	- $15^h\ 40^m$

No observations were carried out between $\sim 10^h\ 50^m$ and $\sim 11^h\ 30^m$ as the telescope was inside the nominal operating zenith limits.

No radio bursts were observed to an upper limit (1σ) of 100mJy. At the time of writing, the X-ray behaviour of the rapid burster MXB1730-335 during these observations had not been forwarded to the author. Figure 7-9 shows the results of the first 60s of observations on 1980 July 31 at $07^h\ 00^m$ UT.

7.5 A0538-66

Recently (Johnson et al. 1979, Skinner et al. 1980) it has been shown that A0538-66 is a periodic flaring X-ray source with a

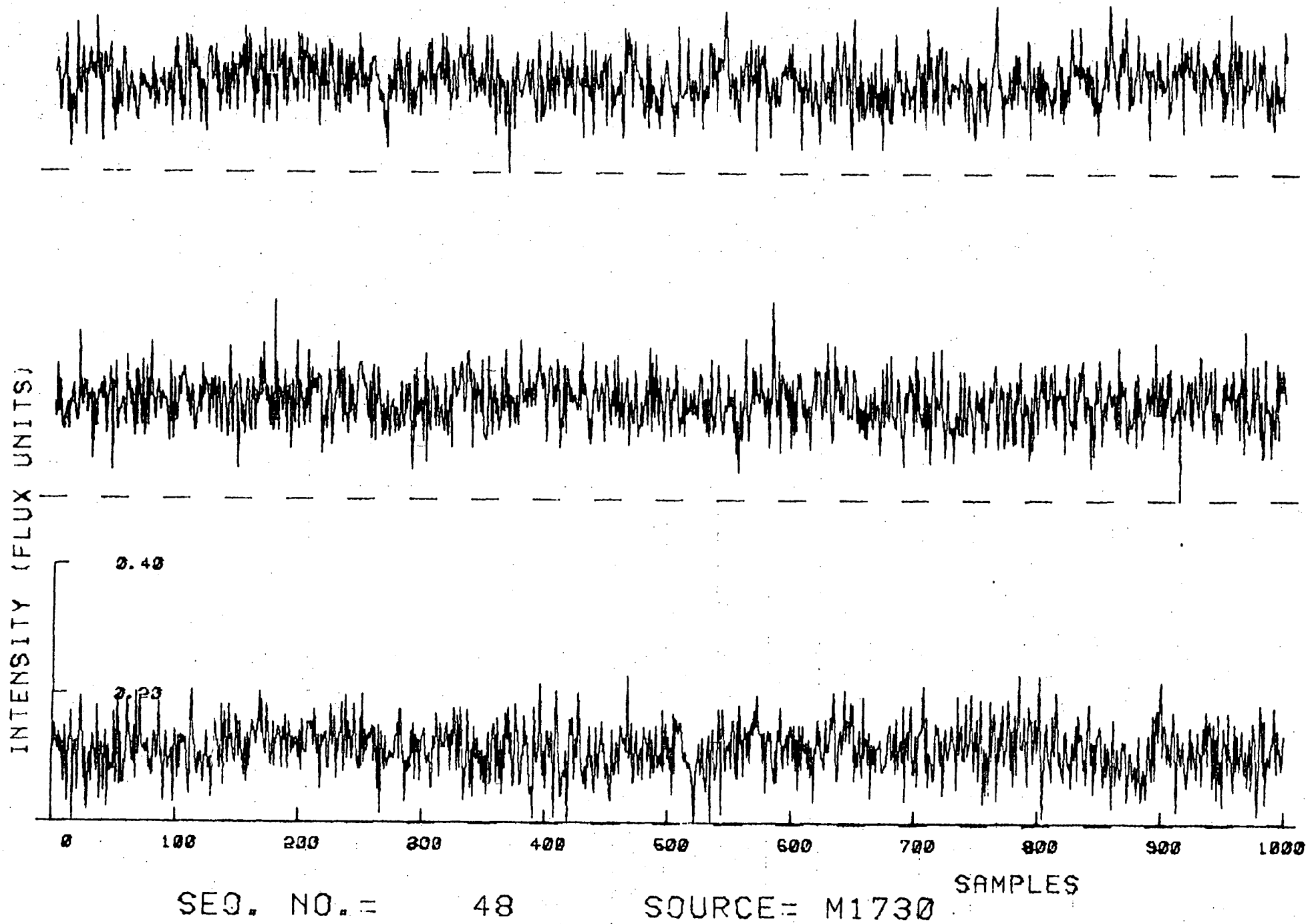

Fig. 7-9 Plots of the first 60s of data during the Burst Watch observations of MXB1730-335.

period of 16.65 day, very similar to CIR X-1 (Duldig et al. 1980b). Radio observations of this source were undertaken each day prior to the expected X-ray flare of 1980 August 4, $18^h\ 12^m$ UT. Table 7-4 shows the time of observations prior to and during the predicted flare. The times are in 1980 August UT.

Table 7-4

A0538-66 Observing Times in August 1980

Date (August)	Observing Period (UT)
2	$17^h\ 00^m - 17^h\ 40^m$
3	$17^h\ 00^m - 17^h\ 20^m$
4	$17^h\ 00^m - 22^h\ 00^m$

No flaring radio activity or point radio source were found to an upper limit (1σ) of 20mJy.

7.6 POSITIVE DETECTIONS

7.6.1 GENERAL

The detections are divided into three classes on the basis of the confusion tests previously described (6.4, 7.3). Radio sources associated with X-ray objects are often variable (see e.g. Haynes et al. 1978b, Matsuoka and Miyamota 1977, Hjellming 1974) and it is therefore not surprising that some of the following radio sources were not always detectable.

The three classes comprise: 1) Detections - the observed flux density exceeded the 3σ significance criterion during each of the five observing sessions and background confusion was negligible;
2) Probable Detections - A significant (3σ) flux density was observed on at least one occasion and observations around the X-ray source position

indicated that confusion effects were small compared with the observed flux density; 3) Detections — but Possibly Confused - A significant (3σ) flux density was observed at least once during the five observing sessions but the background confusion effects may have been present.

The most significant positive λ = 2 cm observations for each source are tabulated in Table 7-5 and observations for most of the detected sources at λ = 2 cm are shown in Figs. 7-13 and 7-14.

Table 7-5

λ = 2 cm Sources at X-ray Source Positions

X-ray Source	Position (1950.0) R.A. h m s	Dec. ° ' "	Posn. error of X-ray posn. (90% conf. radius)	Posn. ref.*	2 cm flux density $\pm\sigma$
2S 0614+091	06 14 22.7	+09 09 08	†	(1)	36±12
A 0620-00	06 20 11.2	-00 19 10	†	(2)	44±14
A 1118-61	11 18 52	-61 34 42	3'.6 arc		14±4
2S 1258-613	12 58 10.7	-61 19 53	†	(3)	see 7.5.4
Cir X-1	15 16 48.3	-56 59 11	†	(4)	1400±50
A 1701-39	17 01 28.8	-39 57 36	3'.6 arc	(5)	19±5
2S 1705-440	15 05 18.2	-44 02 10	20" arc	(6)	24±5
A 1710-34	17 10 52	-34 00 36	2'.8 arc	(5)	23±5
2S 1728-169	17 28 50.4	-16 55 30	20" arc	(6)	14±3
2S 1735-444	17 35 19.5	-44 25 22	20" arc	(6)	15±4

*(1) Murdin et al. (1974); (2) Ward et al. (1975); (3) Mason et al. (1977); (4) Whelan et al. (1977); (5) Carpenter (1977, priv. comm.); (6) Bradt (1978).

†Position is that of the well established optical counterpart.

7.6.2 DETECTIONS

CIR X-1 was clearly observed at both λ = 2 and 6 cm on all occasions. Each observing session coincided with a predicted X-ray transition and subsequent radio flare and on all occasions radio flares of varying sizes were observed. Table 7-6 contains the observed flux densities for the 1977 July and August observations.

Figure 7-10 shows the results from observations of CIR X-1 at λ = 2 cm (Thomas et al. 1978a) throughout the flare of 1978 April 24-26. As can be seen from the diagram the onset of the first peak occurs a few minutes after the predicted X-ray transition as phase zero. The peak fluxes of $\sim$ 300mJy are lower than often reported at this frequency. At least three peaks are present and are separated by $\sim$ 23 hours.

Table 7-6

Circinus X-1, λ = 2 cm Observations in 1977

Date (1977)	Time (UT)	Flux (Jy)	Error(1σ) (Jy)
June 15	$13^h\ 30^m$	1.211	0.035
June 15	$13^h\ 50^m$	1.372	0.047
August 20	$07^h\ 03^m$	1.332	0.041

Figures 7-11 and 7-12 show plots of the flare observations of CIR X-1 at λ = 6 cm from 1980 May and August. Gaps in the data are due to the source being below the 60° zenith angle limit of the Parkes radio-telescope.

Fast time resolution observations of CIR X-1 carried out in 1980 August showed no short timescale variability on timescales ranging from 0.1 to 20 seconds.

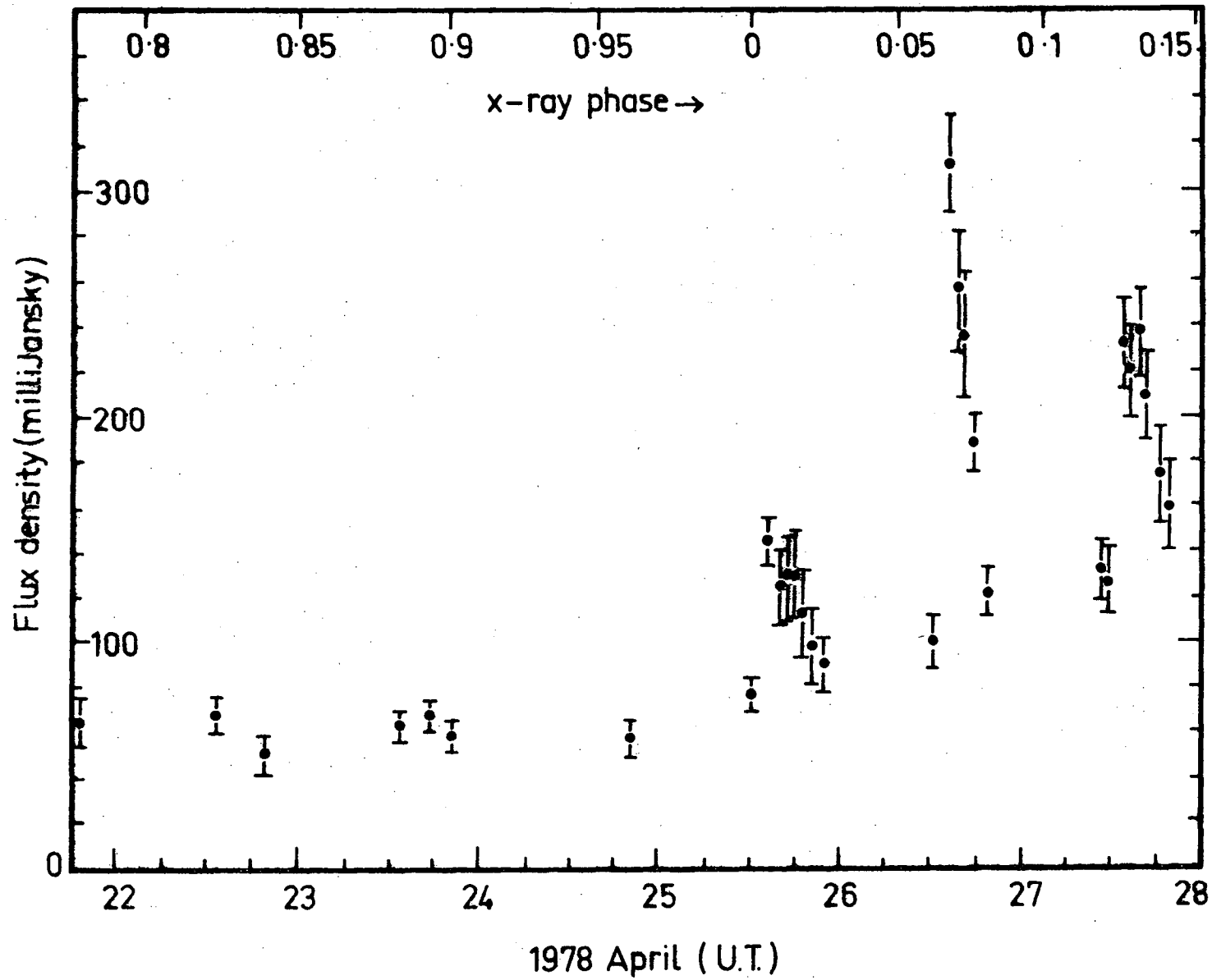

Figure 7-10. 2cm observations of the Circinus X-1 flare of 25 - 28 April. The X-ray phase is shown along the top axis. Error bars are ±1σ.

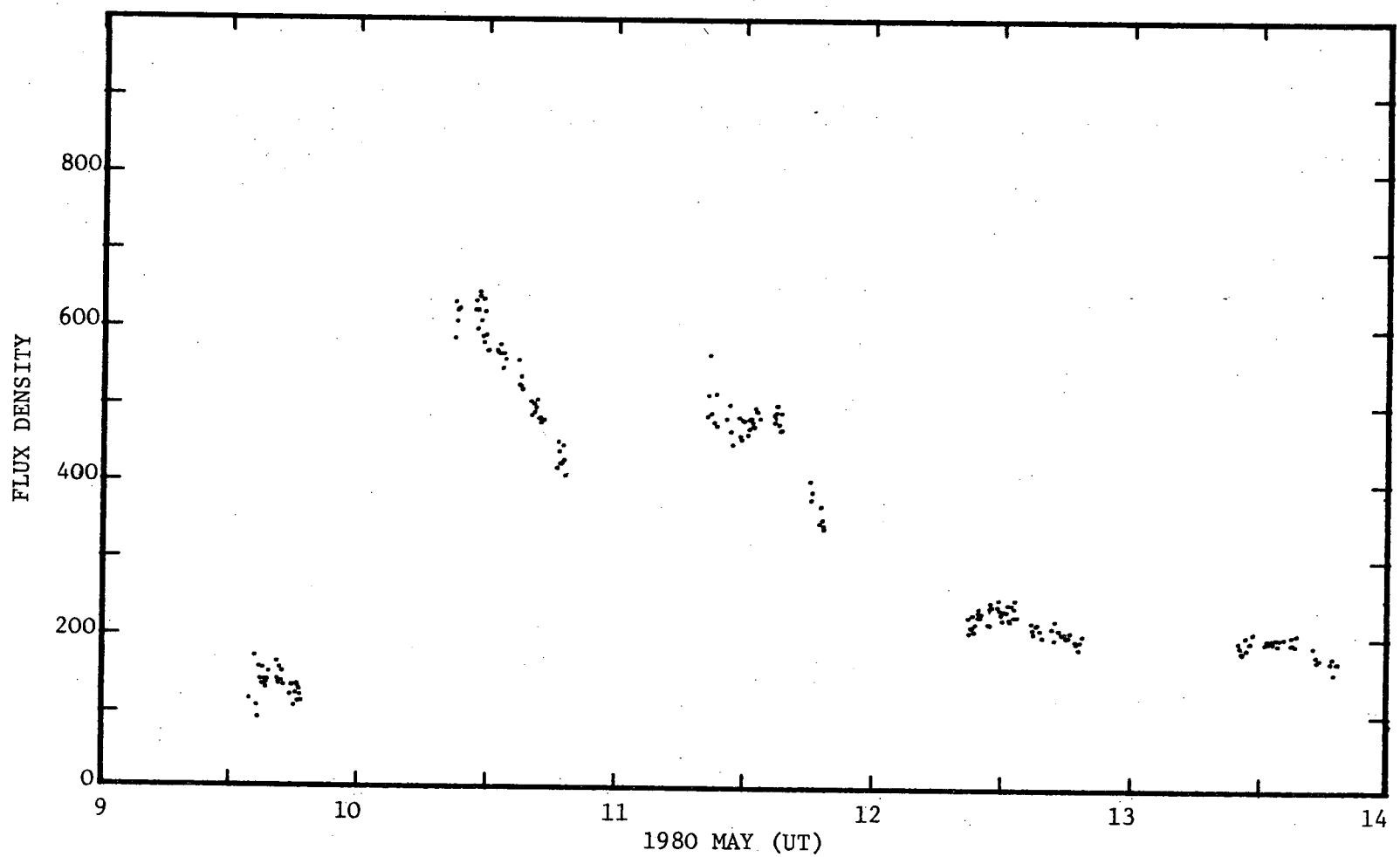

Fig. 7-11 λ = 6 cm Observations of the Circinus Flare of 10 - 13 May. Typical errors for the points are $\pm$20 mJy (1σ).

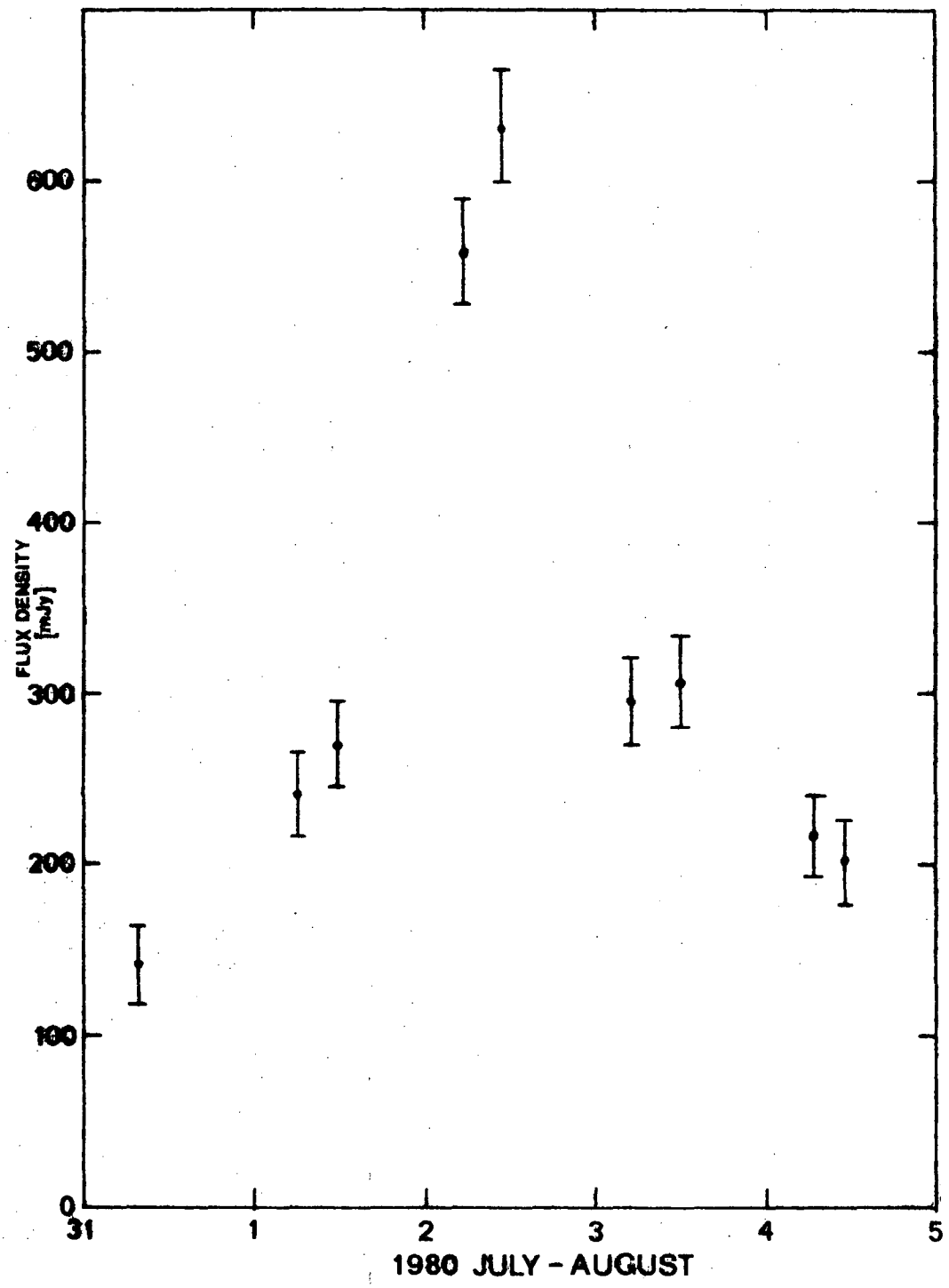

Figure 7-12. 6cm observations of the Circinus X-1 flare of July 31 - August 5. Error bars are ±1σ.

Clearly CIR X-1 is a variable radio source on timescales of hours and days and the significance of these results will be discussed in Chapter 8.

7.6.3 PROBABLE DETECTIONS

2S0614+091 (≡4U0614+09)

This source position was searched twice in 1977 July, five times in 1977 August and once more in 1978 April. The source remained below the receiver detection threshold on all occasions except 1977 August 20, $20^h\ 17^m$ UT. No confusion around this position was evident.

A0620-00 (≡Nova Mon 1975)

The transient X-ray source A0620 was observed twice during each of the λ = 2 cm observing sessions. Again the source produced a significant (3σ) result on only one occasion, that being 1977 June 17, $01^h\ 29^m$ UT. No confusion effects were found in the vicinity of this source position.

A1701-39

This Ariel V, X-ray source was detected at a significant level (3σ) on both occasions that it was observed in 1977 August (16±5mJy on 1977 August 20, $12^h\ 18^m$ UT and 19±5 on 1977 August 21, $10^h\ 30^m$ UT). Four further observations in 1978 April failed to detect the source to an upper limit (1σ) of $\sim$ 5mJy. The radio source position error was smaller than the 3'.6 arc error box for the X-ray source and it would appear to define the position of the X-ray source more precisely. No confusion effects around this source position were apparent.

2S1735-444

This X-ray burst source was observed with a λ = 2 cm flux density of 15±4mJy on 1977 August 21, $14^h\ 35^m$ UT. Three further observations in 1978 April failed to detect a significant flux density.

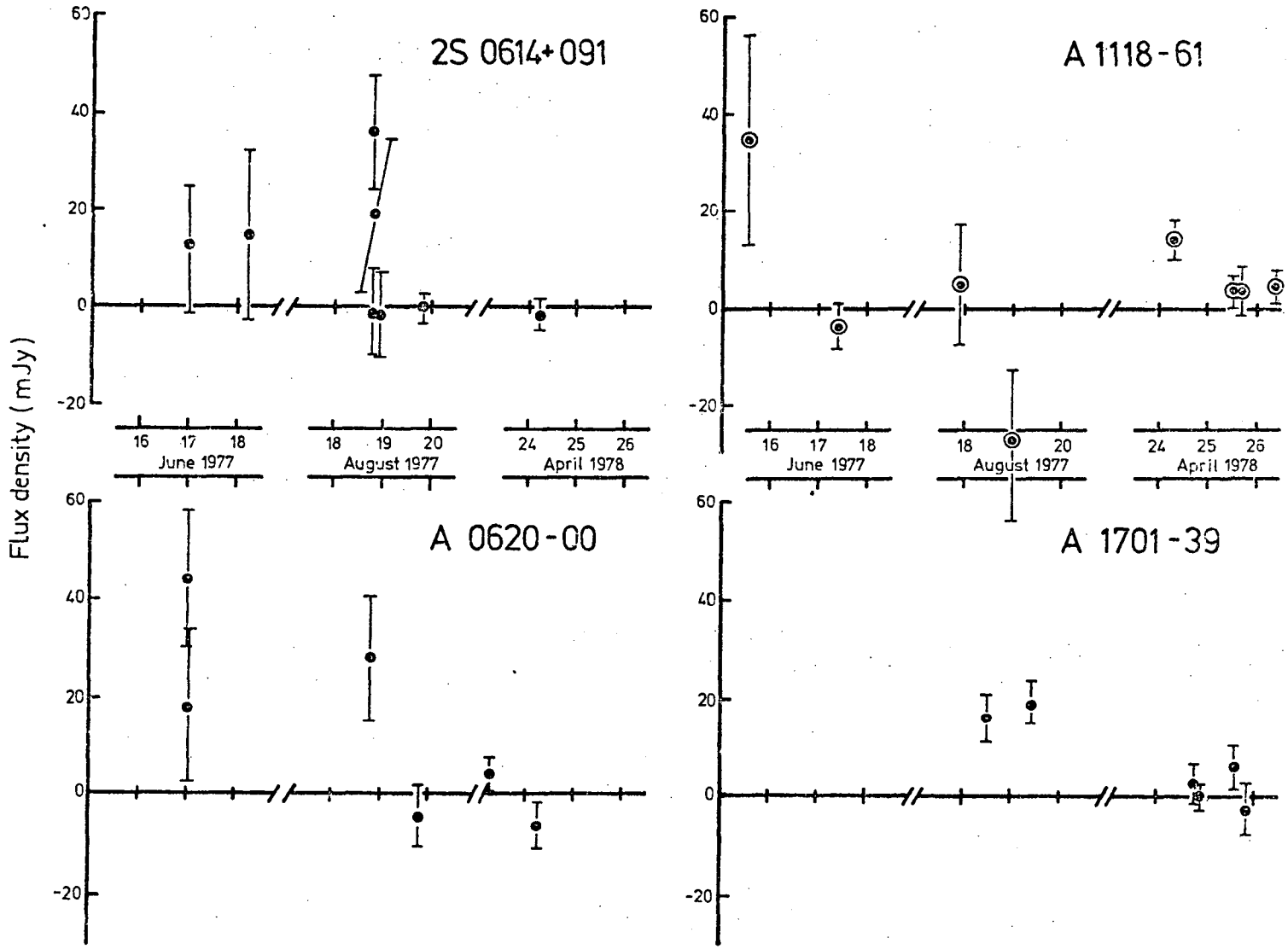

Figure 7-13. Flux density measurements of detected sources at 2cm. Error bars are ±1σ.

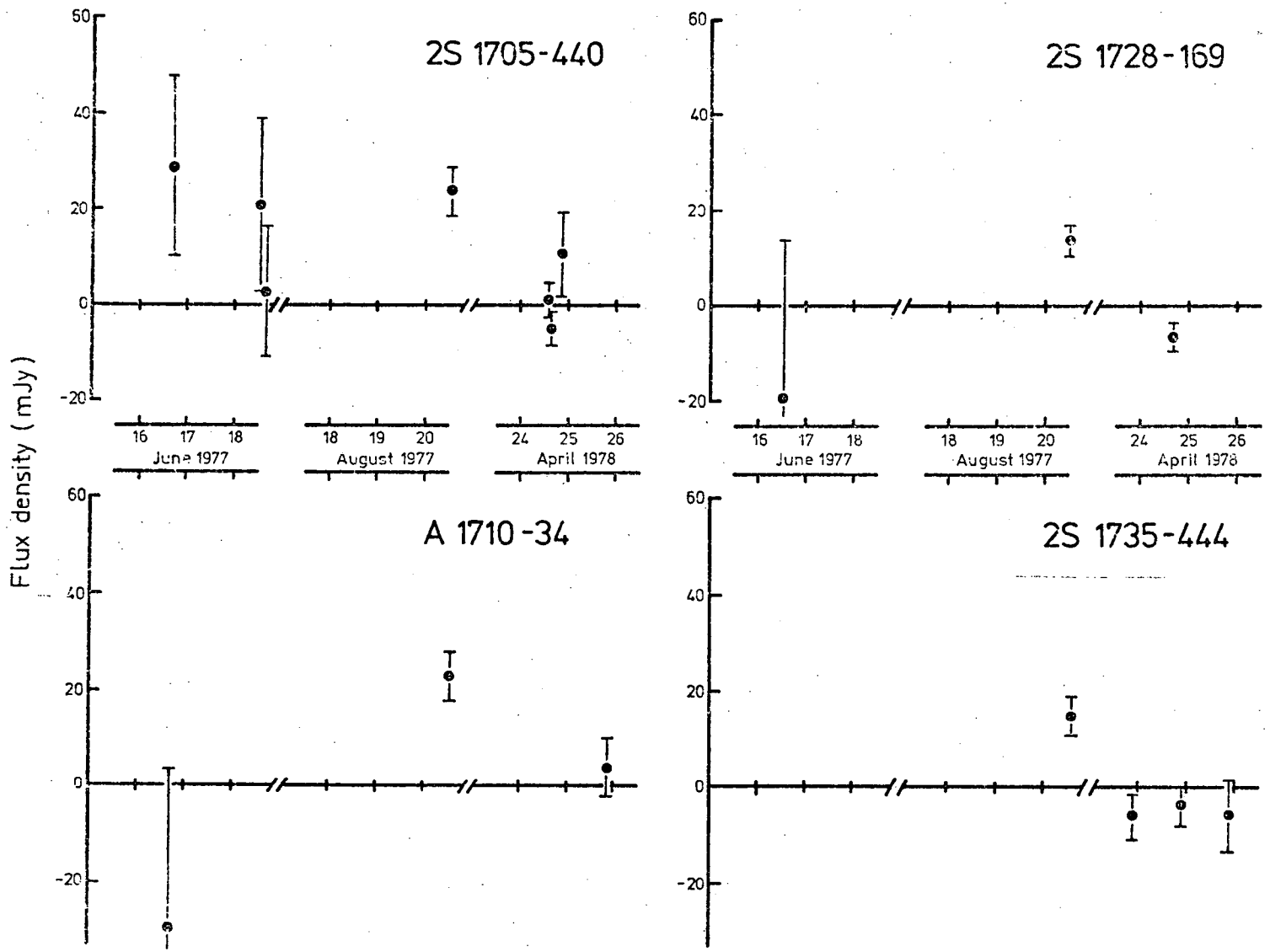

Figure 7-14. Flux density measurements of detected sources at 2cm. Error bars are ±1σ.

Confusion checks about the X-ray source position showed no confusing sources.

SCO X-1

Although SCO X-1 remained undetected at λ = 2 cm during all three observing sessions (7.2.6) a significant (3σ) flux density was recorded on two occasions at λ = 6 cm. The source appeared to weaken over a few days from its highest recorded level as can be seen from table 7-7.

Table 7-7

Sco X-1, = 6 cm Observations, August 1980

Date (August)	Time (UT)	Flux (mJy)	Error(±1σ) (mJy)
2	$06^h\ 15^m$	49	10
3	$05^h\ 40^m$	36	10
3	$11^h\ 45^m$	27	14
4	$07^h\ 20^m$	19	14

7.6.4 DETECTIONS - BUT POSSIBLY CONFUSED

A1118-61

Three attempts to observe this source in 1977 June and August realized upper limits as did three further attempts in 1978 April. On 1978 April 24, $07^h\ 30^m$ UT, however, a flux density of 14±4mJy was observed. Observations around the source at an offset of 1' arc showed a confused background. No search for radio emission during the X-ray nova like acitivity in 1974 December has been published, to the author's knowledge.

2S1258-613 (≡GX304-1, ≡MMV Star)

Nodding measurements around the MMV star, the optical counterpart to 2S1258-613 (Mason, Murdin and Visvanathan 1977), in 1978

April indicated that the coincident radio source is extended in declination by about 3' arc. A peak flux density of 20mJy was observed about 1' arc north of the star. Moreover, scans in declination showed an excess toward the X-ray position. Seaquist (1977) first reported this as a counterpart with a flux density of 33±7mJy at 6 cm.

2S1705-440

Three attempts to find a radio counterpart in 1977 June and again in 1977 August failed to yield any significant results. One observation on 1977 August 21, $13^h\ 32^m$ UT produced a flux density of 24±5mJy. No confusion tests were carried out around this source due to lack of time and therefore the source must be classified as possibly confused even though the significance of the observation was almost 5σ.

A1710-34

Only one observation of this X-ray source position was made during each of the first three observing sessions. A significant signal of 23±5mJy was observed on 1977 August 21, $13^h\ 03^m$ UT. The X-ray error box for this source was improved in follow up observations which were made by Dr. John Greenhill using the SAS-3 satellite as guest investigator (Greenhill et al. 1978). The improved SAS-3 position designated 2S1711-339 was just within the beam response of the λ = 2 cm system we employed but implied that the response to a point source would have been reduced to $\sim$ 13%. No confusion study of the region surrounding this X-ray source position has been made.

2S1728-169 (≡GX9+9)

Four observations of this X-ray source position were made. No significant flux density was recorded in 1977 July and 1978 April. A flux density of 14±3mJy was observed on 1977 August 21, $22^h\ 32^m$ UT.

The final observation of this source position in 1978 April was carried out with a slightly different position angle for the offset

beam and a significant negative flux of -61±8mJy was recorded implying a possible confusion source 6'.2 arc away.

2A0255-132

The position of this high galactic latitude X-ray source was known to 0.041 deg^2. Scans through this source position revealed a radio source of $\sim$ 100mJy located 2' arc south of the centre of the large X-ray error box. This source is distinct from the nearby object PKS0255+13 located just outside the X-ray position error box, but it may be related to the low-frequency source referred to in Table 1 of Cooke et al. (1978).

7.7 REFERENCES

Bradt H. (1978) "Celestial positions of galactic X-ray sources from SAS-3", prepared for the Austin A.A.S. Meeting, paper 12.05.09

Bradt H.V., Apparao K.M.V., Clark G.W., Dower R., Doxsey R., Hearn D.R., Jernigan J.G., Joss P.C., Mayer W., McClintock J. and Walter F. (1977) Nature 269, 21

Braes L.L.E. and Miley G.K. (1973) IAU Symp. No. 55 "X- and Gamma-Ray Astronomy", pp. 86-97, eds Bradt H. and Giaconni R., D. Reidel Dordrecht, Holland.

Braes L.L.E., Miley G.K. and Schoenmaker A.A. (1972) Nature 236, 392

Clark G. and Chartres M. (1978) IAU Circ. 3208

Cooke B.A., Ricketts M.J., Maccacaro T., Pye J.P., Elvis M., Watson M.G., Griffiths R.E., Pounds K.A., McHardy I., Maccagni D., Seward F.D., Page C.G. and Turner M.J.L. (1978) Mon. Not. R. astr. Soc. 182, 489

Davies R.D., Walsh D., Browne I.W.A., Edwards M.R. and Noble R.G. (1976) Nature 261, 476

Davis M., Huchra J., Tonry J. and Latham D. (1978) IAU Circ. 3202

Doxsey R., Bradt H., Gursky H., Johnston M., Schwartz D.A., Schwarz J. (1977) M.I.T. Preprint CSR-77-29

Duldig M.L., Greenhill J.G., Thomas R.M., Haynes R.F., Simons L.W. and Murdin P.G. (1977) IAU Circ. 3108

Duldig M.L., Greenhill J.G., Thomas R.M., Haynes R.F., Simons L.W. and Murdin P.G. (1979a) Mon. Not. R. astr. Soc. 187, 567

Duldig M.L., Thomas R.M., Greenhill J.G., Haynes R.F., Simons L.W. and Murdin P.G. (1979b) Proceedings of the Inaugural Asian/South Pacific Regional Meeting of the IAU, New Zealand Journal of Science, 22, 563

Duldig M.L., Thomas R.M., Haynes R.F. and Murdin P.G. (1980a) Mon. Not. R. astr. Soc. 190, 861

Duldig M.L., Thomas R.M., Haynes R.F. (1980b) Proc. A.S.A. 4, 108.

Epstein H. (1977) Astrophys. J. (Lett) 218, L49

Glass I.S. and Feast M.W. (1978) IAU Circ. 3226

Greenhill J.G., Jernigan J.G., Thomas R.M., Duldig M.L. and Haynes R.F., (1978) Nature 279, 620

Greenhill J.G., Coe M.J., Bell Burnell S.J. Strong K.T. and Carpenter G.F. (1979) Mon. Not. R. astr. Soc. 189, 563

Griffiths R.E., Bradt H., Doxsey D.A., Friedman H., Gursky H., Johnston M., Longmore A., Malin D.F., Murdin P., Schwartz D. and Schwarz J. (1978) Astrophys. J. (Lett) 221, L63

Gursky H., Bradt H., Doxsey R., Schwartz D.A., Schwarz J., Dower R., Fabbiano G., Griffiths R.E., Johnston M., Leach R., Ramsey A. and Spada G. (1977) MIT Preprint CSR-77-30

Haynes R.F., Caswell J.L. and Simons L.W.J. (1978a) Aust. J. Phys. Astrophys. Suppl. No. 45

Haynes R.F., Jauncey D.L., Murdin P.G., Goss W.M., Longmore A.J., Simons L.W., Milne D.K. and Skellern D.J. (1978b) Mon. Not. R. astr. Soc. 185, 629

Hjellming R.M. (1974) "International Conference on X-rays in Space" p.211, ed. Venkatesan D., University of Calgary

Hjellming R.M. (1978) Astrophys. J. 221, 225

Hoffman J.A., Lewin W.H.G. and Doty J. (1977) Astrophys. J. (Lett) 217, L23

Janes A.F., Pounds K.A., Ricketts M.J., Willmore A.P. and Morrison L.V. (1973) Nature 244, 349

Jernigan J.G., Apparao K.M.V., Bradt M.V., Doxsey R.E. and McClintock J.E. (1977) Nature 270, 321

Johnston M.D., Bradt M.V., Doxsey R.E., Gurskey H., Schwartz D.A., Schwarz J. and van Paradijs J. (1978) Astrophys. J. (Lett) 225, L59

Johnston M.D., Bradt M.V., Doxsey R.E., Griffiths R.E., Schwartz D.A. and Schwarz J. (1979) Astrophys. J. (Lett) 230, L11

Mason K.O., Murdin P.G. and Visvanathan N. (1977) IAU Circ. 3054

McGee R.X., Newton Lynette M. and Brooks J.W. (1974) Aust. J. Phys. 27, 729

Miyamoto S. and Matsuoaka M. (1977) Space Sci. Rev. 20, 687

Murdin P., Penston M.J., Penston M.V., Glass I.S., Sanford P.W., Hawkings F.J., Mason K.O. and Willmore A.P. (1974) Mon. Not. R. astr. Soc. 169, 25

Pineda F. and Schnopper H.W. (1978) IAU Circ. 3190

Raply C.G. and Tuohy I.R. (1974) Astrophys. J. (Lett) 191, L113

Sanduleak N. and Dolan J.F. (1974) Astrophys. J. (Lett) 187, L73

Seaquist E.R. (1977) Astrophys. J. 211, 547

Skinner G.K., Shulman S., Share G., Evans W.D., McNutt D., Meeking J., Smathers H., Wood K., Yentis D., Byram E.T., Chubb T.A. and Friedman H. (1980) Astrophys. J. 240, 619

Thomas B. MacA. and Day G.A. (1969) Aust. J. Phys. Astrophys. Suppl. No. 11

Thomas R.M., Duldig M.L., Haynes R.F. and Murdin P.G. (1978a) Mon. Not. R. astr. Soc. 185, 29p.

Thomas R.M., Duldig M.L., Haynes R.F. and Murdin P.G. (1978b) IAU Circ. 3219

Thomas R.M., Duldig M.L., Haynes R.F., Simons L.W., Murdin P., Hoffman J.A., Lewin W.H.G., Wheaton W.A. and Doty J. (1979) Mon. Not. R. astr. Soc. 187, 299

Thorstenson J.R., Charles P.A. and Bowyer S. (1977) IAU Circ. 3088

Ward M.J., Penston M.V., Murray C.A. and Clements E.D. (1975) Nature 257, 659

Whelan J.A.J., Mayo S.K. Wickramasinghe D.T., Murdin P.G., Peterson B.A., Hawarden T.G., Longmore A.J., Haynes R.F., Goss W.M., Simons L.W., Caswell J.L., Little A.G. and McAdam W.B. (1977) Mon. Not. R. astr. Soc. 181, 259

Zuiderwijk E.J. (1978) IAU Circ. 3221

CHAPTER 8

DISCUSSION OF RADIO RESULTS

8.1 GENERAL

The λ = 2 cm radio survey results clearly indicate that very few X-ray sources are strong radio emitters. It will be necessary to resort to synthesis telescopes with their greater sensitivity and improved angular resolution to increase significantly the number of known radio counterparts to X-ray sources.

Although the survey resulted in a low yield of significant observations (<10%), several important contributions to our knowledge of the radio counterparts of X-ray sources were made, not the least of which was the nearly twofold increase in the number now known to exist.

8.2 DETECTED SOURCES

8.2.1 CIRCINUS X-1

Referring back to figure 7-10 we can see that the flare activity of Cir X-1 near 1978 April 26 was complex. At least three flares were observed, separated by $\sim$ 23hr, in agreement with the typical separation of 18 - 22hr observed by Haynes et al. (1978). The HLM model, summarized in Chapter 1 (Haynes et al. 1980a), proposes that $\sim 2 \times 10^4$s after formation the shock front will have dissipated. Mass accretion will subsequently recommence and after a delay corresponding to the free fall time of the accreting matter, a further shock may be generated. The free-fall time for the initial infall approaching periastron passage is estimated to be $\sim 10^4$s.

The van der Laan expansion of the shock will proceed but radio emission at a frequency ν will not escape until $\nu > \nu_p$ the plasma frequency ($\sim 10^4$sec). Thus we would expect a delay of $\sim 4 \times 10^4$sec

(∿10hr) between flares.However,subsequent blast fronts are formed in the debris remaining from previous shocks and so this estimate of the delay between flares should be considered as purely indicative of the time scales involved and as such is consistent with the results presented in 7.5.2 and Figure 7-10.

The sharp rise of these flares may also be used to determine an upper limit of 10 A.U. for the λ = 2 cm emission region size. The HLM model proposes an emission region size of a few A.U. well within this upper limit.

Figures 7-11 and 7-12 showed the λ = 6 cm observations of 1980 May and July-August. The 'front porch' effect discussed by Murdin et al. (1980a) and Haynes et al. (1980a) is not observed in the May results. During the July-August observations there is a suggestion of an enhancement prior to the flare but in the absence of further observational data around the expected 'front porch' effect time no conclusions may be drawn. Clearly no 'front porch' was observed at λ = 2 cm, although this may be related to the weakness of the flaring activity during those particular observations.

Haynes et al. (1980b) predict that the orbit of Cir X-1 will circularize within $\sim$ 500 yr and that the period should decrease by about 5×10^{-2} day per year. Figure 8-1 shows the period determinations for Cir X-1 at various wavelengths. The points are plotted with error bars showing the accuracy of the period determination and the period over which this determination was made. The points labelled 1 are from Kaluzienski et al. (1976) at X-ray energies. No error was quoted for the earlier Uhuru data. Point 2 is from Kaluzienski and Holt (1977) also at X-ray energies. Point 3 is from λ = 6 cm radio observations of Haynes et al. (1978) whilst point 4 has been calculated by the author using

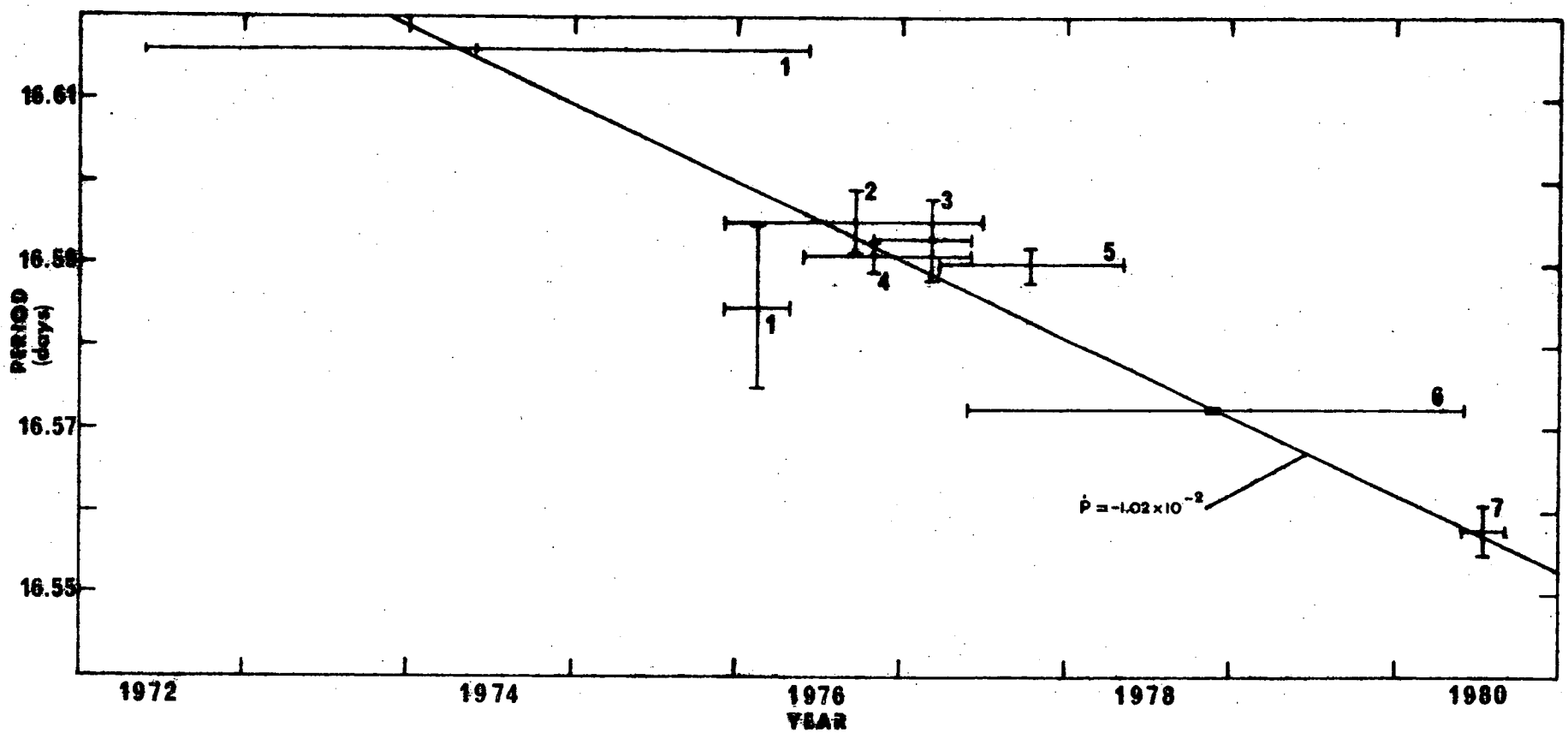

Figure 8-1. Period determinations of Circinus X-1. For the meaning of the numbers associated with each point refer to the text. Horizontal error bars represent the epoch over which the period determinations were made. Vertical error bars are the error (±1σ) in the period determinations. No error was quoted for the earliest Uhuru X-ray determination.

data from Whelan et al. (1977) combined with observations obtained by Haynes et al. (1978). Point 5 is the λ = 2 cm period determination from this work (Thomas et al. 1978) and point 6 is a combination of the 1980 May observations reported here and the last reported observation of a flare in Haynes et al. (1978). Finally point 7 is from the two λ = 6 cm flares observed by the author.

A weighted least squares linear regression was carried out on these data and a best fit $\dot{P}$ of $-1.02 \pm 0.07 \times 10^{-2}$ day per year was found with a correlation coefficient $r = 0.966$. This rate of decrease in orbital period is in reasonable agreement with the predictions of Haynes et al. (1980b).

Fast time resolution observations showed no significant variability on short timescales. If the radio emission arose within the accretion disc some short time scale structure might be expected. Shock driven radiation would not, however, be expected to show this kind of structure. Therefore this result is compatible with the HLM model for Cir X-1 but would not support an accretion driven mechanism for the radio flare production. The purely accretion mechanism proposed by Murdin et al. (1980a) for the 'front porch' effect would suggest that such short timescale features might be expected at that time. Further observations of this type should be carried out during a 'front porch' observation to test this mechanism.

8.2.2 2S0614+091

As stated in section 7.5.3 this source was only observed on one occasion at a significant level. Murdin et al. (1974) have suggested a faint blue variable star as the optical counterpart. This optical candidate bears a resemblance to Sco X-1 as does the X-ray source itself (White et al. 1978). This similarity to Sco X-1 at X-ray and optical

wavelengths suggests that the radio counterpart may also be Sco X-1 like and therefore highly variable.

8.2.3 A0620-00

This source first observed as an X-ray nova event in August 1975 showed a radio flux density which decayed below the detection threshold within a few weeks of the nova (Ward et al. 1975, Davis et al. 1975, Bieging and Downes 1975, Little et al. 1976). No recent X-ray observations have been published, however, the optical spectrum contained emission lines and a blue continuum early in 1978 (Murdin et al. 1980b) indicating that mass loss from the primary was still occurring and that an accretion disc was still present around the secondary. This single, significant observation may be associated with such a mass transfer process and the radio source may be intermittently active at a low level.

8.2.4 A1118-61

There is very little that we can conclude from the radio observations of this X-ray transient source. The results suggest that the source may still be active, again at a low level.

8.2.5 2S1258-613

This X-ray object position is contained within an extended radio source. Scans through the radio source in declination show the radio object to be asymmetrical about its peak with an excess toward the X-ray position. A double source interpretation, with an unresolved point radio source of $\lesssim$ 15 mJy at the X-ray source position and a slightly stronger 20 mJy source 1' arc north is possible. Further studies with a synthesis telescope would be of great value.

8.2.6 A1701-39

No additional conclusions other than the improvement in source position already mentioned can be made from the radio observations of this

source. However it is noted that the Parkes 6 cm survey shows no coincident radio source to an upper limit of $\sim$ 260 mJy. The X-ray source is known to be highly variable (Carpenter priv. comm.).

8.2.7 2S1705-440

Very little is known about this X-ray source and no new conclusions may be drawn from the present radio results.

8.2.8 A1710-34

The SAS-3 observations undertaken as guest investigators were carried out to improve the X-ray position determination following the radio source discovery (7.6.4). The resulting improved position was offset from the earlier determination and thus the radio search position. The telescope response to a point radio source at this improved position, during the observations in the direction of the earlier estimate, was 13%. If the single significant observation resulted from a radio flare of the X-ray source this reduced efficiency would imply a peak flux density of $\sim$ 100 mJy. Therefore further radio observations are strongly urged at the improved X-ray source position.

8.2.9 2S1728-169

The X-ray source and its suggested optical counterpart are both similar to Sco X-1 and the single significant radio observation obtained suggests that the radio counterpart may also be highly variable, as in Sco X-1.

8.2.10 2S1735-444

This source is a known X-ray burster with an optical candidate showing a spectrum very similar to Sco X-1. Once again the radio behaviour may be similar to Sco X-1.

8.2.11 SCO X-1

The radio spectrum of Sco X-1 is highly variable (Hjellming and Wade 1971) and non-thermal. The spectral index is, however, usually

near -0.5 in the range 2695 to 8085 MHz. If this spectral shape extends to 14.7 GHz (λ=2cm) then the expected flux density at this frequency would be << 1 mJy. During times of intense flaring the radio counterpart may become visible with a flux density > 10 mJy at λ = 2 cm. Major flaring is present in Sco X-1 only about 15% of the time (Wade and Hjellming 1971) and therefore it is not surprising that no significant flux densities were observed at λ = 2 cm.

On two occasions Sco X-1 was observed at a significant level at λ = 6 cm. This result would imply that Sco X-1 was highly active between 1980 August 2nd and August 3rd and subsequently declined in its activity over the next day or so.

It is clear that more sensitive equipment is required to obtain significant insight into the radio emission mechanism of Sco X-1 at these frequencies.

8.3 VARIABILITY

Hjellming (1974) points out that the discovery of a variable point radio source coincident with the X-ray source position is strong evidence for the physical association of the two objects. Obviously, correlated behaviour will confirm such an association.

In the case of Cir X-1 there is no doubt that the radio source is closely related to the X-ray and optical objects. Other X-ray sources are also in this category (viz. A0620-00 during its nova activity of 1975, Cyg X-1, Cyg X-3 and Sco X-1).

The present observations have resulted in the detection of twelve coincident radio sources. It is worthwhile to consider what evidence for variability exists for these sources.

Since the flux densities involved are small, statistical techniques have been used to investigate the significance of any variability (Duldig et al. 1979).

Two methods are employed. Firstly, the familiar χ^2 test in which the quantity

$$\chi^2 = \sum_{l=1} \frac{\left(\overline{S}_l - \overline{S}_\omega\right)^2}{\sigma_l^2}$$ was calculated.

$\overline{S}_l \pm \sigma_l$ $(l = 1,n)$ is the mean flux density and error for the lth set of observations and $\overline{S}_\omega$ is the weighted mean of the flux densities $\overline{S}_l$. The probability, for n-1 degrees of freedom, that the observed value of χ^2 could have occurred by chance in a source of constant flux density, is then determined. Secondly we use the Behrens-Fisher test (B-F test) for an analysis of the means of two independent samples $\overline{S}_l \pm \sigma_l$ and $\overline{S}_j \pm \sigma_j$, where $\sigma_l \neq \sigma_j$ (Snedecor 1962). The statistic

$$t' = \frac{\overline{S}_l - \overline{S}_j}{\frac{\sigma_l^2}{n_l} + \frac{\sigma_j^2}{n_j}}$$ is calculated with n_l and n_j being the number of observations made to determine the flux densities $\overline{S}_l$ and $\overline{S}_j$.

To find the significance of t' we use t tables with (n -1) degrees of freedom. The two values t_l and t_j at the desired significance level are then used to determine the significance of the t' statistic. If the calculated t' is larger than

$$\left(\frac{\sigma_l^2 t_l}{n_l} + \frac{\sigma_j^2 t_j}{n_j}\right) \Big/ \left(\frac{\sigma_l^2}{n_l} + \frac{\sigma_j^2}{n_j}\right)$$ then the result is significant at the chosen significance level of the t_l and t_j.

It may reasonably be asked why use the somewhat complex B-F test rather than the simpler χ^2 test, especially when the B-F test may only be used to compare two individual observations? The

answer to this question is related to the fact that observations of this type separated by several months with different observing conditions and a slightly different receiver response may well result in observations with a different noise level. This will be reflected in the observed 'estimate' of σ_l. The χ^2 test assumes that the parent population has a well determined value of σ and the observationally determined 'estimates' may not conform well to a χ^2 distribution in this case.

The results of these tests are given in table 8-1. Generally the B-F test is more conservative and as noted above the results of the χ^2 test should be treated with caution. It would appear that the two tests are in general agreement and that the observing conditions were sufficiently similar to allow the χ^2 test to be used. The results for 2S0614+091 however clearly show that the two tests are not totally equivalent.

Table 8-1

Statistical Tests for Constant Source Flux Density

Source	χ^2			B-F	Comments
	Σ	dof	sig%	sig%	
2S0614+091	12.92	7	7	1	Sco X-1 like
A0620-00	18.70	5	0.4	1	Radio var. during Nova, opt. active
A1118-61	16.02	7	3	2	Transient X-ray source
A1701-39	19.11	5	0.3	<1	
2S1705-440	25.83	6	<0.1	1	P.A. not constant, see text
A1710-34	7.71	2	2.0	4	
2S1728-169	27.45	2	$\ll$0.1	<0.1	Sco X-1 like
2S1735-444	17.21	3	<0.1	<1	Sco X-1 like

These results are suggestive of variability for all the sources tabulated with the exception of 2S1705-440 as the position angle of the offset beam was not the same for all observations of this source and therefore no conclusions can be drawn. Interestingly,all of the Sco X-1 like objects show evidence of variability, two of them resulting in strong evidence.

Variability studies have not been made for the X-ray source 2A0255-132. Due to the very large error box for the X-ray position and the offset of 2' arc from the centre of the error box for the radio source it was decided that the observation time would be more usefully spent studying other objects. Thus only the one observation of this position was undertaken. The X-ray source 2S1258-613 was observed to be positionally coincident with an extended radio object (7.6.4, 8.2.5). Due to this extended nature variability studies were not practicable.

It would appear that most of the observed radio sources may be variable,strengthening the identifications as counterparts of their respective X-ray sources.

8.4 UPPER LIMITS

8.4.1 HII REGIONS

In section 7.2.7 the suggestions of Sanduleak and Dolan (1974) and Seaquist (1977) of an association between the radio source G339.6 - 0.1 and the X-ray source 4U1642-45 were mentioned. Figure 8-2 shows the 1415 MHz (λ = 21cm) Fleurs synthesis map (54" arc HPBW) of G339.6 - 0.1 obtained by Dr. Ray Haynes in follow up observations of this region (Haynes et al. 1979). As can be seen from the map, no point radio source is found coincident with the X-ray source position. The optical field is shown in figure 8-3 overlayed with a simplified radio map. The extended radio feature has a flat thermal spectrum and radio

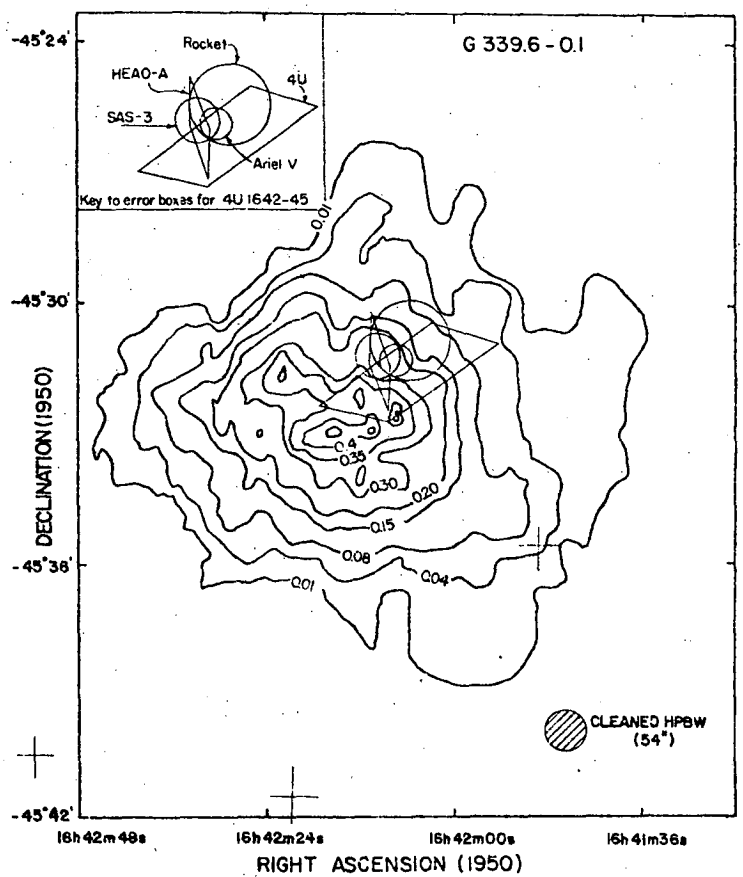

Map of the region near G 339.6 – 0.1 obtained with the Fleurs synthesis telescope at 1415 MHz. The contour interval is specified in terms of janskys per beam. No contours are shown below the 0.01 Jy level. 0.01 Jy per beam is 2.06 K brightness temperature. The map was 'cleaned' using an iterative beam subtraction and restoration process down to a level of 0.02 Jy per beam. Key to error boxes is in upper left corner, and labels are explained in text. Crosses denote SAO positional reference stars

Figure 8-2.

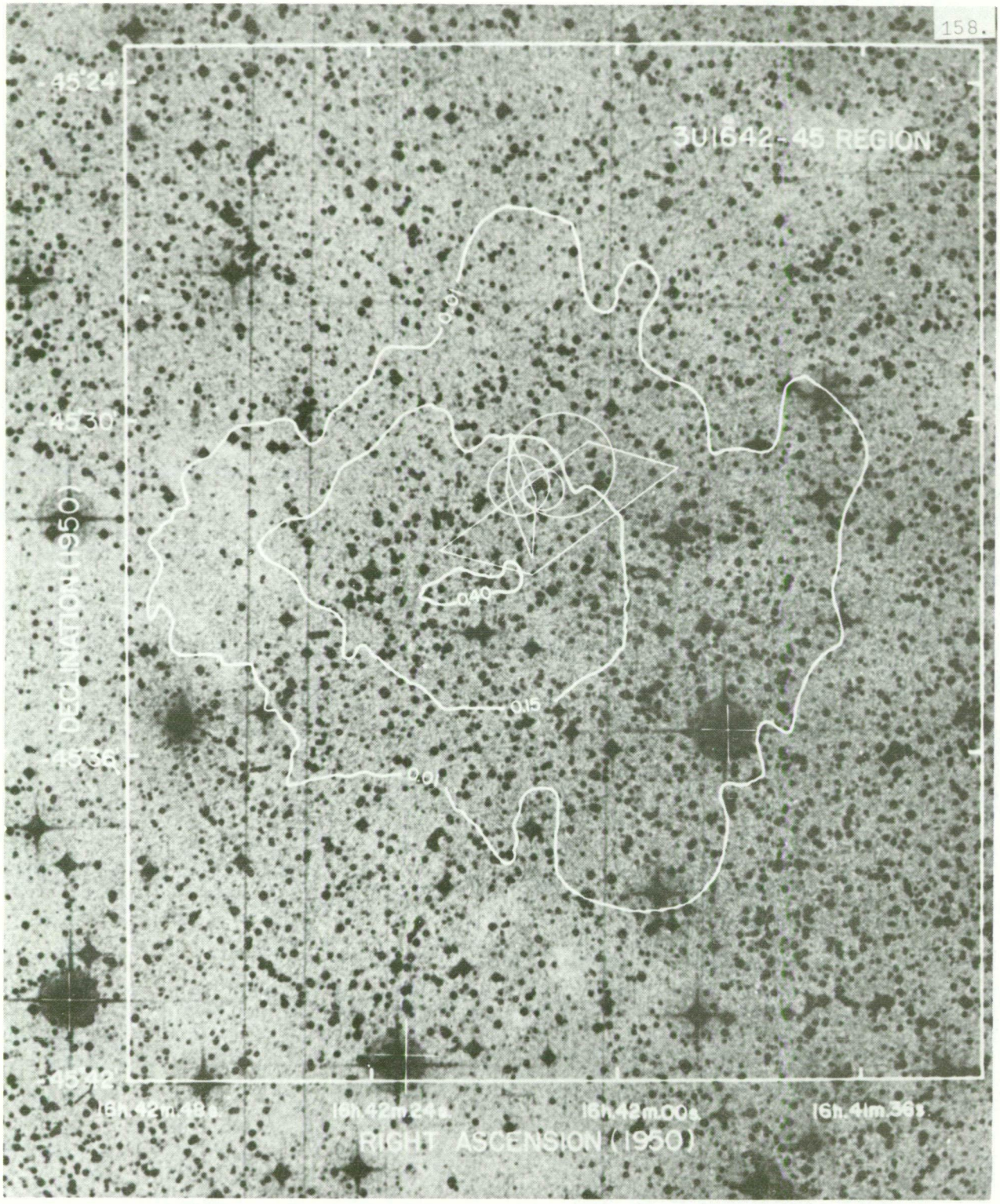

Figure 8-3. Simplified radio contours of the 2S1642-455 region overlayed onto the optical field. The X-ray positions are those of figure 8-2.

recombination lines typical of an HII region.

Figure 8-2 has been 'cleaned' (Högbom 1974) to remove the effects of near-in negative sidelobe responses of the beam. The X-ray source position determinations are also shown and are from Rappaport et al. (1971) 'Rocket'; Wilson et al. (1977) 'Ariel V'; Apparao et al. (1978) 'SAS-3'; Gursky et al. (1978) 'HEAO-A'; and Forman et al. (1979) '4U'.

The average radial velocity of the H109α recombination line, OH emission and water vapour emission of -28 ± 8 km/s combined with the Schmidt rotation model of the galaxy implies that G339.6 - 0.1 is at a distance of 2.6 ± 0.6 or 16.1 ± 0.6 kpc. Arguments based on the optical absorption in the direction of G339.6 - 0.1 imply that the larger distance is preferable (Haynes et al. 1979). Further evidence for the larger distance estimate is the apparent absence of an obvious exciting star in the centre of the radio source (Fig. 8-3).

The X-ray source distance may be estimated from the severe low energy cut off of the X-ray source spectrum. This would imply a distance greater than 2 kpc unless the X-ray object is surrounded by a large amount of circumstellar material. A further distance estimate of 13 kpc may be deduced if the X-ray source has an Eddington limit luminosity for an object of Chandrasekhar mass. This assumption is supported by the fact that many X-ray sources are found to have luminosities close to this value.

It would therefore appear that the X-ray source and radio object may be at about the same distance although these distance estimates are based on weak assumptions.

It is difficult to envisage a mechanism for X-ray production in an HII region. However, in a recent paper by Halpern and Grindlay (1980)

the authors have shown that an X-ray source accreting matter from a dense medium could excite a small HII region. Such a mechanism may be important in X-ray sources like 4U1642-45. However the X-ray source would be expected to lie very near the centre of the HII region if it were causing the excitation and it would therefore appear unlikely that the X-ray source is associated with the HII region in this way. Similar comments apply for an association between the X-ray source 2S1624-490 and the HII region G339.4 - 0.3 and also between LMC X-1 and the HII region M77 which are both members of the Large Magellanic Cloud (Duldig et al. 1980a).

8.4.2 ARE 2S0535-668 AND GX301-2, LIKE CIR X-1?

Both of these sources show similarities to Cir X-1 (Duldig et al. 1980b). 2S0535-668 (A0538-66) has been shown to be a recurrent transient X-ray source with a period of $16^{d}.7$ between outbursts (Johnston et al. 1979, Skinner et al. 1980) whilst Kelley et al. (1979) have concluded that GX301-2 (4U1223-62, WRA977) has an orbital period of $35^{d}.0$ and a high orbital eccentricity of 0.44.

Seaquist suggested that the extended object shown in figure 7-2 may be an HII region on the basis of its flat spectrum between λ = 3.5 and 6 cm. The peak flux density from these observations at λ = 2 cm was 80 ± 15 mJy and may indicate a non-thermal source origin. Only one observation was carried out during the critical phase window ($0< \phi <0.15$) in which radio flaring may be expected (Table 8-2) and therefore, although this measurement was slightly greater than the others the data are inconclusive and further observations should be made at higher angular resolution during the phase interval ϕ = 0 - 0.15.

Table 8-2

λ = 2 cm Observations of GX301-2

Epoch JD 2443000+	Orbital phase*	Flux Density ± rms mJy	Beam Centre (1950.0) α	δ
311.6	0.99	77 15	12 24 00.7	-62 33 45
312.3	0.01	70 3	12 23 40	-62 29 40
374.2	0.78	17 9	12 23 40	-62 29 40
377.1	0.86	58 11	12 23 40	-62 29 40
377.2	0.86	66 10	12 23 40	-62 29 40
626.5	0.99	35 6	12 23 40	-62 29 40

*ϕ = 0 corresponds to periastron

Observations carried out throughout an expected X-ray flare of 2S0535-668 failed to detect any λ = 6 cm emission.

Clearly any radio emission from GX301-2 of the Cir X-1 type would have to be intrinsically much weaker, in view of the fact that the source is only 2 - 3 kpc distant (Vidal 1973, Thomas et al. 1979) compared with 10 kpc for Cir X-1 (Whelan et al. 1977). It therefore appears that GX301 is dissimilar to Cir X-1.

The flare X-ray luminosity of 2S0535-668 of $\sim 8 \times 10^{38}$ erg/sec (Johnston et al. 1980) is sufficiently high to permit the formation of luminosity-driven shocks and radio flares. The author is unaware of any X-ray coverage at the time of the radio observations and owing to the highly variable nature of the X-ray flare intensities from this source it is possible that the source was very weak throughout the predicted X-ray flare period. Therefore no conclusions may be drawn regarding the Cir X-1 like nature of this source at radio wavelengths but further radio monitoring is strongly suggested.

8.4.3 RADIO EMISSION FROM X-RAY BURST SOURCES

The results presented in section 7.4 showed no radio emission greater than $\sim$ 100 mJy is associated with X-ray burst sources at λ = 6 and 2 cm. In contrast to these results Calla et al. (1979, 1980a and 1980b) have reported radio "burst like" behaviour from MXB1730-335.

At the time of writing the X-ray behaviour of MXB1730-335 during the May 1980 observations had not been forwarded to the author.

Few conclusions may be drawn regarding the null result of this work however a steep radio spectrum may explain the λ = 2 cm results. No conclusions regarding correlated X-ray/radio emission can be made from the λ = 6 cm observations at this stage.

It is notable that no other observers have published detections of radio emission from MXB1730-335 whilst the Ahmedabad group have presented detections from a number of periods of radio burst activity. The identification of these radio events as associated with X-ray burst activity in MXB1730-335 must remain tentative until the level of source confusion in the nearby region is established and further coordinated X-ray and radio observations provide a definite correlation between the radio and X-ray emission.

8.5 REFERENCES

Apparao K.M.V., Bradt H.V., Dower R.G., Doxsey R.C., Jernigan J.G. and Li F. (1978) Nature 271, 225

Bieging J. and Downes D. (1975) Nature 258, 307

Calla O.P.N., Bhandari S.M., Desphande M.R. and Vats O.M. (1979) I.A.U. Circ. 3347

Calla O.P.N., Barathy S., Snagol A.K., Bhandar S.M., Desphande M.R. and Vyas H.O. (1980a) I.A.U. Circ. 3458

Calla O.P.N., Sangal A.K. and Barathy S. (1980b) I.A.U. Circ. 3467

Davis, Morison and Spencer (1975) I.A.U. Circ. 2822

Duldig M.L., Thomas R.M., Greenhill J.G., Haynes R.F., Simons L.W. and Murdin P.G. (1979) I.A.U. Colloquium No. 46 "Changing Trends in Variable Star Research", eds. Bateson F., Smak J. and Urch I.H. University of Waikato

Duldig M.L., Thomas R.M., Greenhill J.G., Haynes R.F. and Murdin P.G. (1980a) Mon. Not. R. astr. Soc. 190, 861

Duldig M.L., Thomas R.M. and Haynes R.F. (1980b) Proc. A.S.A. 4, 108

Forman W., Jones C. and Tananbaum H. (1976) Astrophys. J. 208, 849

Gursky H., Bradt H., Doxsey R., Schwartz D.A. Schwarz J., Dower R., Fabbiano G., Griffiths R.C., Johnston M., Leach R., Ramsay A. and Spada G. (1978) Harvard/Smithsonian Center for Astrophysics Preprint CFA/HEA-78-201

Halpern J.P. and Grindlay J.E. (1980) Harvard/Smithsonian Center for Astrophysics Preprint CFA/HEA-80-293

Haynes R.F., Jauncey D.L., Murdin P.G., Goss W.M., Longmore A.J., Simons L.W.J., Milne D.K. and Skellern D.J. (1978) Mon. Not. R. astr. Soc. 185, 661

Haynes R.F., Murdin P., Thomas R.M., Duldig M.L. and Greenhill J.G. (1979) Mon. Not. R. astr. Soc. 188, 13

Haynes R.F., Learch I. and Murdin P. (1980a) Astr. Astrophys. 87, 299

Haynes R.F., Jauncey David L., Learch I. and Murdin P. (1980b) Aust. J. Phys. 32, 43

Hjellming R.M. and Wade C.M. (1971) Astrophys. J. Lett. 164, L1

Hjellming R.M. (1974) "International Conference on X-rays in Space", p. 211 ed. Venkatesan D. University of Calgary

Högbom J.A. (1974) Astr. Astrophys. Suppl. 15, 417

Johnston M.D., Griffiths R.E. and Ward M.J. (1979) Astrophys. J. (Lett) 230, L11

Kaluzienski L.J., Holt S.S., Boldt E.A. and Serlemitsos P.J. (1976) Astrophys. J. Lett. 208, L71

Kaluzienski L.J. and Holt S.S. (1977) I.A.U. Circ. 3099

Kelley R., Rappaport S. and Petre R. (1979) M.I.T. Preprint CSR/HEA-79-34

Little A.G., Crawford D.F. and Murdoch H.S. (1976) Nature 261, 113

Murdin P., Penston M.J., Penston M.V., Glass I.S., Sanford P.W., Hawkings F.J., Mason K.O. and Willmore A.P. (1974) Mon. Not. R. astr. Soc. 169, 25

Murdin P., Jauncey D.L., Haynes R.F., Learch I., Nicholson G.D., Holt S.S. and Kaluzienski L.J. (1980a) Astr. Astrophys. 87, 292

Murdin Paul, Allen David A., Morton Donald C., Whelan John A.J. and Thomas Richard M. (1980b) Mon. Not. R. astr. Soc. 192, 709

Rappaport S., Zauman W., Doxsey P. and Mayer W. (1971) Astrophys. J. Lett. 169, L93

Sanduleak N. and Dolan J.F. (1974) Astrophys. J. Lett. 187, L73

Seaquist E.R. (1977) Astrophys. J. 211, 547

Skinner G.K., Shulman S., Share G., Evans W.D., McNutt D., Meekings J., Smathers H., Wood K., Yentis D., Byram E.T., Chubb T.A. and Friedman H. (1980) Astrophys. J. 240, 619

Snedecor G.W. (1962) "Statistical Methods" Fifth Edition, Iowa State University Press p.67

Thomas R.M., Duldig M.L., Haynes R.F. and Murdin Paul (1978) Mon. Not. R. astr. Soc. 185, 29p

Thomas R.M., Morton D.C. and Murdin P.G. (1979) Mon. Not. R. astr. Soc. 188, 19

Vidal N.V. (1973) Astrophys. J. Lett. 186, L81

Wade C.M. and Hjellming R.M. (1971) Astrophys. J. 170, 523

Ward M.J., Penston M.V., Murray C.A. and Clements E.D. (1975) Nature 257, 659

Whelan J.A.J., Mayo S.K., Wickramasinghe D.T., Murdin P.G., Peterson B.A., Howarden T.G., Longmore A.J., Haynes R.F., Goss W.M., Simons L.W., Caswell J.L., Little A.G. and McAdam W.B. (1977) Mon. Not. R. astr. Soc.181, 259

White N.E., Mason K.O., Sanford P.W., Johnson H.M. and Catamura R.C. (1978) Astrophys. J. 220, 600

Wilson A.M., Carpenter E.F., Eyles C.J., Skinner G.K. and Willmore A.P. (1977) Astrophys. J. Lett. 215, L11

CHAPTER 9

BIBLIOGRAPHY

Ables J.G. (1969) Astrophys. J. Lett. 155, L27

Agrawal P.C., Biswas S., Gokhale G.S., Iyengar V.S., Kunte P.K., Manchanda R.K. and Sreekantan B.V. (1976) Nature 224, 51

Andrews B.H. and Purton C.R. (1968) Nature 218, 855

Apparao K.M.V., Bradt H.V., Dower R.G., Doxsey R.C., Jernigan J.G. and Li F. (1978) Nature 271, 225

Becker R.H., Rothschild R.E., Boldt E.A., Holt S.S., Pravdo S.H., Serlemitsos P.J. and Swank J.H. (1978) Astrophys. J. 221, 912

Bieging J. and Downes D. (1975) Nature 258, 307

Bradt H. (1978) "Celestial positions of galactic X-ray sources from SAS-3", prepared for the Austin A.A.S. Meeting, paper 12.05.09

Bradt H.V., Apparao K.M.V., Clark G.W., Dower R., Doxsey R., Hearn D.R., Jernigan J.G., Joss P,C., Mayer W., McClintock J. and Walter F. (1977) Nature 269, 21

Braes L.L.E. and Miley G.K. (1973) IAU Symp. No. 55 "X- and Gamma-Ray Astronomy", pp. 86-97, eds Bradt H. and Giaconni R., D. Reidel Dordrecht, Holland.

Braes L.L.E., Miley G.K. and Schoenmaker A.A. (1972) Nature 236, 392

Buselli G., Clancey M.C., Davison P.J.N., Edwards P.J., McCracken K.G. and Thomas R.M. (1968) Nature 219, 1124

Calla O.P.N., Bhandari S.M., Desphande M.R. and Vats O.M. (1979) I.A.U. Circ. 3347

Calla O.P.N., Barathy S., Snagol A.K., Bhandar S.M., Desphande M.R. and Vyas H.O. (1980a) I.A.U. Circ. 3458

Calla O.P.N., Sangal A.K. and Barathy S. (1980b) I.A.U. Circ. 3467

Coe M.J., Dennis B.R., Dolan J.F., Crannel C.J., Maurer G.S., Frost K.J., Orwig L.E., Graf W. and Price K.M. (1980) Astrophys. J. 237,148

Clark D.H., Parkinson J.H. and Caswell J.L. (1975) Nature 254, 674

Clark G. and Chartres M. (1978) I.A.U. Circ. 3208

Cooke B.A., Ricketts M.J., Maccacaro T., Pye J.P., Elvis M., Watson M.G., Griffiths R.E., Pounds K.A., McHardy I., Maccagni D., Seward F.D., Page C.G. and Turner M.J.L. (1978) Mon. Not. R. astr. Soc. 182, 489

Cooley J.W. and Tukey J.W. (1965) Math. Computation 19, 297

Craft H.D. (1975) I.A.U. Circ. 2822

Crane R.K. (1976) "Methods of Experimental Physics" ed. Meeks M.L., Acad. Press, Vol. 12, part B pp 177-182

Davies R.D., Walsh D., Browne I.W.A., Edwards M.R. and Noble R.G. (1976) Nature 261, 476

Davis M., Huchra J., Tonry J. and Latham D. (1978) I.A.U. Circ. 3202

Davis, Morison and Spencer (1975) I.A.U. Circ. 2822

Dolan J.F. (1972) Astrophys. Space Sci. 17, 472

Doxsey R., Bradt H., Gursky H., Johnston M., Schwartz D.A., Schwarz J. (1977) M.I.T. Preprint CSR-77-29

Duldig M.L., Emery M.W., Fenton A.G., Fenton K.B., Greenhill J.G. and Thomas R.M. (1977) Proc. A.S.A. Vol. 3 No. 2 p.117

Duldig M.L., Greenhill J.G., Thomas R.M., Haynes R.F., Simons L.W. and Murdin P.G. (1977) I.A.U. Circ. 3108

Duldig M.L., Greenhill J.G., Thomas R.M., Haynes R.F., Simons L.W. and Murdin P.G. (1979a) Mon. Not. R. astr. Soc. 187, 576

Duldig M.L., Thomas R.M. Greenhill J.G., Haynes R.F., Simons L.W. and Murdin P.G. (1979b) Proceedings of the Inaugural Asian/South Pacific Regional Meeting of the I.A.U., New Zealand Journal of Science 22, 563

Duldig M.L., Thomas R.M., Greenhill J.G., Haynes R.F., Simons L.W. and Murdin P.G. (1979) I.A.U. Colloquium No. 46 "Changing Trends in Variable Star Research", eds. Bateson F., Smak J. and Urch I.H. University of Waikato

Duldig M.L., Thomas R.M., Haynes R.F. and Murdin P.G. (1980a) Mon. Not. R. astr. Soc. 190, 861

Duldig M.L., Thomas R.M., Haynes R.F. (1980b) Proc. A.S.A. 4, 108.

Epstein H. (1977) Astrophys. J. (Lett) 218, L49

Forman W., Jones C., Cominsky L., Julian P., Murray S., Peters G., Tananbaum H. and Giacconi R. (1978) Astrophy. J. Suppl. 38

Forman W., Jones C. and Tananbaum H. (1976) Astrophys. J. 208, 849

Giacconi R., Gursky H., Paolini F.R. and Rossi B. (1962) Phys. Rev. Lett. 9, 439

Glass I.S. and Feast M.W. (1978) I.A.U. Circ. 3226

Gottlieb E.W., Wright E.L. and Liller W. (1975) Astrophys. J. (Lett) 195,L33

Greenhill J.G., Coe M.J., Burnell S.J., Strong K.T. and Carpenter G.F. (1979) Mon. Not. R. astr. Soc. 189, 563

Greenhill J.G., Jernigan J.G., Thomas R.M., Duldig M.L. and Haynes R.F., (1978) Nature 279, 620

Greenhill J.G., Duldig M.L., Emery M.W., Fenton A.G., Fenton K.B., Thomas R.M. and Watts D.J. (1979a) Proc. A.S.A. Vol. 3 Nos. 5 & 6 p.349

Greenhill J.G., Fenton A.G., Fenton K.B., Thomas R.M., Duldig M.L., Emery M.W., Cooke D.J., Phillips J., Watts D.J., Hudson R.M., Middleton E. and Salmon G. (1979b) Proc. 16th Int. Cosmic Ray Conf., Kyoto, Japan, Vol. 11, T1-4., 8

Griffiths R.E., Bradt H., Doxsey D.A., Friedman H., Gursky H., Johnston M., Longmore A., Malin D.F., Murdin P., Schwartz D. and Schwarz J. (1978) Astrophys. J. (Lett) 221, L63

Gursky H., Bradt H., Doxsey R., Schwartz D.A., Schwarz J., Dower R., Fabbiano G., Griffiths R.E., Johnston M., Leach R., Ramsey A. and Spada G. (1977) MIT Preprint CSR-77-30

Gursky H., Bradt H., Doxsey R., Schwartz D.A. Schwarz J., Dower R., Fabbiano G., Griffiths R.C., Johnston M., Leach R., Ramsay A. and Spada G. (1978) Harvard/Smithsonian Center for Astrophysics Preprint CFA/HEA-78-201

Halpern J.P. and Grindlay J.E. (1980) Harvard/Smithsonian Center for Astrophysics Preprint CFA/HEA-80-293

Haymes R.C., Harnden F.R., Johnson W.N. and Prichard H.M. (1972) Astrophys. J. (Lett) 172, L47

Haynes R.F., Caswell J.L. and Simons L.W.J. (1978) Aust. J. Phys. Astrophys. Suppl. No. 45

Haynes R.F., Jauncey David L., Lerche I. and Murdin P. (1980b) Aust. J. Phys. 32, 43

Haynes R.F., Jauncey D.L., Murdin P.G., Goss W.M., Longmore A.J., Simons L.W.J., Milne D.K. and Skellern D.J. (1978) Mon. Not. R. astr. Soc. 185, 661

Haynes R.F., Lerche I. and Murdin P. (1980a) Astr. Astrophys. 87, 299

Haynes R.F., Murdin P., Thomas R.M., Duldig M.L. and Greenhill J.G. (1979) Mon. Not. R. astr. Soc. 188, 13

Hjellming R.M. (1974) "International Conference on X-rays in Space" p.211, ed. Venkatesan D., University of Calgary

Hjellming R.M. (1978) Astrophys. J. 221, 225

Hjellming R.M. and Wade C.M. (1971) Astrophys. J. Lett. 164, L1

Hoffman J.A., Lewin W.H.G. and Doty J. (1977) Astrophys. J. (Lett) 217, L23

Högbom J.A. (1974) Astr. Astrophys. Suppl. 15, 417

Jain A.K., Jayanthi V.B., Kasturirangan K. and Rao U.R. (1973) Astrophys. Space Sci. 21, 107

Janes A.F., Pounds K.A., Ricketts M.J., Willmore A.P. and Morrison L.V. (1973) Nature 244, 349

Jernigan J.G., Apparao K.M.V., Bradt M.V., Doxsey R.E. and McClintock J.E. (1977) Nature 270, 321

Johnston K.J., Robinson B.J., Caswell J.L. and Batchelor R.A. (1972) Astrophys. Lett. 10, 93

Johnston M.D., Bradt M.V., Doxsey R.E., Gurskey H., Schwartz D.A., Schwarz J. and van Paradijs J. (1978) Astrophys. J. (Lett) 225, L59

Johnston M.D., Bradt M.V., Doxsey R.E., Griffiths R.E., Schwartz D.A. and Schwarz J. (1979) Astrophys. J. (Lett) 230, L11

Johnston M.D., Griffiths R.E. and Ward M.J. (1979) Astrophys. J. (Lett) 230, L11

Johnson W.N., Kurfess J.D., Maurer G.S. and Strickman M.S. (1980) Astrophys. J. 238, 982

Kaluzienski L.J., Holt S.S., Boldt E.A. and Serlemitsos P.J. (1976) Astrophys. J. Lett. 208, L71

Kaluzienski L.J. and Holt S.S. (1977) I.A.U. Circ. 3099

Kelley R., Rappaport S. and Petre R. (1979) M.I.T. Preprint CSR/HEA-79-34

Lamb P. and Sanford P.W. (1979) Mon. Not. R. astr. Soc. 188, 555

Lewin W.H.G., McClintock I.E., Ryckman S.G., Glass I.S. and Smith W.B. (1970) Astrophys. J. (Lett) 162, L109

Little A.G., Crawford D.F. and Murdoch H.S. (1976) Nature 261, 113

Lloyd K.H. (1968) Am. J. Phys. 37, 329

McClintock J.E., Rappaport S., Joss P.C., Bradt H., Buff J., Clark G.W., Hearn D., Lewin W.H.G., Matilsky T., Mayer W. and Primine F. (1976) Astrophys. J. Lett. 206, L99

McGee R.X., Newton Lynette M. and Brooks J.W. (1974) Aust. J. Phys. 27, 729

Mason K.O., Murdin P.G. and Visvanathan N. (1977) I.A.U. Circ. 3054

Matsuoka M., Fujii M., Miyamoto S., Nishimura J., Oda M., Ogawara Y., Hayakawa S., Kasahara I., Makino F., Tanaka Y., Agrawal P.C. and Sreekantan B.V. (1972) Astrophys. Space Sci. 18, 472

Miyamoto S. and Matsuoka M. (1977) Space Sci. Rev. 20, 687

Murdin Paul, Allen David A., Morton Donald C., Whelan John A.J. and Thomas Richard M. (1980b) Mon. Not. R. astr. Soc. 192, 709

Murdin P., Jauncey D.L., Haynes R.F., Lerche I., Nicholson G.D., Holt S.S. and Kaluzienski L.J. (1980a) Astr. Astrophys. 87, 292

Murdin P., Penston M.J., Penston M.V., Glass I.S., Sanford P.W., Hawkings F.J., Mason K.O. and Willmore A.P. (1974) Mon. Not. R. astr. Soc. 169, 25

Pineda F. and Schnopper H.W. (1978) I.A.U. Circ. 3190

Raply C.G. and Tuohy I.R. (1974) Astrophys. J. (Lett) 191, L113

Rappaport S., Zauman W., Doxsey P. and Mayer W. (1971) Astrophys. J. Lett. 169, L93

Reigler G.R. (1969) NASA Report X-611-69-1, Goddard Space Flight Center, Greenbelt, Maryland

Reigler G.R. Boldt E.A. and Serlemitsos P.J. (1970) Nature 226, 1041

Sanduleak N. and Dolan J.F. (1974) Astrophys. J. Lett. 187, L73

Seaquist E.R. (1977) Astrophys. J. 211, 547

Skinner G.K., Shulman S., Share G., Evans W.D., McNutt D., Meekings J., Smathers H., Wood K., Yentis D., Byram E.T., Chubb T.A. and Friedman H. (1980) Astrophys. J. 240, 619

Snedecor G.W. (1962) "Statistical Methods" Fifth Edition, Iowa State University Press p.67

Staubert R., Kendziona E., Pietsch W., Reppin C., Trumper J. and Voges W. (1980) preprint

Stein J.A. and Lewin W.H.G. (1967) J. Geophys. Res. 72, 383

Terrell J. and Olsen K.H. (1970) Astrophys. J. 161, 399

Terrell N.J. (1972) Astrophys. J. (Lett) 174, L35

Thomas B. MacA. and Day G.A. (1969) Aust. J. Phys. Astrophys. Suppl. No. 11

Thomas R.M., Duldig M.L., Haynes R.F. and Murdin P.G. (1978a) Mon. Not. R. astr. Soc. 185, 29p.

Thomas R.M., Duldig M.L., Haynes R.F. and Murdin P.G. (1978b) I.A.U. Circ. 3219

Thomas R.M., Duldig M.L., Haynes R.F., Simons L.W., Murdin P., Hoffman J.A., Lewin W.H.G., Wheaton W.A. and Doty J. (1979) Mon. Not. R. astr. Soc. 187, 299

Thorstenson J.R., Charles P.A. and Bowyer S. (1977) I.A.U. Circ. 3088

Vidal N.V. (1973) Astrophys. J. Lett. 186, L81

Wade C.M. and Hjellming R.M. (1971) Astrophys. J. 170, 523

Walters J.W. (1976) "Methods of Experimental Physics" ed. Meeks M.L., Acad. Press, Vol. 12, part B pp 173-174

Ward M.J., Penston M.V., Murray C.A. and Clements E.D. (1975) Nature 257, 659

Watts D.J. and Thomas R.M. (1979) Astrophys. Space Sci. 64, 213

Welch P.D. (1967) IEEE Trans. Audio and Electroacoustics Vol AU-15,p70

Ward M.J., Penston M.V., Murray C.A. and Clements E.D. (1975) Nature 257, 659

Whelan J.A.J., Mayo S.K., Wickramasinghe D.T., Murdin P.G., Peterson B.A., Howarden T.G., Longmore A.J., Haynes R.F., Goss W.M., Simons L.W., Caswell J.L., Little A.G. and McAdam W.B. (1977) Mon. Not. R. astr. Soc. 181, 259

White N.E., Mason K.O. and Sanford P.W. (1976) Mon. Not. R. astr. Soc. 176, 91

White N.E., Mason K.O., Sanford P.W., Johnson H.M. and Catamura R.C. (1978) Astrophys. J. 220, 600

Wilson A.M., Carpenter E.F., Eyles C.J., Skinner G.K. and Willmore A.P. (1977) Astrophys. J. Lett. 215, L11

Yabsley D.E. (1975) "IREE Convention Digest, International Electronics Convention '75' (IREE Aust., Sydney)" p.203

Yabsley D.E. (1977) Proc. A.S.A. 3, 113

Zuiderwijk E.J. (1978) I.A.U. Circ. 3221

APPENDIX A

PUBLICATION LIST

"A Review of Some Significant Galactic X-ray Sources" Duldig M.L. Journal of the Astronomical Society of Victoria 30,No. 6, December (1977)

International Astronomical Union Circular No. 3108 Duldig M.L., Greenhill J.G., Thomas R.M., Haynes R.F., Simons L.W. and Murdin P. (1977)

"Balloon Observations of the X-ray Pulsar Vela XR-1" Duldig M.L., Emery M.W., Fenton A.G., Fenton K.B., Greenhill J.G. and Thomas R.M. Proc.A.S.A. Vol. 3, No. 2, 117 (1977)

"The 20 keV Break in the Diffuse X-ray Background Spectrum" Hudson R.M., Thomas R.M. and Duldig M.L. Proc. A.S.A. Vol.3, No. 2, 131 (1977)

"Spectral Variability in X-ray Sources" Thomas R.M. Duldig M.L. and Greenhill J.G. Nature 267, 332 (1977)

"Flare Observations of Circinus X-1 at 2 Cm Wavelength" Thomas R.M., Duldig M.L., Haynes R.F. and Murdin P. Mon. Not. R. astr. Soc. 185, 29p (1978)

International Astronomical Union Circular No. 3219 Thomas R.M., Duldig M.L., Haynes R.F. and Murdin P.G. (1978)

"Radio Identification of 11 X-ray Sources at 2 Cm" Duldig M.L., Greenhill J.G., Thomas R.M., Haynes R.F., Simons L.W. and Murdin P.G. Mon. Not. R. astr. Soc. 187, 576 (1979)

"Radio Variability of X-ray Source" Duldig M.L., Thomas R.M., Greenhill J.G., Haynes R.F., Simons L.W. and Murdin P.G. Proc. International Astronomical Union Colloquium No. 46, University of Walkato, Hamilton, N.Z., p.432 (1979)

"2 Cm Observations of X-ray Sources" Duldig M.L., Thomas R.M., Greenhill J.G., Haynes R.F., Simons L.W. and Murdin P.G. N.Z. Journal of Science 22, 519 (1979)

"Balloon Observations of Several Southern X-ray Sources" Greenhill J.G., Duldig M.L., Emery M.W., Fenton A.G., Fenton K.B., Thomas R.M. and Watts D.J. Proc. A.S.A. Vol.3, Nos. 5 & 6, 349 (1979)

"A Large Area Proportional Counter for Balloon-Borne X-ray Astronomy" Greenhill J.G., Fenton A.G., Fenton K.B., Thomas R.M., Duldig M.L., Emery M.W., Cook D.J., Phillips J., Watts D.J., Hudson R.M., Middleton E. and Salmon G. Proc. 16th International Cosmic Ray Conference, Kyoto, Japan, Vol. 11, 11-4, 8 (1979)

"A1710-34 X-ray, Optical and Radio Observations" Greenhill J.G., Jernigan J.G., Murdin P., Thomas R.M., Duldig M.L. and Haynes R.F. Nature 279, 620 (1979)

"High Resolution Map of G339.6-0.1 and its Possible Association with 4U1642-45" Haynes R.F., Murdin P.G., Thomas R.M., Duldig M.L. and Greenhill J.G. Mon. Not. R. astr. Soc. 188, 13 (1979)

"Simultaneous Radio and X-ray Observations of the X-ray Burst Source MXB1636-53" Thomas R.M., Duldig M.L., Haynes R.F., Simons L.W., Murdin P.G., Hoffman J.A., Lewin W.H.G., Wheaton W.A. and Doty J. Mon. Not. R. astr. Soc. 187, 299 (1979)

"Observations of the LMC X-1 Region at 2 Cm" Duldig M.L., Thomas R.M., Haynes R.F. and Murdin P. Mon. Not. R. astr. Soc. 190, 861 (1980)

"Comparison of the X-ray Sources Cir X-1, GX301-2 and 2S0535-668"
Duldig M.L., Thomas R.M. and Haynes R.F. Proc. A.S.A. Vol.4, No. 1, 108 (1980)

"X-Ray, Radio and Infrared Observations of the Rapid Burster (MXB1730-335) During 1980" Lawrence A., Cominsky L., Lewin W.H.G., Oda M., Dashido T., Oka R., Ohkawa T., Maruyama T., Yokoyama T., Nicholson G., Balonek T., Dent W., Glass I., Jones A., Giles B., Rao A., Vengupal V., Haynes R., Duldig M.L., Okuda H., Sato S., Kobayaski Y., Jugaku J., Pogge R. and Backman D. (in preparation 1981)

UNPUBLISHED WORK

"A Study of the Emission Properties of Compact Objects"
Duldig M.L. Honours Thesis, University of Tasmania 1975

APPENDIX B

BALLOON FLIGHT PAYLOAD CALIBRATIONS

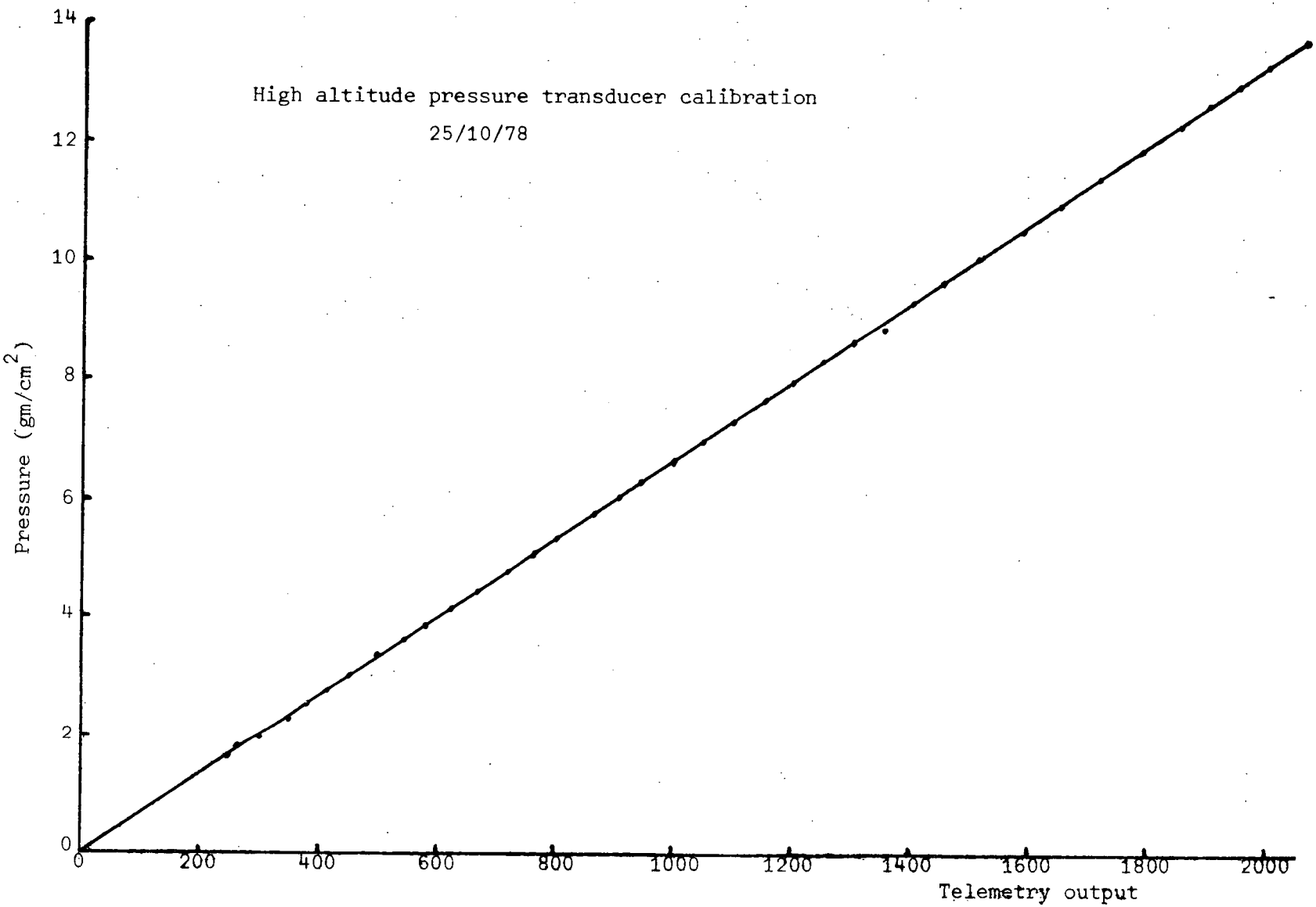
High altitude pressure transducer calibration
25/10/78
Pressure (gm/cm^2)
0
2
4
6
8
10
12
14
0
200
400
600
800
1000
1200
1400
1600
1800
2000
Telemetry output

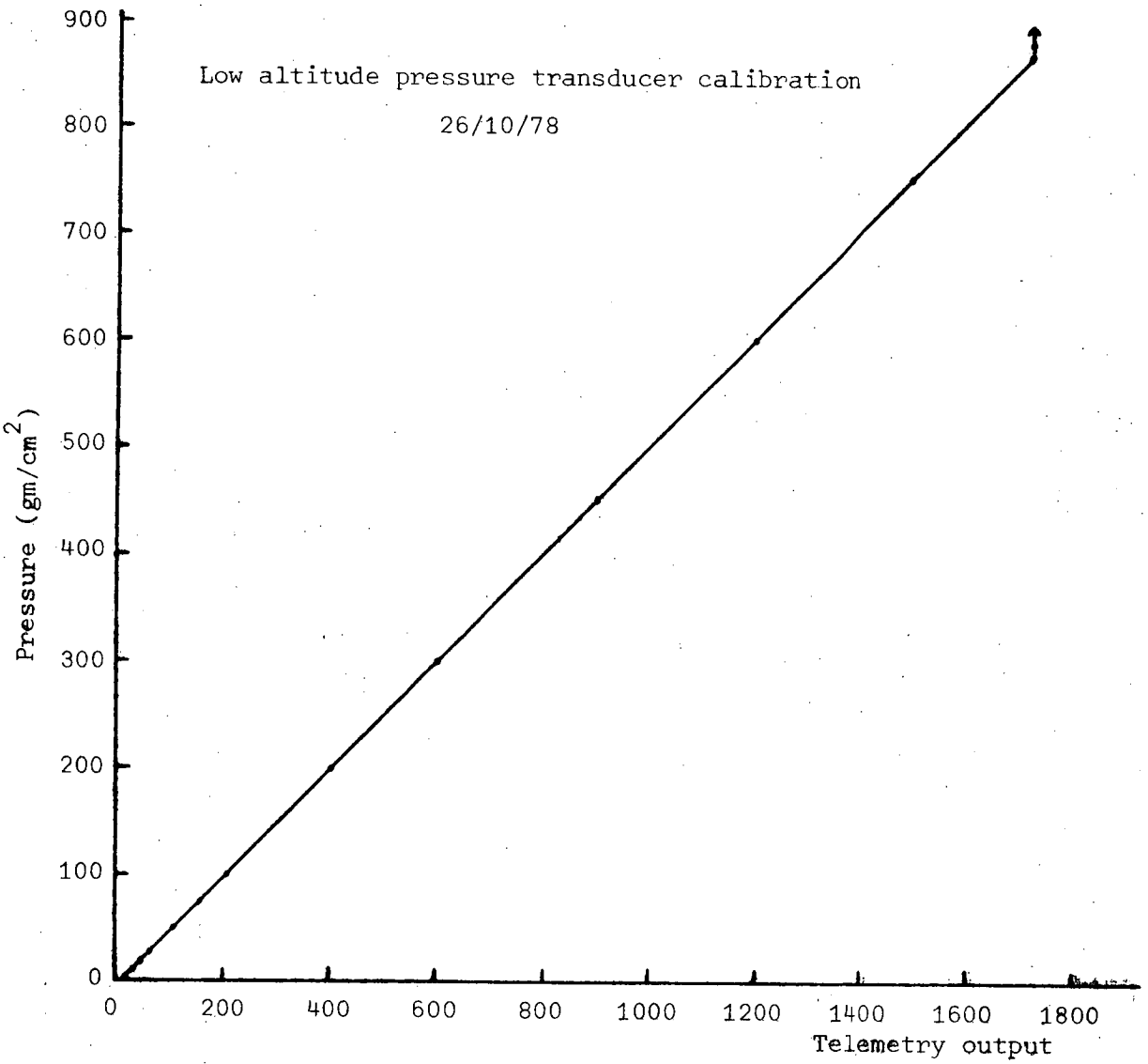
Low altitude pressure transducer calibration
26/10/78
Pressure (gm/cm^2)
900
800
700
600
500
400
300
200
100
0
0
200
400
600
800
1000
1200
1400
1600
1800
Telemetry output

Battery and Regulated 12 volt supply
voltage vs. Telemetry output
28/10/78

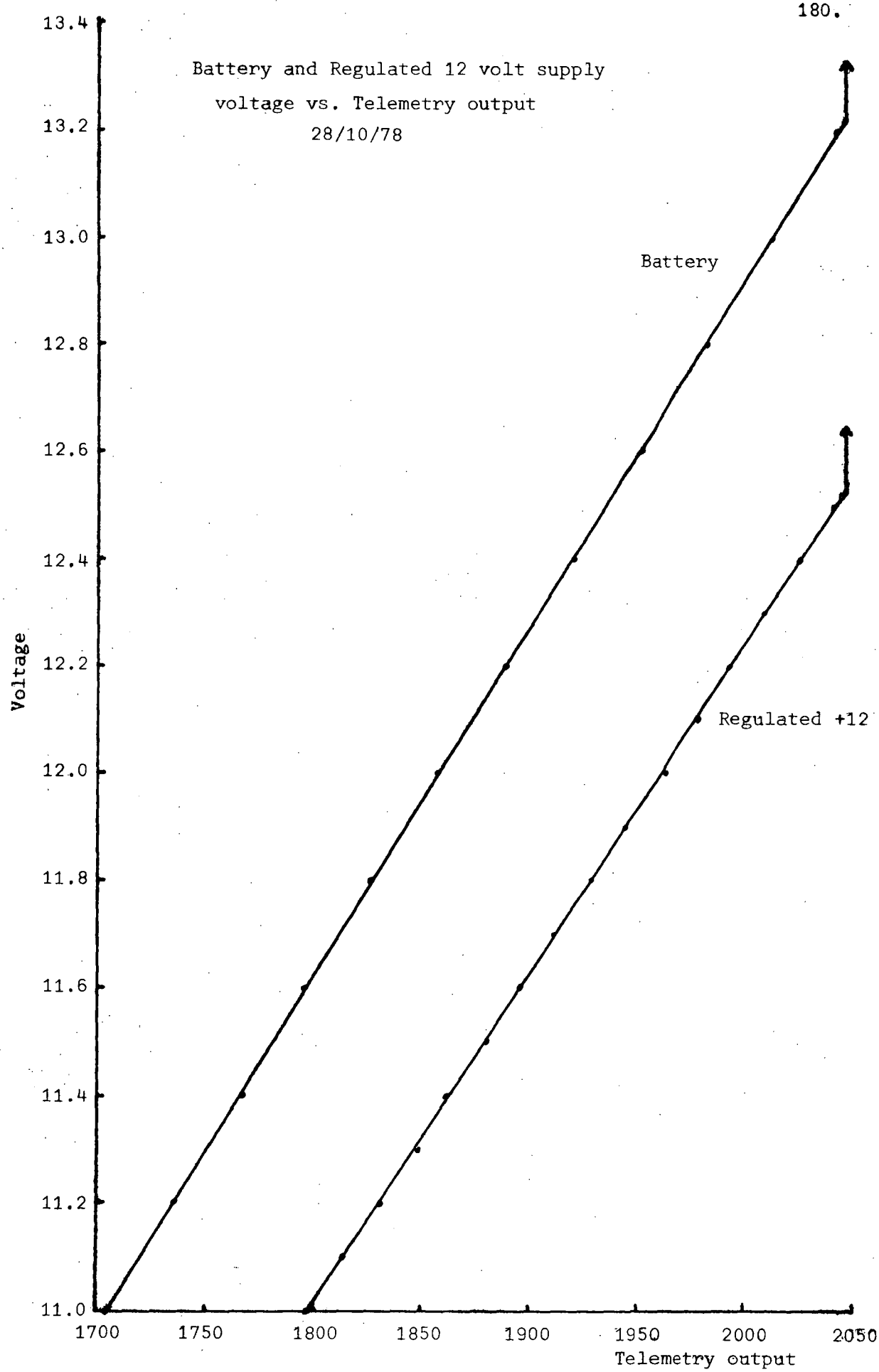

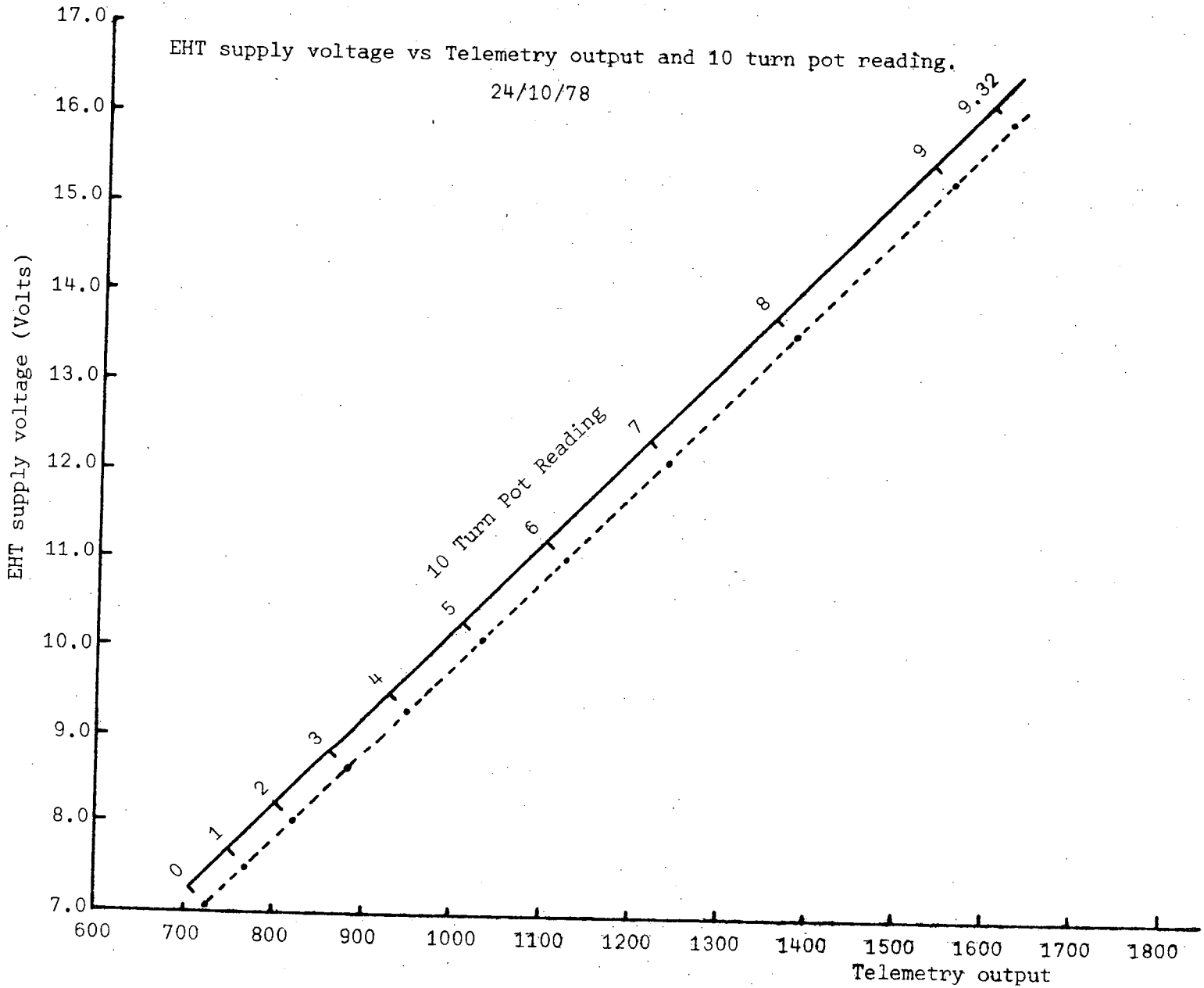
EHT supply voltage vs Telemetry output and 10 turn pot reading.
24/10/78
EHT supply voltage (Volts)
17.0
16.0
15.0
14.0
13.0
12.0
11.0
10.0
9.0
8.0
7.0
10 Turn Pot Reading
0
1
2
3
4
5
6
7
8
9
9.32
600
700
800
900
1000
1100
1200
1300
1400
1500
1600
1700
1800
Telemetry output

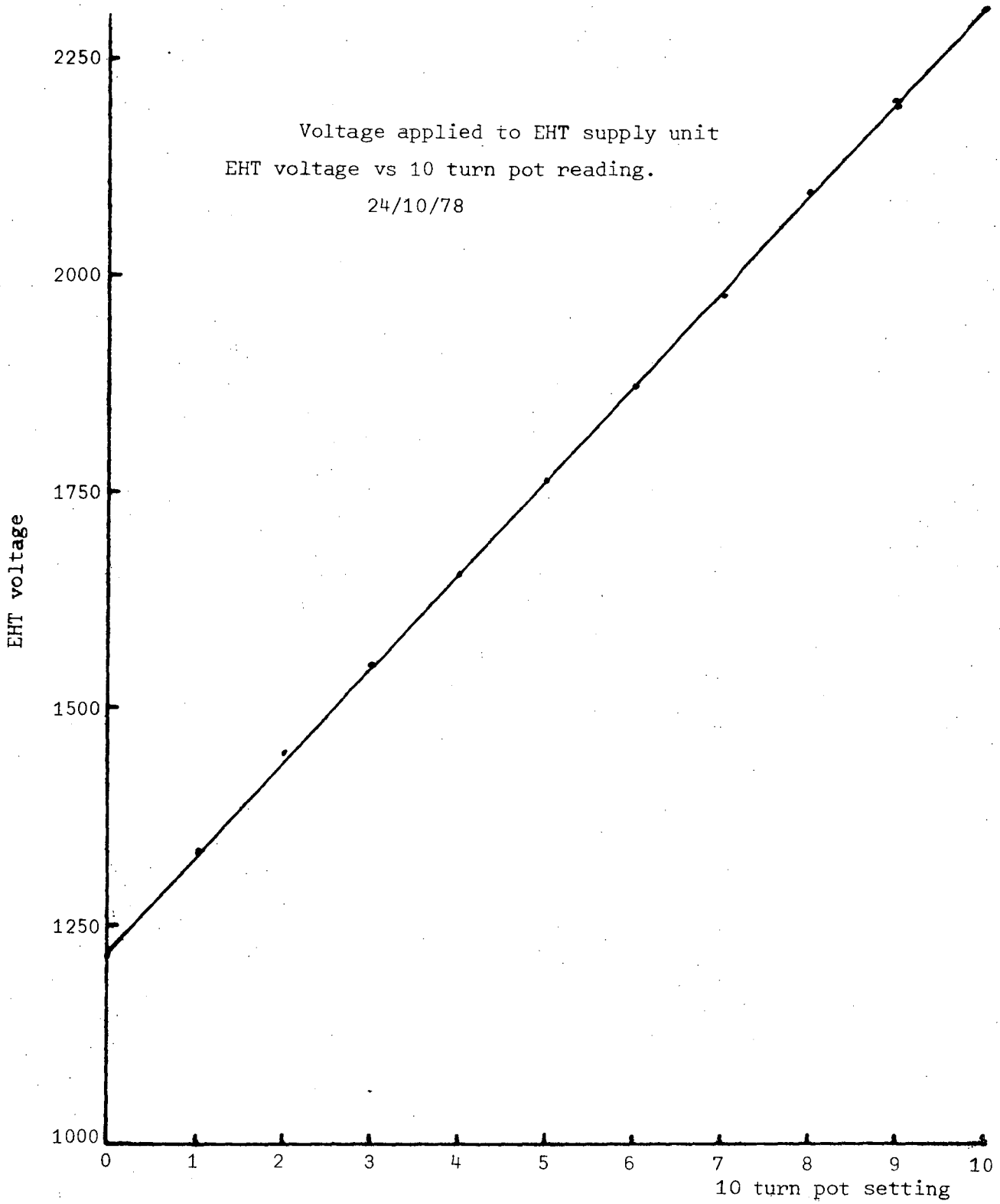
Voltage applied to EHT supply unit
EHT voltage vs 10 turn pot reading.
24/10/78
EHT voltage
2250
2000
1750
1500
1250
1000
0
1
2
3
4
5
6
7
8
9
10
10 turn pot setting

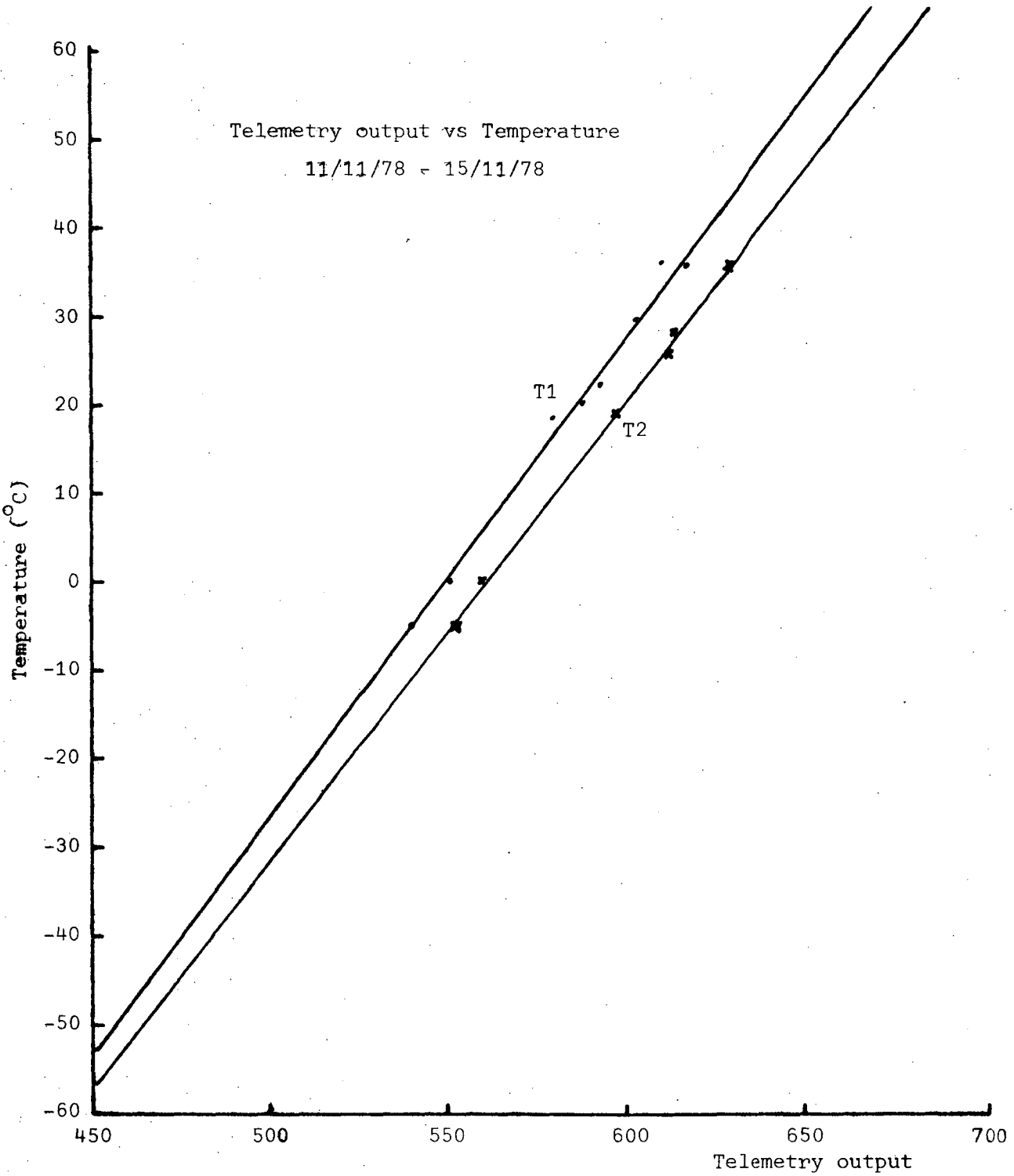
Telemetry output vs Temperature
11/11/78 - 15/11/78
T1
T2
Temperature (°C)
60
50
40
30
20
10
0
-10
-20
-30
-40
-50
-60
450
500
550
600
650
700
Telemetry output

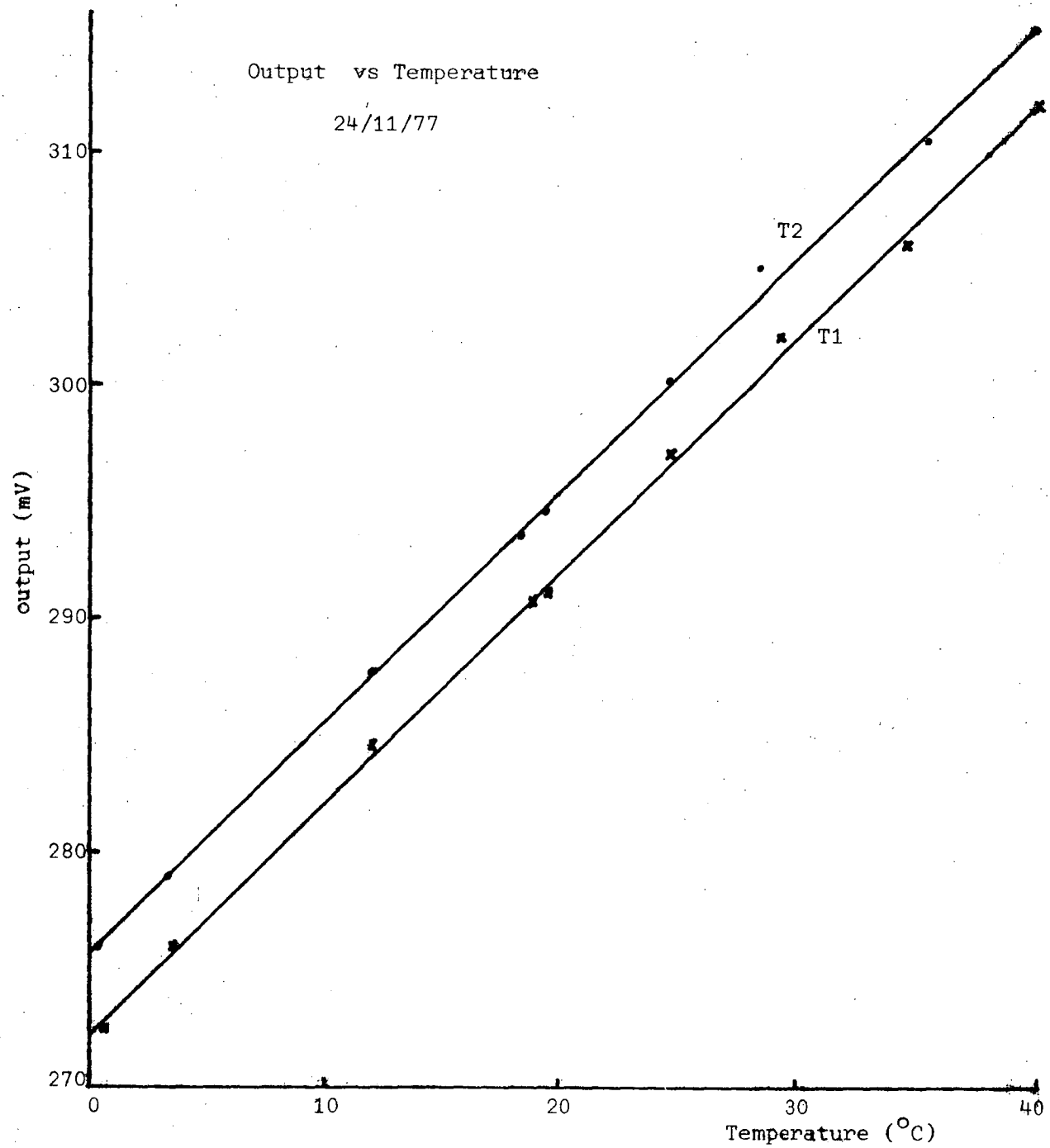
Output vs Temperature
24/11/77
T2
T1
output (mV)
310
300
290
280
270
0
10
20
30
40
Temperature (°C)

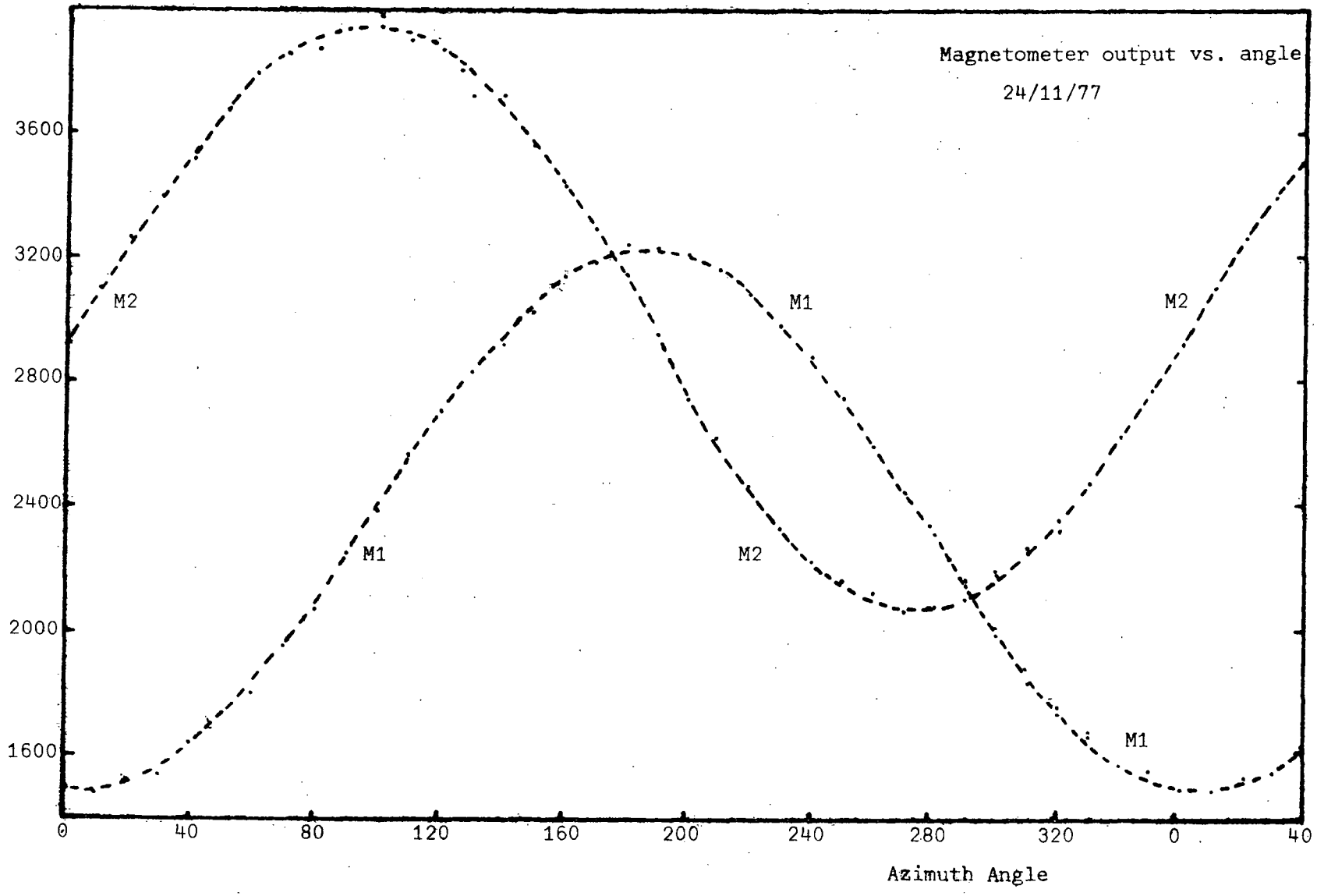
Magnetometer output vs. angle
24/11/77
3600
3200
2800
2400
2000
1600
M2
M1
M1
M2
M2
M1
0
40
80
120
160
200
240
280
320
0
40
Azimuth Angle

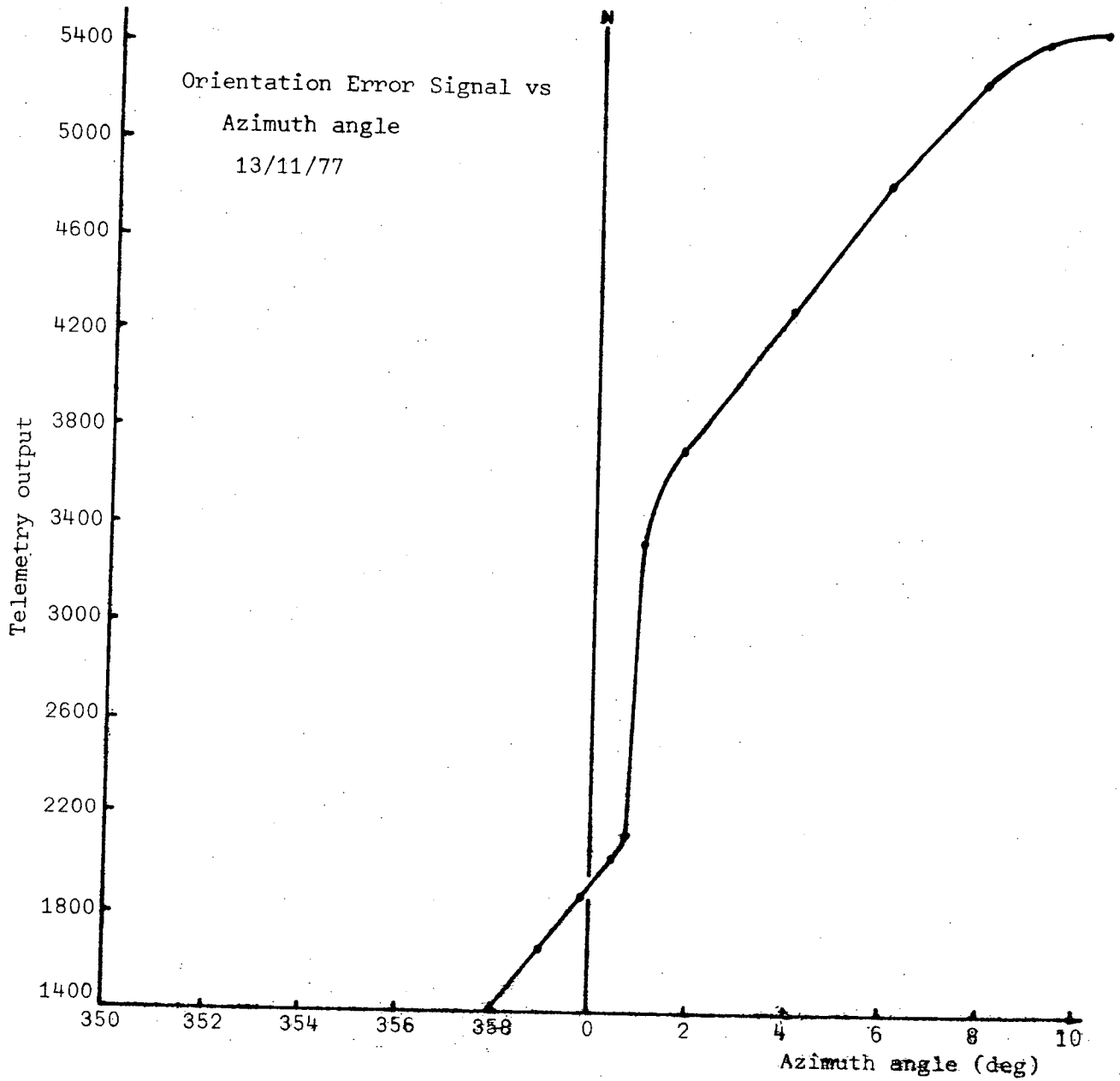
Orientation Error Signal vs
Azimuth angle
13/11/77
N
5400
5000
4600
4200
3800
3400
3000
2600
2200
1800
1400
Telemetry output
350
352
354
356
358
0
2
4
6
8
10
Azimuth angle (deg)

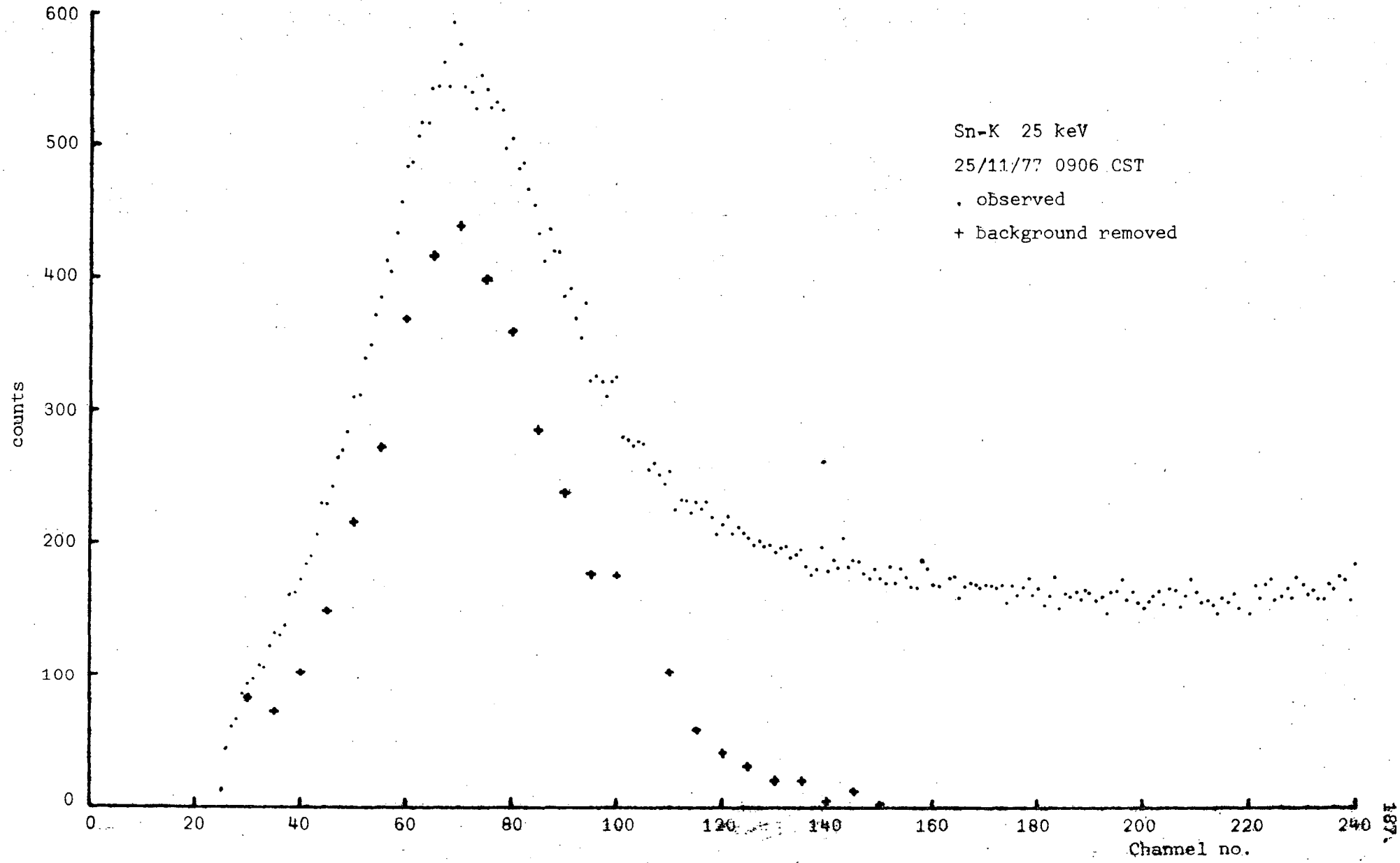
Sn-K 25 keV
25/11/77 0906 CST
. observed
+ background removed
counts
Channel no.
0
100
200
300
400
500
600
0
20
40
60
80
100
120
140
160
180
200
220
240

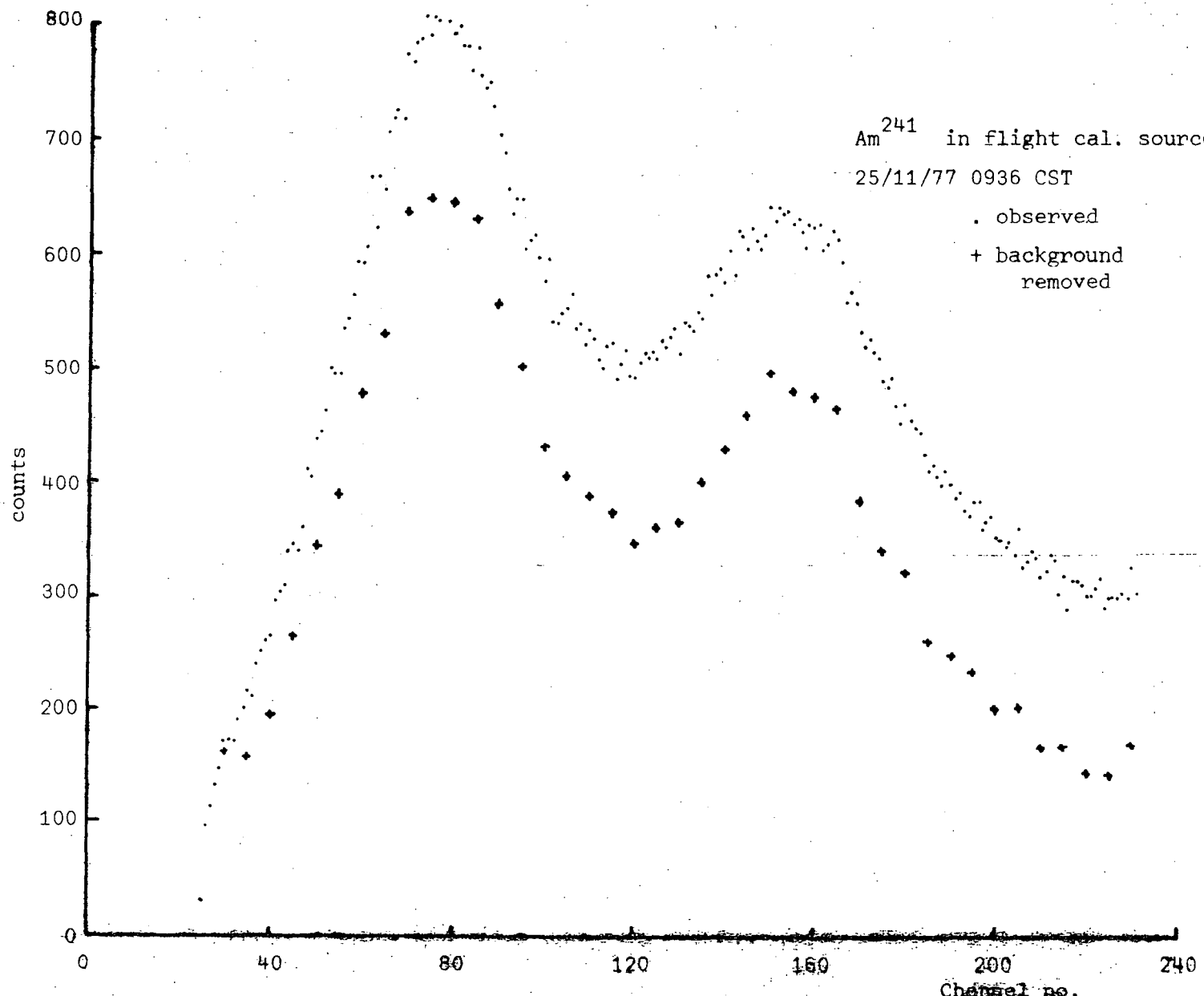
800
700
600
500
400
300
200
100
0
counts
0
40
80
120
160
200
240
Channel no.
Am241 in flight cal. source
25/11/77 0936 CST
. observed
+ background removed

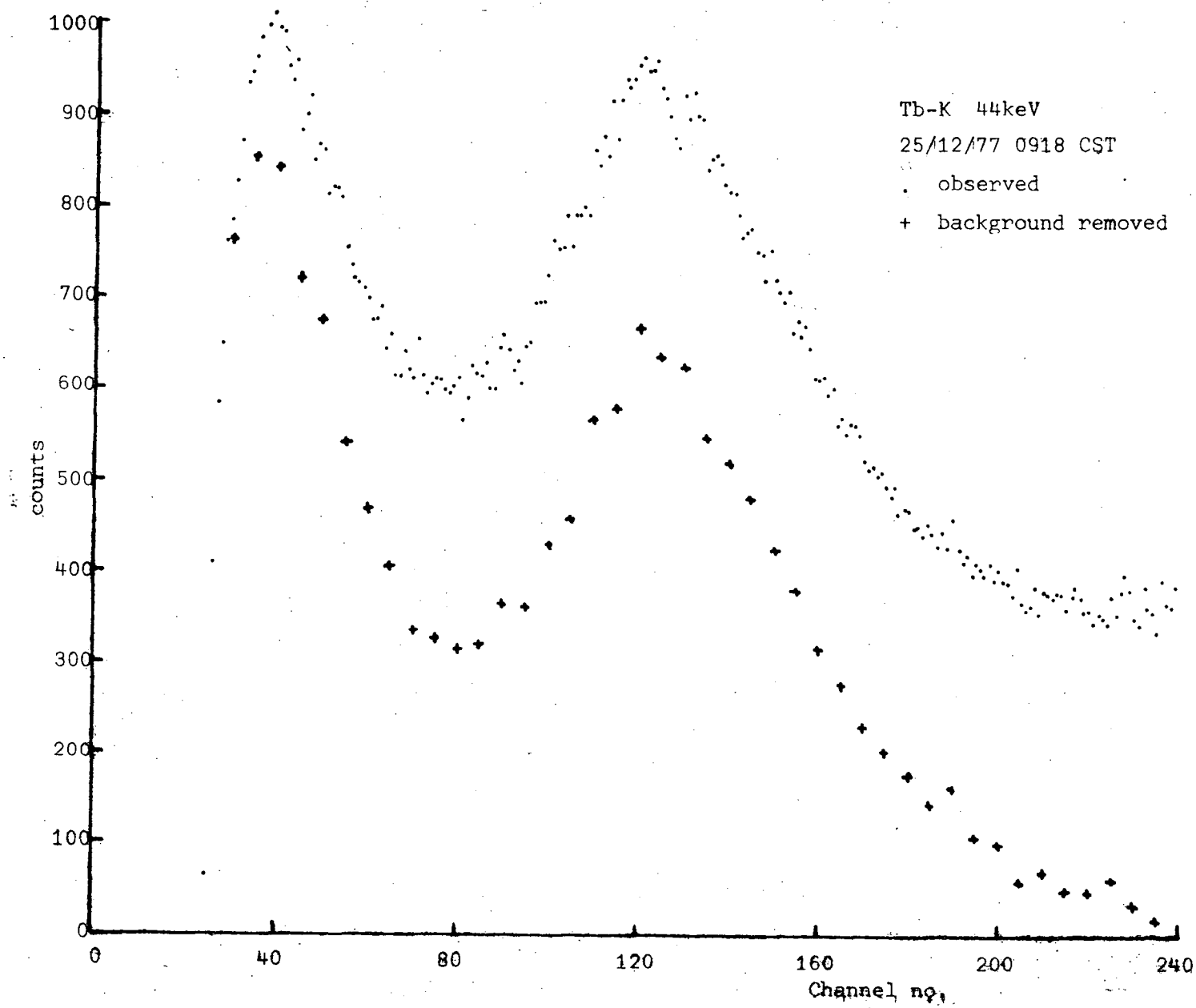
Tb-K 44keV
25/12/77 0918 CST
. observed
+ background removed
counts
Channel no.
0
100
200
300
400
500
600
700
800
900
1000
0
40
80
120
160
200
240

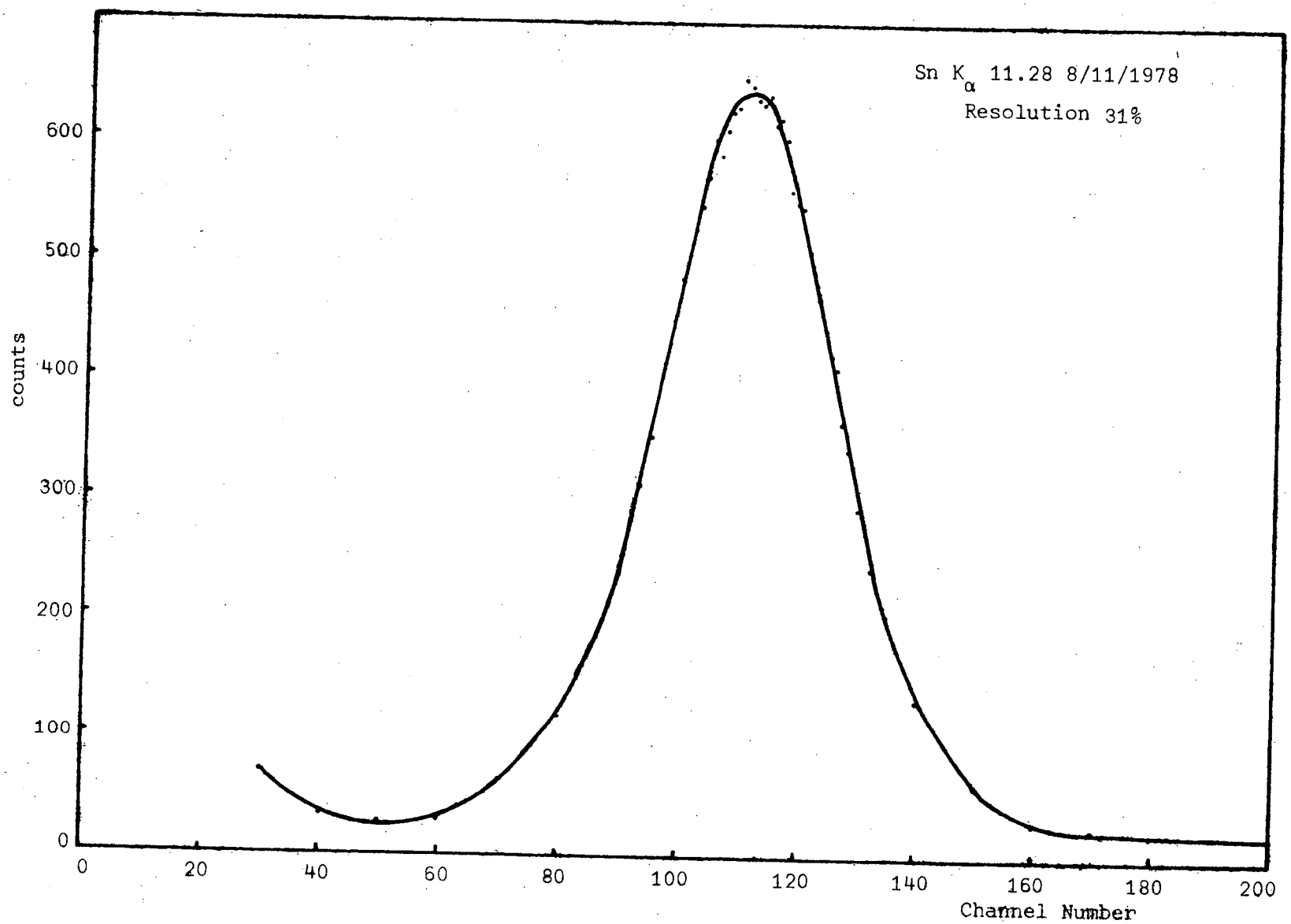
Sn K_α 11.28 8/11/1978
Resolution 31%
counts
0
100
200
300
400
500
600
0
20
40
60
80
100
120
140
160
180
200
Channel Number

APPENDIX C

TABLES OF APODIZATION RESULTS

AND

SPECTRAL FIT PLOTS

APODIZATION

("Best" Fit Counter Parameters)

FIRST SCAN	POWER SCAN	BLACK BODY	THERMAL	THERMAL & GAUNT
COMBINED				
χ^2	2.70	5.15	4.02	3.86
A	2.0×10^{-4}	2.6×10^{-3}	5.84	6.78
kT or α	5.03	3.80	6.75	7.52
HIGH				
χ^2	1.23	3.76	2.57	2.41
A	2.8×10^{-4}	2.1×10^{-3}	5.35	6.03
kT or α	4.82	4.06	7.47	3.40
LOW				
χ^2	7.47	10.13	9.29	9.15
A	9.8×10^{-5}	2.0×10^{-2}	17.15	20.66
kT or α	6.0	2.80	4.79	5.29
SECOND SCAN				
COMBINED				
χ^2	2.81	5.04	3.82	3.68
A	1.9×10^{-4}	1.5×10^{-3}	3.65	4.12
kT or α	4.70	4.04	7.40	8.32
HIGH				
χ^2	2.25	3.90	2.95	2.84
A	2.1×10^{-4}	1.4×10^{-3}	3.68	4.12
kT or α	4.63	4.10	7.56	8.52
LOW				
χ^2	1.02	1.58	1.33	1.29
A	1.1×10^{-4}	2.1×10^{-3}	4.07	4.76
kT or α	5.17	3.64	6.42	7.14

APODIZATION

("Calibration" Fit Counter Parameters)

FIRST SCAN	POWER LAW	BLACK BODY	THERMAL	THERMAL & GAUNT
COMBINED				
χ^2	2.73	5.20	4.06	3.55
A	5.4×10^{-4}	7.6×10^{-3}	16.86	18.81
kT or α	5.07	3.78	6.68	10.36
HIGH				
χ^2	1.14	3.68	2.49	2.03
A	7.6×10^{-4}	5.9×10^{-3}	15.25	12.77
kT or α	4.85	4.06	7.43	12.41
LOW				
χ^2	2.42	3.27	2.86	3.06
A	4.6×10^{-4}	8.0×10^{-3}	17.38	8.51
kT or α	5.16	3.70	6.42	12.79
SECOND SCAN				
COMBINED				
χ^2	2.37	4.60	3.25	2.76
A	6.0×10^{-4}	3.4×10^{-3}	9.03	7.86
kT or α	4.53	4.20	7.83	13.09
HIGH				
χ^2	2.04	3.45	2.61	2.26
A	6.6×10^{-4}	3.3×10^{-3}	9.03	7.58
kT or α	4.46	4.27	8.03	13.59
LOW				
χ^2	0.77	1.36	1.09	0.96
A	3.4×10^{-4}	5.5×10^{-3}	10.89	11.62
kT or α	5.02	3.70	6.61	10.39

"BEST" FIT COUNTER PARAMETER

SPECTRAL PLOTS

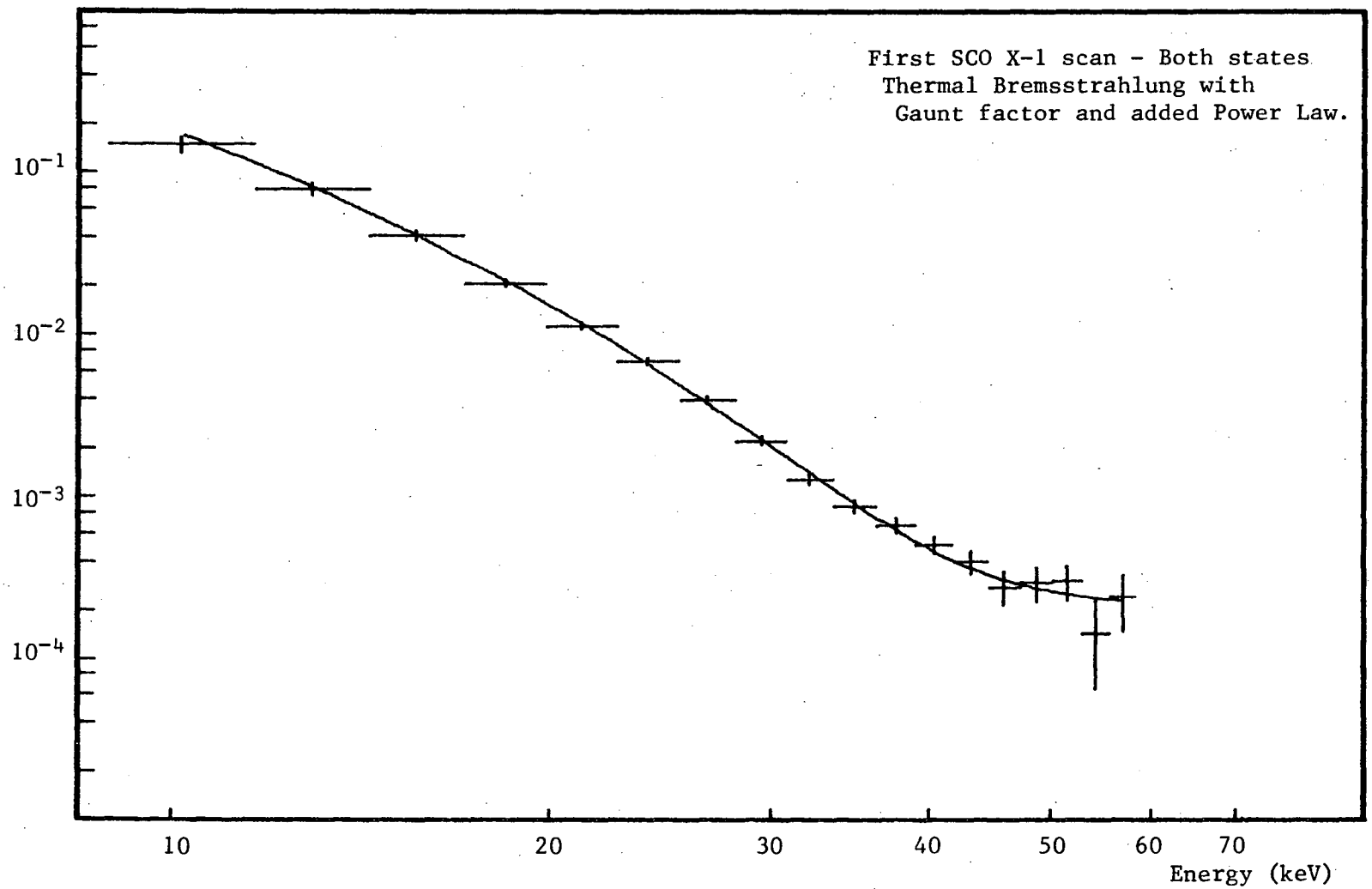
First SCO X-1 scan - Both states
Thermal Bremsstrahlung with
Gaunt factor and added Power Law.
10^{-1}
10^{-2}
10^{-3}
10^{-4}
10
20
30
40
50
60
70
Energy (keV)

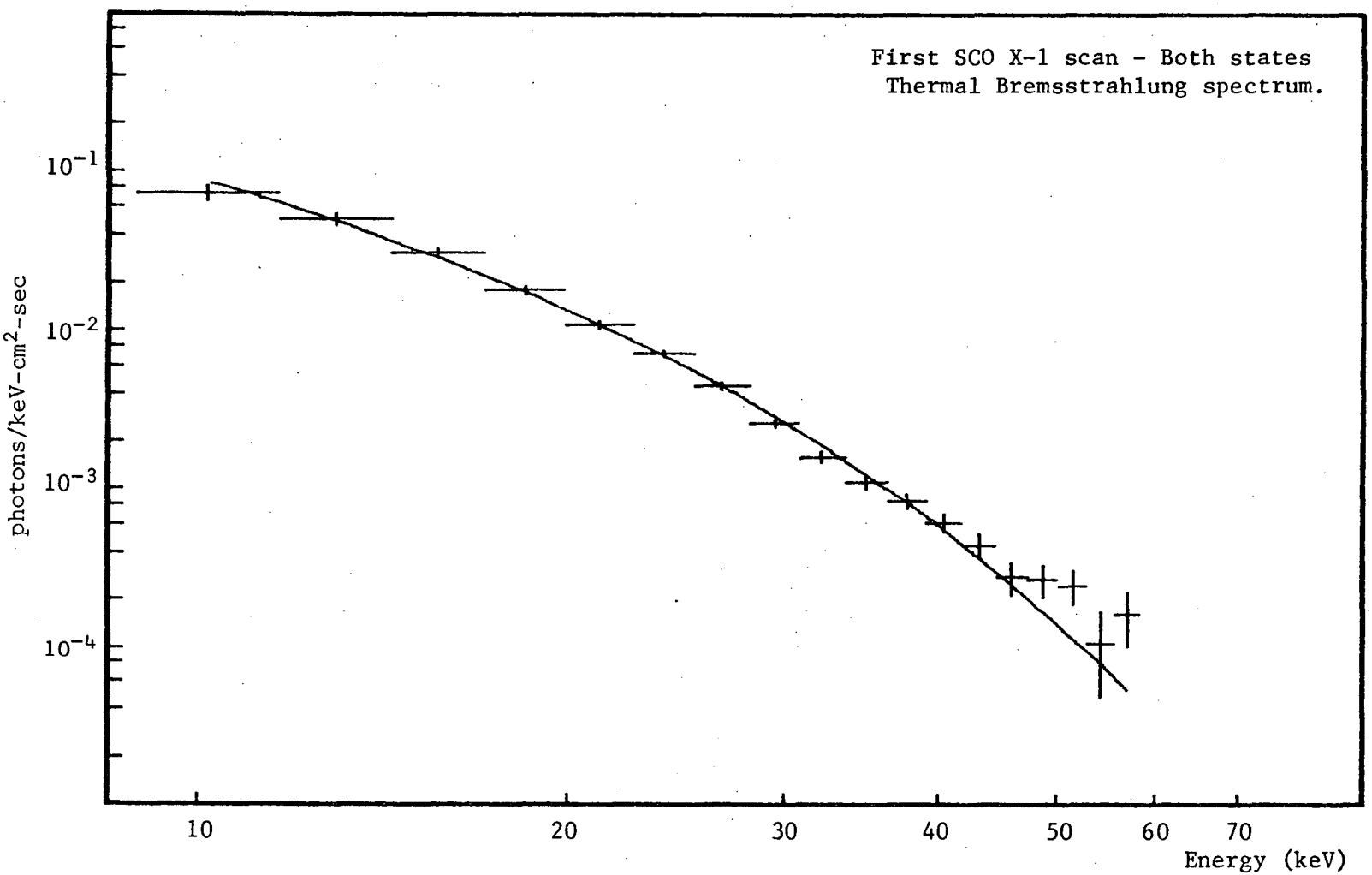
First SCO X-1 scan - Both states
Thermal Bremsstrahlung spectrum.
photons/keV-cm^2-sec
10^{-1}
10^{-2}
10^{-3}
10^{-4}
10
20
30
40
50
60
70
Energy (keV)

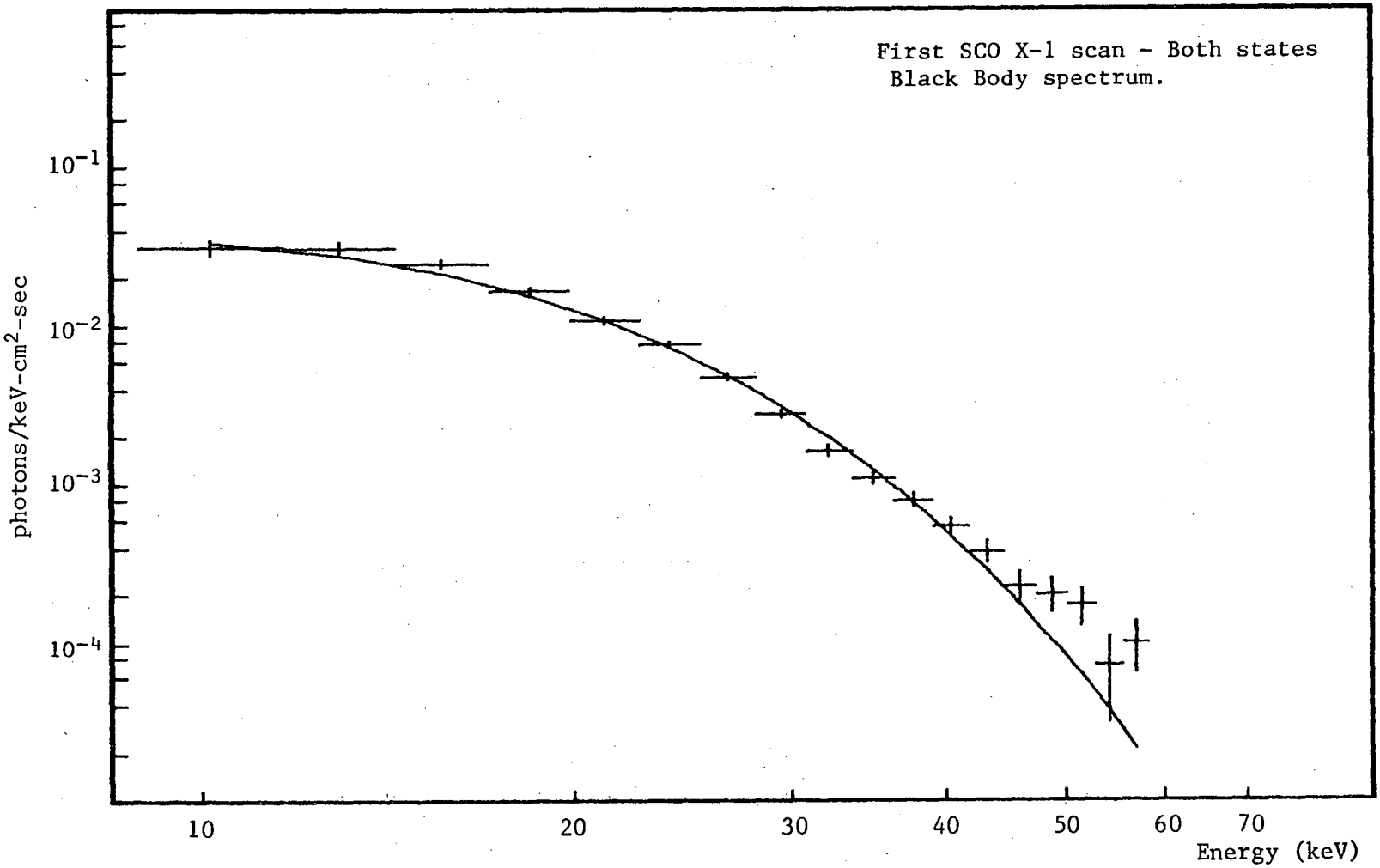
First SCO X-1 scan - Both states
Black Body spectrum.
photons/keV-cm^2-sec
10^{-1}
10^{-2}
10^{-3}
10^{-4}
10
20
30
40
50
60
70
Energy (keV)

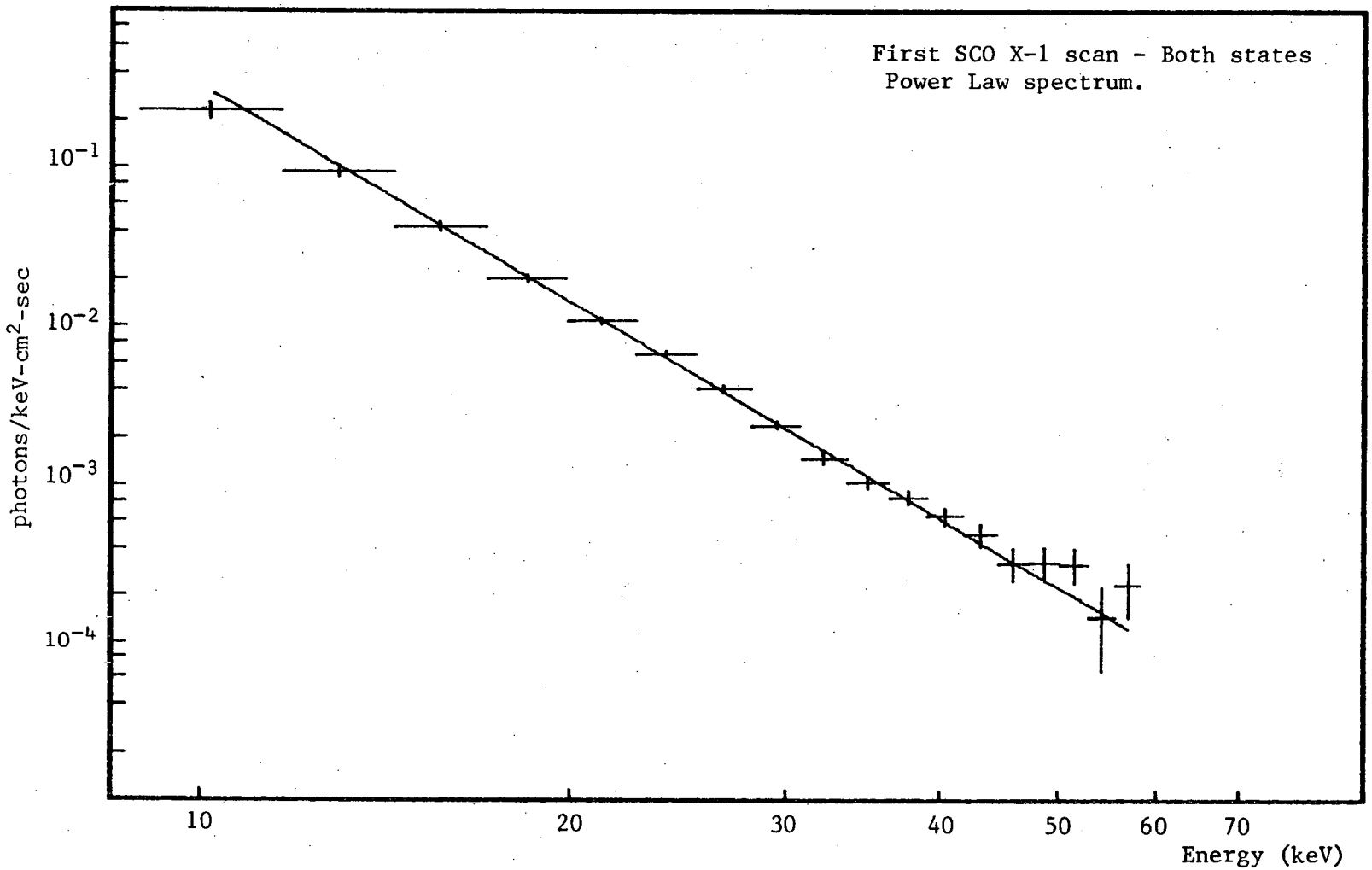
First SCO X-1 scan - Both states
Power Law spectrum.
photons/keV-cm^2-sec
10^{-1}
10^{-2}
10^{-3}
10^{-4}
10
20
30
40
50
60
70
Energy (keV)

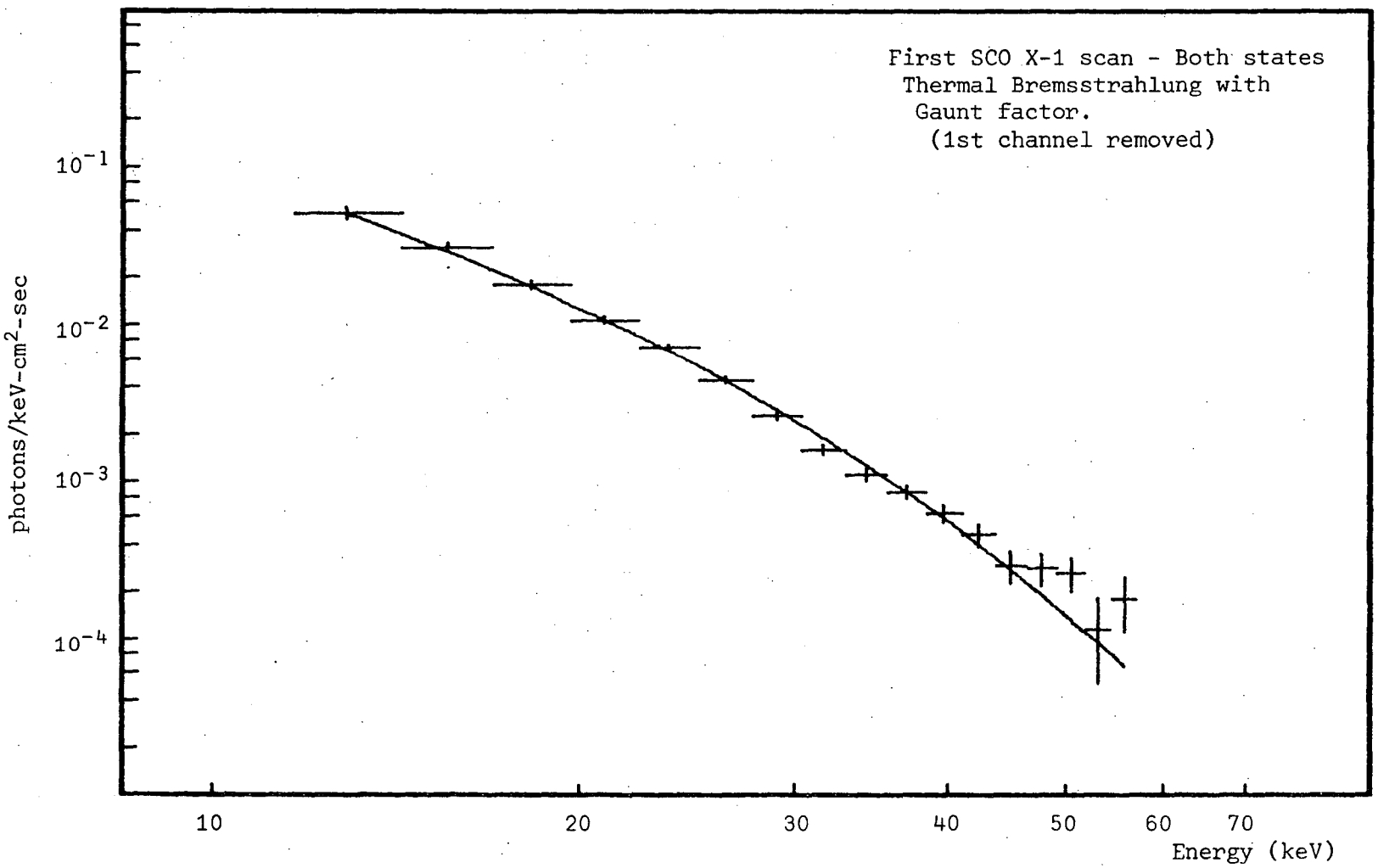
First SCO X-1 scan - Both states
Thermal Bremsstrahlung with
Gaunt factor.
(1st channel removed)
photons/keV-cm^2-sec
10^{-1}
10^{-2}
10^{-3}
10^{-4}
10
20
30
40
50
60
70
Energy (keV)

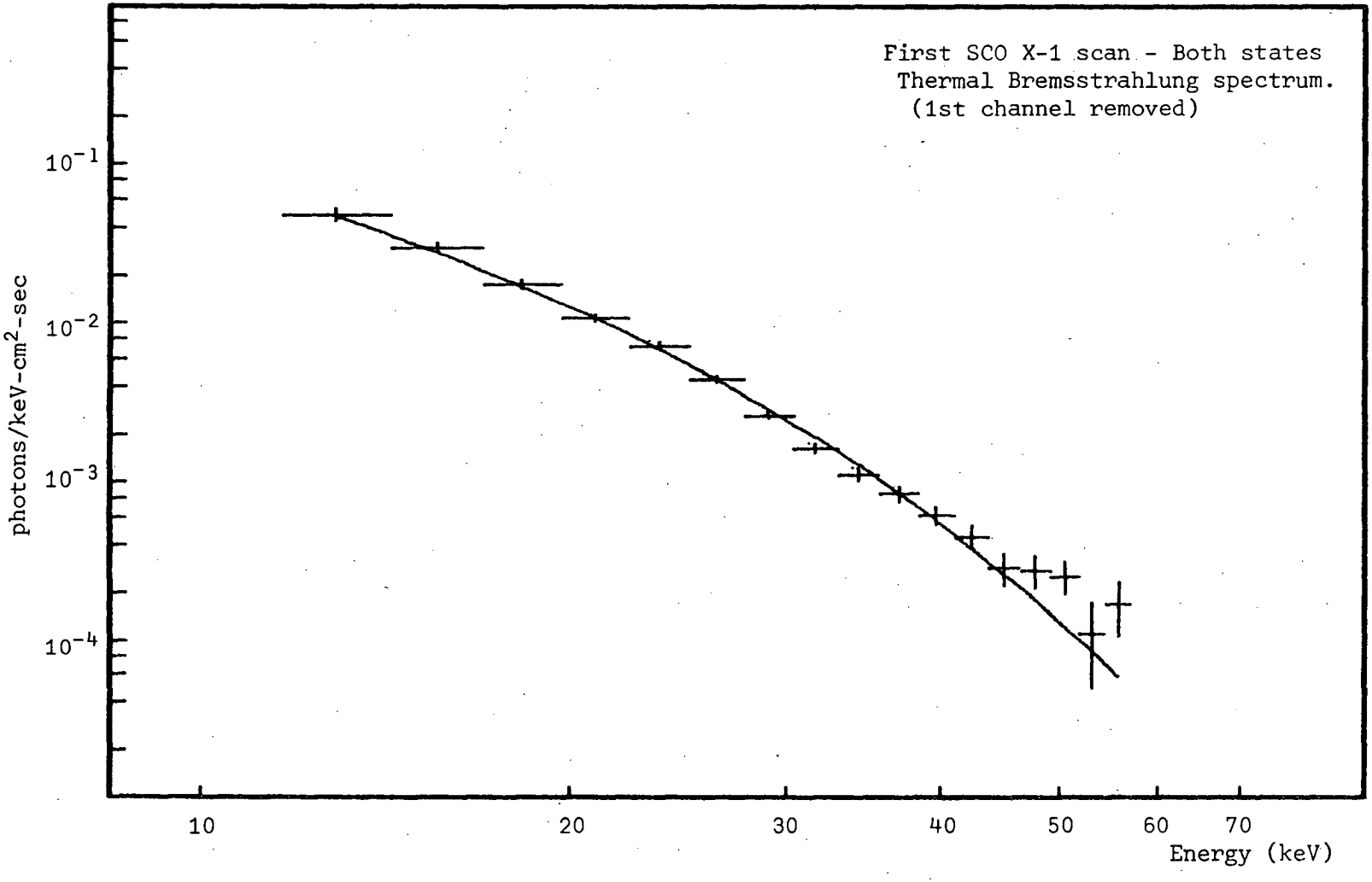
First SCO X-1 scan - Both states
Thermal Bremsstrahlung spectrum.
(1st channel removed)
photons/keV-cm^2-sec
10^{-1}
10^{-2}
10^{-3}
10^{-4}
10
20
30
40
50
60
70
Energy (keV)

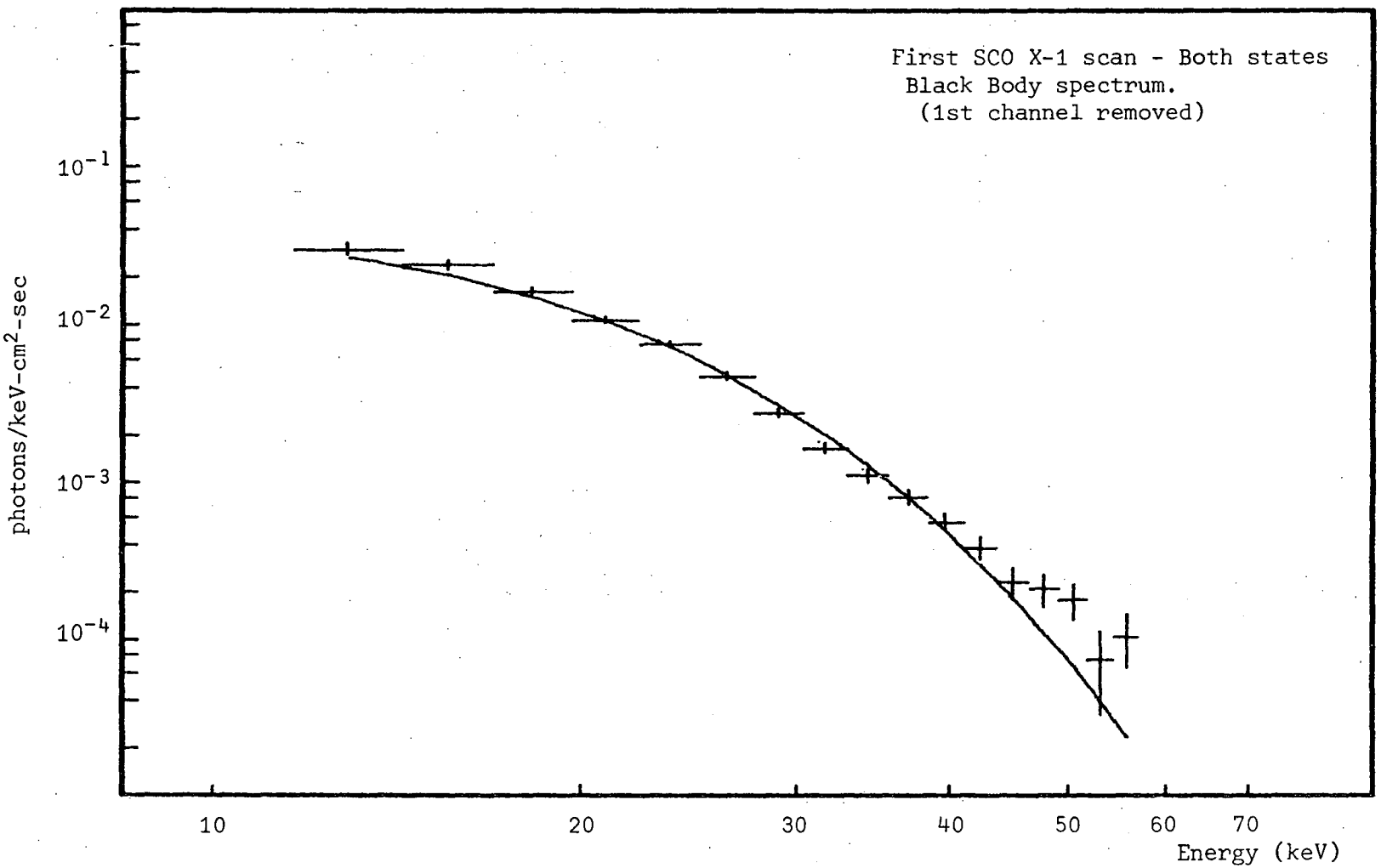
First SCO X-1 scan - Both states
Black Body spectrum.
(1st channel removed)
photons/keV-cm^2-sec
10^{-1}
10^{-2}
10^{-3}
10^{-4}
10
20
30
40
50
60
70
Energy (keV)

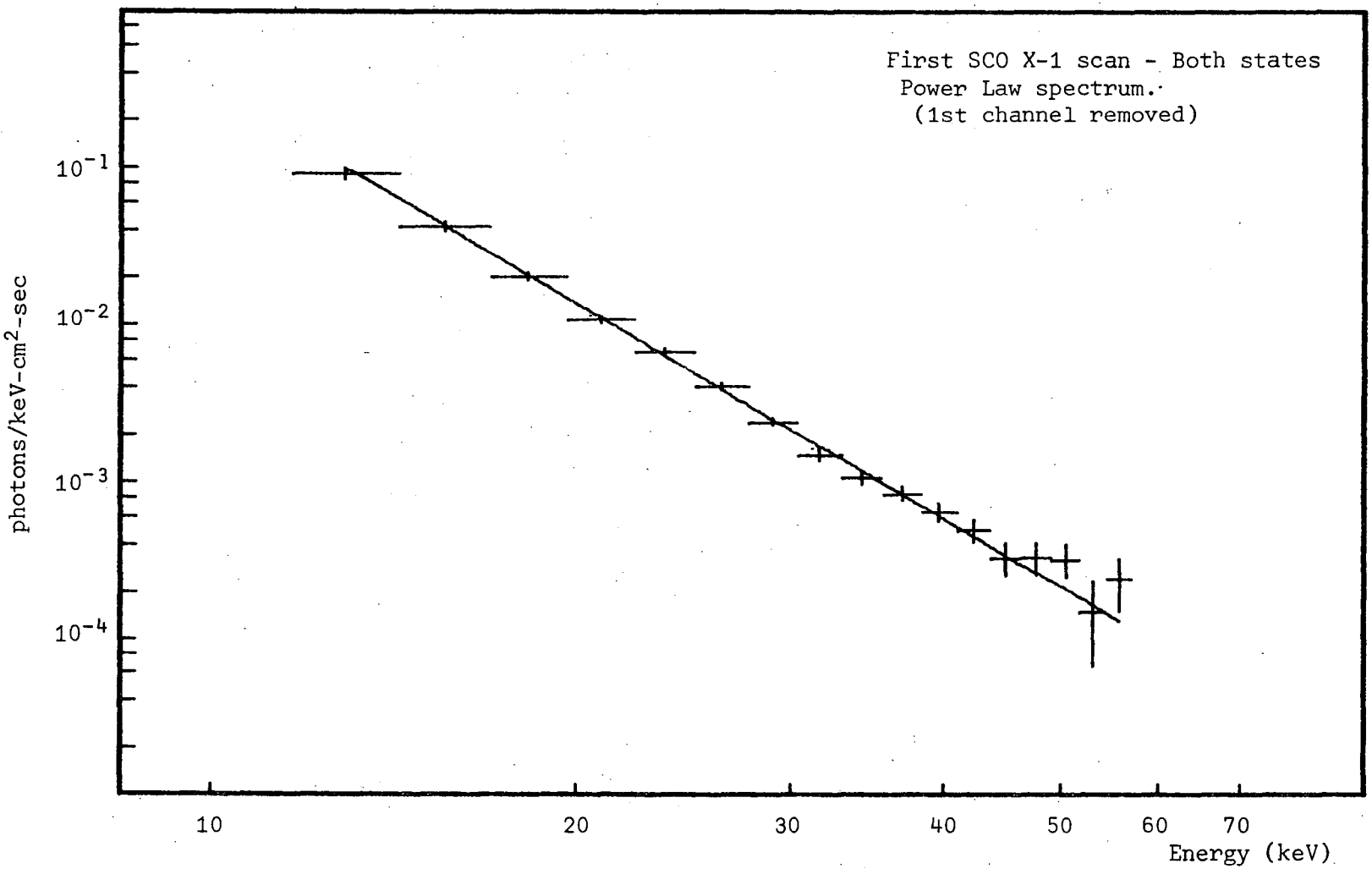
First SCO X-1 scan - Both states
Power Law spectrum.
(1st channel removed)
photons/keV-cm^2-sec
10^{-1}
10^{-2}
10^{-3}
10^{-4}
10
20
30
40
50
60
70
Energy (keV)

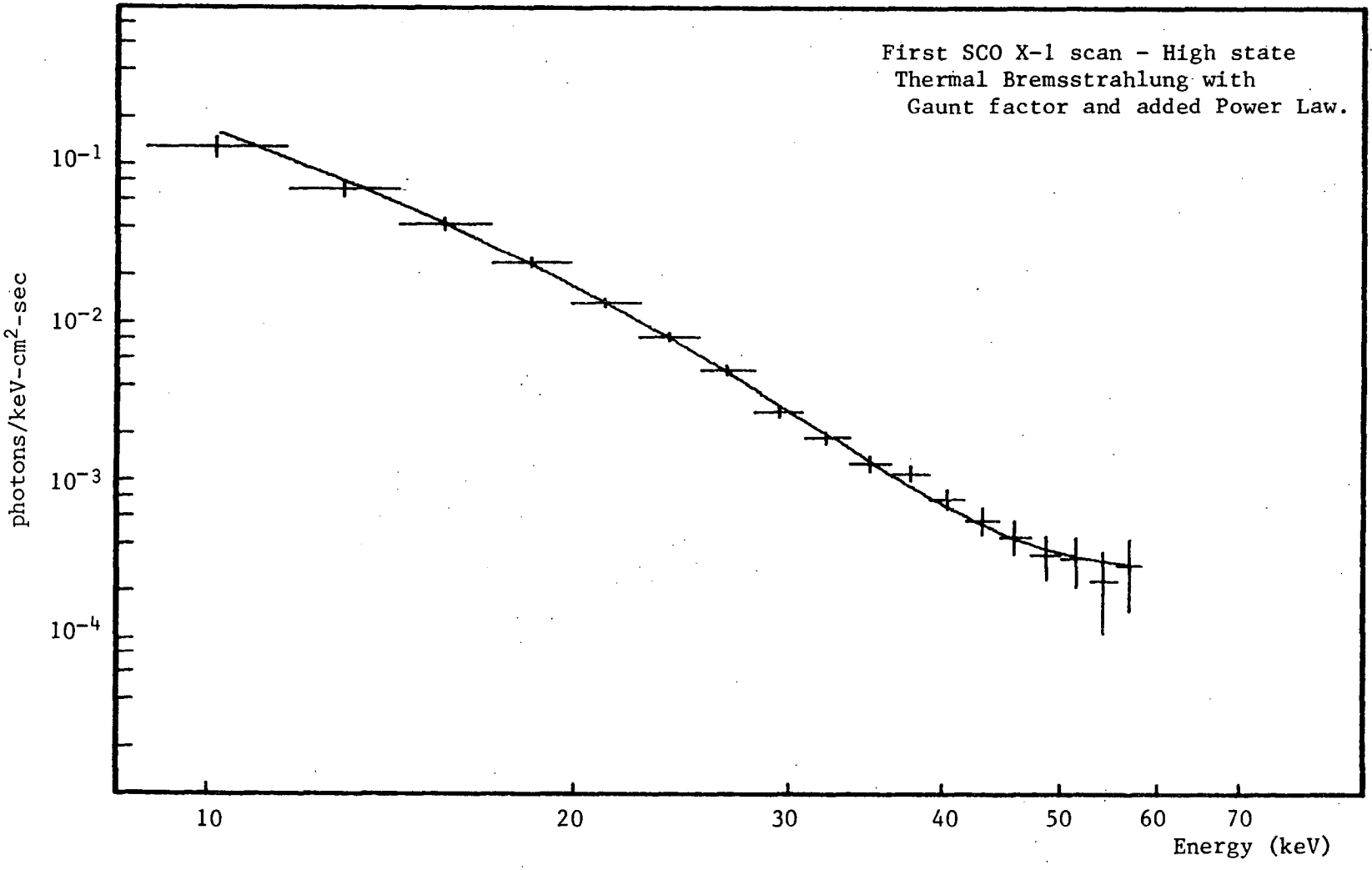
First SCO X-1 scan - High state
Thermal Bremsstrahlung with
Gaunt factor and added Power Law.
photons/keV-cm^2-sec
10^{-1}
10^{-2}
10^{-3}
10^{-4}
10
20
30
40
50
60
70
Energy (keV)

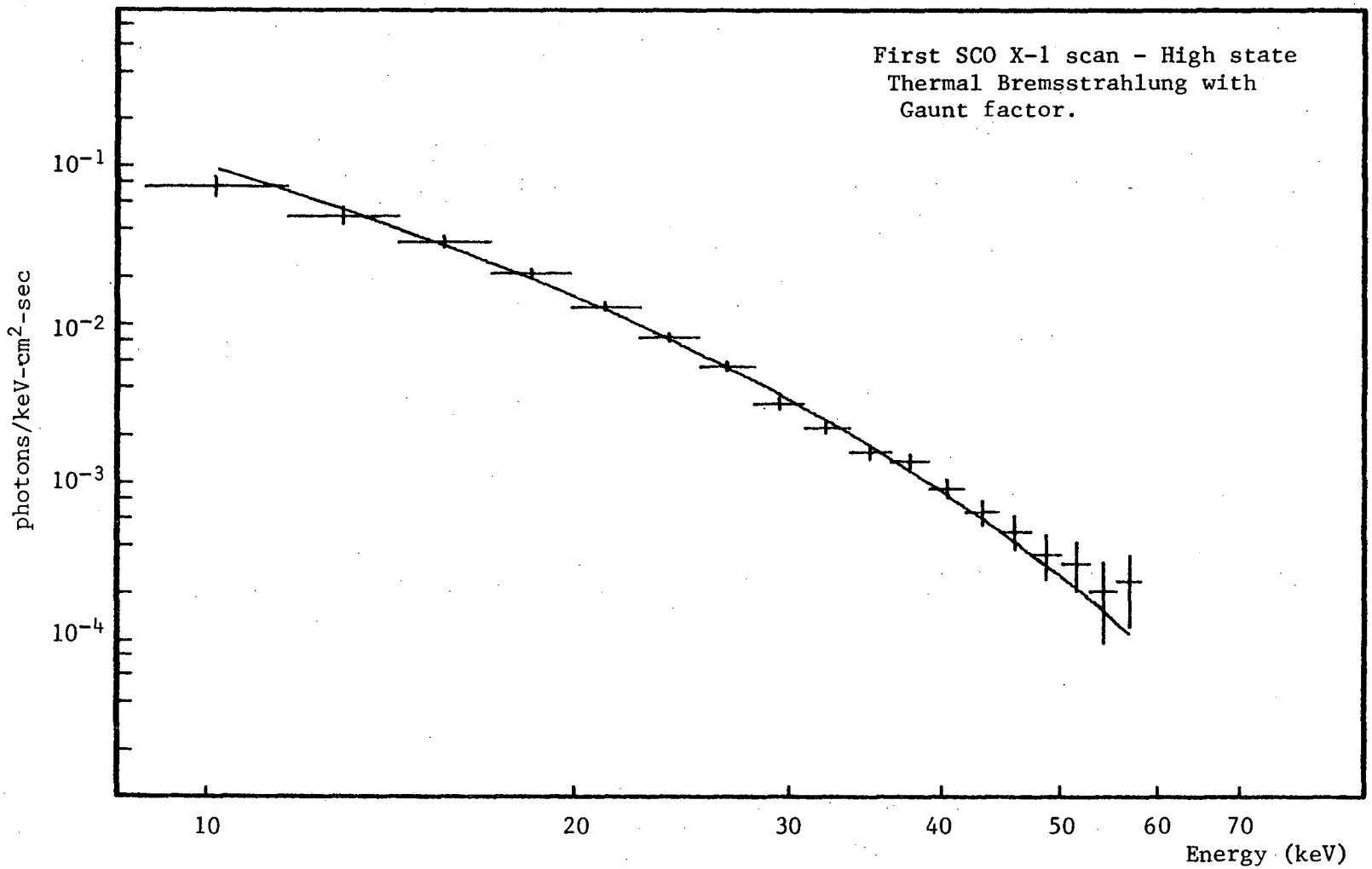
First SCO X-1 scan - High state
Thermal Bremsstrahlung with
Gaunt factor.
photons/keV-cm^2-sec
10^{-1}
10^{-2}
10^{-3}
10^{-4}
10
20
30
40
50
60
70
Energy (keV)

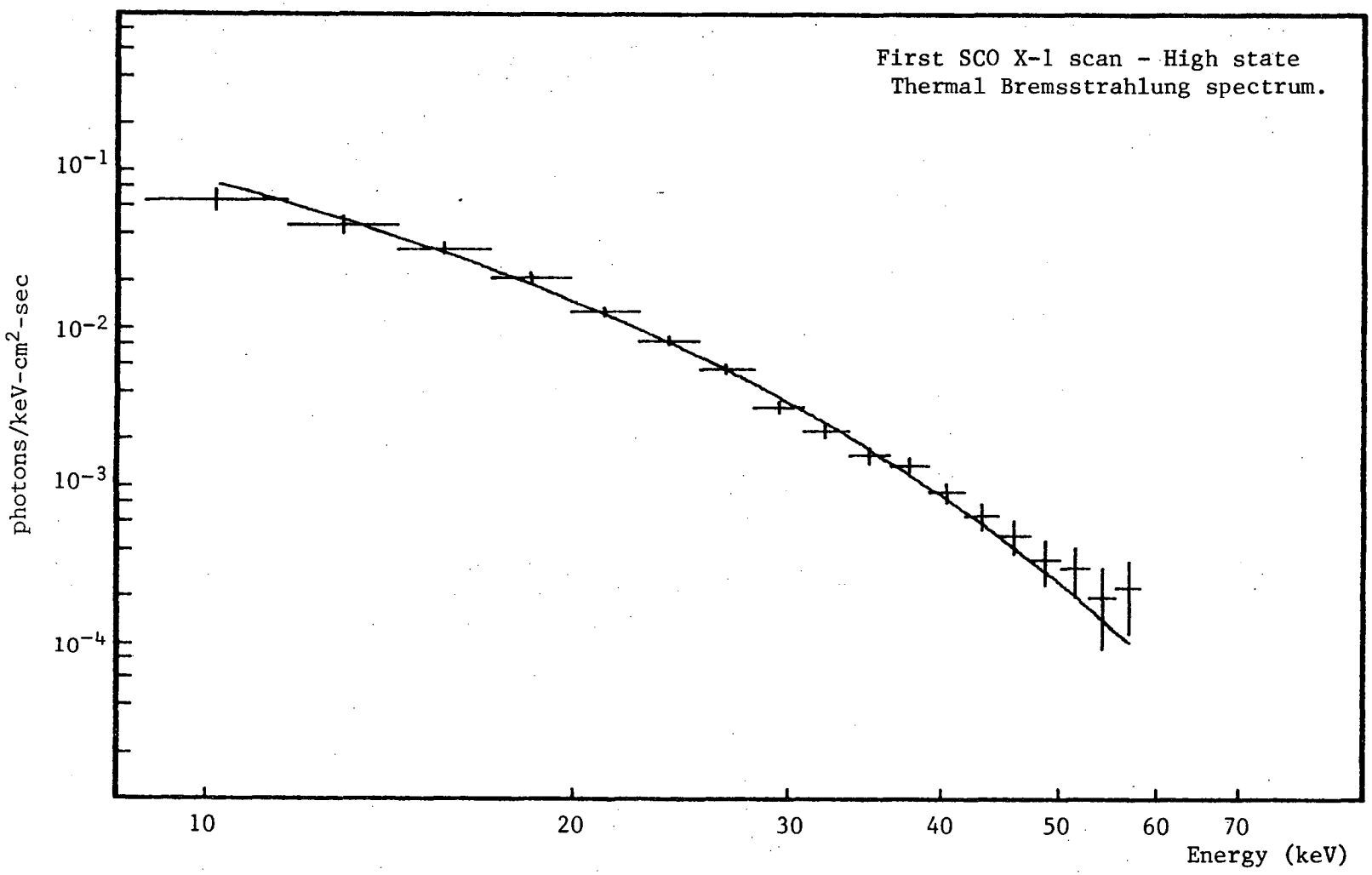
First SCO X-1 scan - High state
Thermal Bremsstrahlung spectrum.
photons/keV-cm^2-sec
10^{-1}
10^{-2}
10^{-3}
10^{-4}
10
20
30
40
50
60
70
Energy (keV)

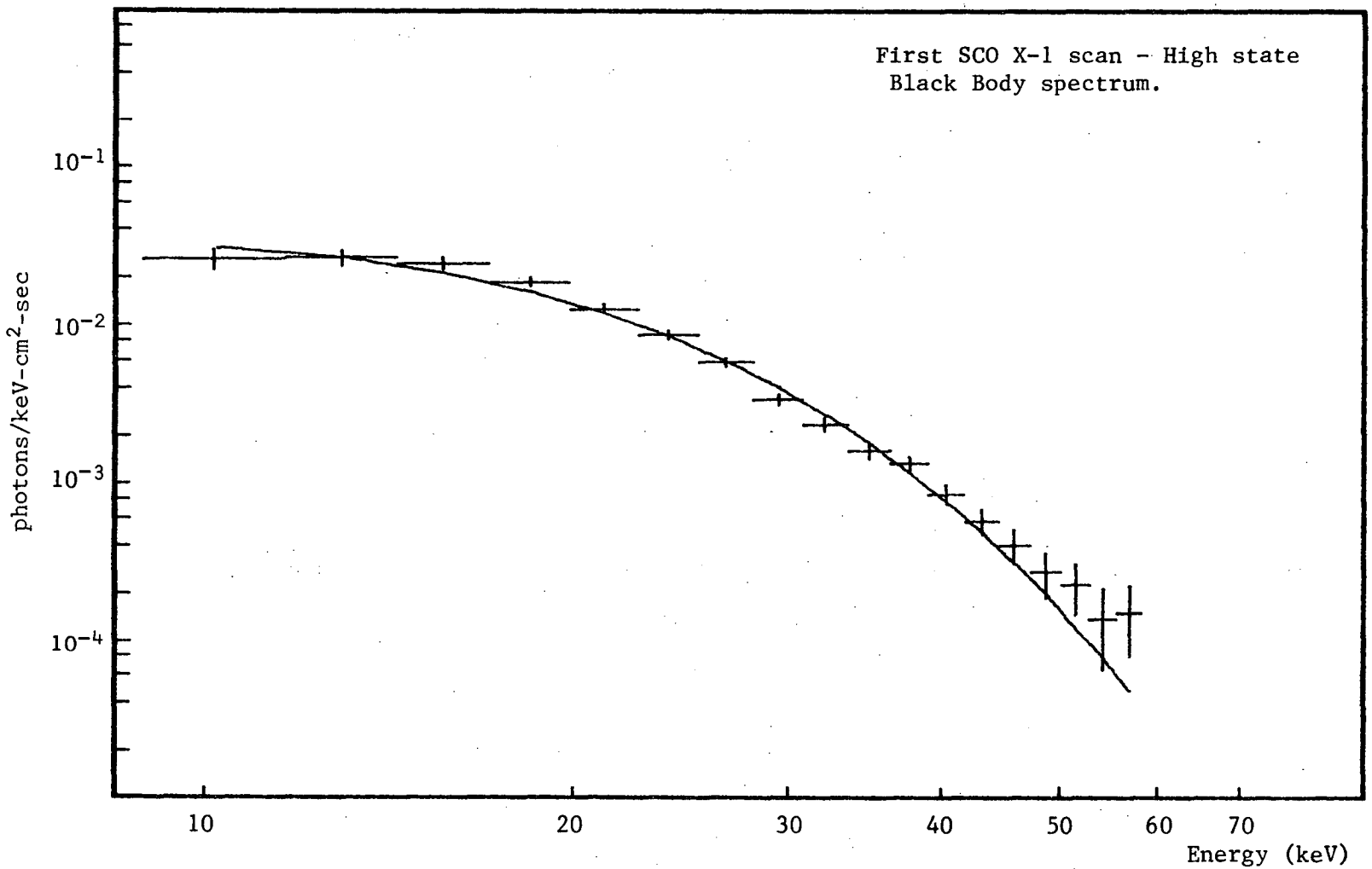
First SCO X-1 scan - High state
Black Body spectrum.
photons/keV-cm^2-sec
10^{-1}
10^{-2}
10^{-3}
10^{-4}
10
20
30
40
50
60
70
Energy (keV)

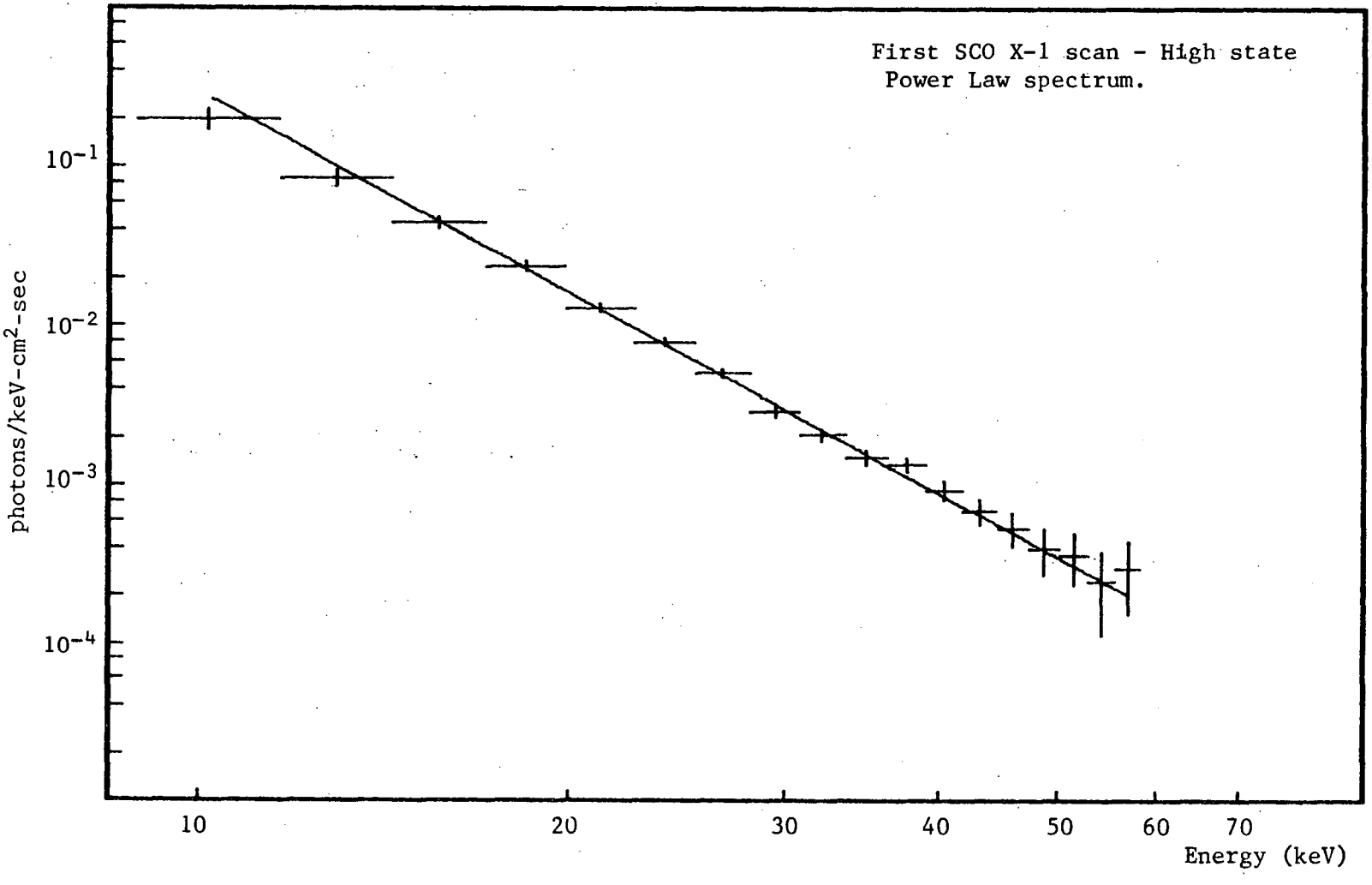
First SCO X-1 scan - High state
Power Law spectrum.
photons/keV-cm^2-sec
10^{-1}
10^{-2}
10^{-3}
10^{-4}
10
20
30
40
50
60
70
Energy (keV)

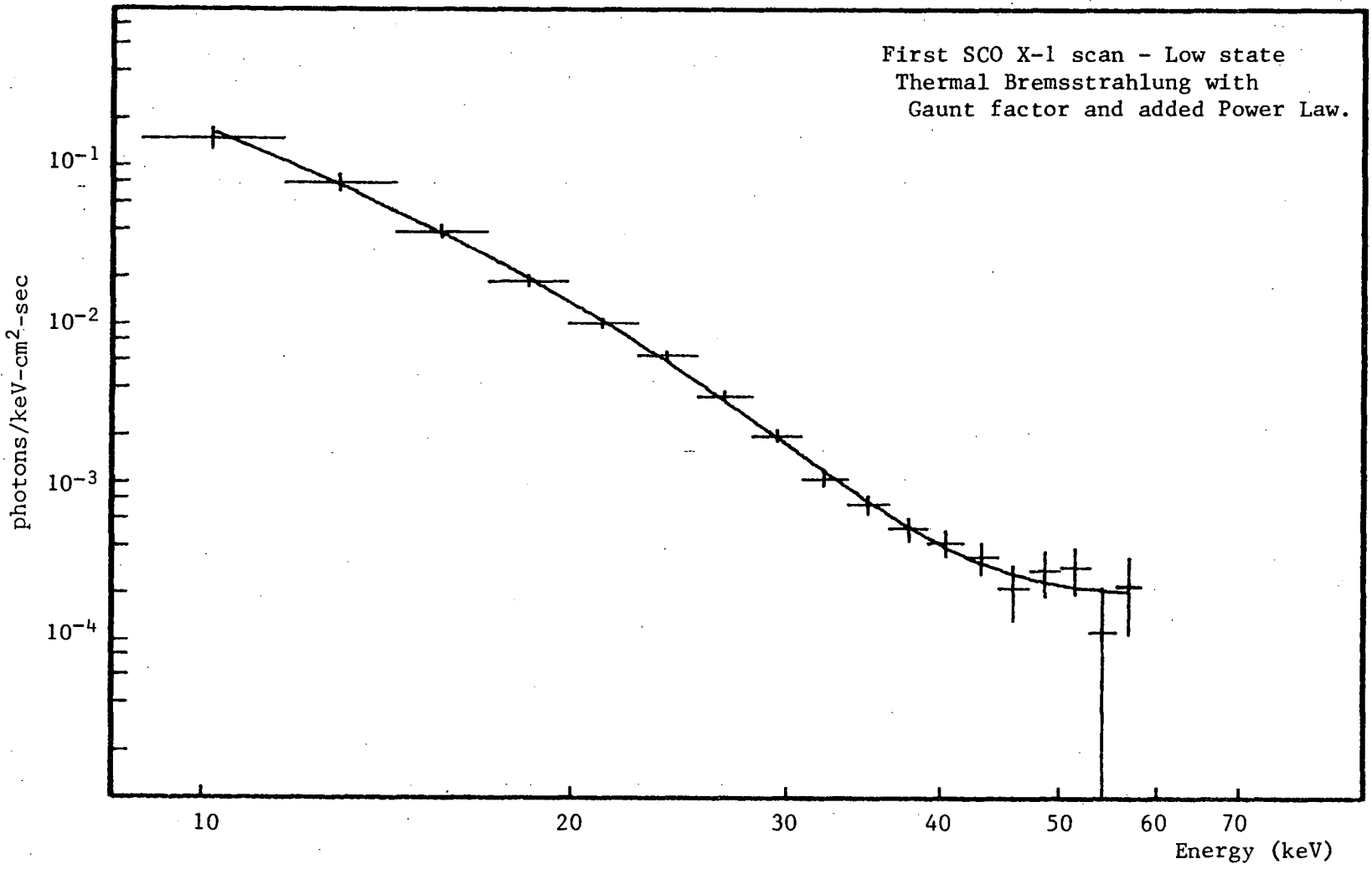
First SCO X-1 scan - Low state
Thermal Bremsstrahlung with
Gaunt factor and added Power Law.
photons/keV-cm^2-sec
10^{-1}
10^{-2}
10^{-3}
10^{-4}
10
20
30
40
50
60
70
Energy (keV)

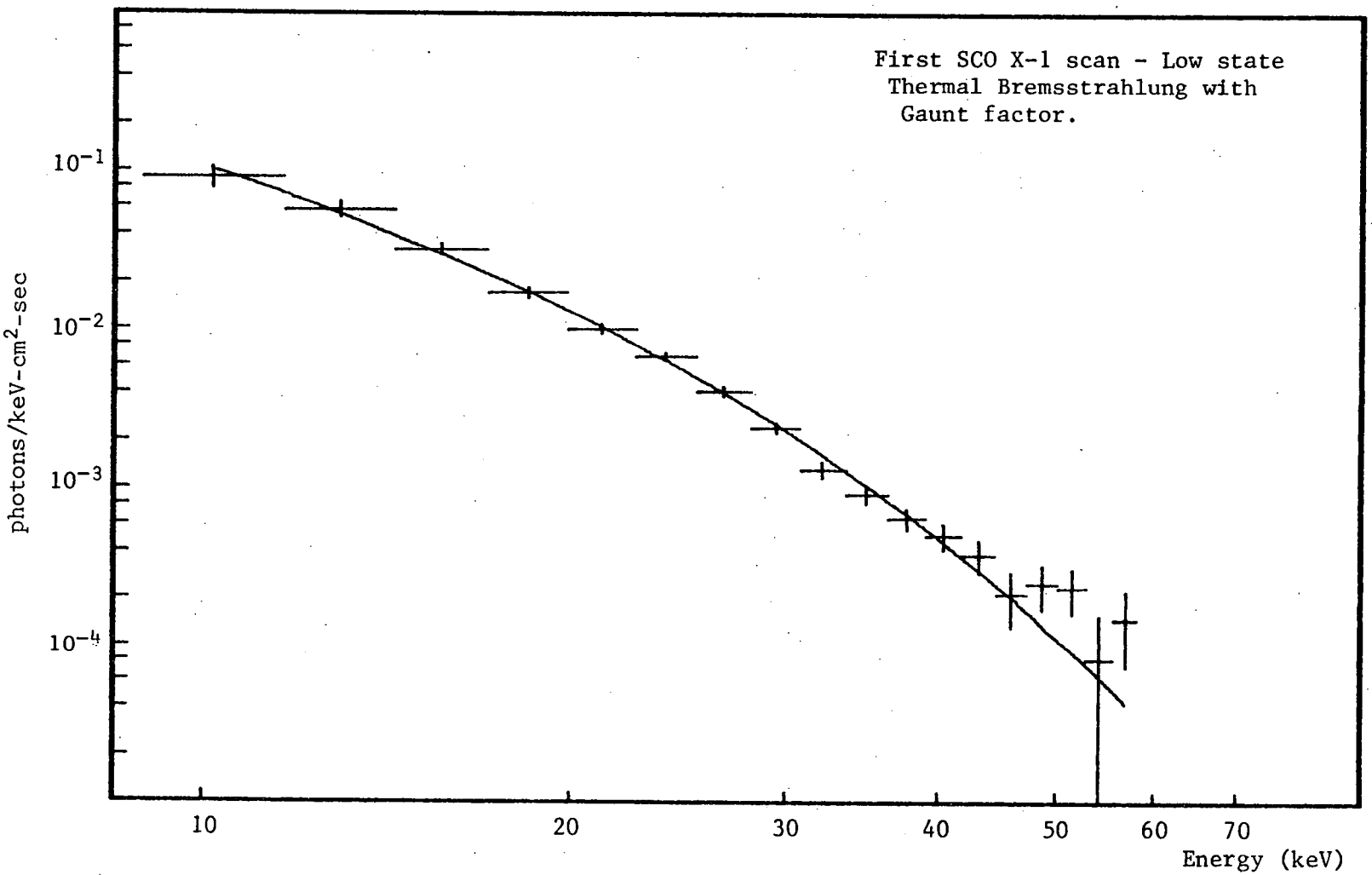
First SCO X-1 scan - Low state
Thermal Bremsstrahlung with
Gaunt factor.
photons/keV-cm^2-sec
10^{-1}
10^{-2}
10^{-3}
10^{-4}
10
20
30
40
50
60
70
Energy (keV)

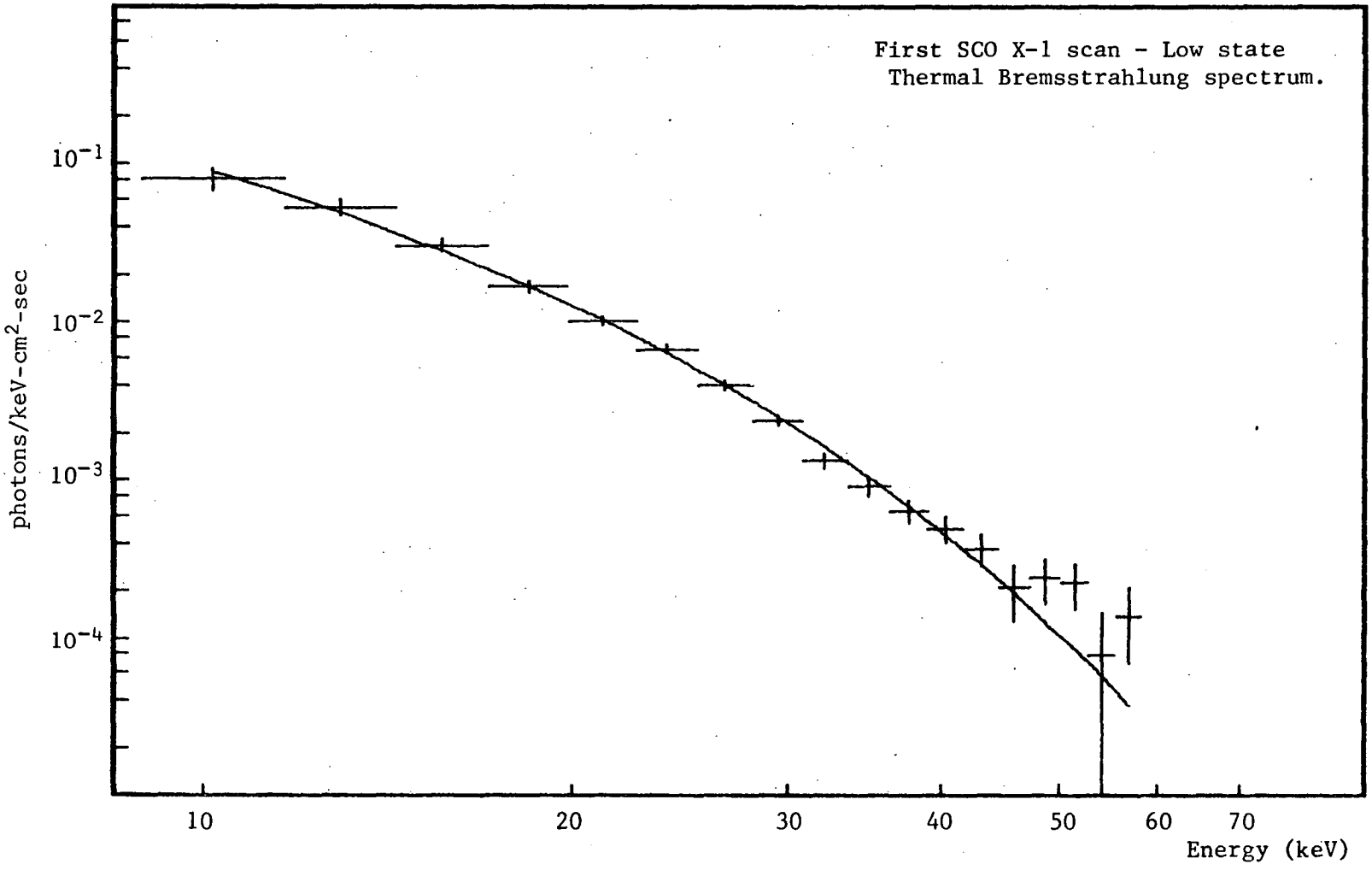
First SCO X-1 scan - Low state
Thermal Bremsstrahlung spectrum.
photons/keV-cm^2-sec
10^{-1}
10^{-2}
10^{-3}
10^{-4}
10
20
30
40
50
60
70
Energy (keV)

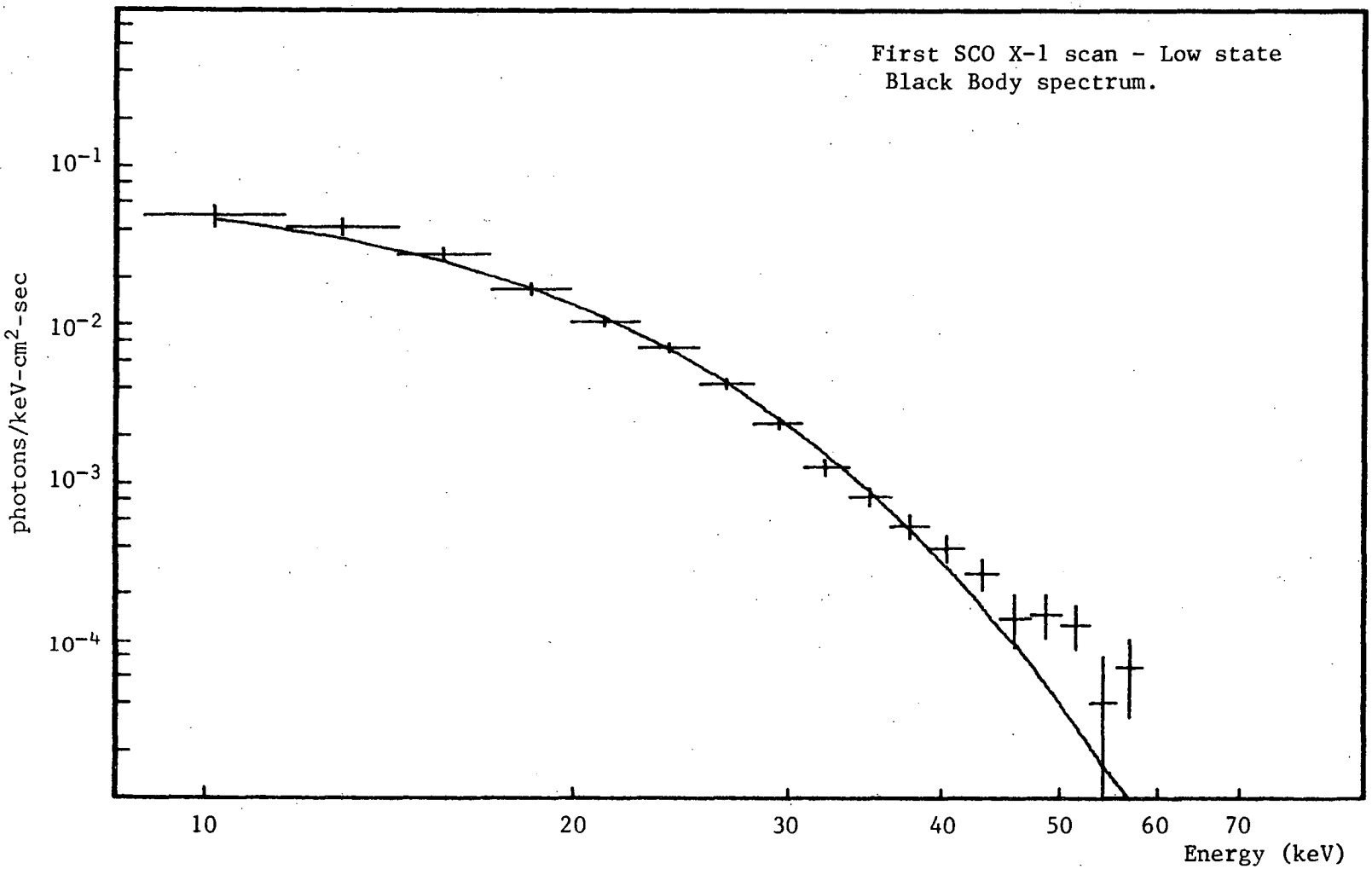
First SCO X-1 scan - Low state
Black Body spectrum.
photons/keV-cm^2-sec
10^{-1}
10^{-2}
10^{-3}
10^{-4}
10
20
30
40
50
60
70
Energy (keV)

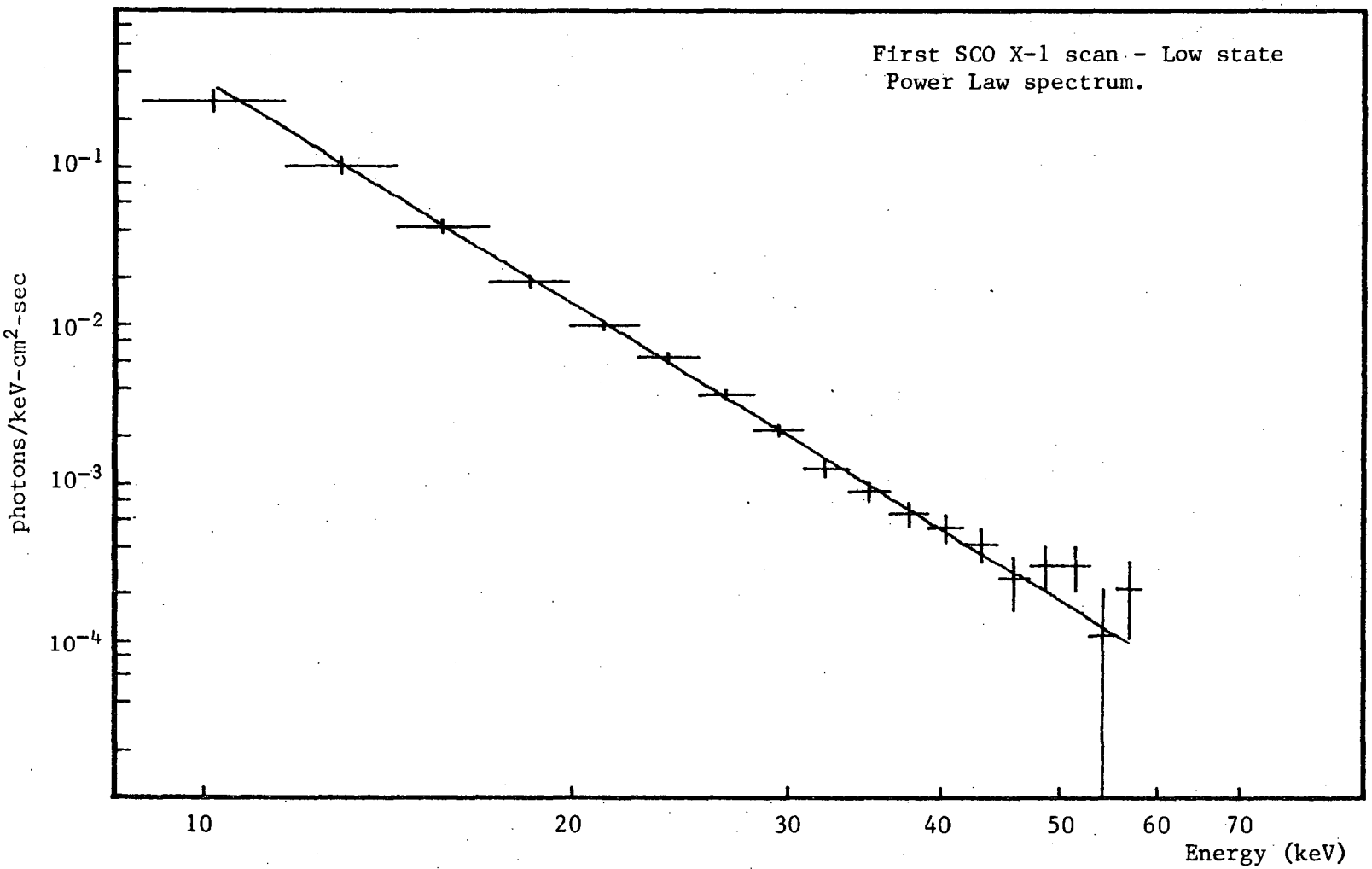
First SCO X-1 scan - Low state
Power Law spectrum.
photons/keV-cm^2-sec
10^{-1}
10^{-2}
10^{-3}
10^{-4}
10
20
30
40
50
60
70
Energy (keV)

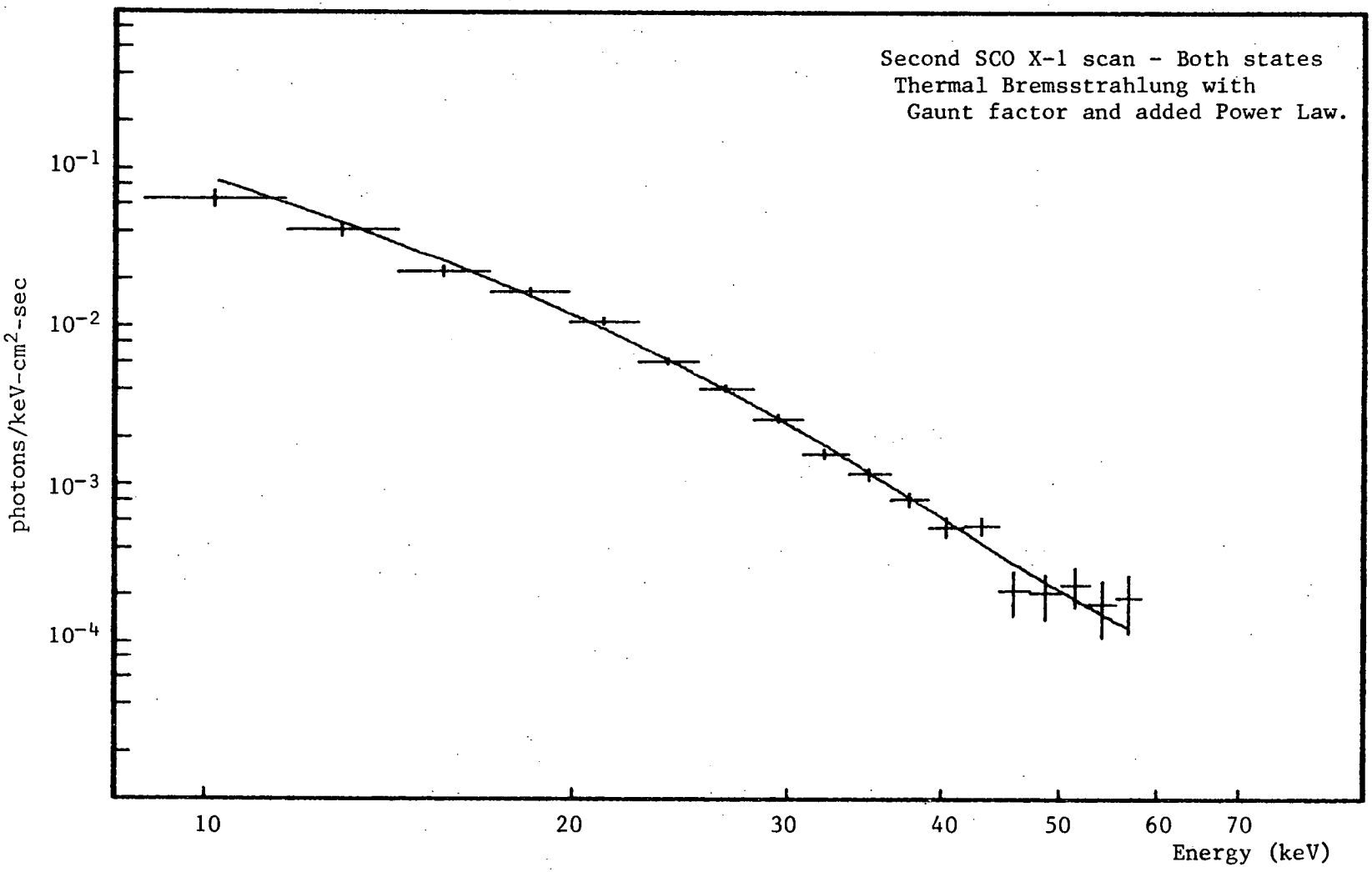
Second SCO X-1 scan - Both states
Thermal Bremsstrahlung with
Gaunt factor and added Power Law.
photons/keV-cm^2-sec
10^{-1}
10^{-2}
10^{-3}
10^{-4}
10
20
30
40
50
60
70
Energy (keV)

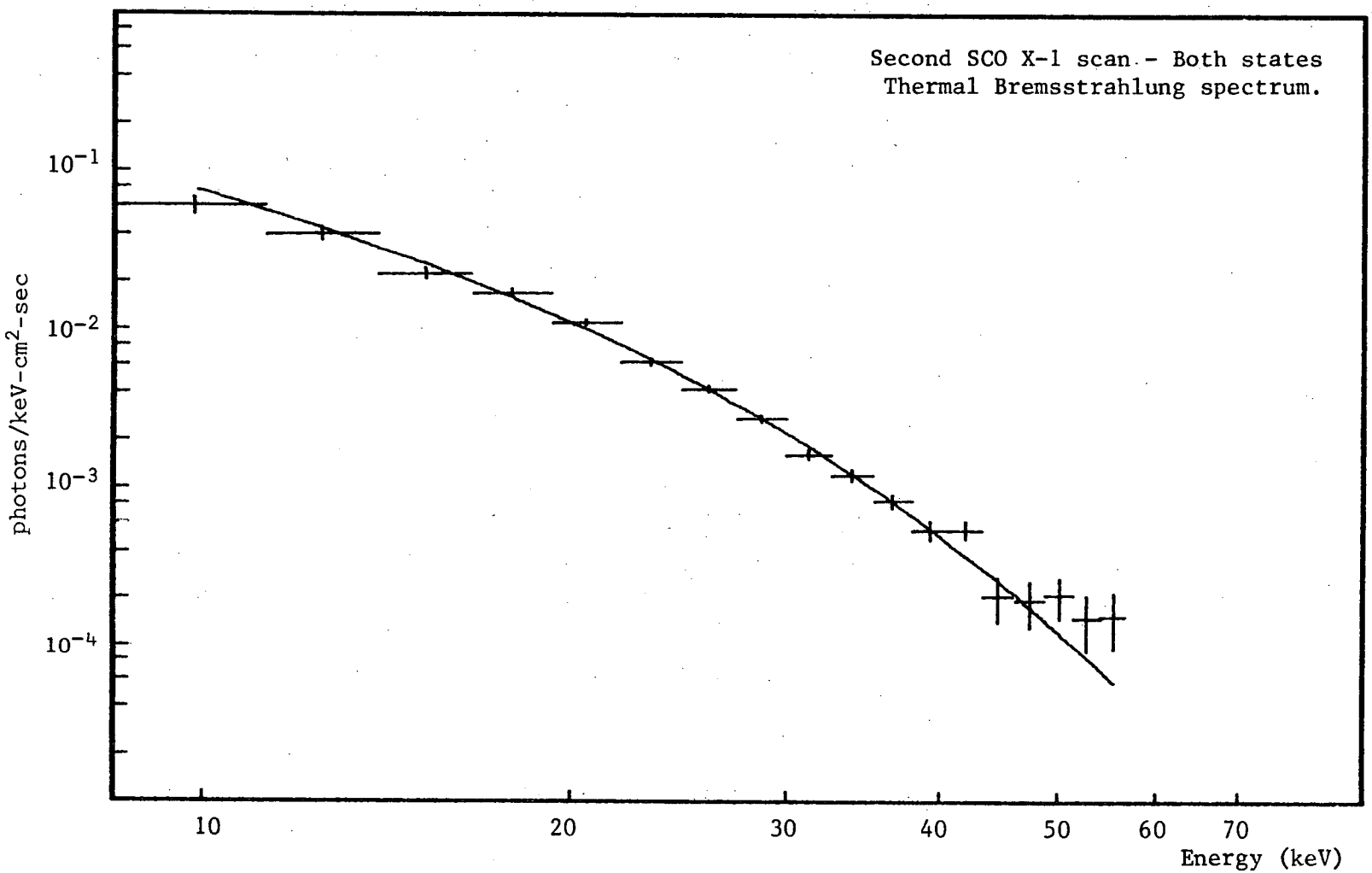
Second SCO X-1 scan - Both states
Thermal Bremsstrahlung spectrum.
photons/keV-cm^2-sec
10^{-1}
10^{-2}
10^{-3}
10^{-4}
10
20
30
40
50
60
70
Energy (keV)

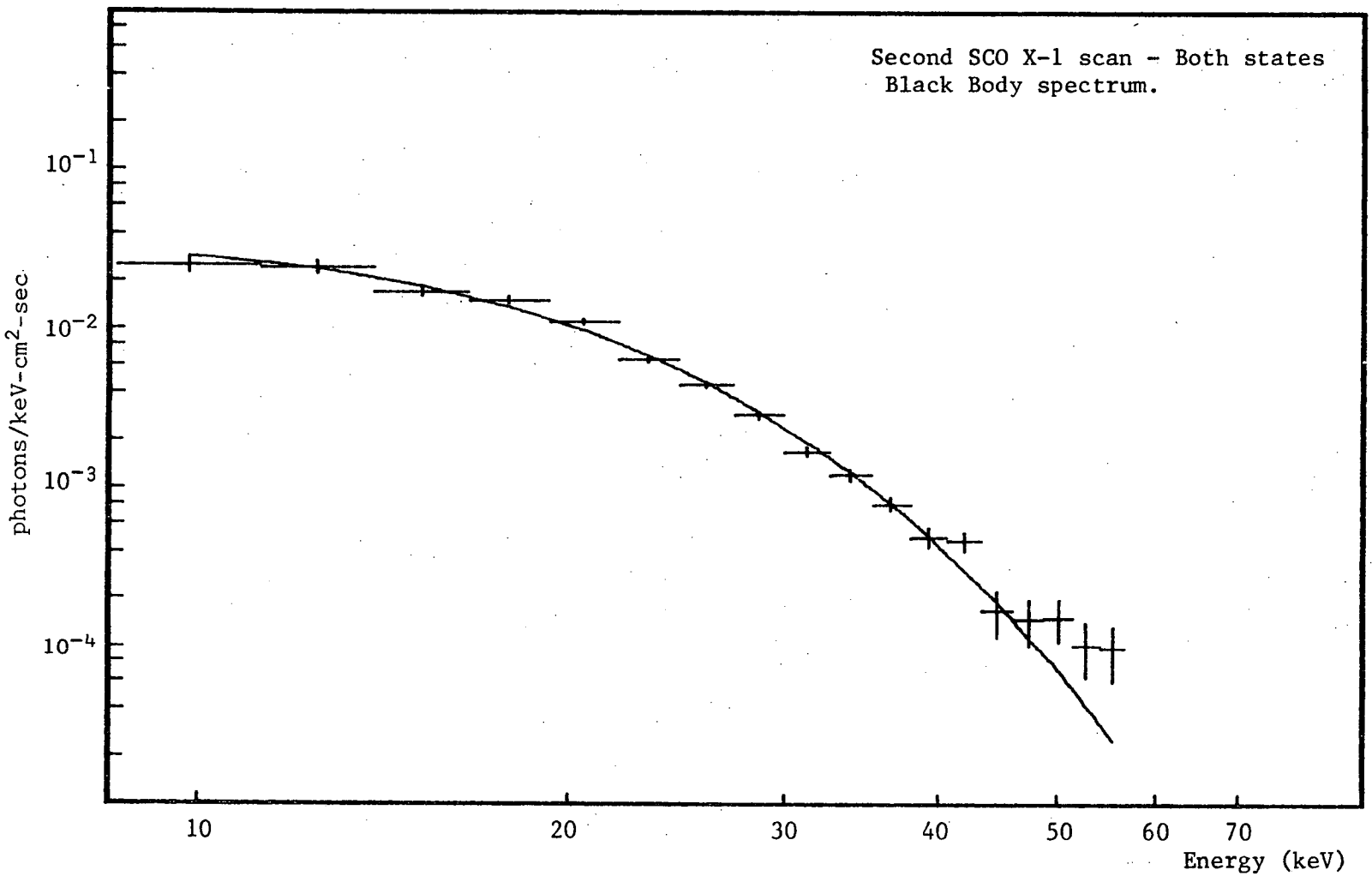
Second SCO X-1 scan - Both states
Black Body spectrum.
photons/keV-cm^2-sec
10^{-1}
10^{-2}
10^{-3}
10^{-4}
10
20
30
40
50
60
70
Energy (keV)

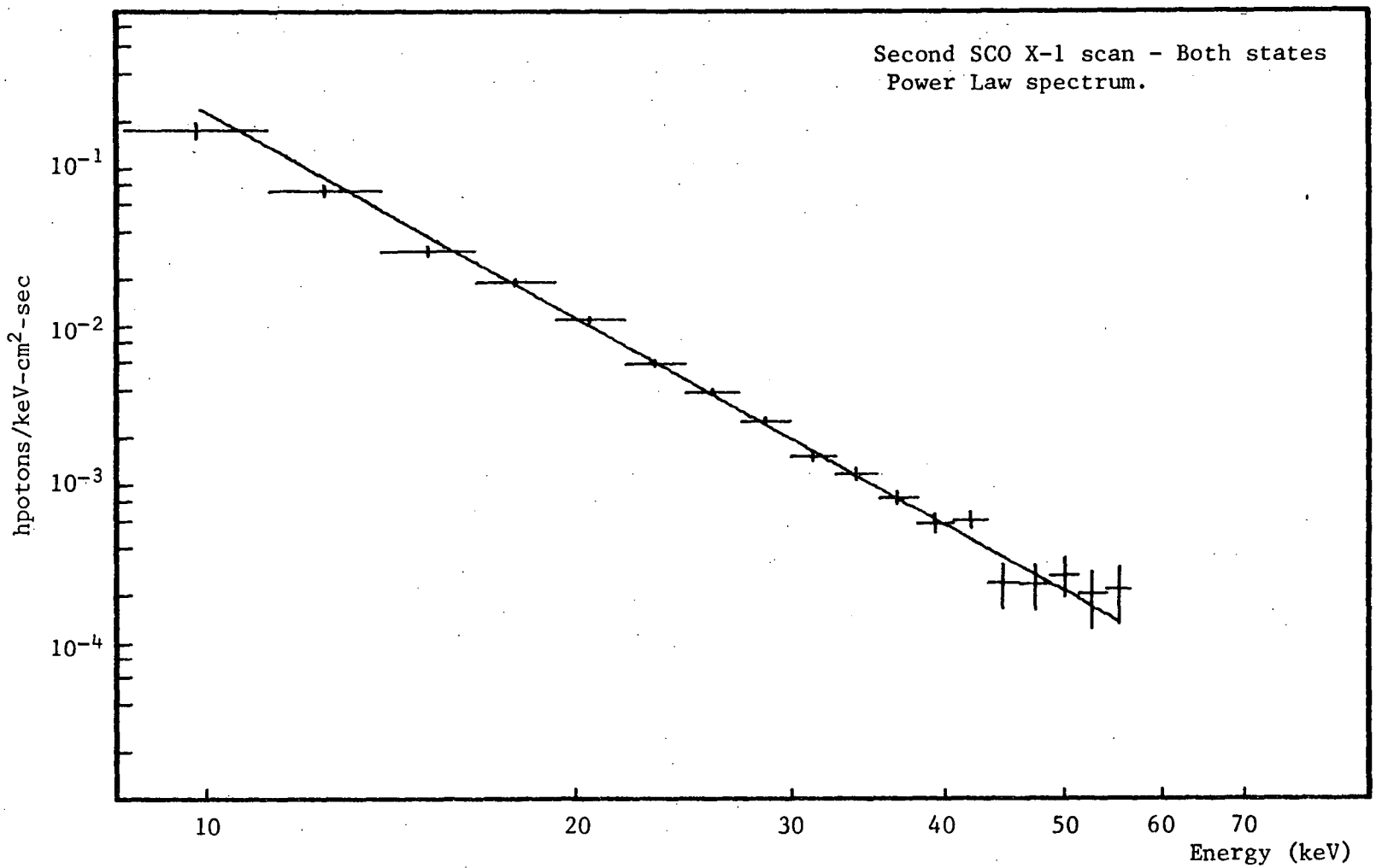
Second SCO X-1 scan - Both states
Power Law spectrum.
hpotons/keV-cm^2-sec
10^{-1}
10^{-2}
10^{-3}
10^{-4}
10
20
30
40
50
60
70
Energy (keV)

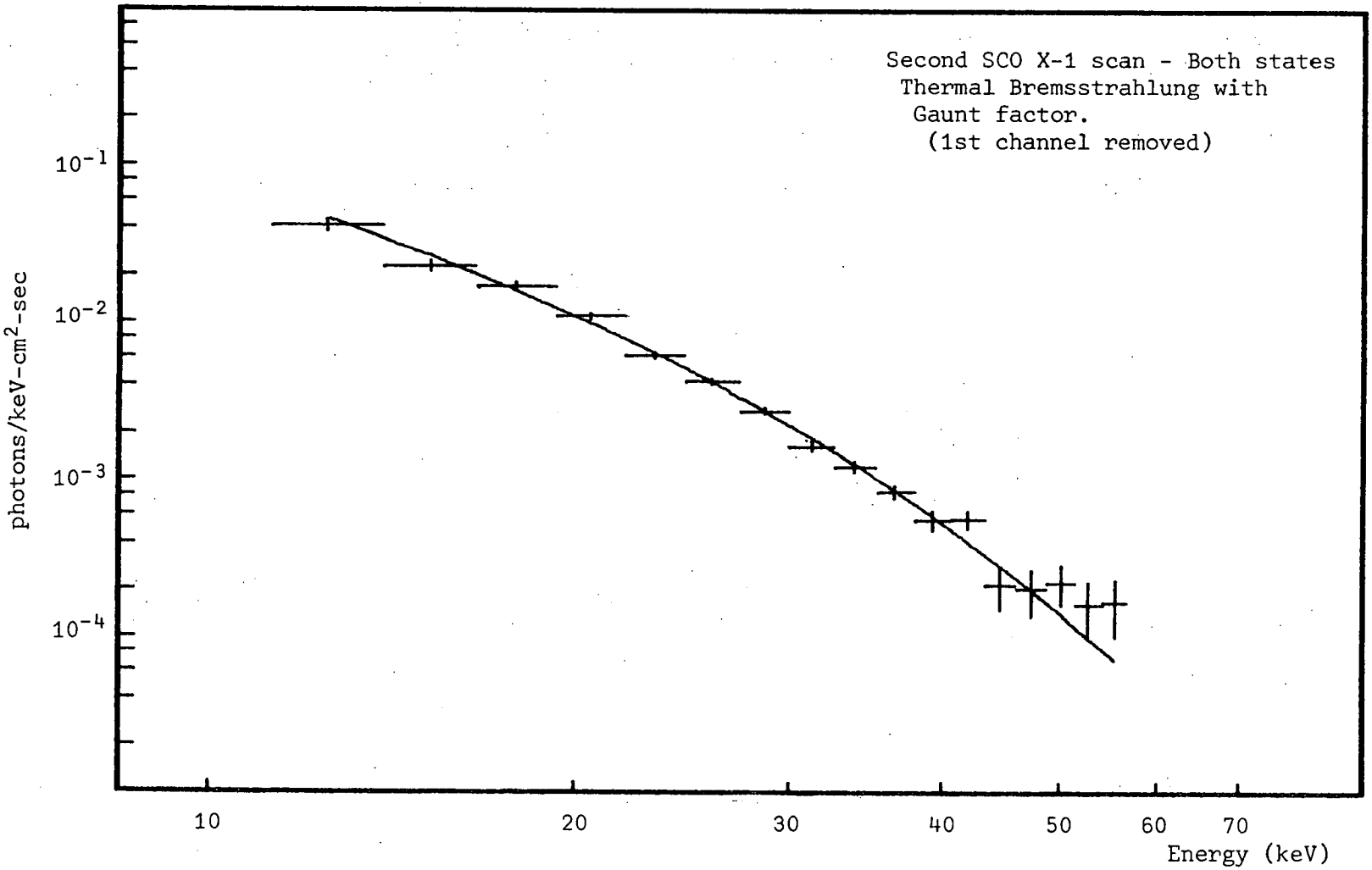
Second SCO X-1 scan - Both states
Thermal Bremsstrahlung with
Gaunt factor.
(1st channel removed)
photons/keV-cm^2-sec
10^{-1}
10^{-2}
10^{-3}
10^{-4}
10
20
30
40
50
60
70
Energy (keV)

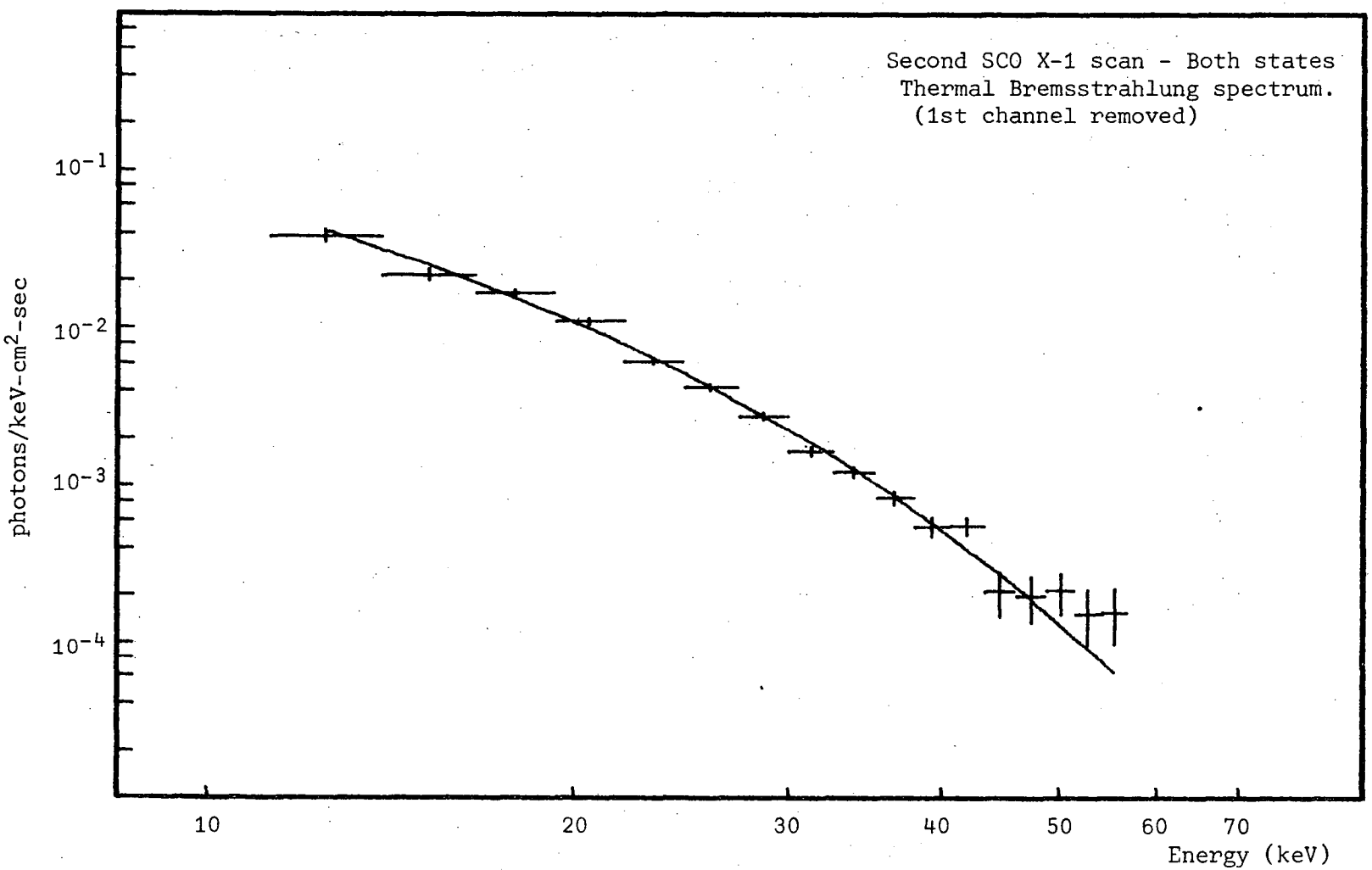
Second SCO X-1 scan - Both states
Thermal Bremsstrahlung spectrum.
(1st channel removed)
photons/keV-cm^2-sec
10^{-1}
10^{-2}
10^{-3}
10^{-4}
10
20
30
40
50
60
70
Energy (keV)

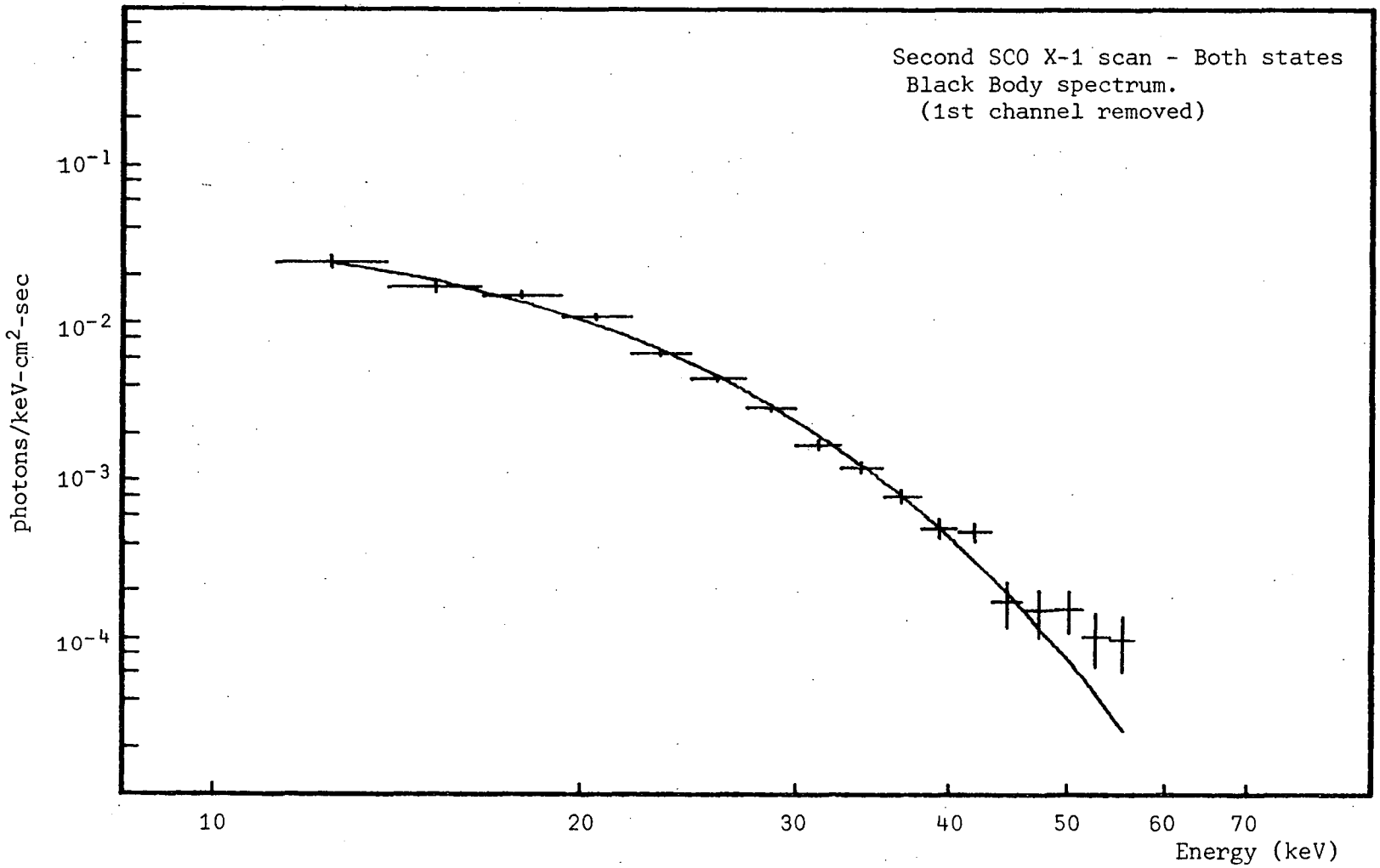
Second SCO X-1 scan - Both states
Black Body spectrum.
(1st channel removed)
photons/keV-cm^2-sec
10^{-1}
10^{-2}
10^{-3}
10^{-4}
10
20
30
40
50
60
70
Energy (keV)

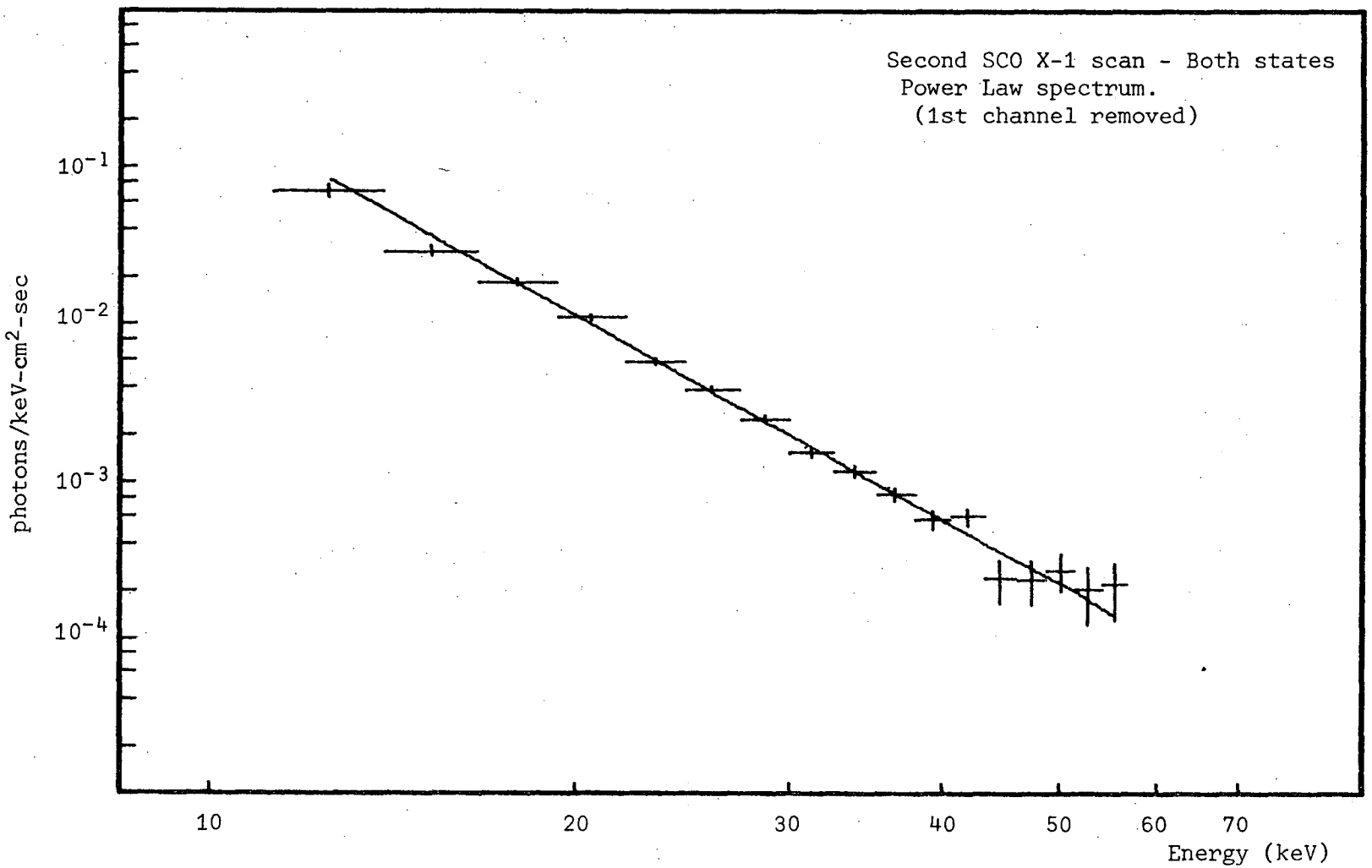
Second SCO X-1 scan - Both states
Power Law spectrum.
(1st channel removed)
photons/keV-cm^2-sec
10^{-1}
10^{-2}
10^{-3}
10^{-4}
10
20
30
40
50
60
70
Energy (keV)

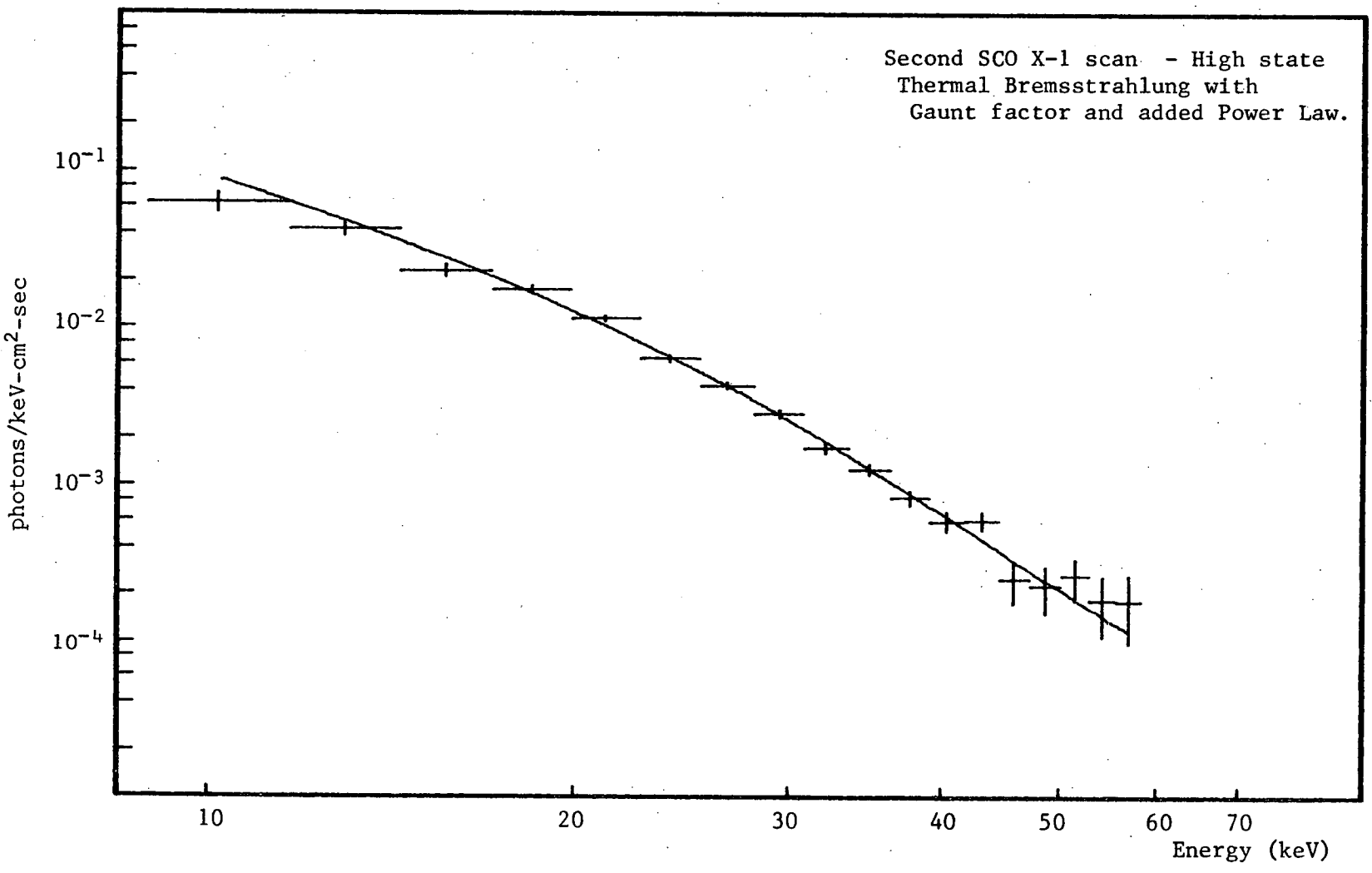
Second SCO X-1 scan - High state
Thermal Bremsstrahlung with
Gaunt factor and added Power Law.
photons/keV-cm²-sec
10⁻¹
10⁻²
10⁻³
10⁻⁴
10
20
30
40
50
60
70
Energy (keV)

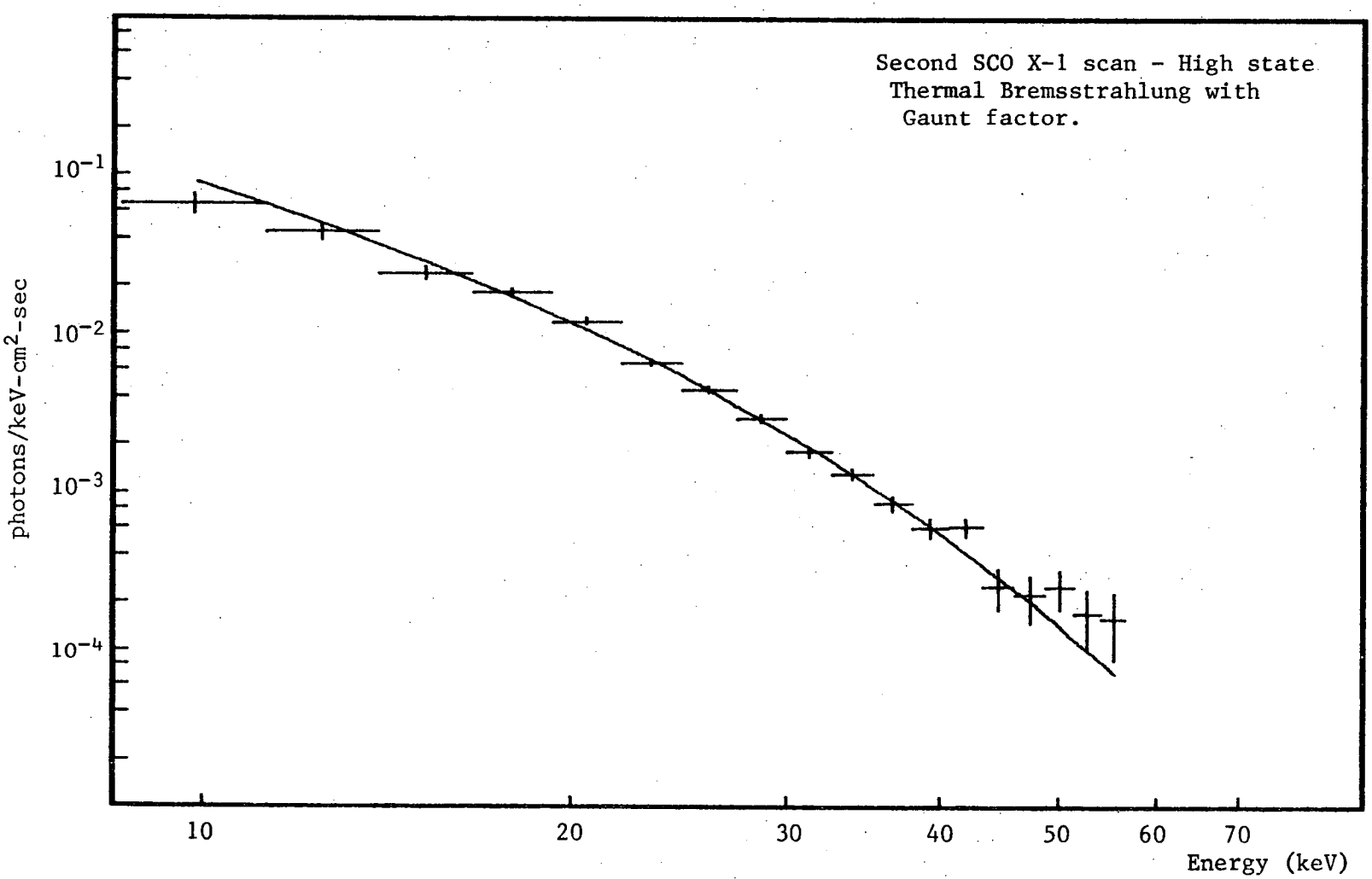
Second SCO X-1 scan - High state
Thermal Bremsstrahlung with
Gaunt factor.
photons/keV-cm^2-sec
10^{-1}
10^{-2}
10^{-3}
10^{-4}
10
20
30
40
50
60
70
Energy (keV)

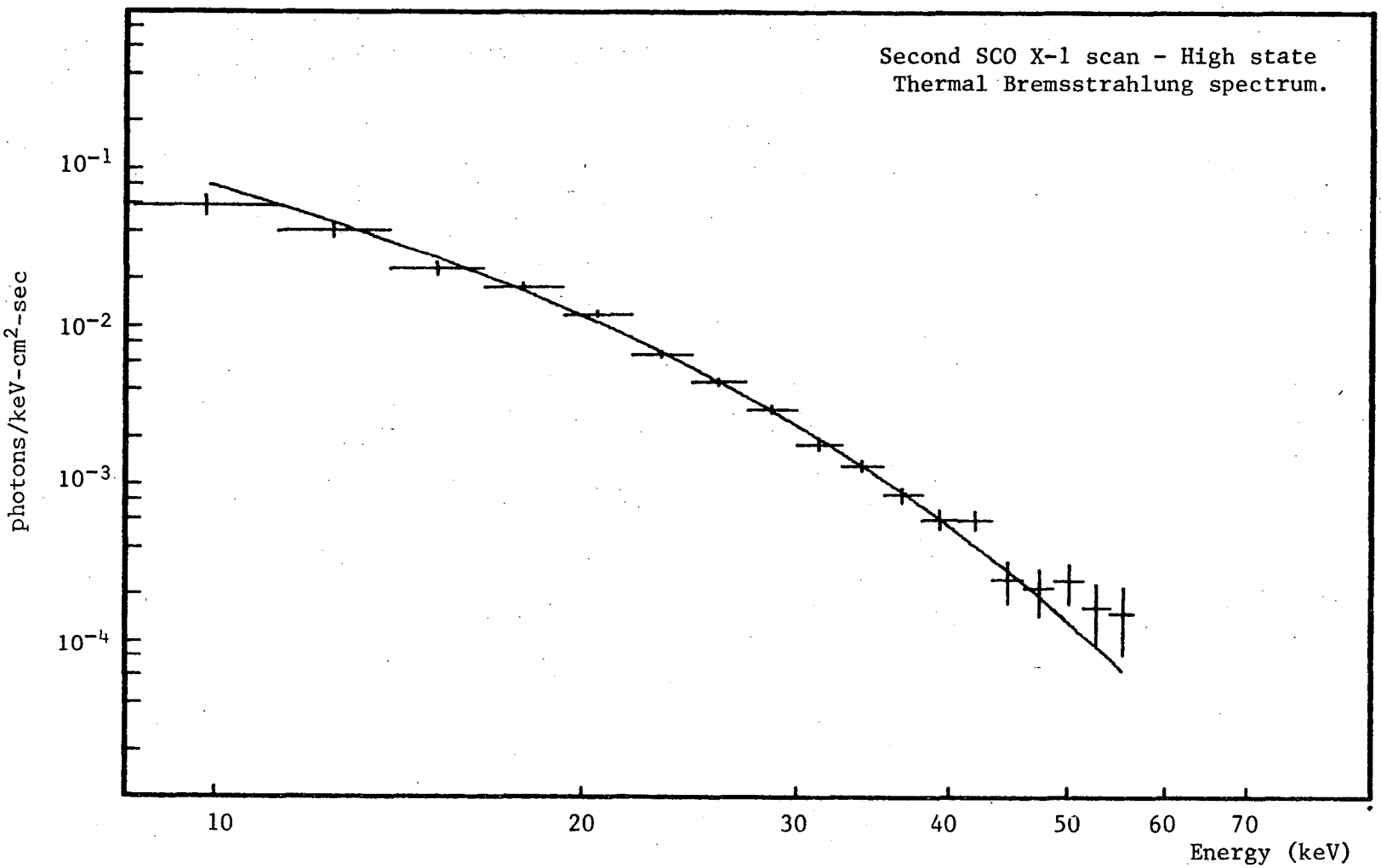
Second SCO X-1 scan - High state
Thermal Bremsstrahlung spectrum.
photons/keV-cm^2-sec
10^{-1}
10^{-2}
10^{-3}
10^{-4}
10
20
30
40
50
60
70
Energy (keV)

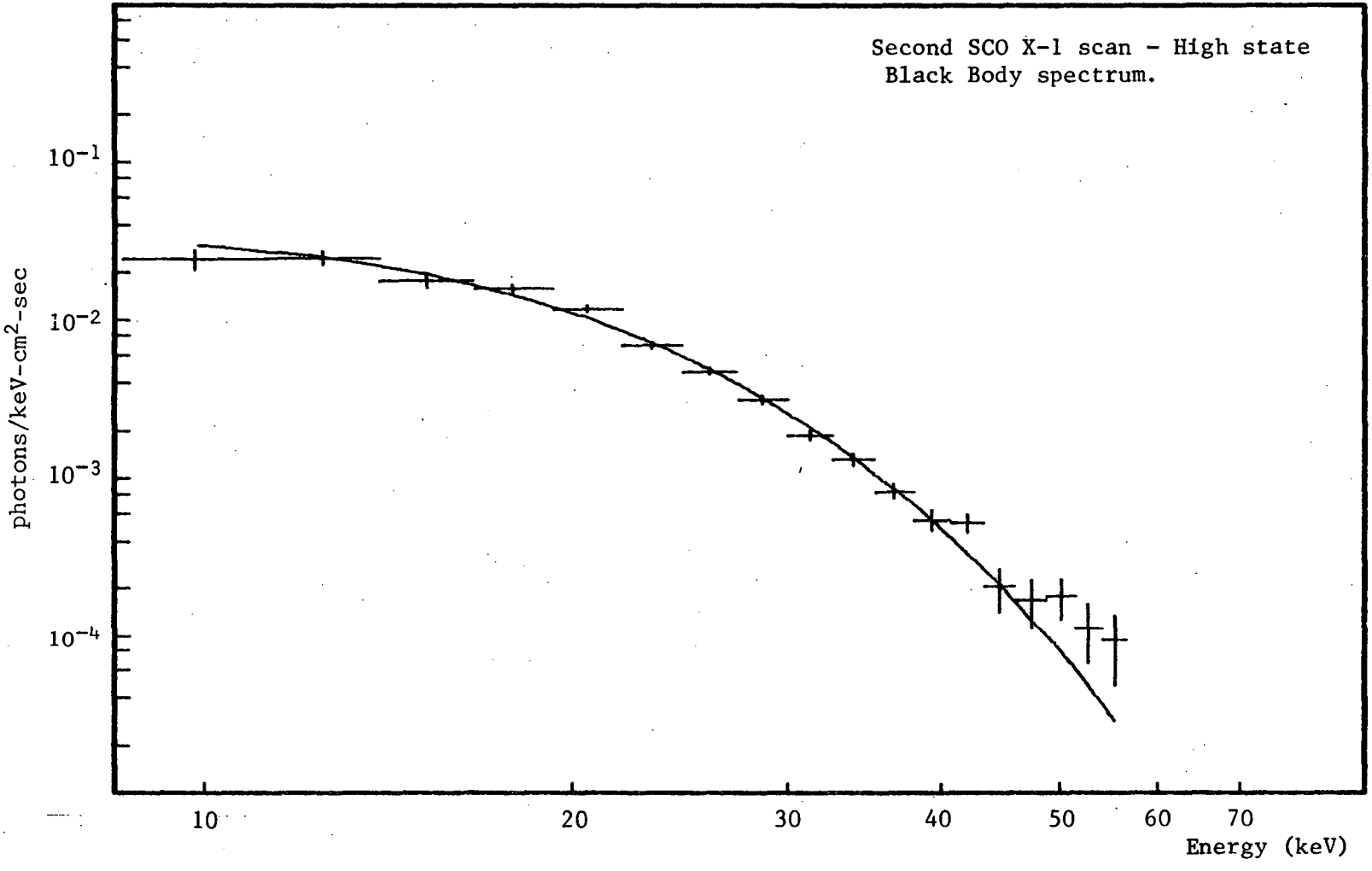
Second SCO X-1 scan - High state
Black Body spectrum.
photons/keV-cm^2-sec
10^{-1}
10^{-2}
10^{-3}
10^{-4}
10
20
30
40
50
60
70
Energy (keV)

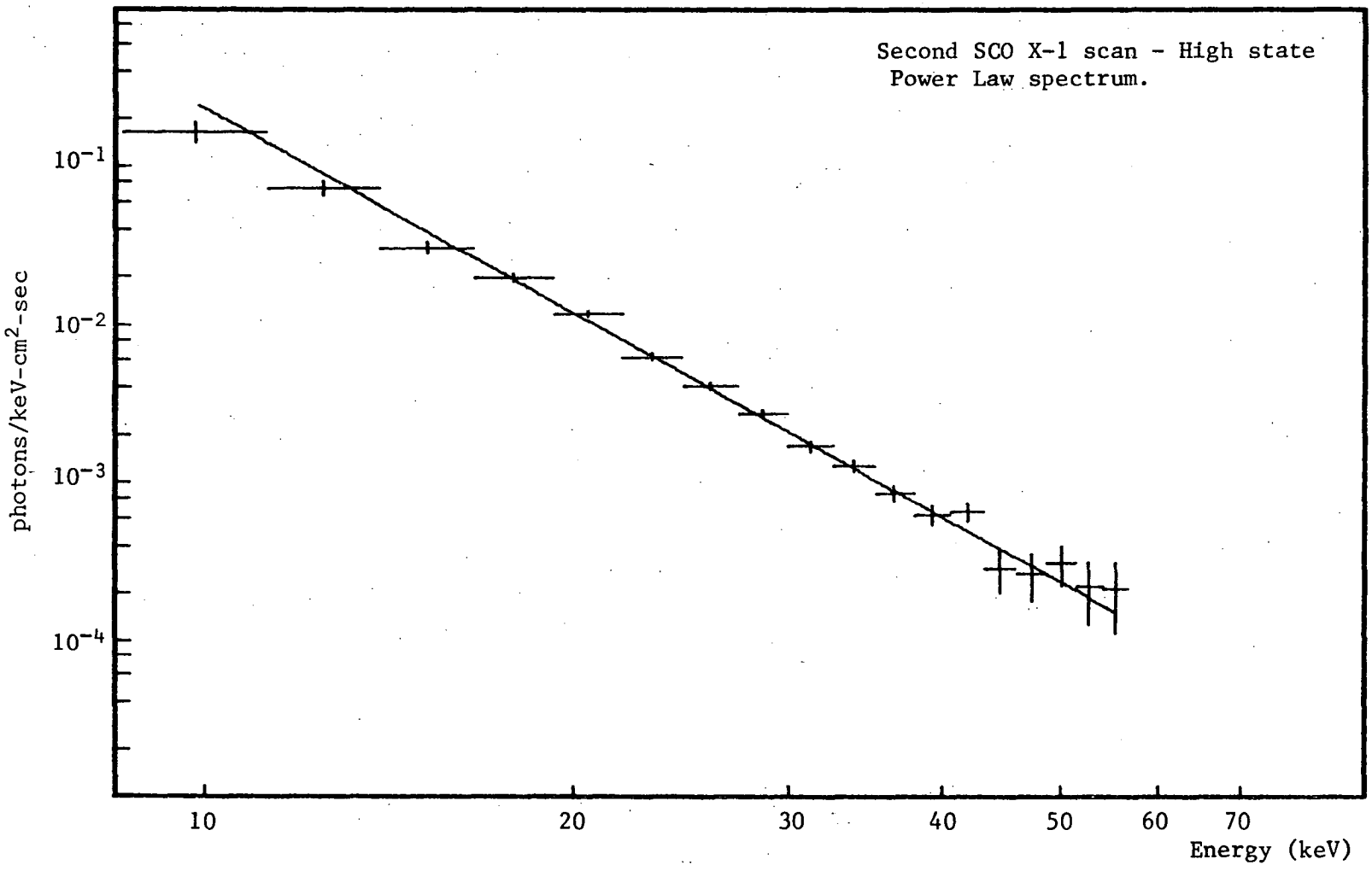
Second SCO X-1 scan - High state
Power Law spectrum.
photons/keV-cm^2-sec
10^{-1}
10^{-2}
10^{-3}
10^{-4}
10
20
30
40
50
60
70
Energy (keV)

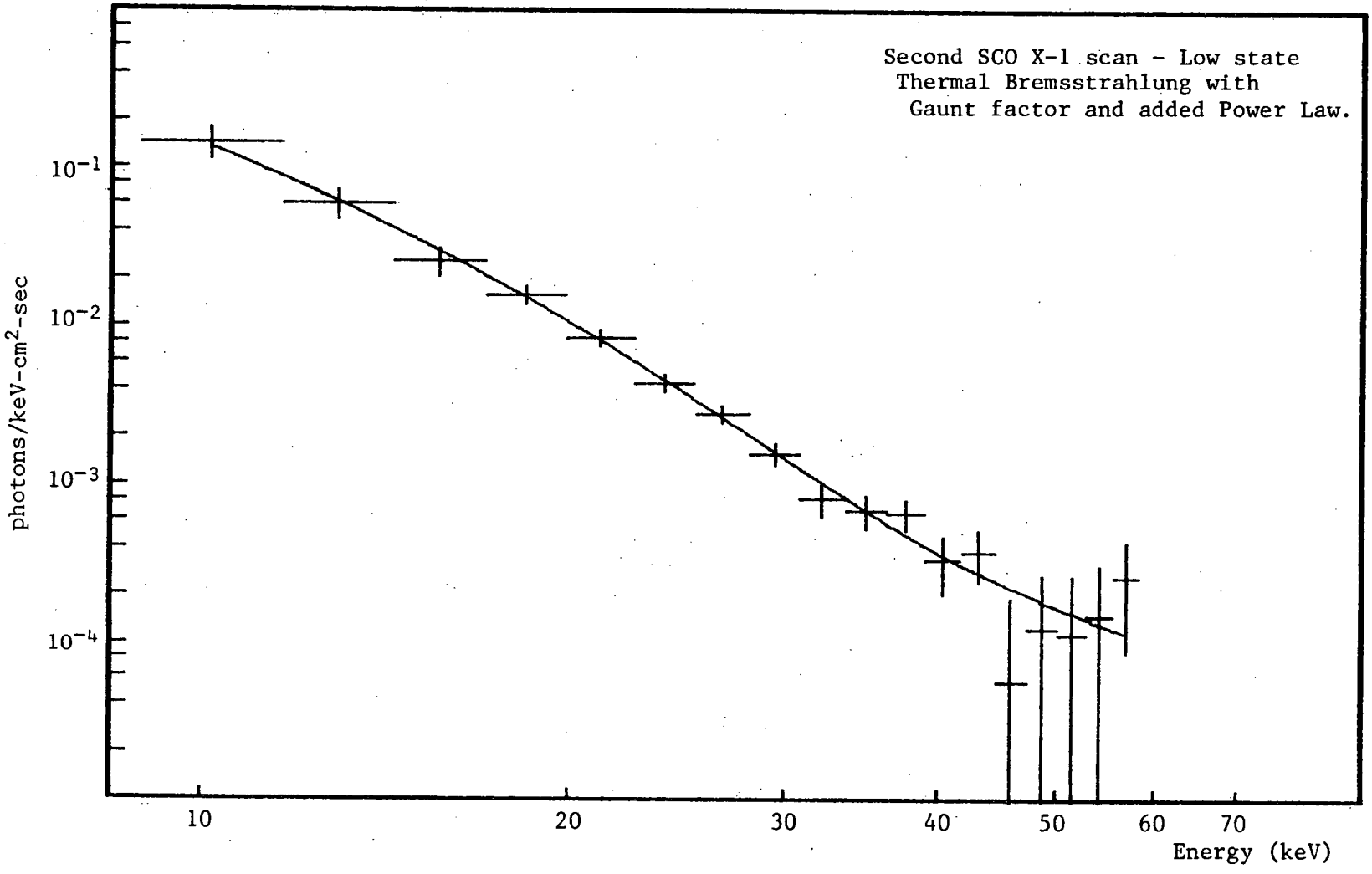
Second SCO X-1 scan - Low state
Thermal Bremsstrahlung with
Gaunt factor and added Power Law.
photons/keV-cm^2-sec
10^{-1}
10^{-2}
10^{-3}
10^{-4}
10
20
30
40
50
60
70
Energy (keV)

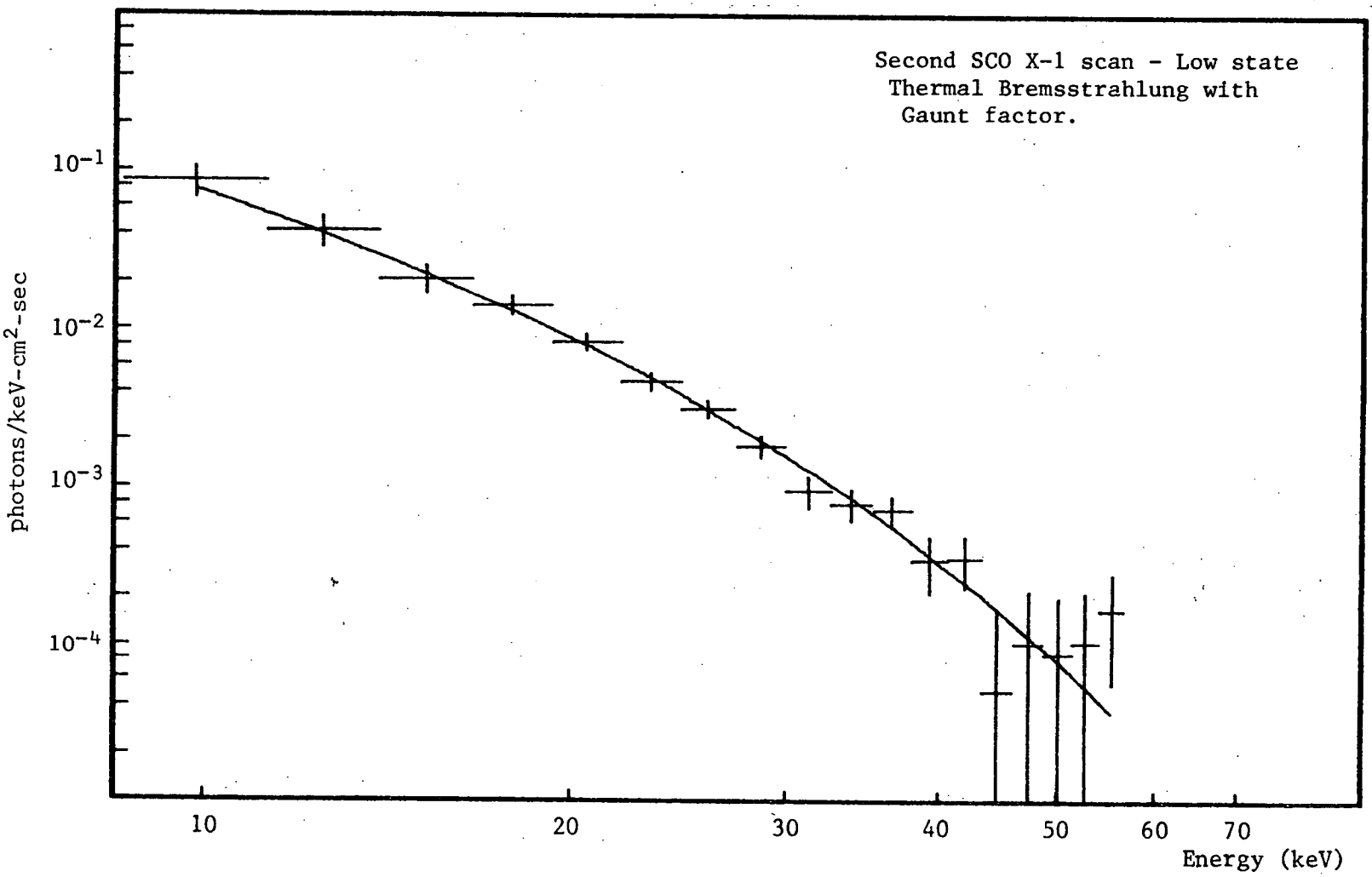
Second SCO X-1 scan - Low state
Thermal Bremsstrahlung with
Gaunt factor.
photons/keV-cm^2-sec
10^{-1}
10^{-2}
10^{-3}
10^{-4}
10
20
30
40
50
60
70
Energy (keV)

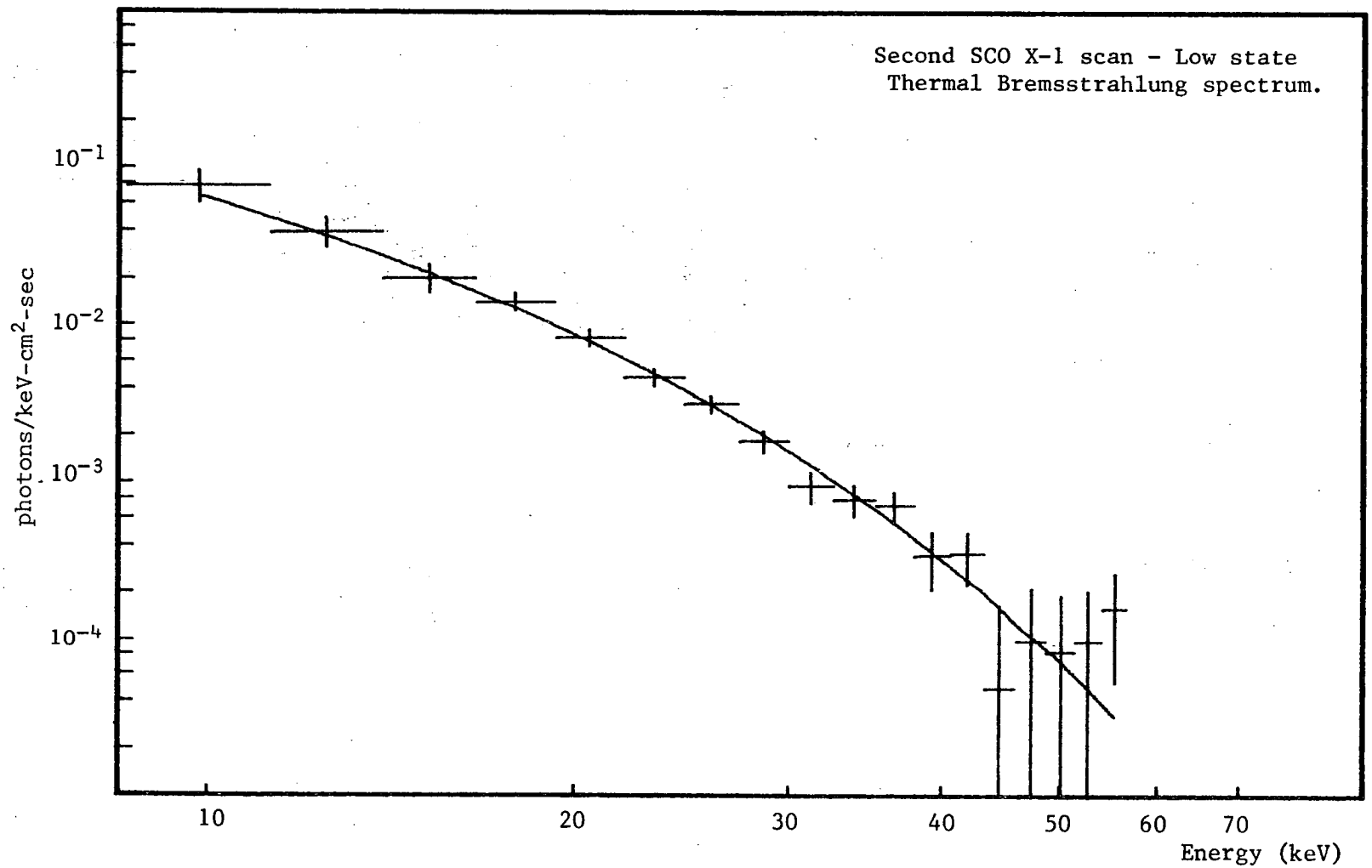
Second SCO X-1 scan - Low state
Thermal Bremsstrahlung spectrum.
photons/keV-cm^2-sec
10^{-1}
10^{-2}
10^{-3}
10^{-4}
10
20
30
40
50
60
70
Energy (keV)

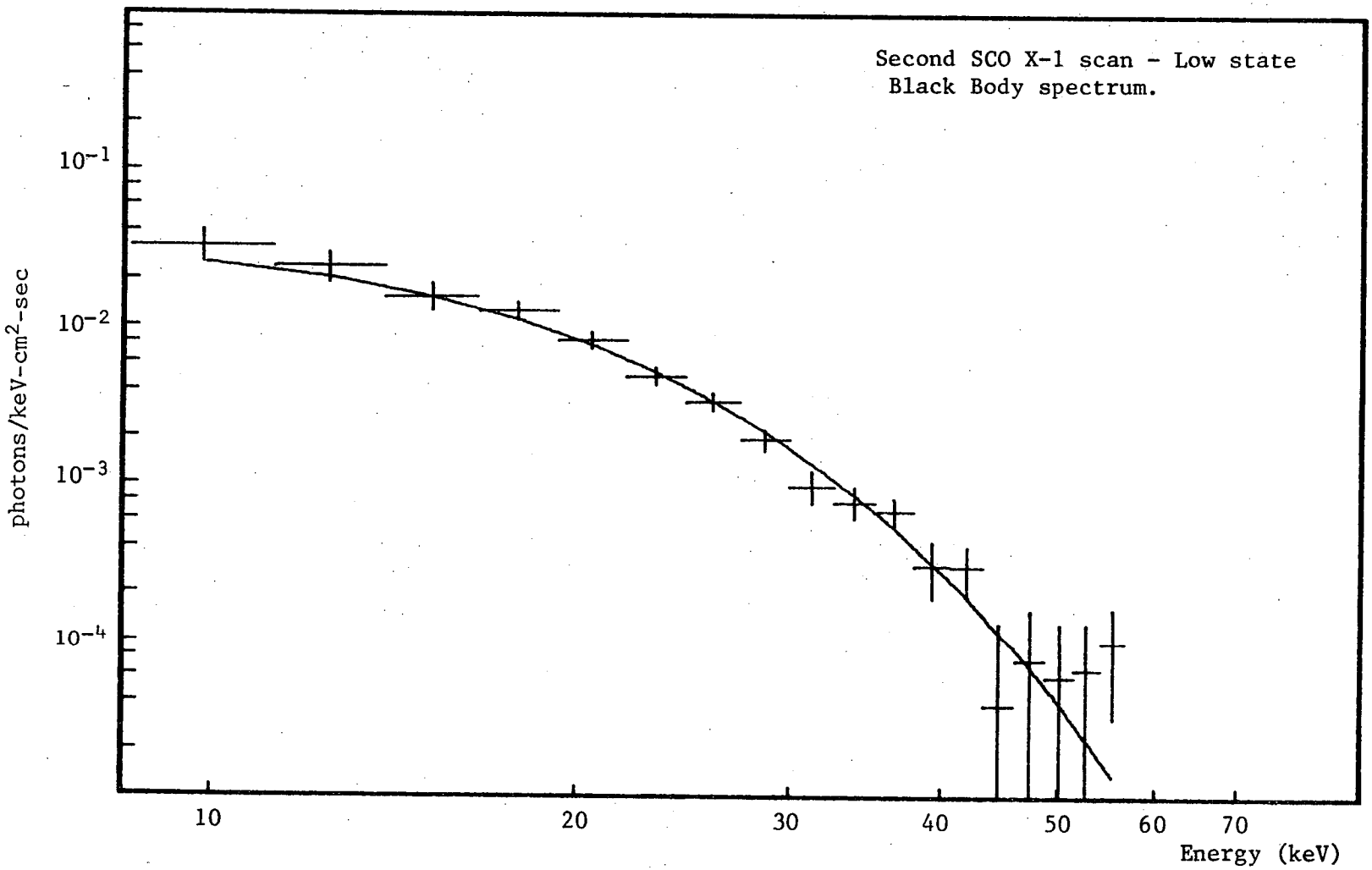
Second SCO X-1 scan - Low state
Black Body spectrum.
photons/keV-cm^2-sec
10^{-1}
10^{-2}
10^{-3}
10^{-4}
10
20
30
40
50
60
70
Energy (keV)

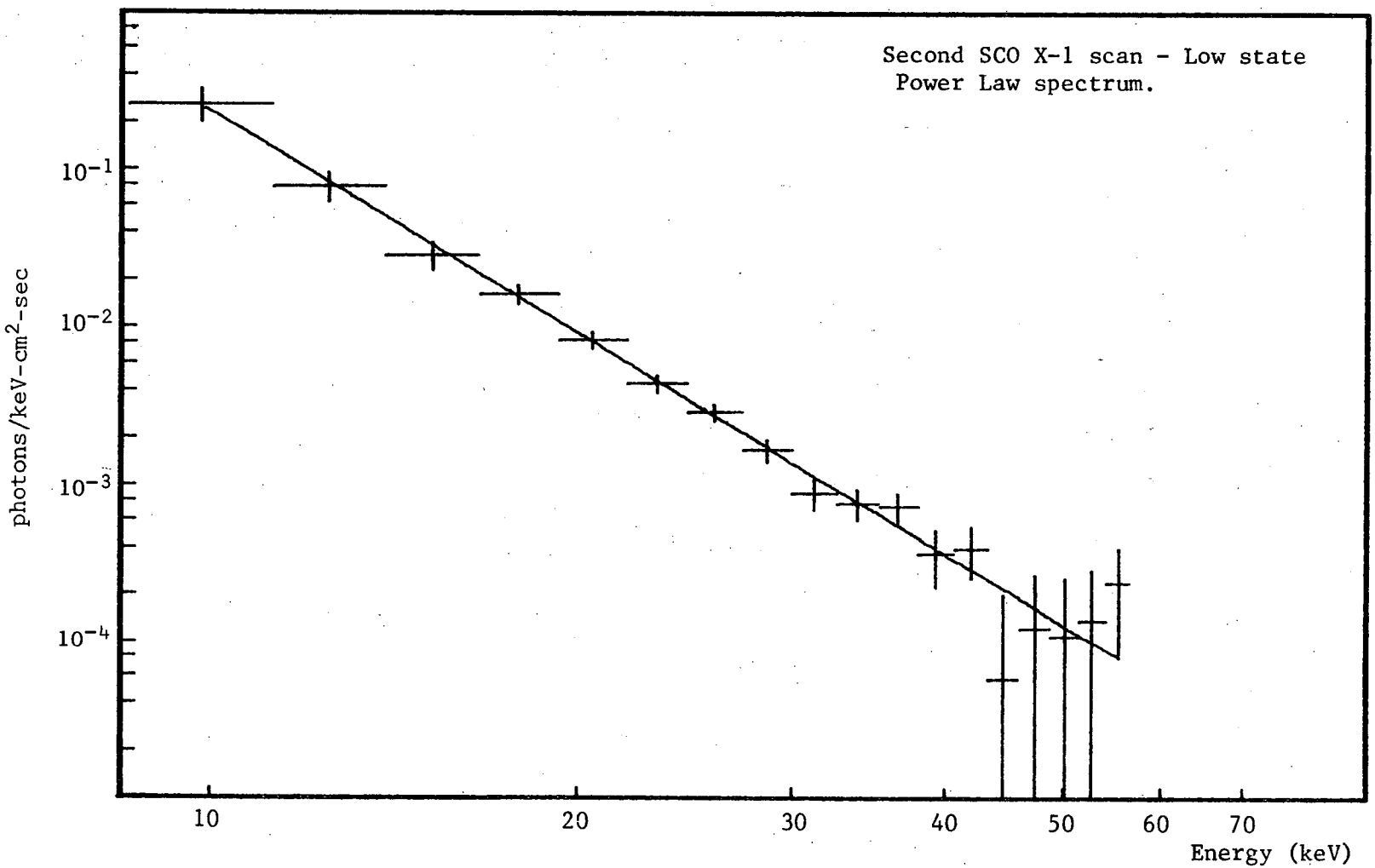
Second SCO X-1 scan - Low state
Power Law spectrum.
photons/keV-cm^2-sec
10^{-1}
10^{-2}
10^{-3}
10^{-4}
10
20
30
40
50
60
70
Energy (keV)

"CALIBRATION" FIT COUNTER PARAMETER

SPECTRAL PLOTS

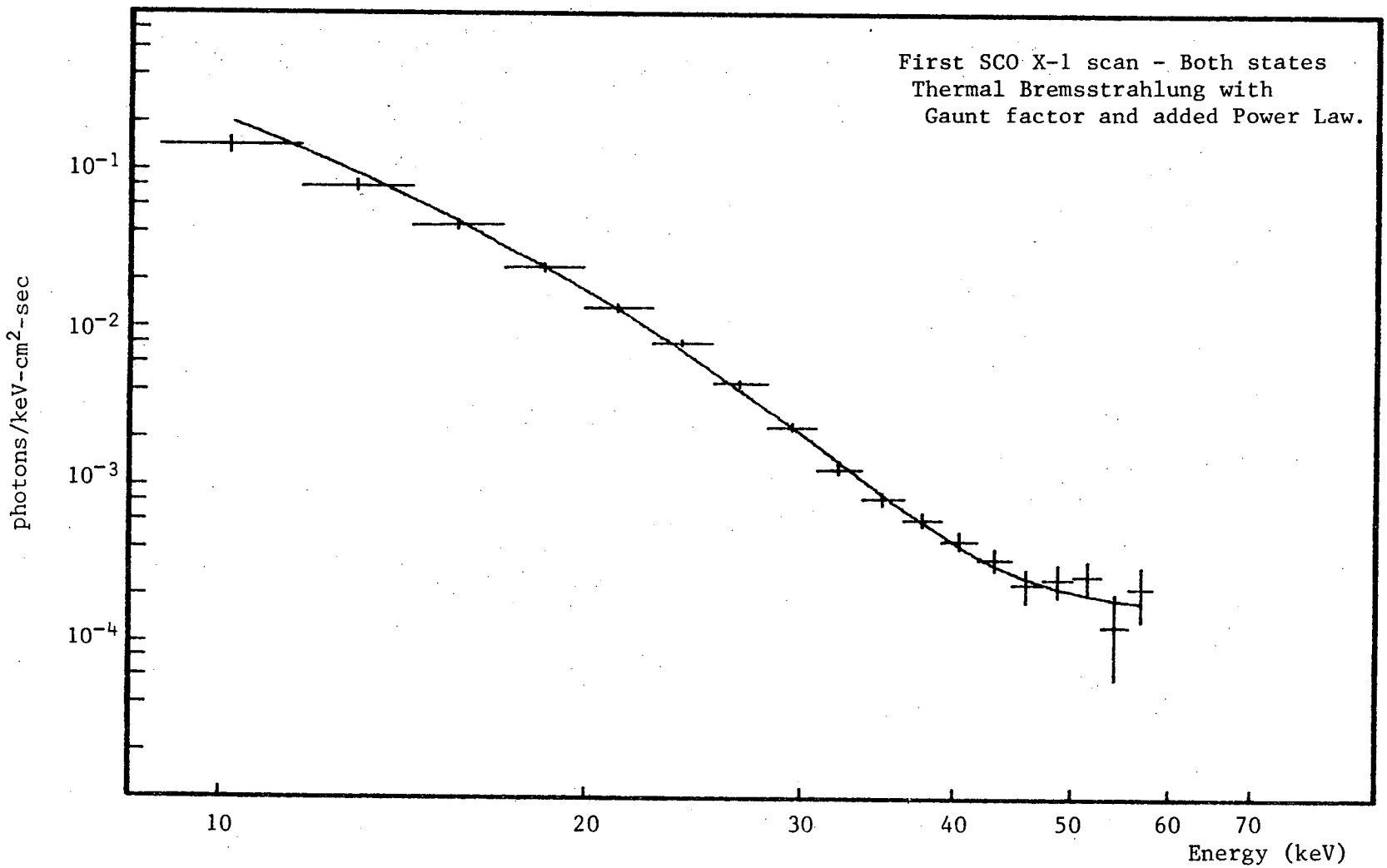
First SCO X-1 scan - Both states
Thermal Bremsstrahlung with
Gaunt factor and added Power Law.
photons/keV-cm^2-sec
10^{-1}
10^{-2}
10^{-3}
10^{-4}
10
20
30
40
50
60
70
Energy (keV)

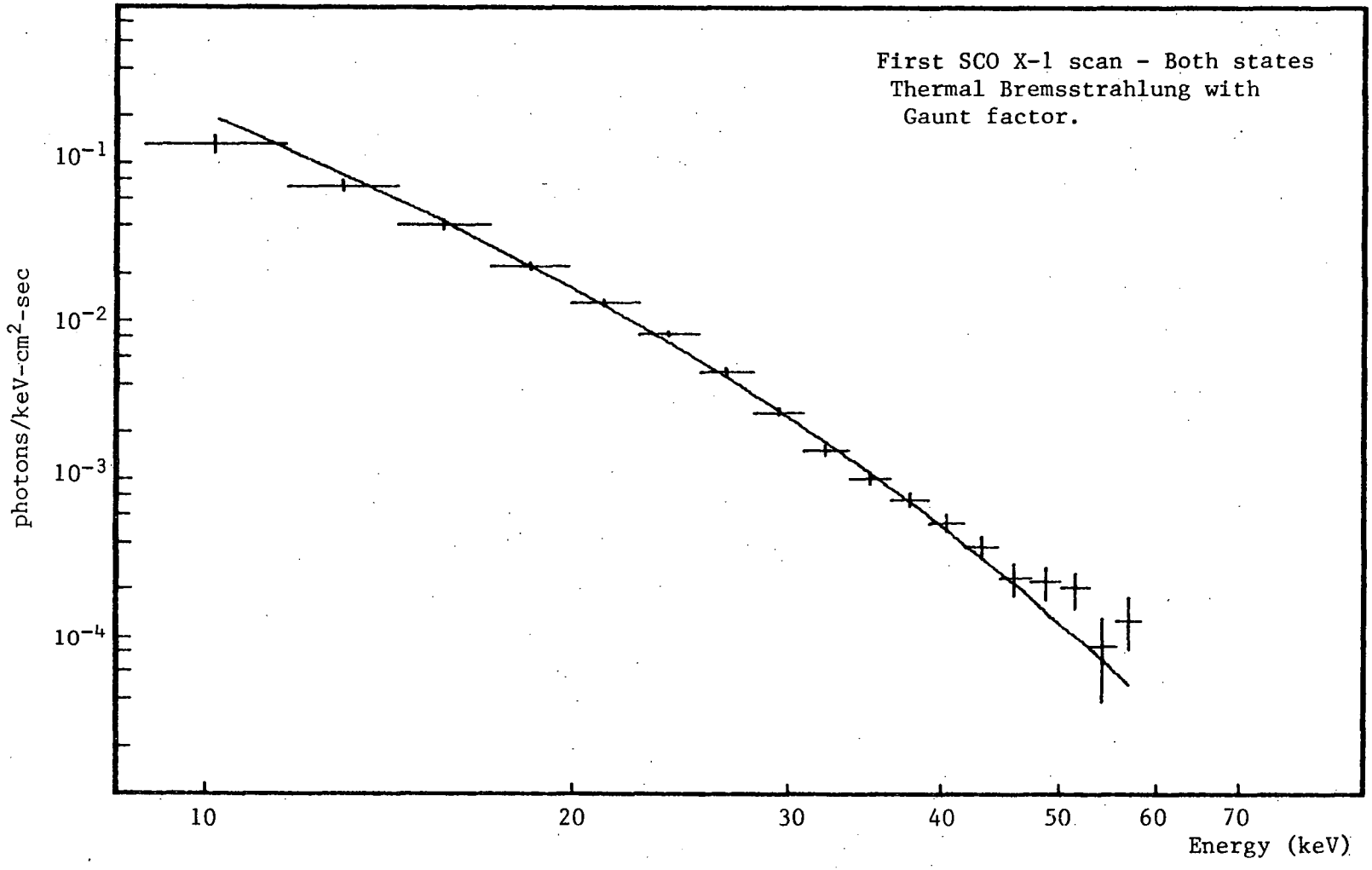
First SCO X-1 scan - Both states
Thermal Bremsstrahlung with
Gaunt factor.
10^{-1}
10^{-2}
10^{-3}
10^{-4}
photons/keV-cm^2-sec
10
20
30
40
50
60
70
Energy (keV)

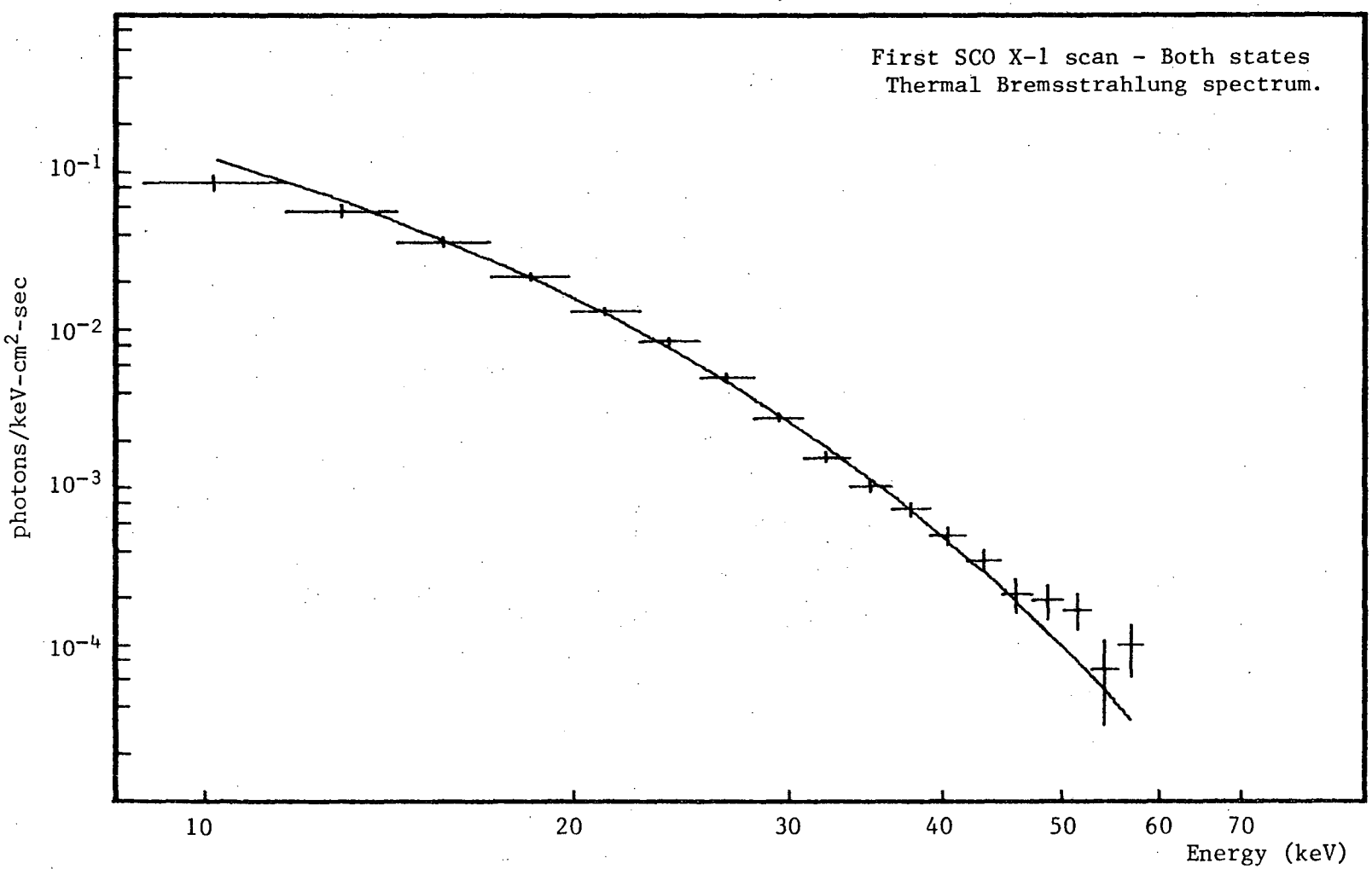
First SCO X-1 scan - Both states
Thermal Bremsstrahlung spectrum.
photons/keV-cm^2-sec
10^{-1}
10^{-2}
10^{-3}
10^{-4}
10
20
30
40
50
60
70
Energy (keV)

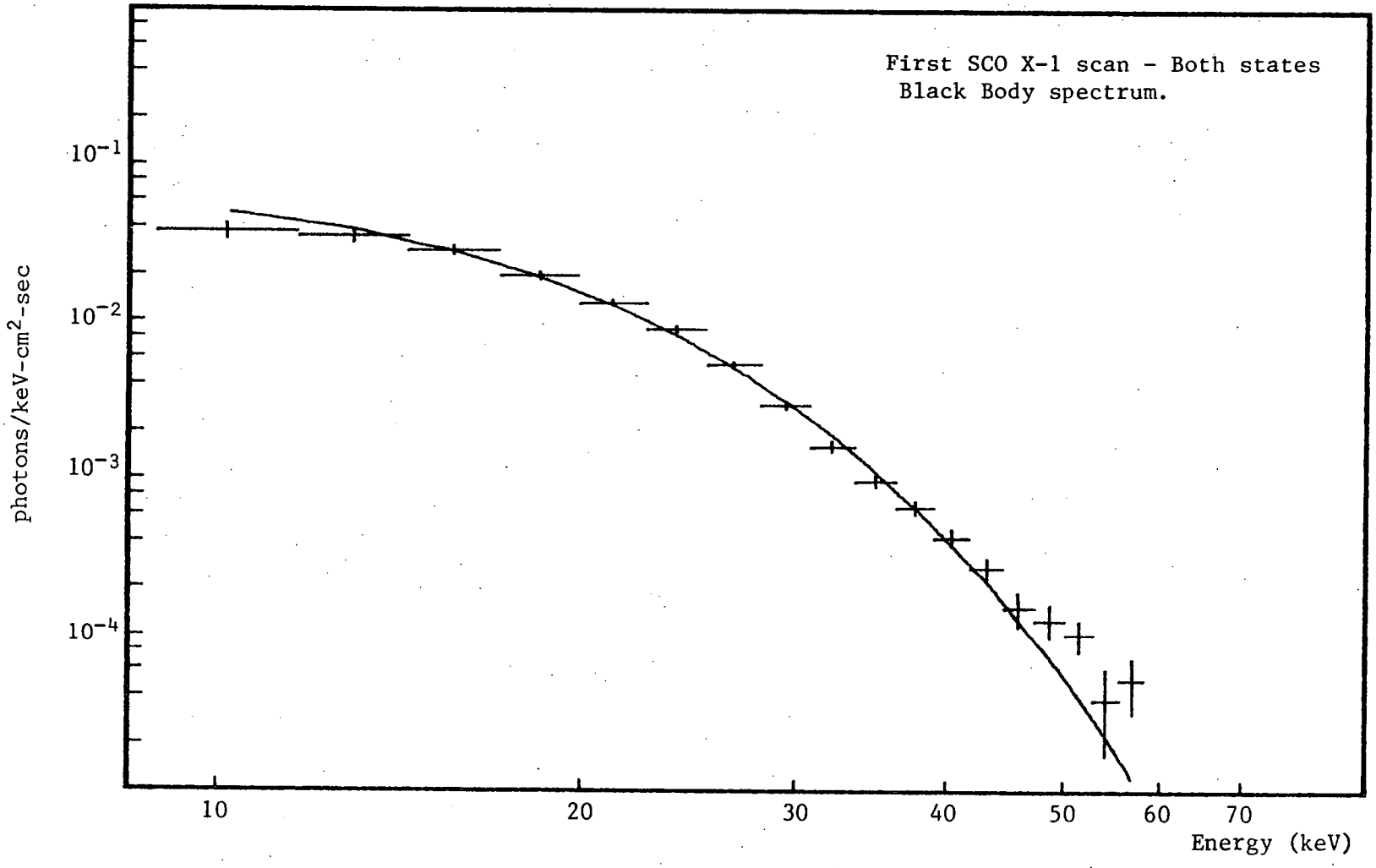
First SCO X-1 scan - Both states
Black Body spectrum.
photons/keV-cm^2-sec
10^{-1}
10^{-2}
10^{-3}
10^{-4}
10
20
30
40
50
60
70
Energy (keV)

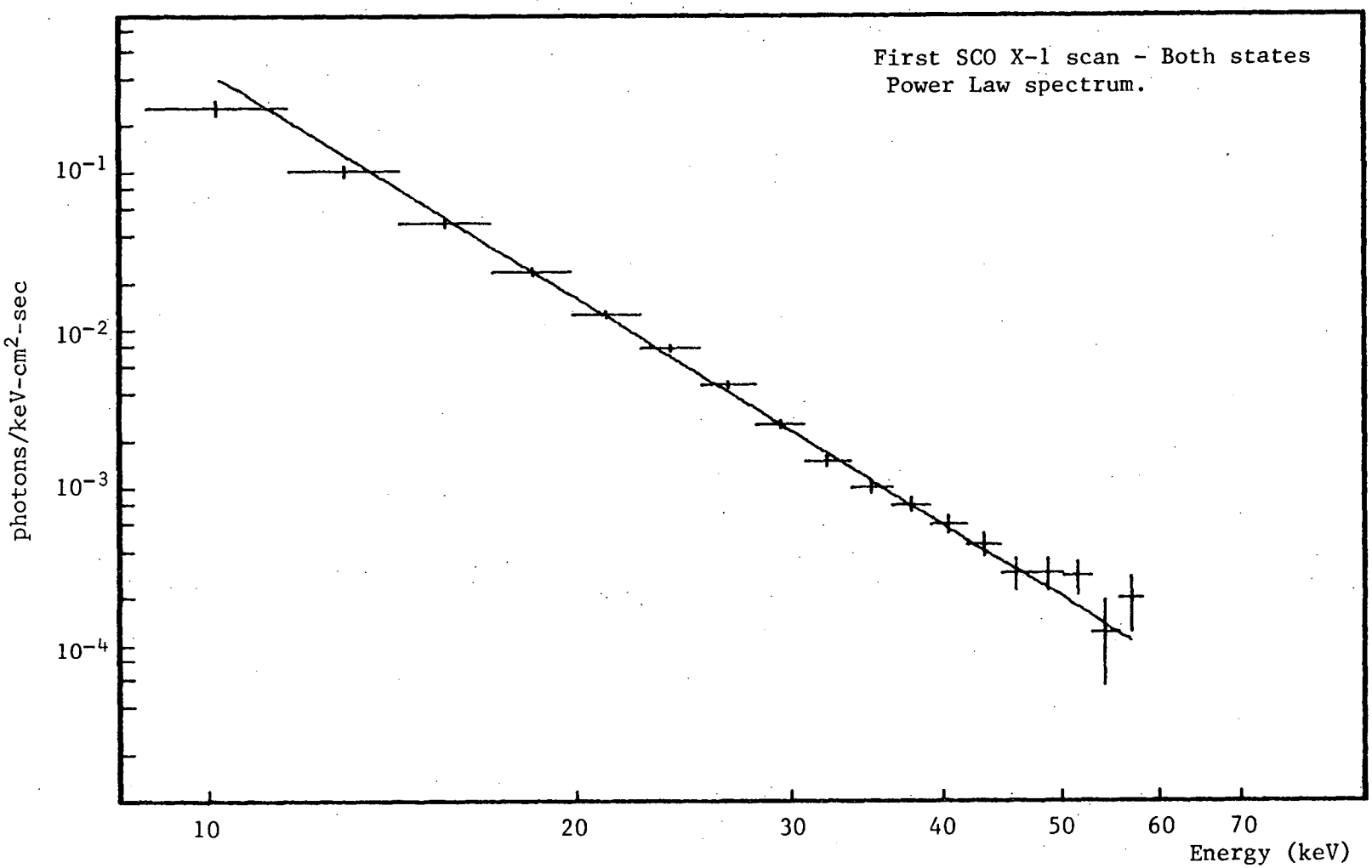
First SCO X-1 scan - Both states
Power Law spectrum.
photons/keV-cm^2-sec
10^{-1}
10^{-2}
10^{-3}
10^{-4}
10
20
30
40
50
60
70
Energy (keV)

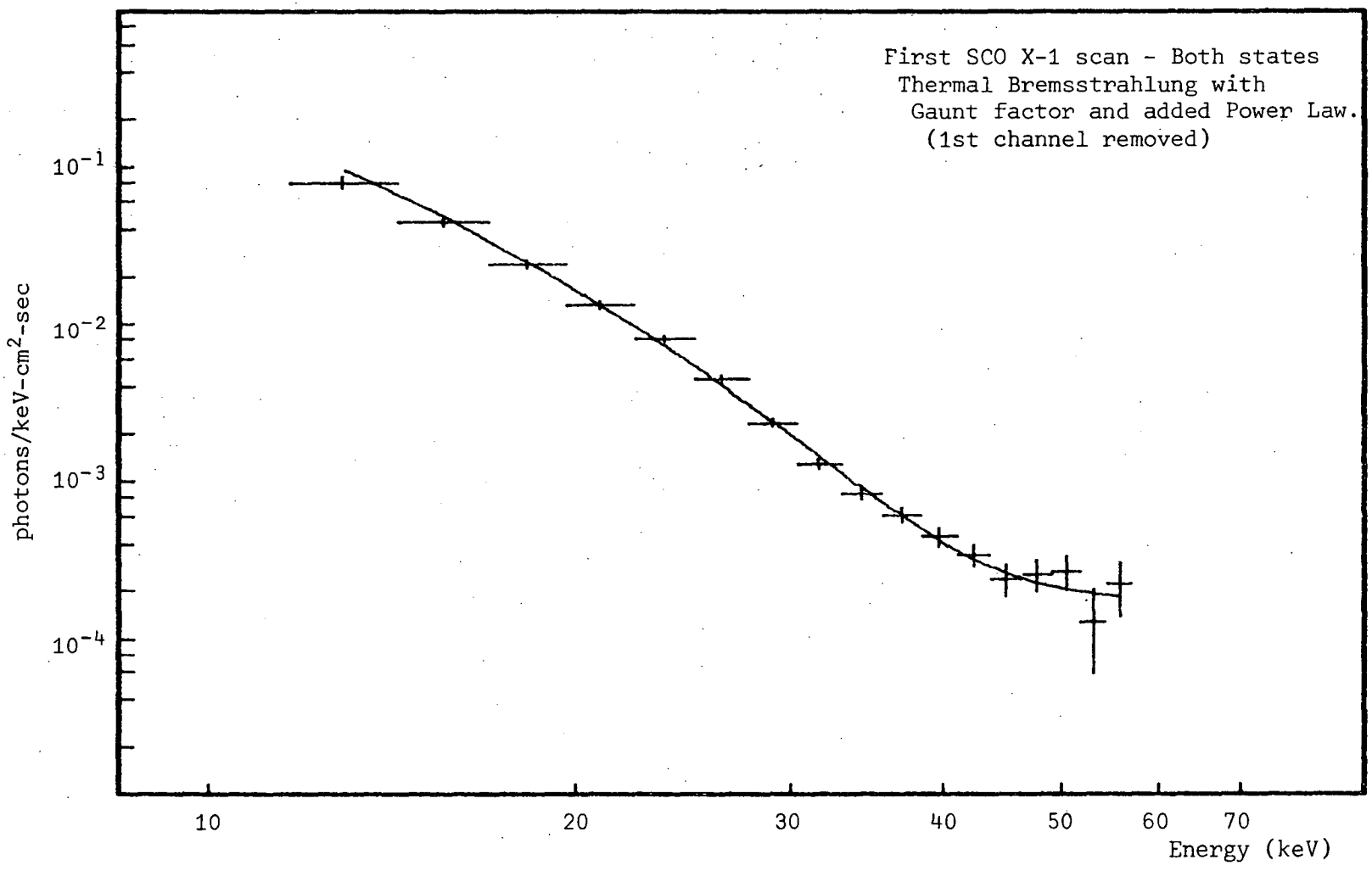
First SCO X-1 scan - Both states
Thermal Bremsstrahlung with
Gaunt factor and added Power Law.
(1st channel removed)
photons/keV-cm^2-sec
10^{-1}
10^{-2}
10^{-3}
10^{-4}
10
20
30
40
50
60
70
Energy (keV)

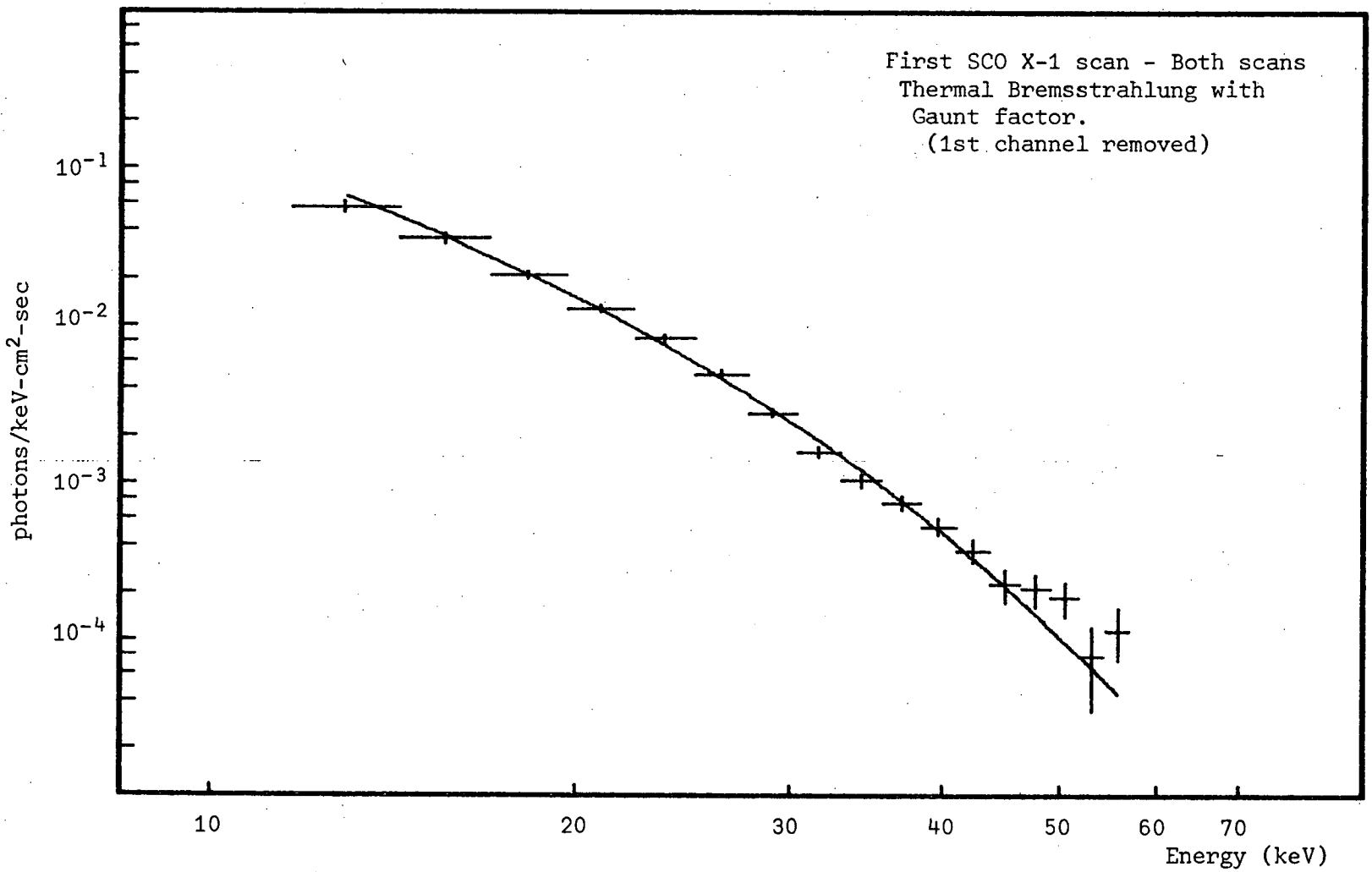
First SCO X-1 scan - Both scans
Thermal Bremsstrahlung with
Gaunt factor.
(1st channel removed)
photons/keV-cm^2-sec
10^{-1}
10^{-2}
10^{-3}
10^{-4}
10
20
30
40
50
60
70
Energy (keV)

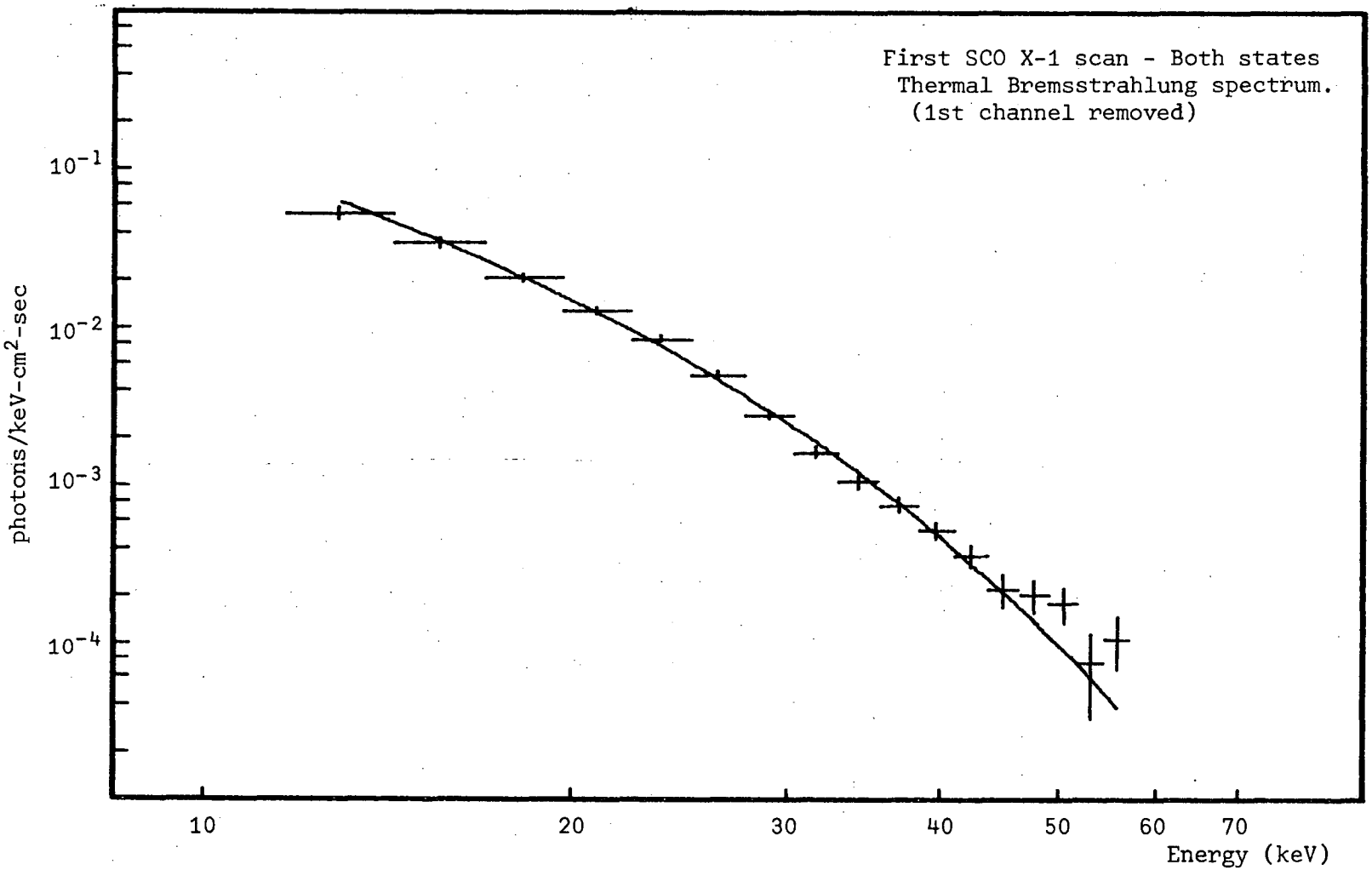
First SCO X-1 scan - Both states
Thermal Bremsstrahlung spectrum.
(1st channel removed)
photons/keV-cm^2-sec
10^{-1}
10^{-2}
10^{-3}
10^{-4}
10
20
30
40
50
60
70
Energy (keV)

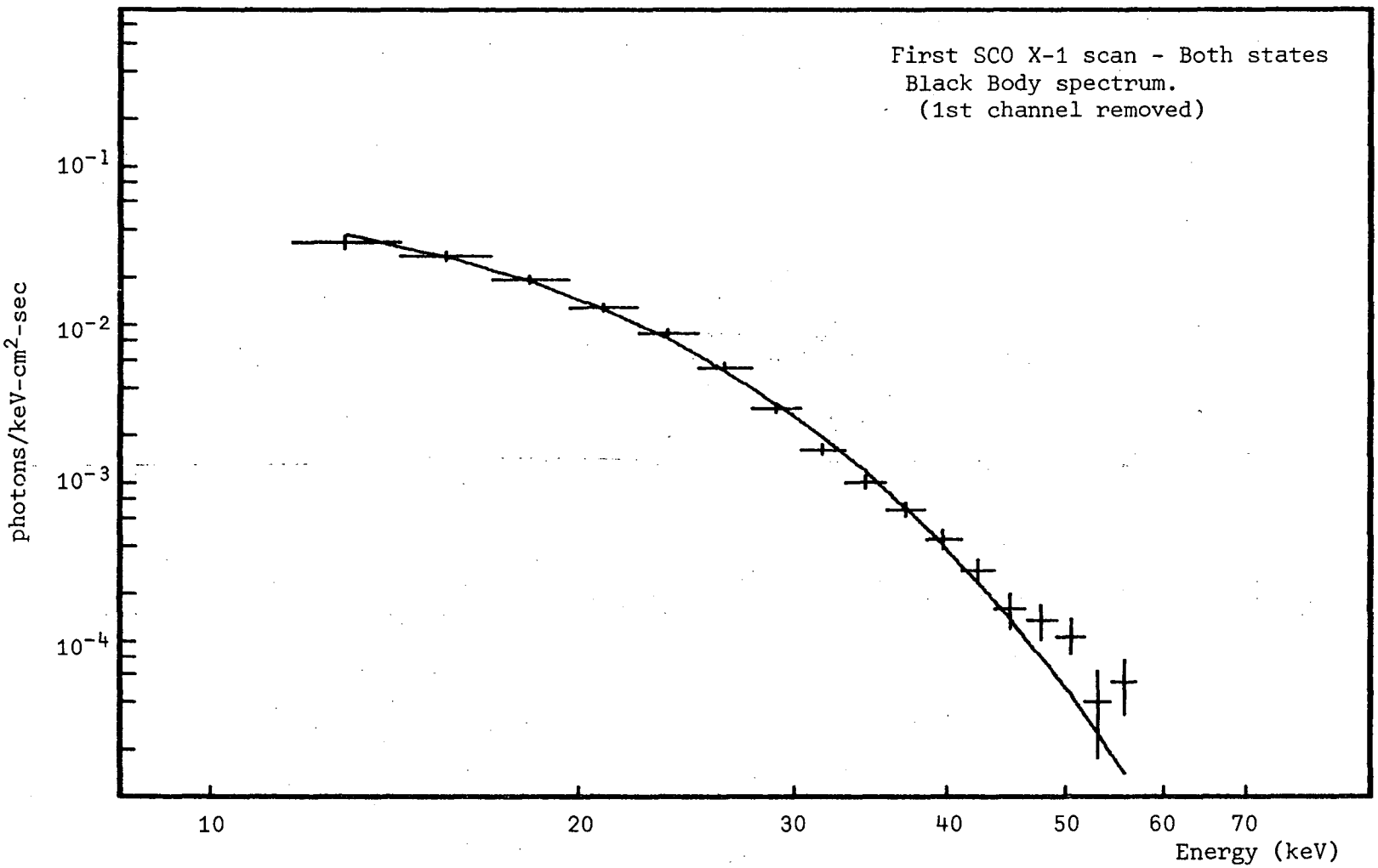
First SCO X-1 scan - Both states
Black Body spectrum.
(1st channel removed)
photons/keV-cm^2-sec
10^{-1}
10^{-2}
10^{-3}
10^{-4}
10
20
30
40
50
60
70
Energy (keV)

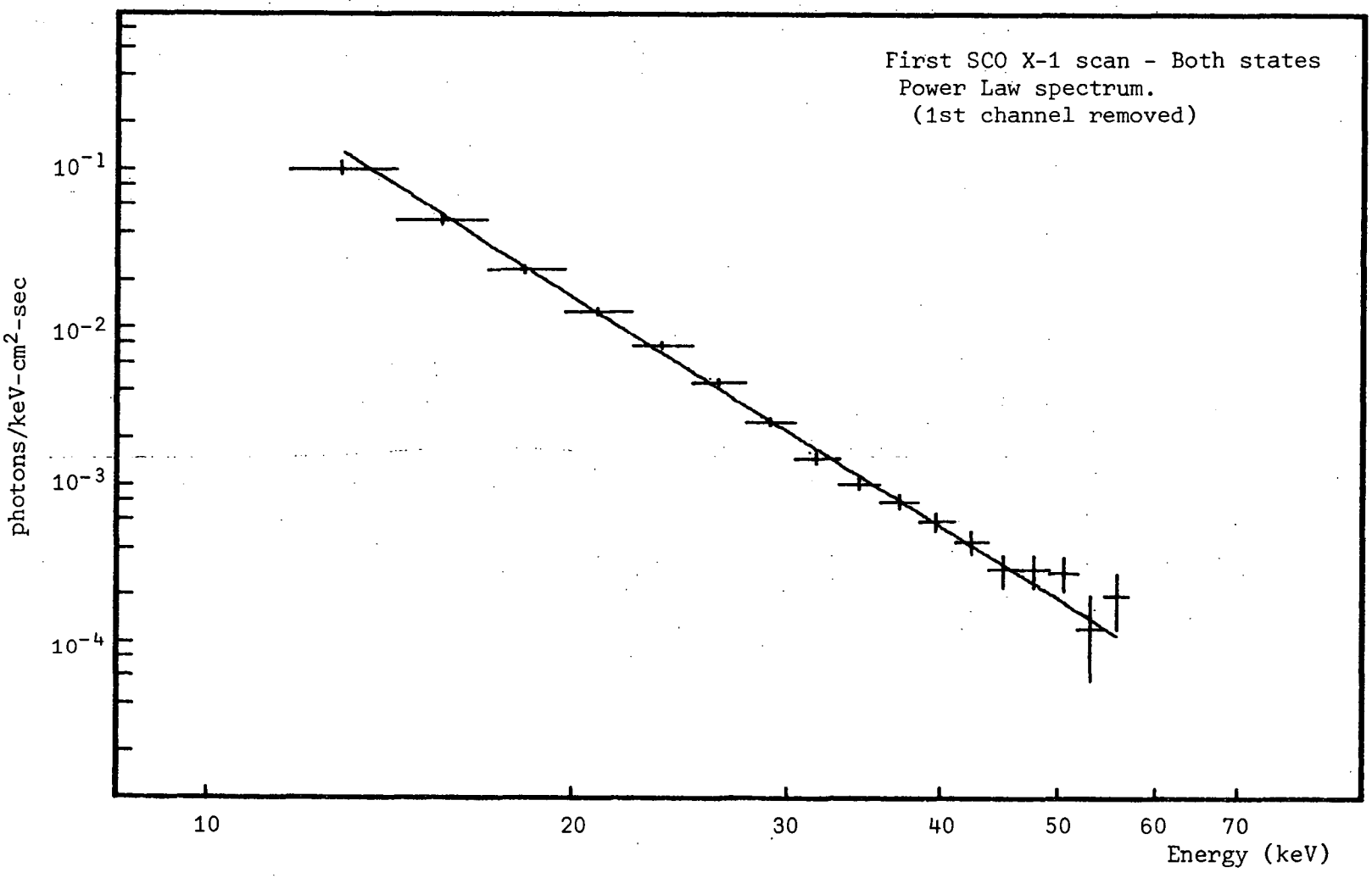
First SCO X-1 scan - Both states
Power Law spectrum.
(1st channel removed)
photons/keV-cm^2-sec
10^{-1}
10^{-2}
10^{-3}
10^{-4}
10
20
30
40
50
60
70
Energy (keV)

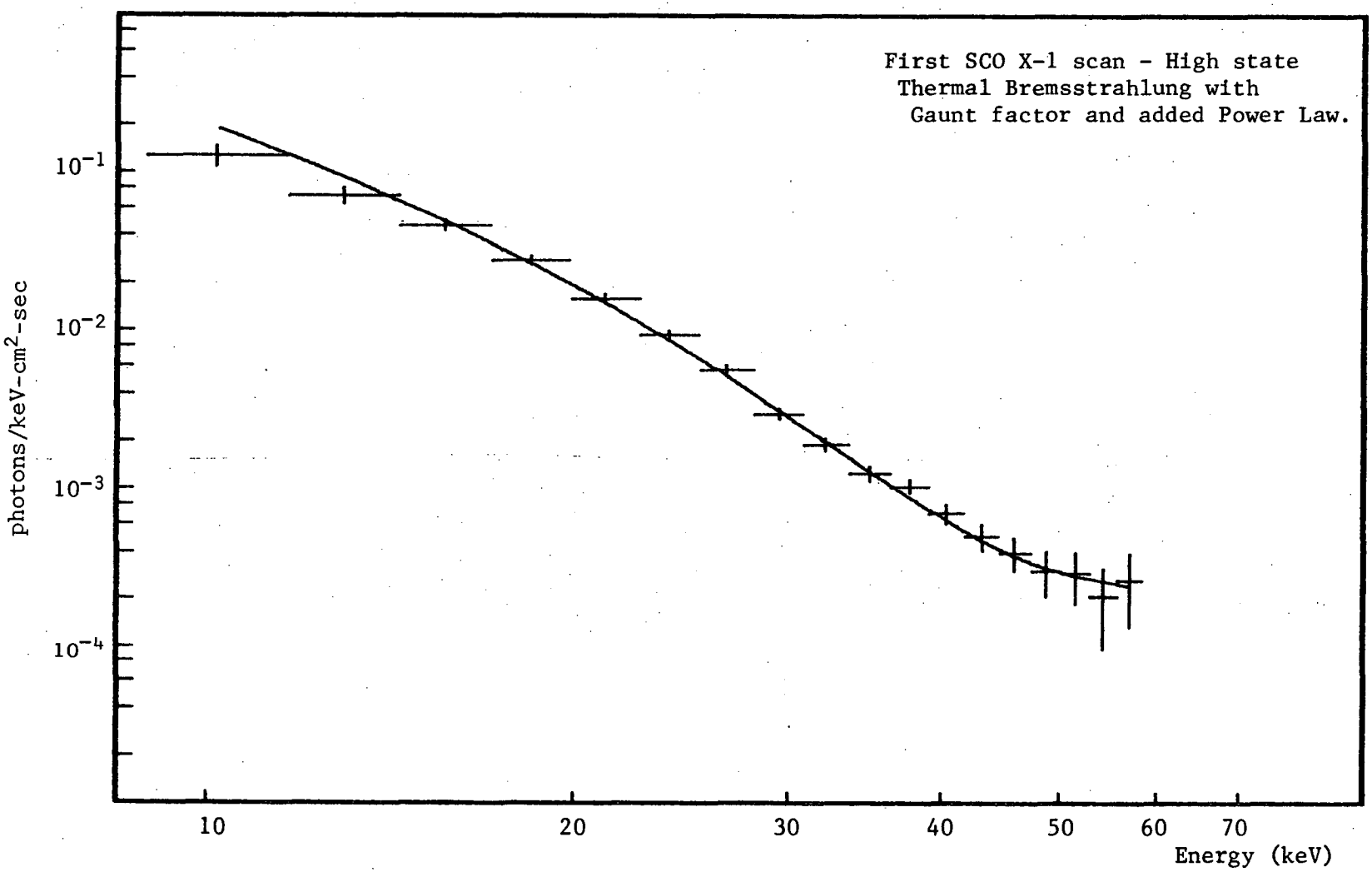
First SCO X-1 scan - High state
Thermal Bremsstrahlung with
Gaunt factor and added Power Law.
photons/keV-cm^2-sec
10^{-1}
10^{-2}
10^{-3}
10^{-4}
10
20
30
40
50
60
70
Energy (keV)

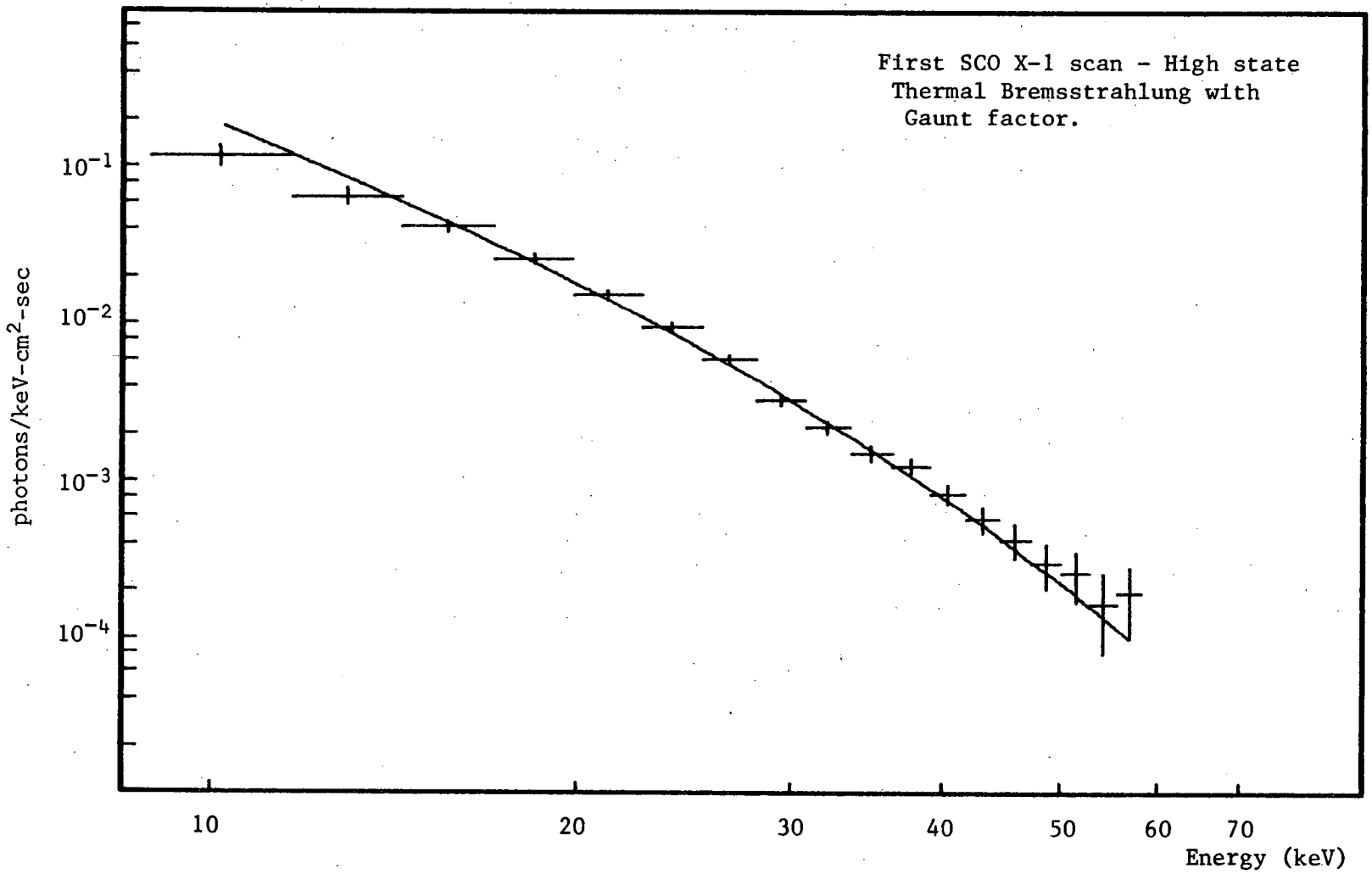
First SCO X-1 scan - High state
Thermal Bremsstrahlung with
Gaunt factor.
photons/keV-cm^2-sec
10^{-1}
10^{-2}
10^{-3}
10^{-4}
10
20
30
40
50
60
70
Energy (keV)

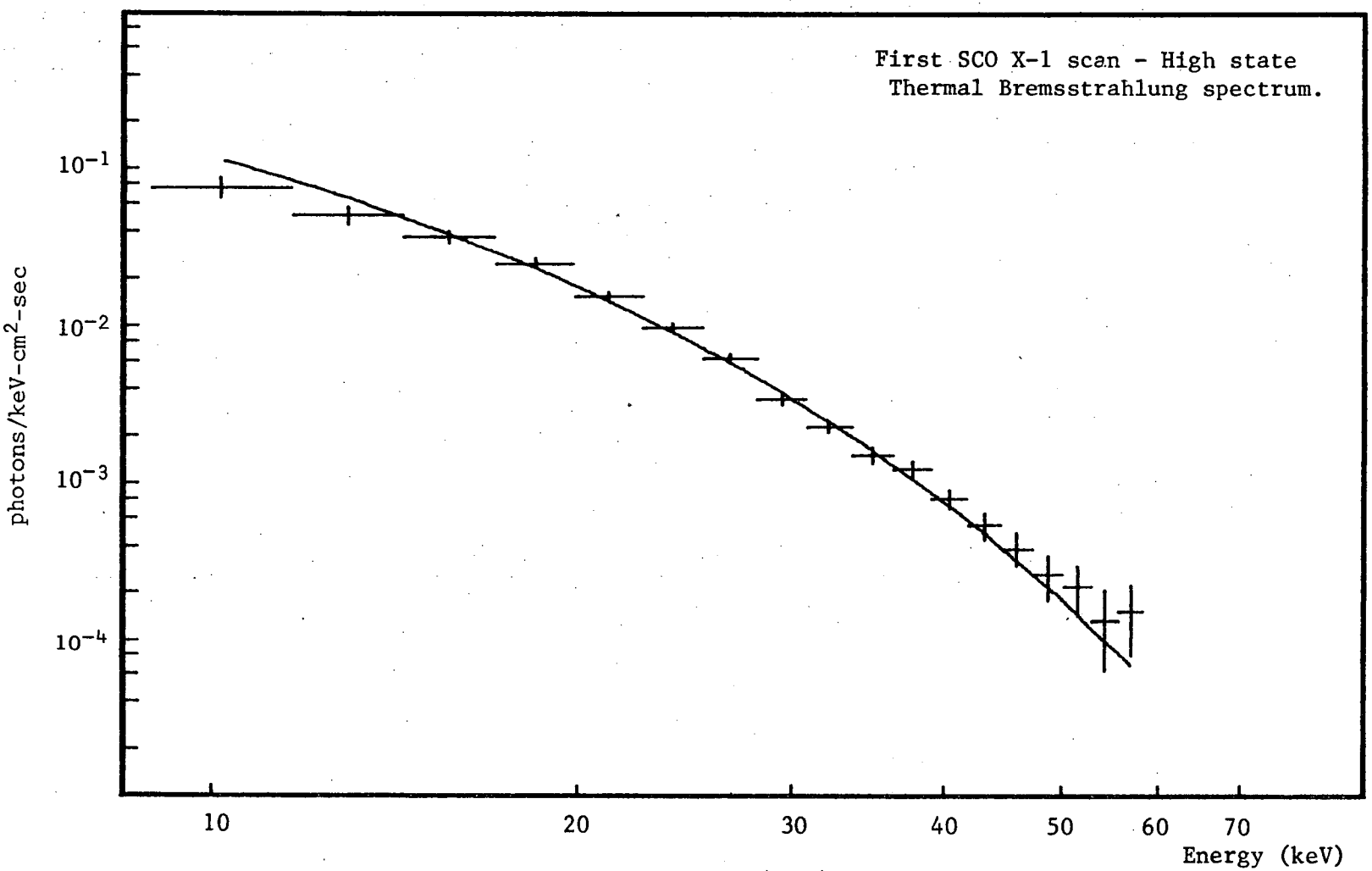
First SCO X-1 scan - High state
Thermal Bremsstrahlung spectrum.
photons/keV-cm^2-sec
10^{-1}
10^{-2}
10^{-3}
10^{-4}
10
20
30
40
50
60
70
Energy (keV)

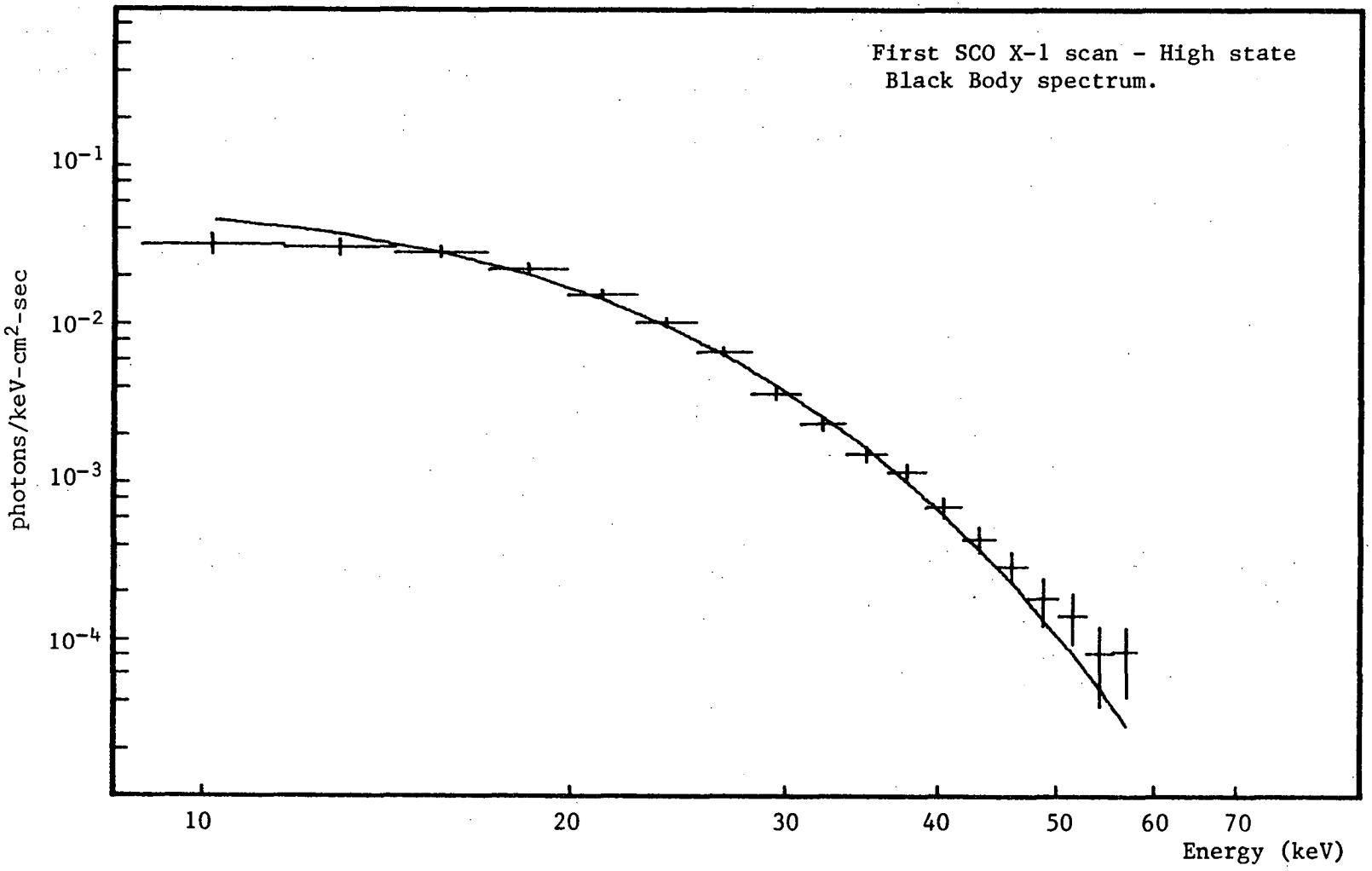
First SCO X-1 scan - High state
Black Body spectrum.
10^{-1}
10^{-2}
10^{-3}
10^{-4}
photons/keV-cm^2-sec
10
20
30
40
50
60
70
Energy (keV)

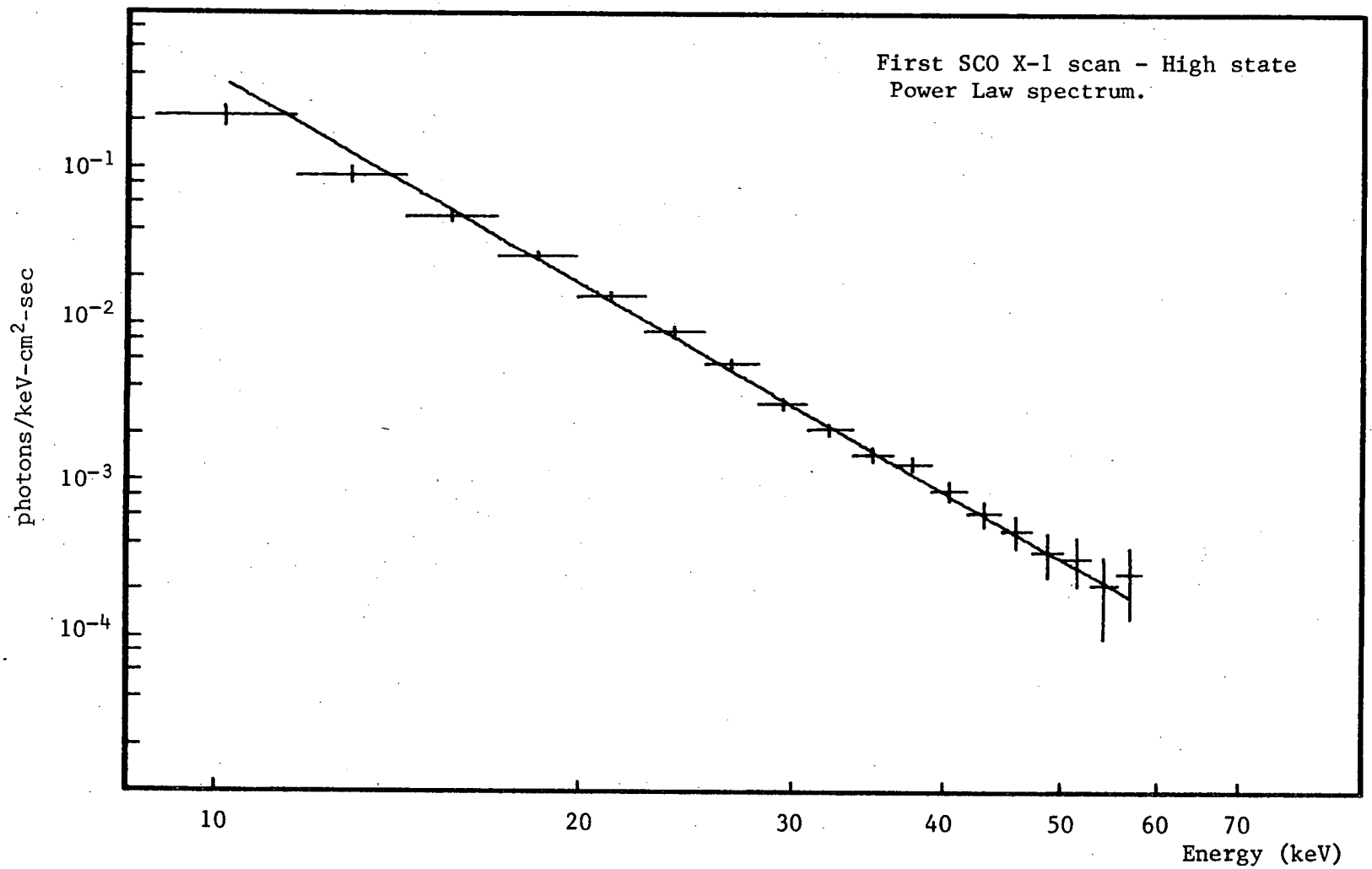
First SCO X-1 scan - High state
Power Law spectrum.
photons/keV-cm^2-sec
10^{-1}
10^{-2}
10^{-3}
10^{-4}
10
20
30
40
50
60
70
Energy (keV)

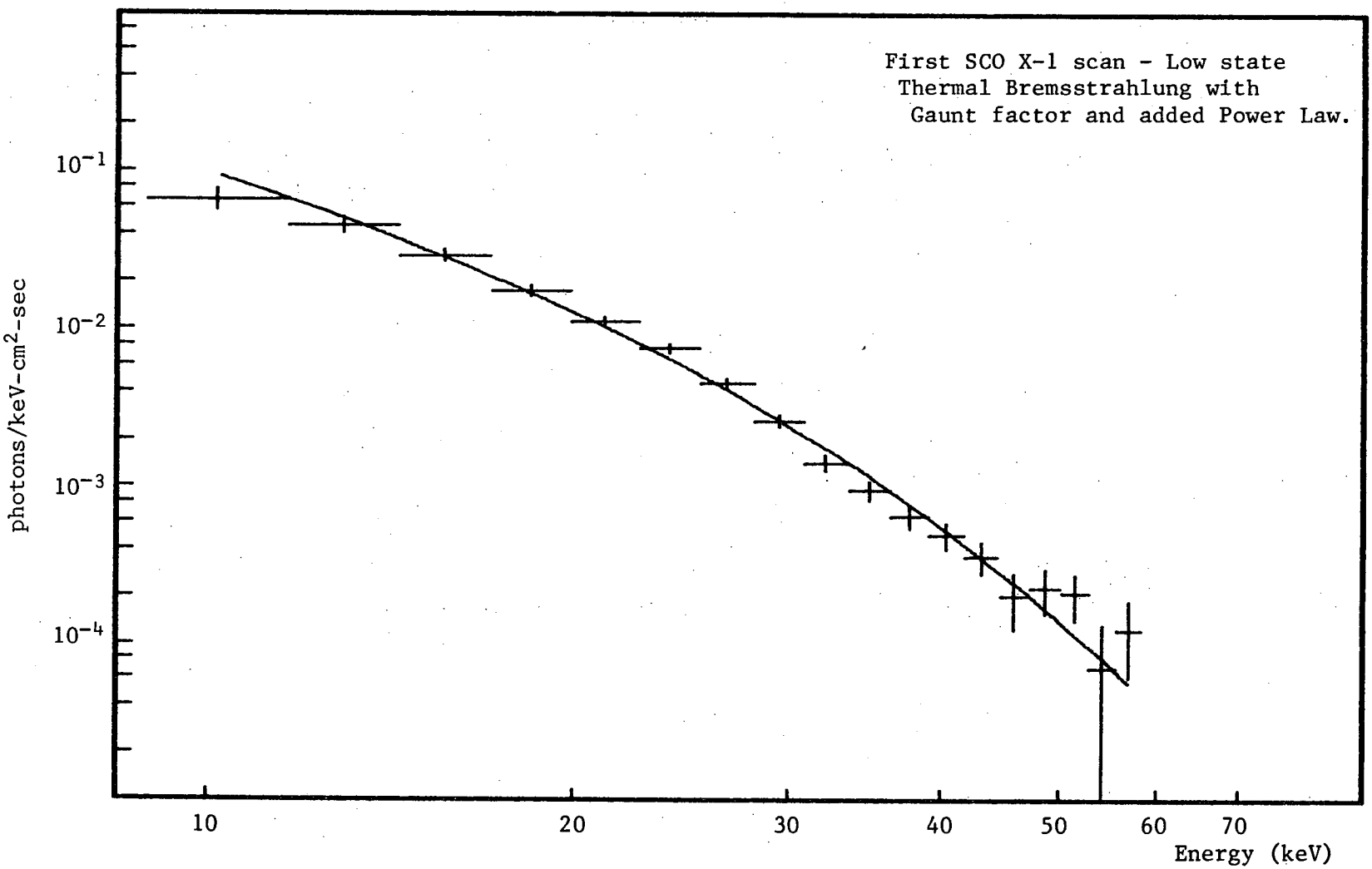
First SCO X-1 scan - Low state
Thermal Bremsstrahlung with
Gaunt factor and added Power Law.
photons/keV-cm^2-sec
10^{-1}
10^{-2}
10^{-3}
10^{-4}
10
20
30
40
50
60
70
Energy (keV)

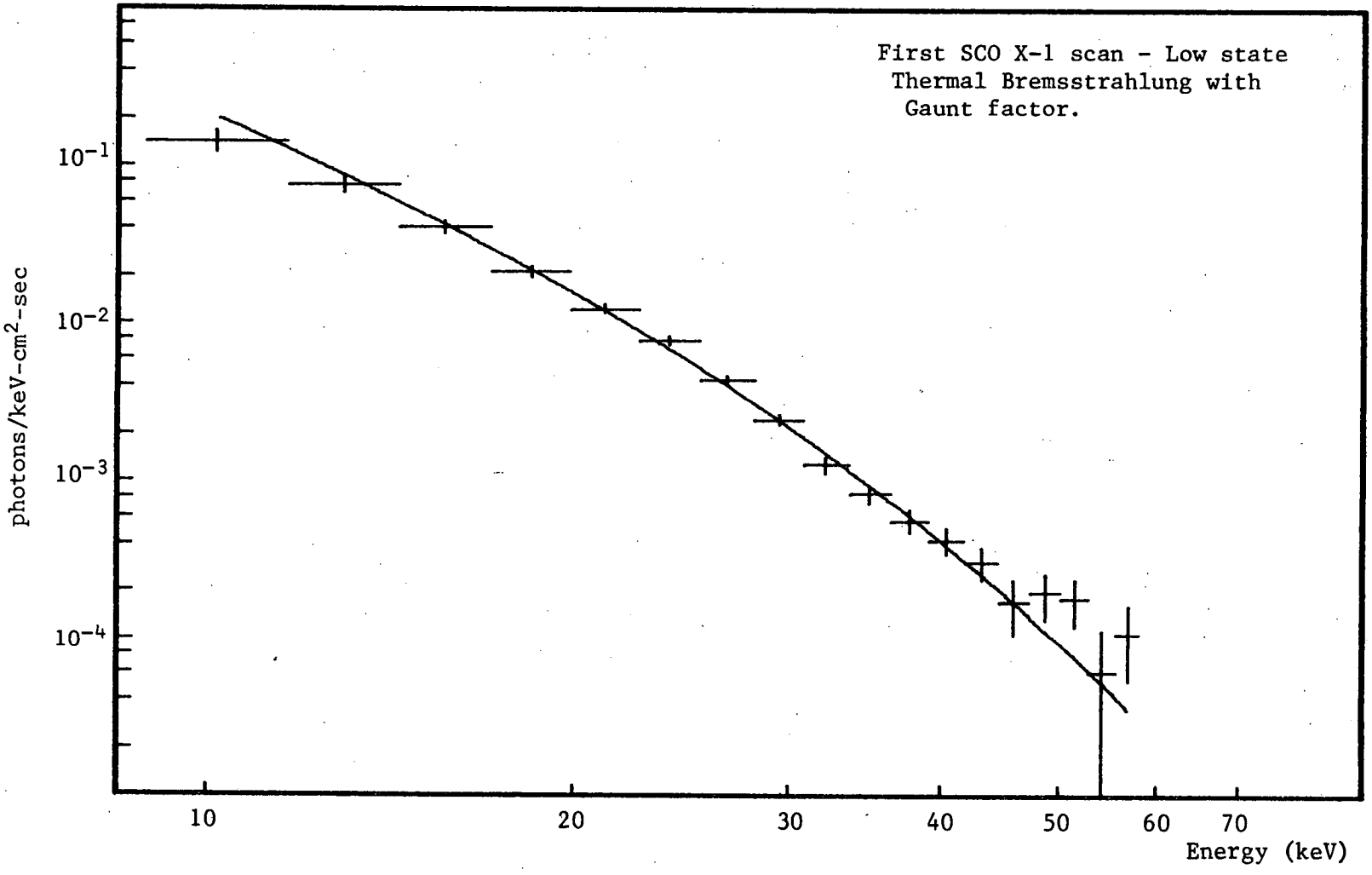
First SCO X-1 scan - Low state
Thermal Bremsstrahlung with
Gaunt factor.
photons/keV-cm^2-sec
10^{-1}
10^{-2}
10^{-3}
10^{-4}
10
20
30
40
50
60
70
Energy (keV)

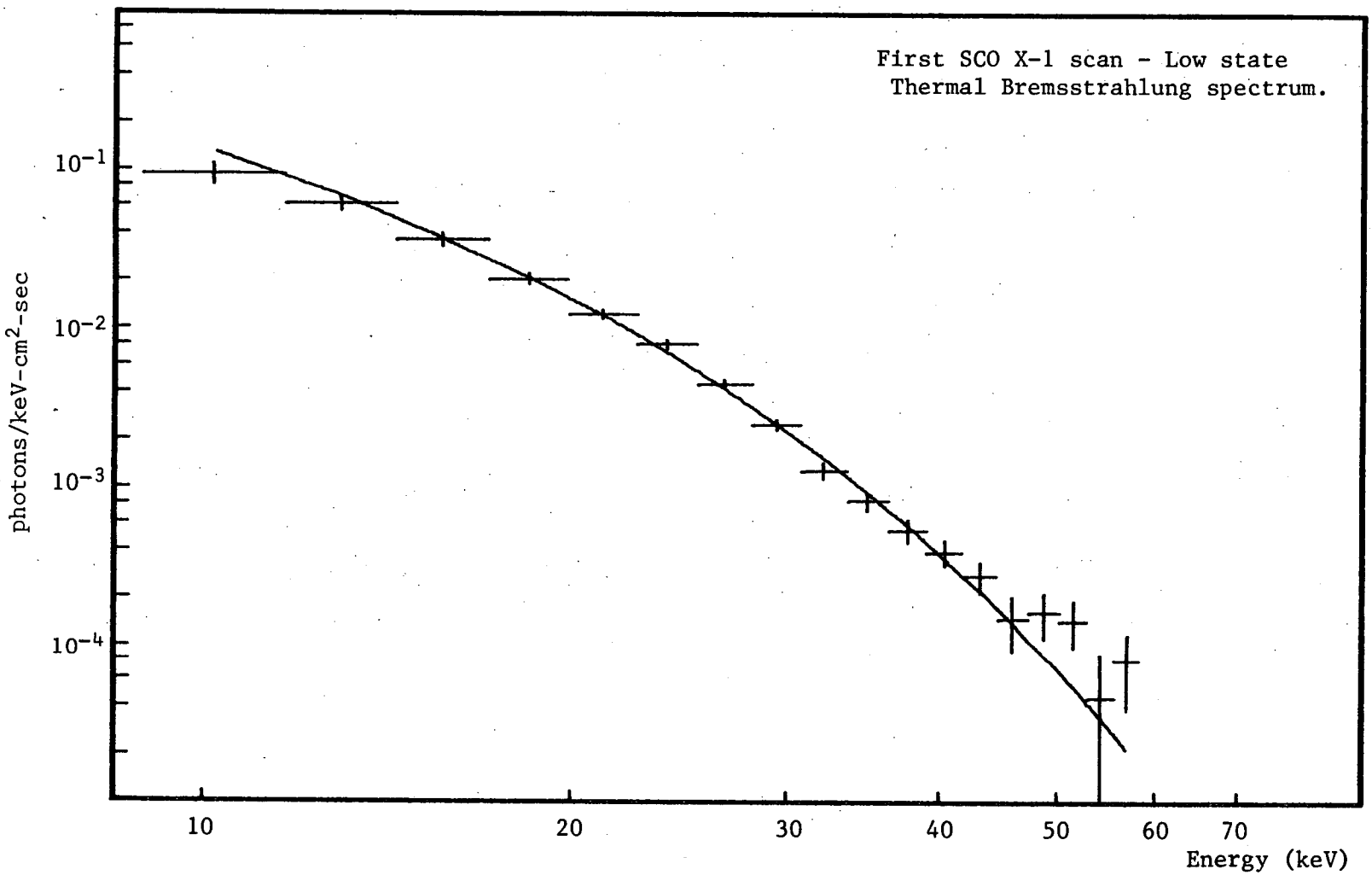
First SCO X-1 scan - Low state
Thermal Bremsstrahlung spectrum.
photons/keV-cm^2-sec
10^{-1}
10^{-2}
10^{-3}
10^{-4}
10
20
30
40
50
60
70
Energy (keV)

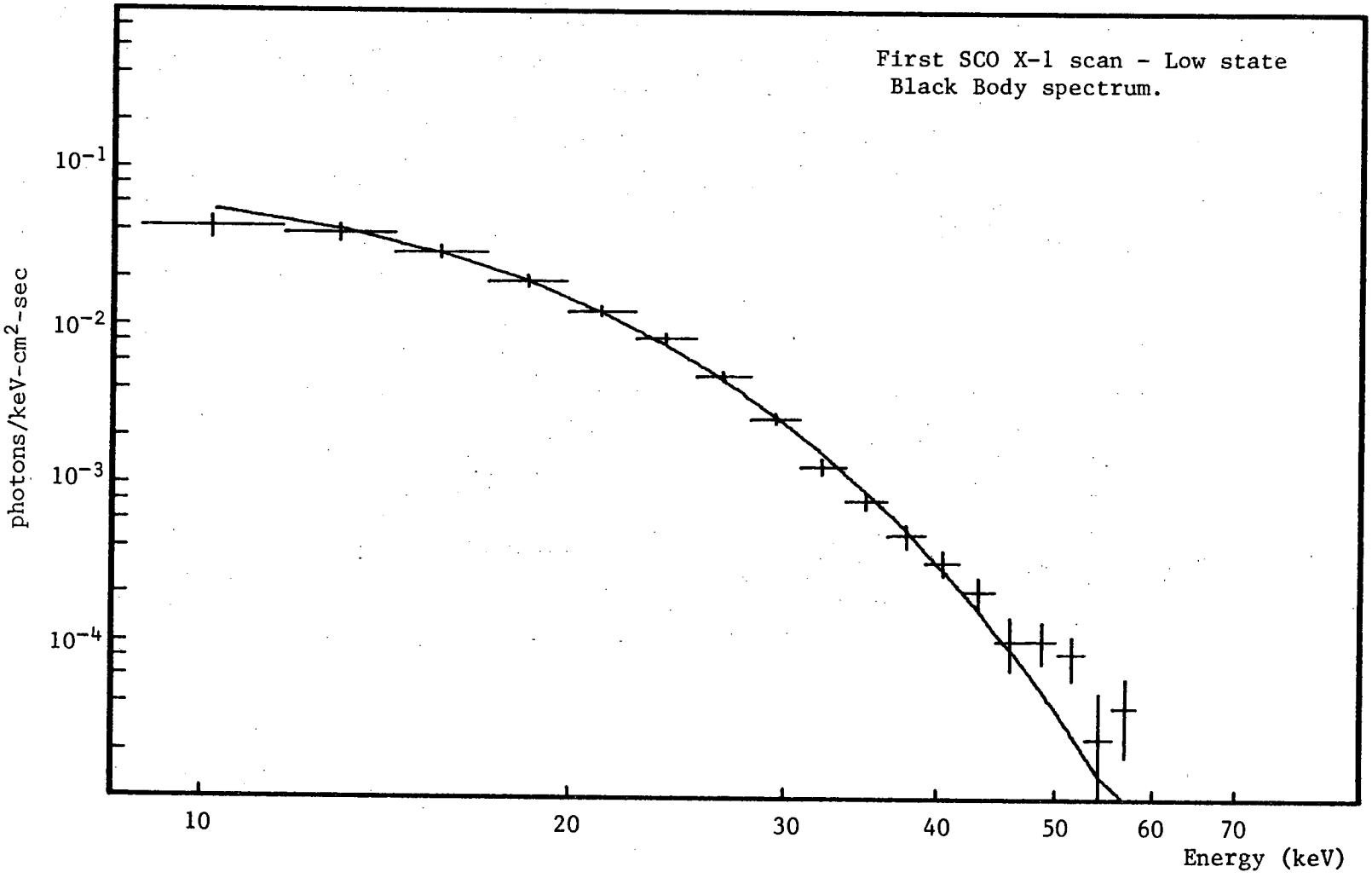
First SCO X-1 scan - Low state
Black Body spectrum.
photons/keV-cm^2-sec
10^{-1}
10^{-2}
10^{-3}
10^{-4}
10
20
30
40
50
60
70
Energy (keV)

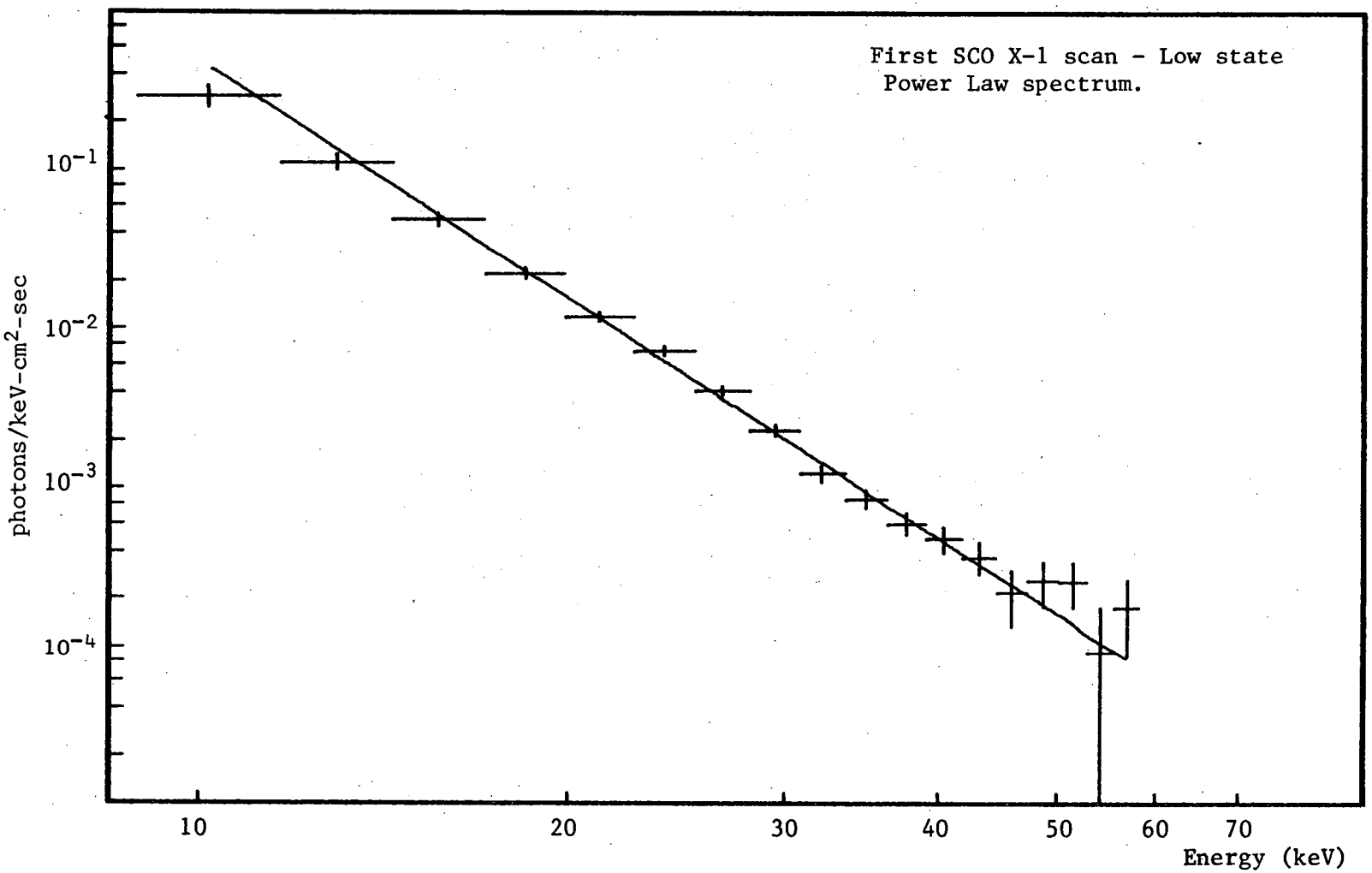
First SCO X-1 scan - Low state
Power Law spectrum.
photons/keV-cm^2-sec
10^{-1}
10^{-2}
10^{-3}
10^{-4}
10
20
30
40
50
60
70
Energy (keV)

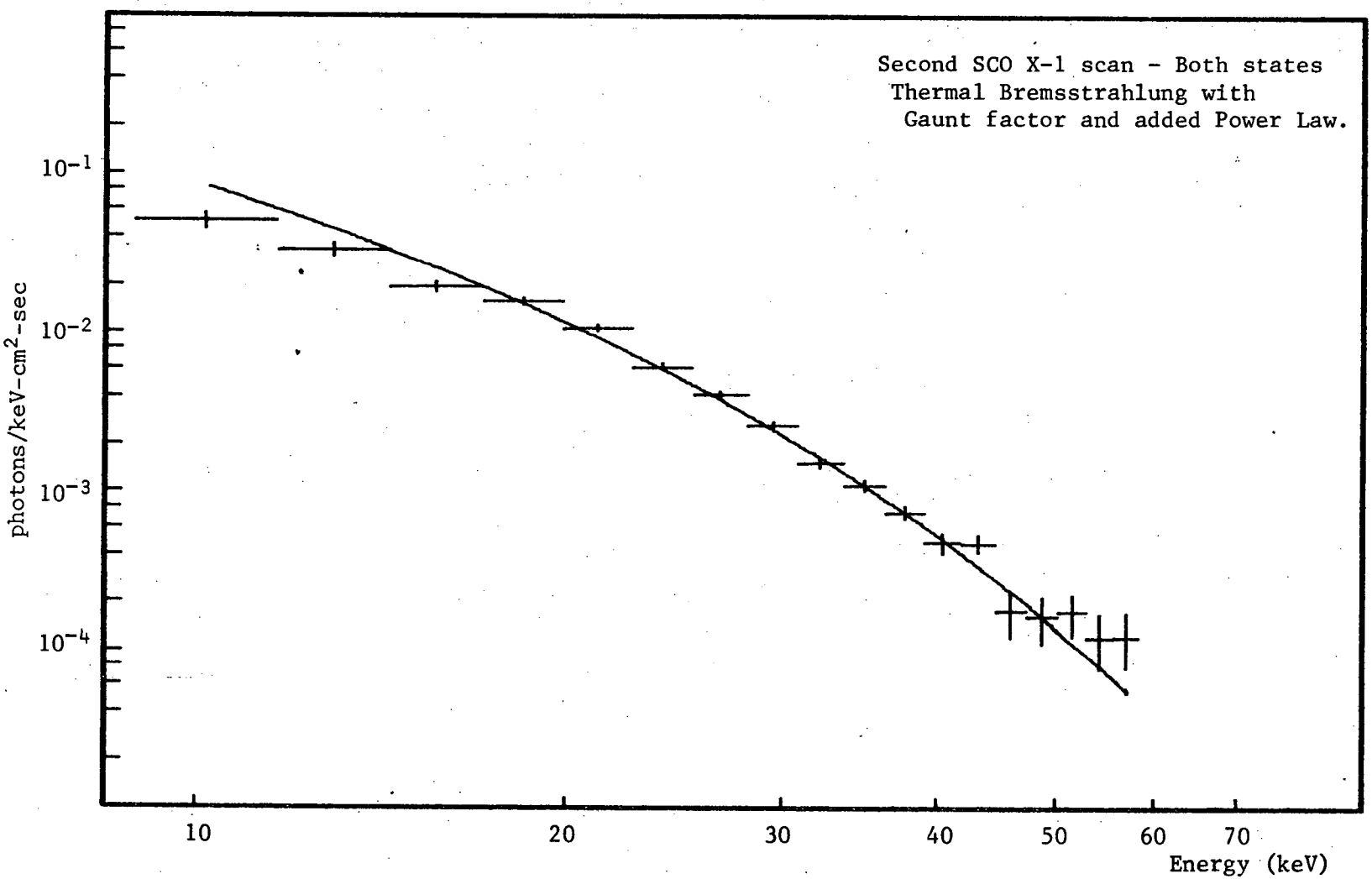
Second SCO X-1 scan - Both states
Thermal Bremsstrahlung with
Gaunt factor and added Power Law.
photons/keV-cm^2-sec
10^{-1}
10^{-2}
10^{-3}
10^{-4}
10
20
30
40
50
60
70
Energy (keV)

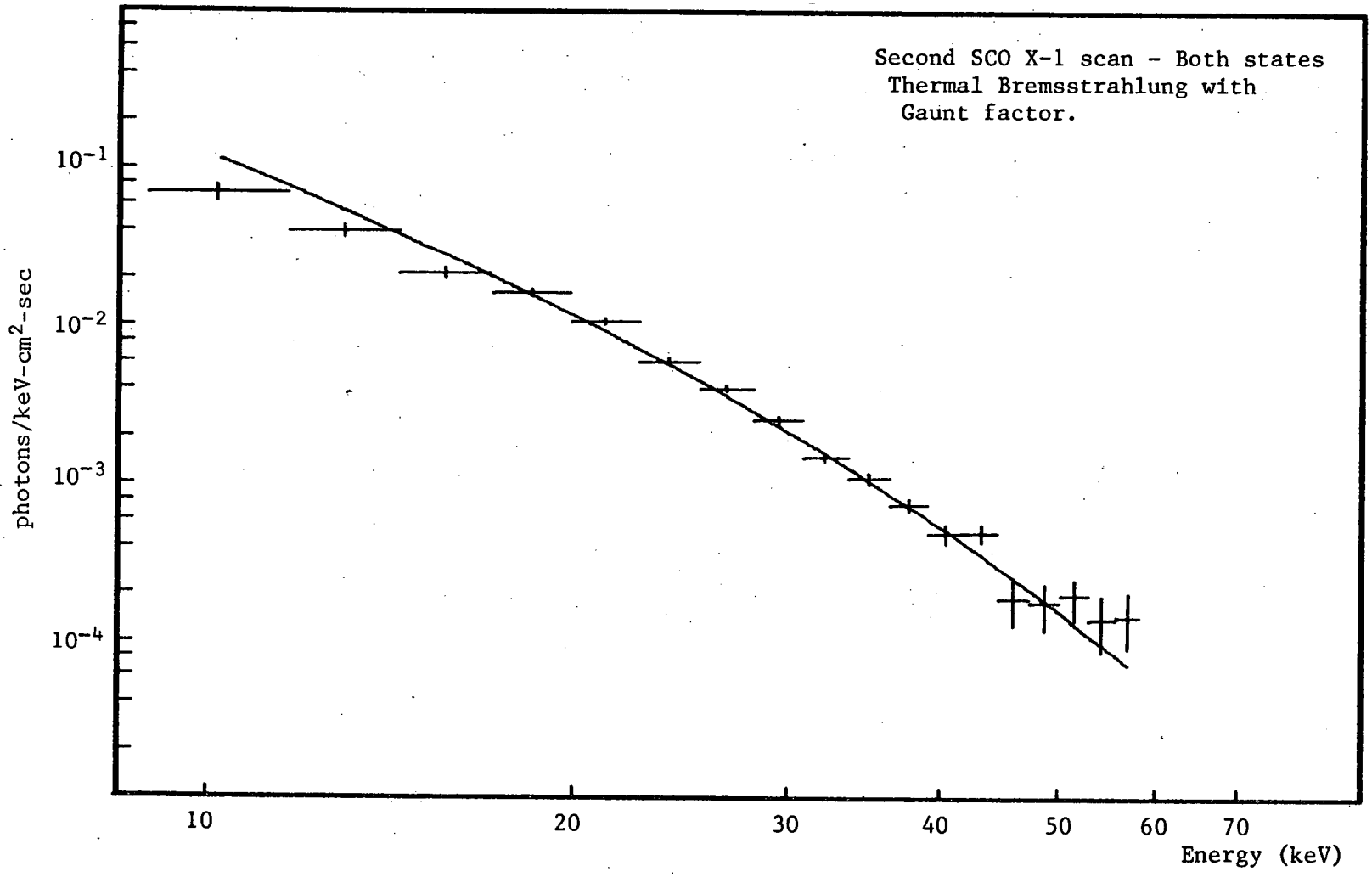
Second SCO X-1 scan - Both states
Thermal Bremsstrahlung with
Gaunt factor.
photons/keV-cm^2-sec
10^{-1}
10^{-2}
10^{-3}
10^{-4}
10
20
30
40
50
60
70
Energy (keV)

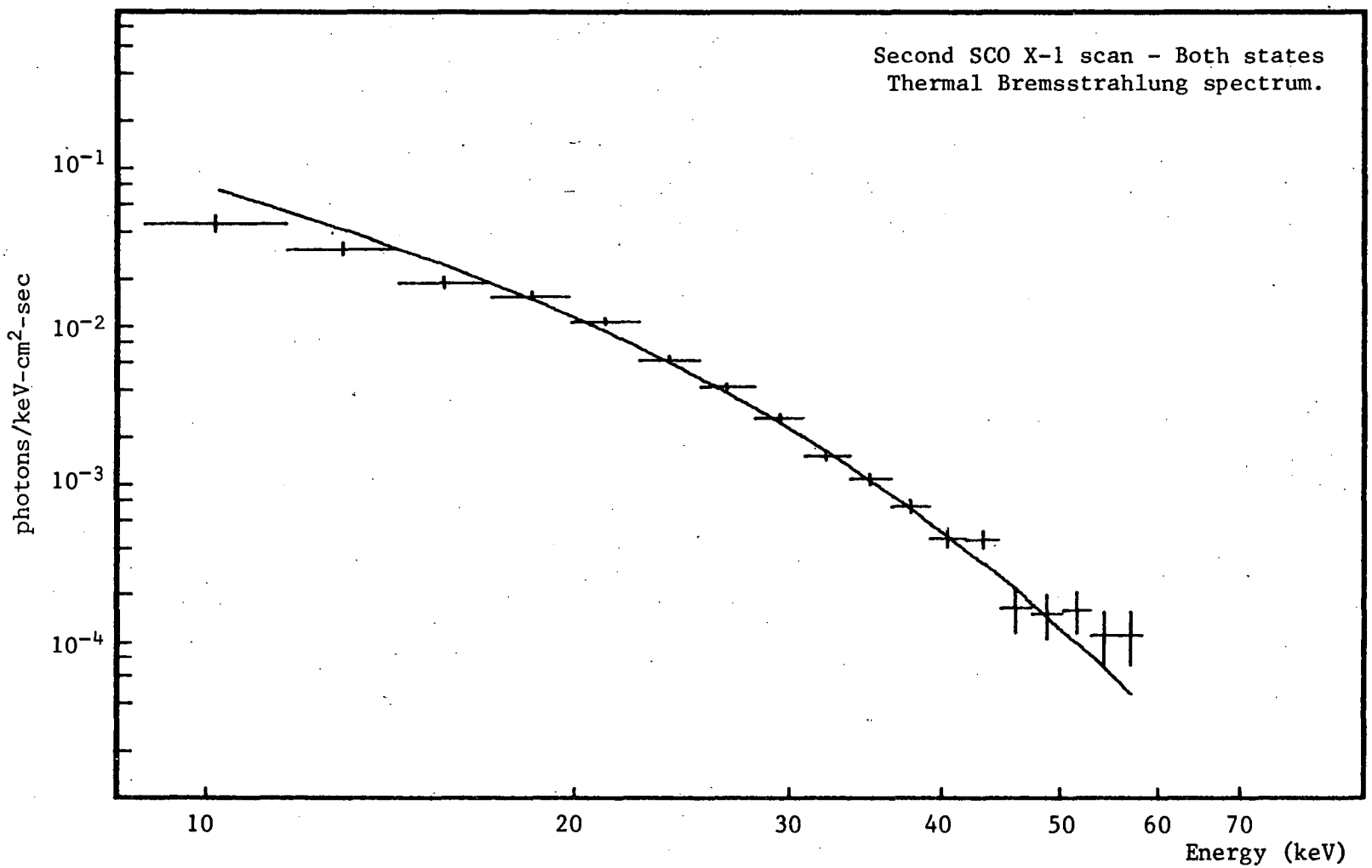
Second SCO X-1 scan - Both states
Thermal Bremsstrahlung spectrum.
photons/keV-cm^2-sec
10^{-1}
10^{-2}
10^{-3}
10^{-4}
10
20
30
40
50
60
70
Energy (keV)

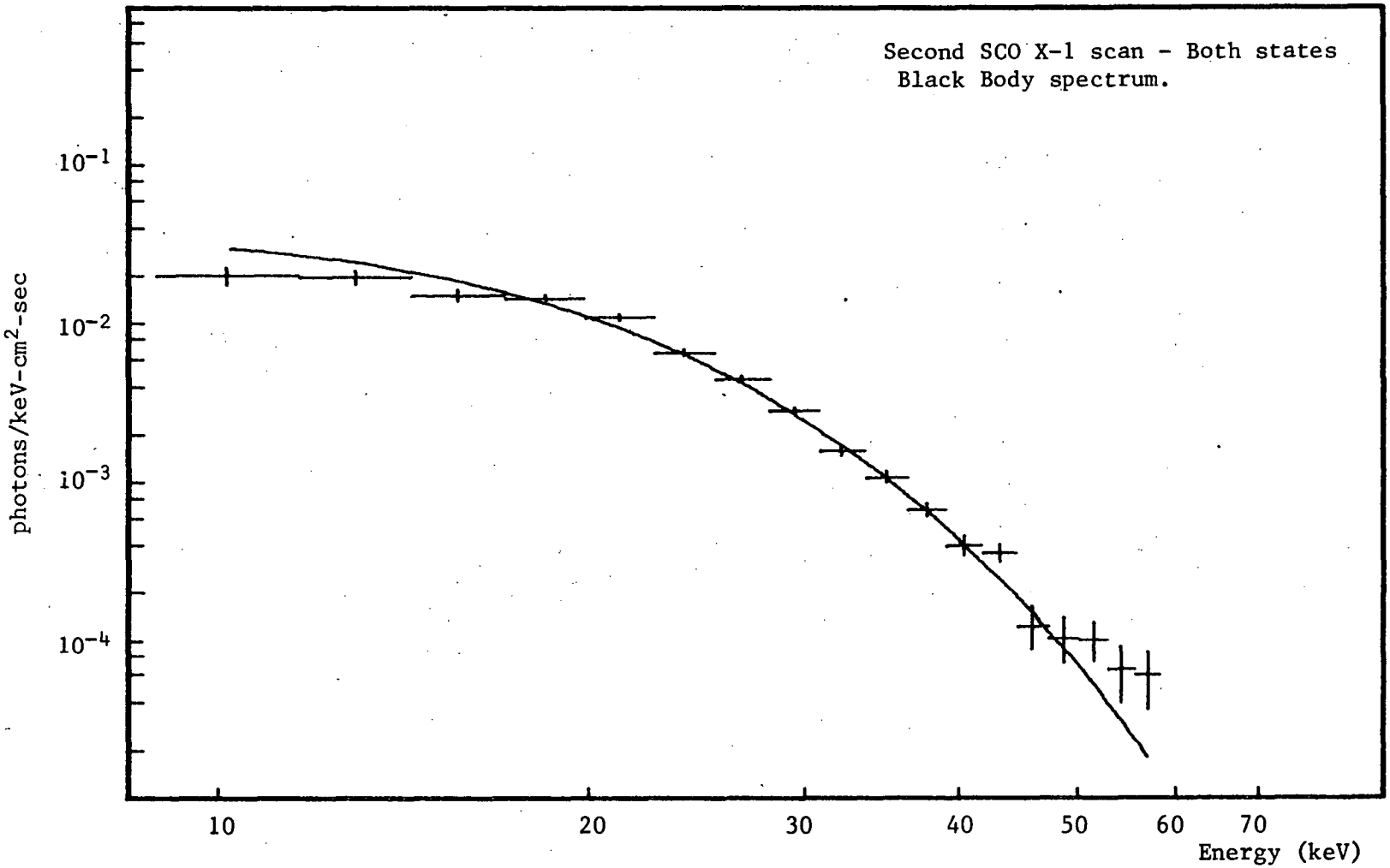
Second SCO X-1 scan - Both states
Black Body spectrum.
photons/keV-cm^2-sec
10^{-1}
10^{-2}
10^{-3}
10^{-4}
10
20
30
40
50
60
70
Energy (keV)

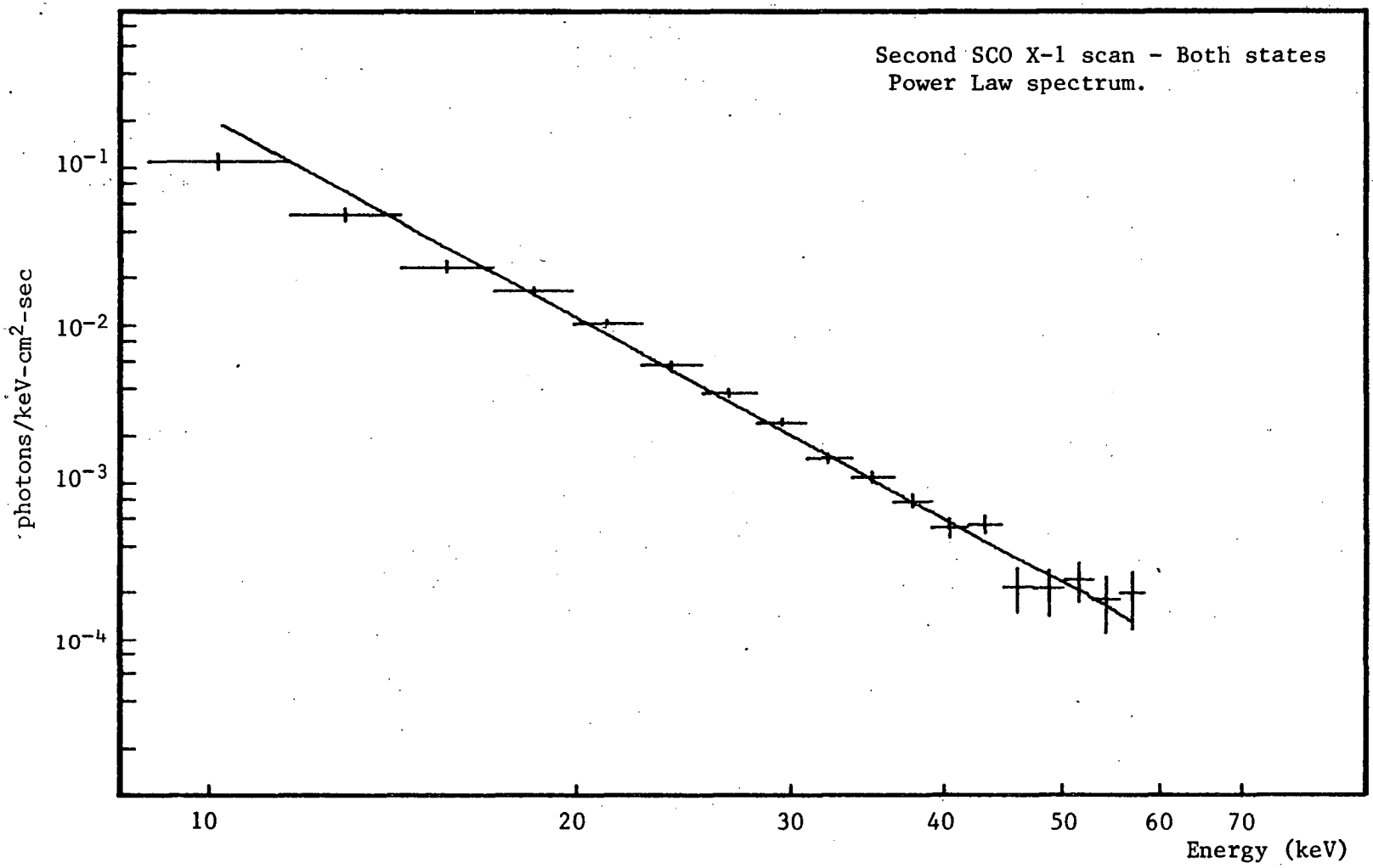
Second SCO X-1 scan - Both states
Power Law spectrum.
photons/keV-cm^2-sec
10^{-1}
10^{-2}
10^{-3}
10^{-4}
10
20
30
40
50
60
70
Energy (keV)

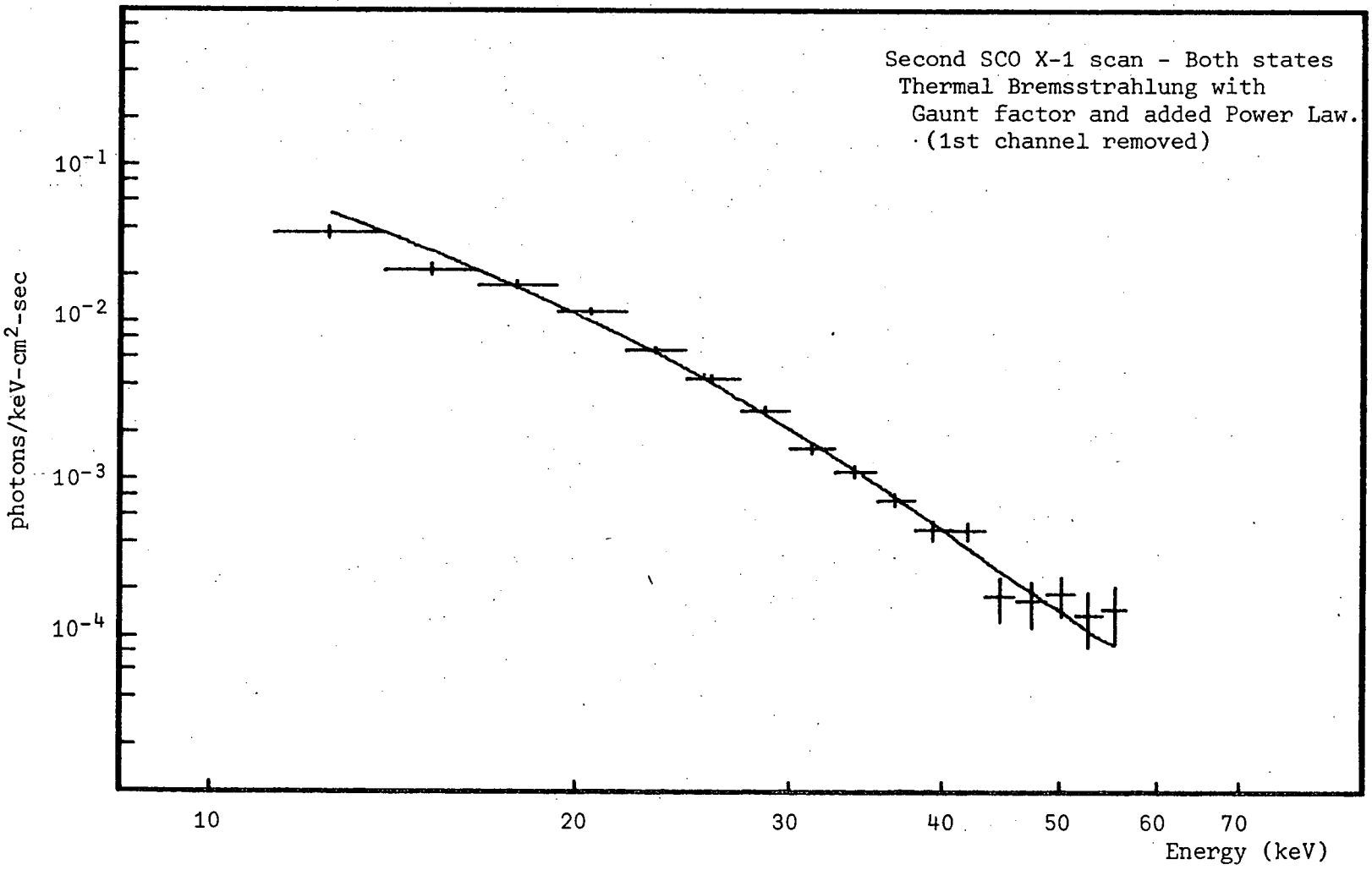
Second SCO X-1 scan - Both states
Thermal Bremsstrahlung with
Gaunt factor and added Power Law.
(1st channel removed)
photons/keV-cm^2-sec
10^{-1}
10^{-2}
10^{-3}
10^{-4}
10
20
30
40
50
60
70
Energy (keV)

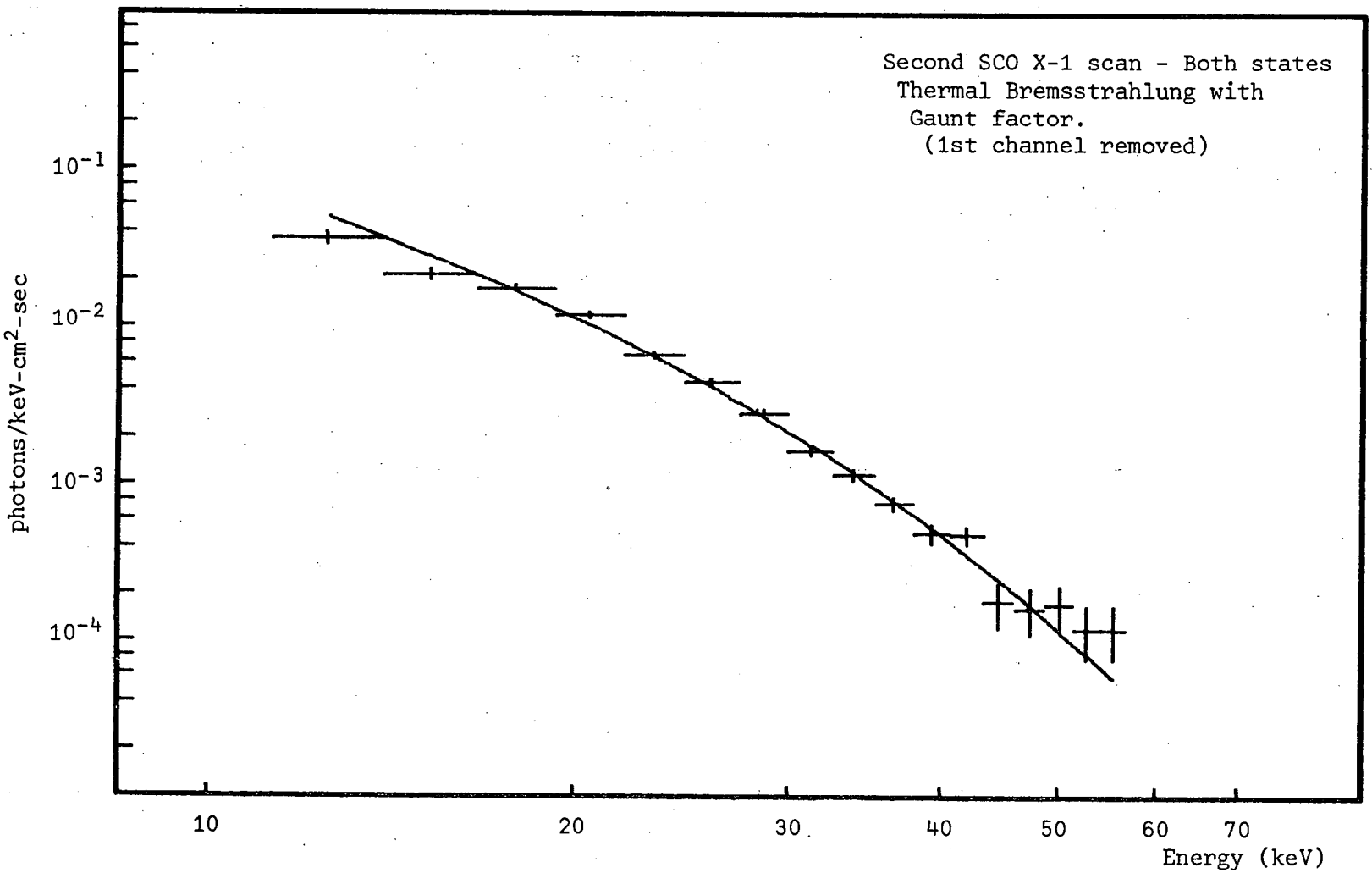
Second SCO X-1 scan - Both states
Thermal Bremsstrahlung with
Gaunt factor.
(1st channel removed)
photons/keV-cm^2-sec
10^{-1}
10^{-2}
10^{-3}
10^{-4}
10
20
30
40
50
60
70
Energy (keV)

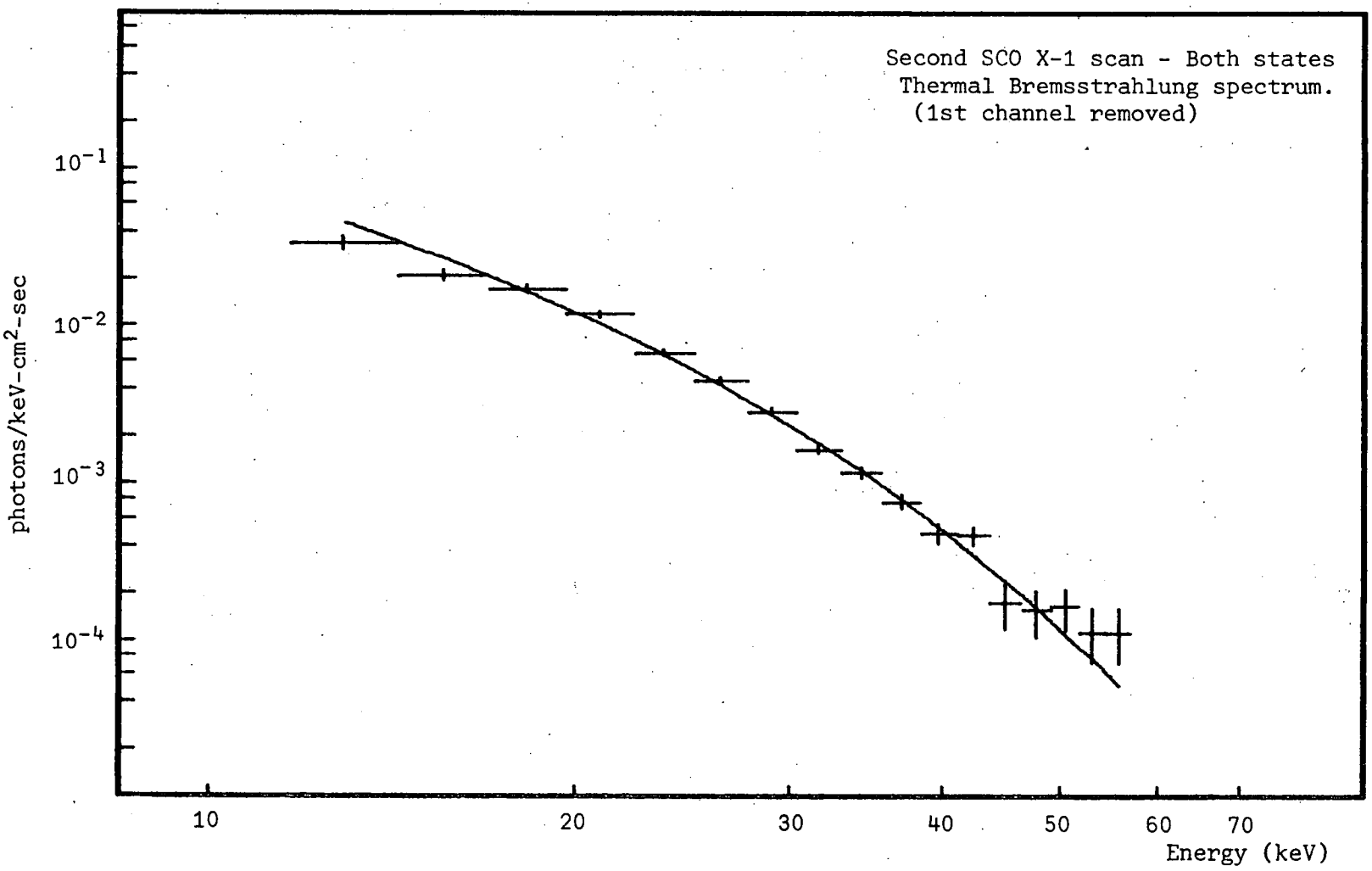
Second SCO X-1 scan - Both states
Thermal Bremsstrahlung spectrum.
(1st channel removed)
photons/keV-cm^2-sec
10^{-1}
10^{-2}
10^{-3}
10^{-4}
10
20
30
40
50
60
70
Energy (keV)

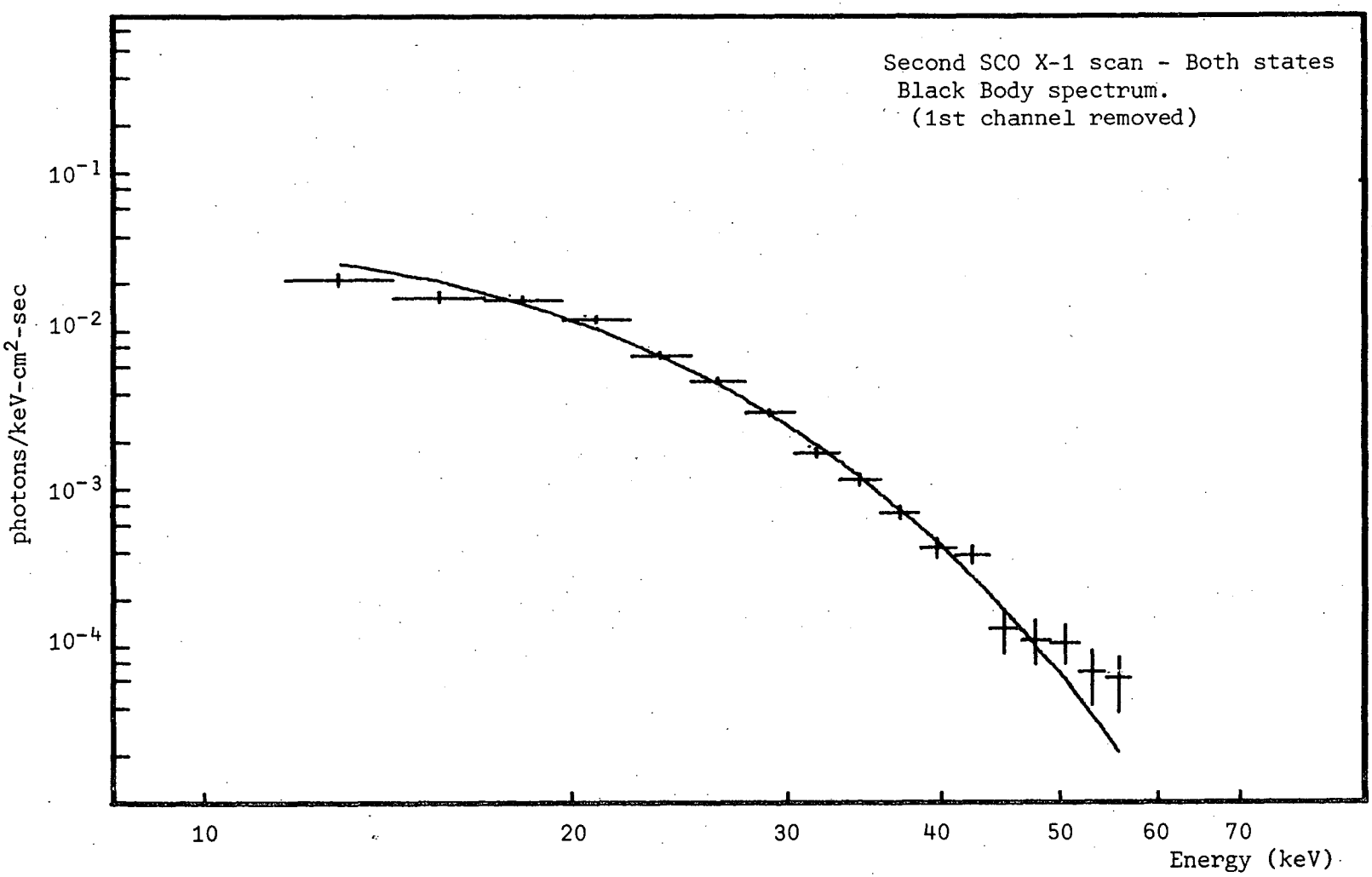
Second SCO X-1 scan - Both states
Black Body spectrum.
(1st channel removed)
photons/keV-cm^2-sec
10^{-1}
10^{-2}
10^{-3}
10^{-4}
10
20
30
40
50
60
70
Energy (keV)

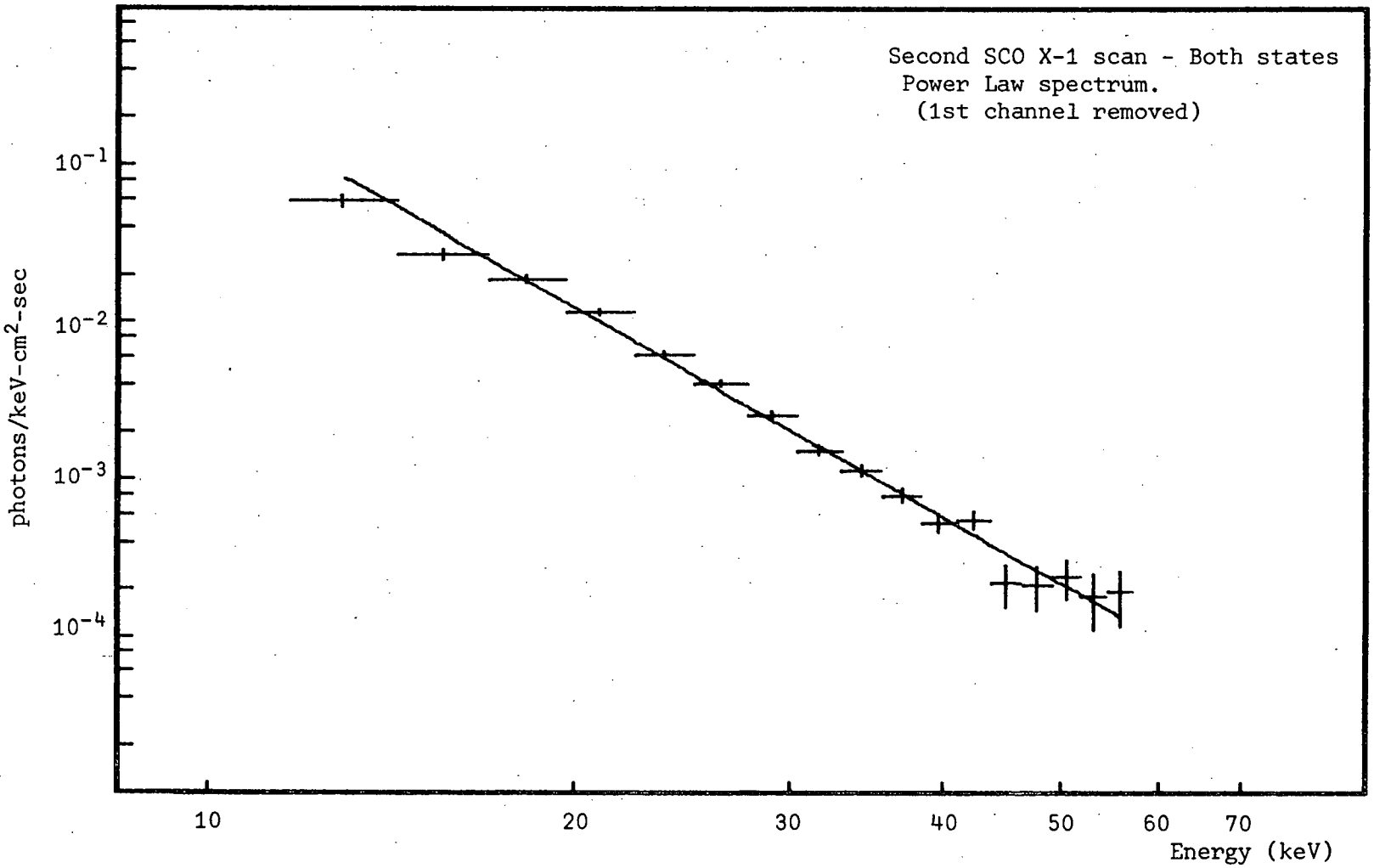
Second SCO X-1 scan - Both states
Power Law spectrum.
(1st channel removed)
photons/keV-cm^2-sec
10^{-1}
10^{-2}
10^{-3}
10^{-4}
10
20
30
40
50
60
70
Energy (keV)

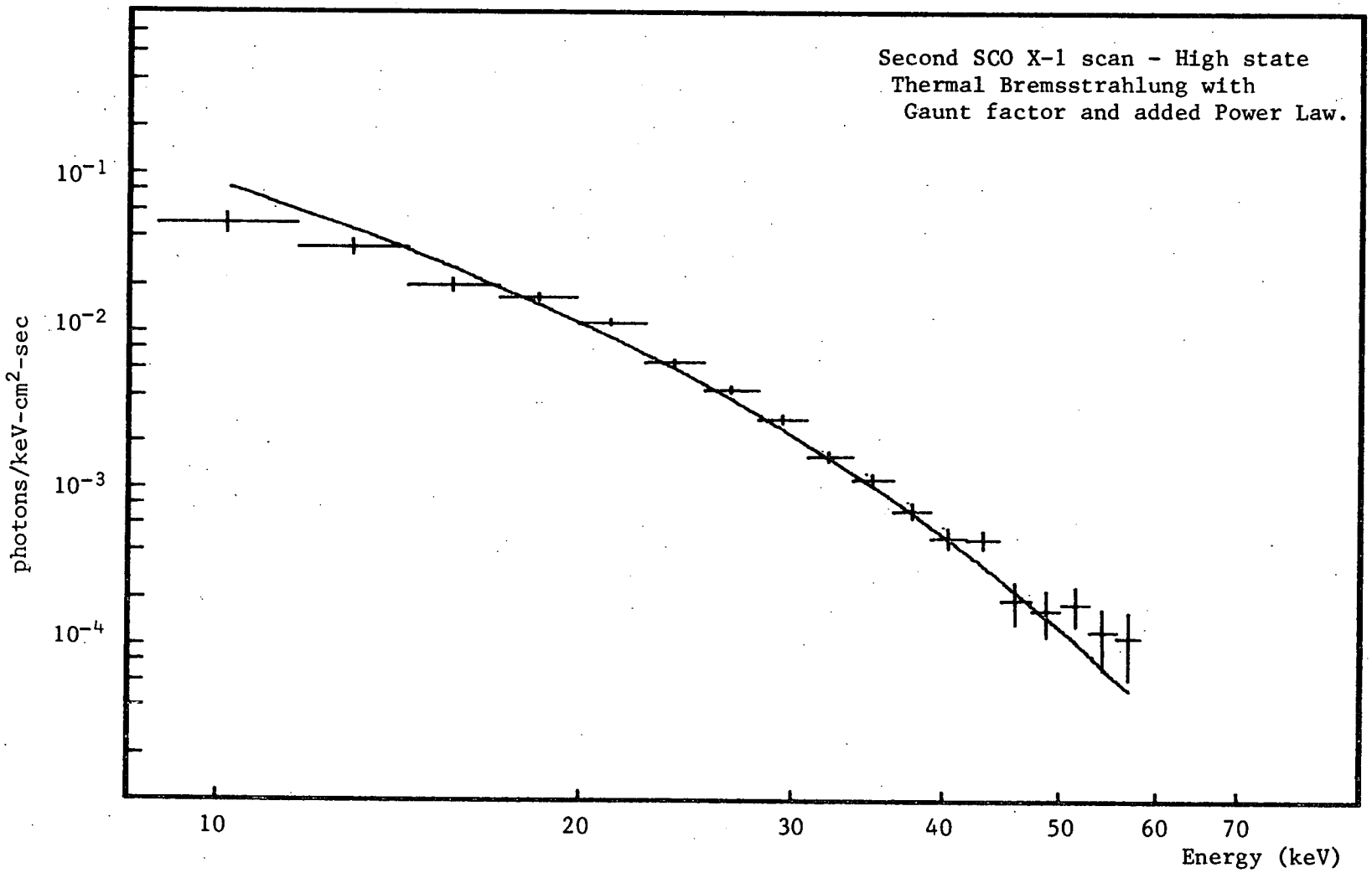
Second SCO X-1 scan - High state
Thermal Bremsstrahlung with
Gaunt factor and added Power Law.
10^{-1}
10^{-2}
10^{-3}
10^{-4}
photons/keV-cm^2-sec
10
20
30
40
50
60
70
Energy (keV)

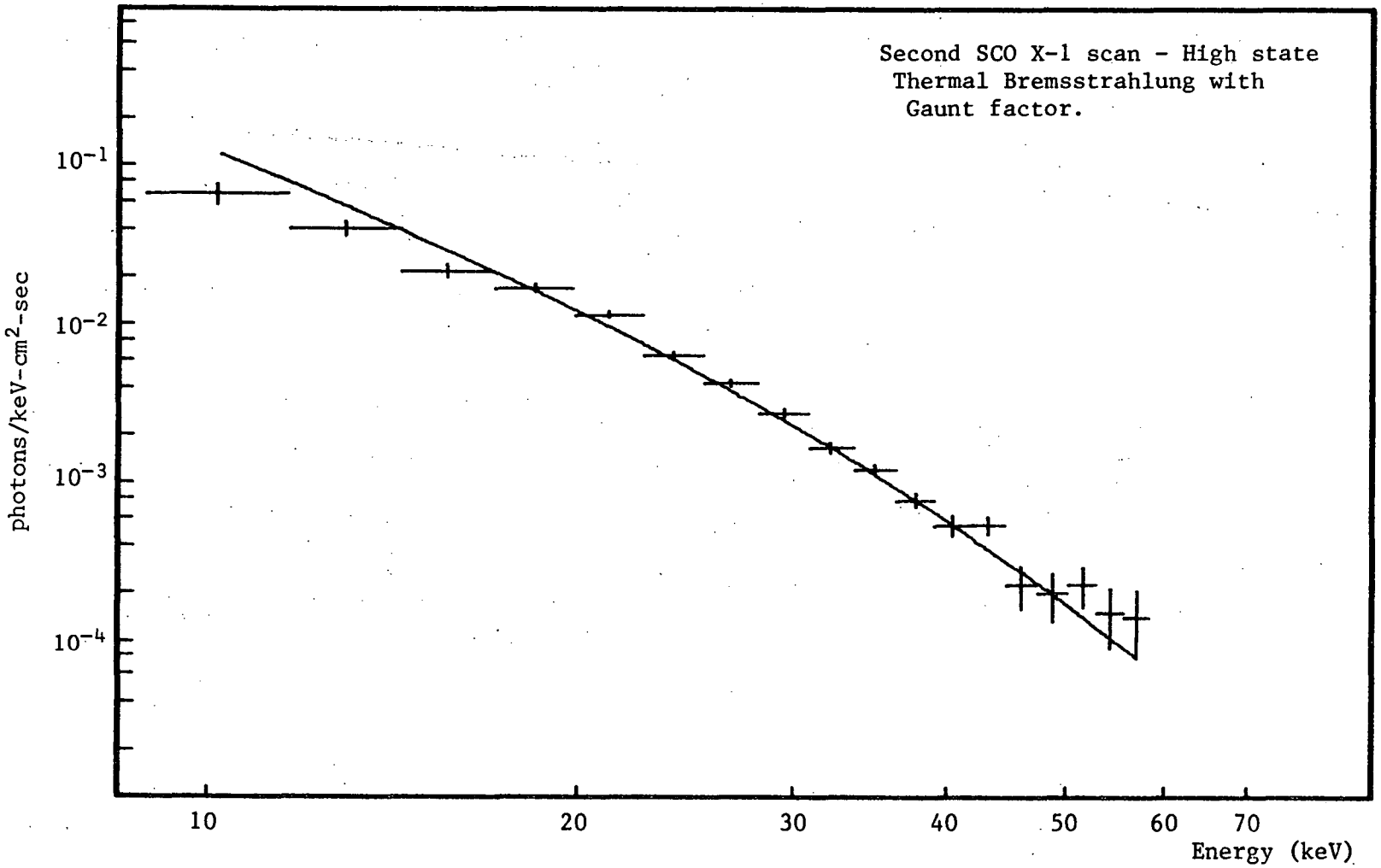
Second SCO X-1 scan - High state
Thermal Bremsstrahlung with
Gaunt factor.
photons/keV-cm^2-sec
10^{-1}
10^{-2}
10^{-3}
10^{-4}
10
20
30
40
50
60
70
Energy (keV)

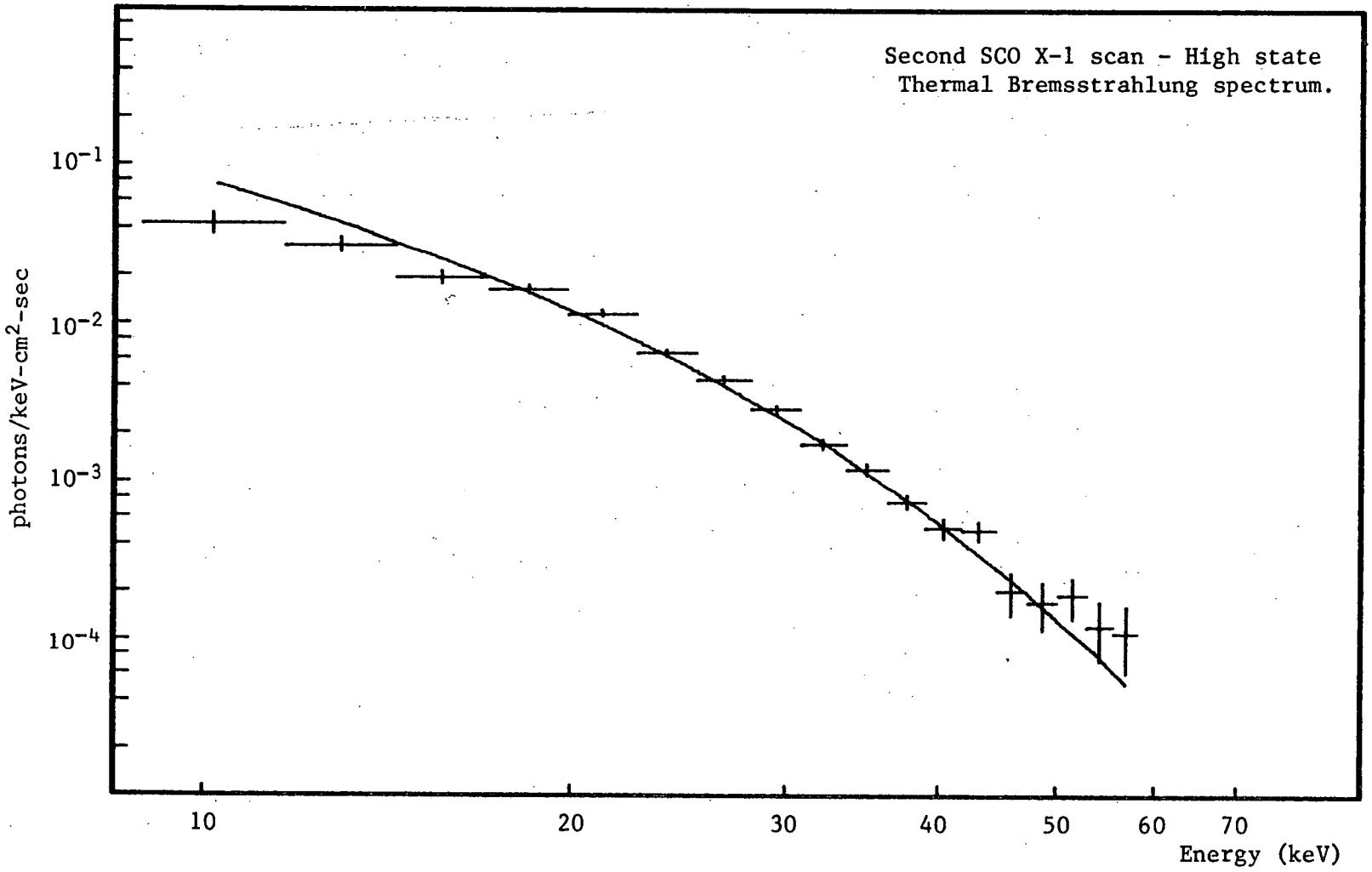
Second SCO X-1 scan - High state
Thermal Bremsstrahlung spectrum.
photons/keV-cm^2-sec
10^{-1}
10^{-2}
10^{-3}
10^{-4}
10
20
30
40
50
60
70
Energy (keV)

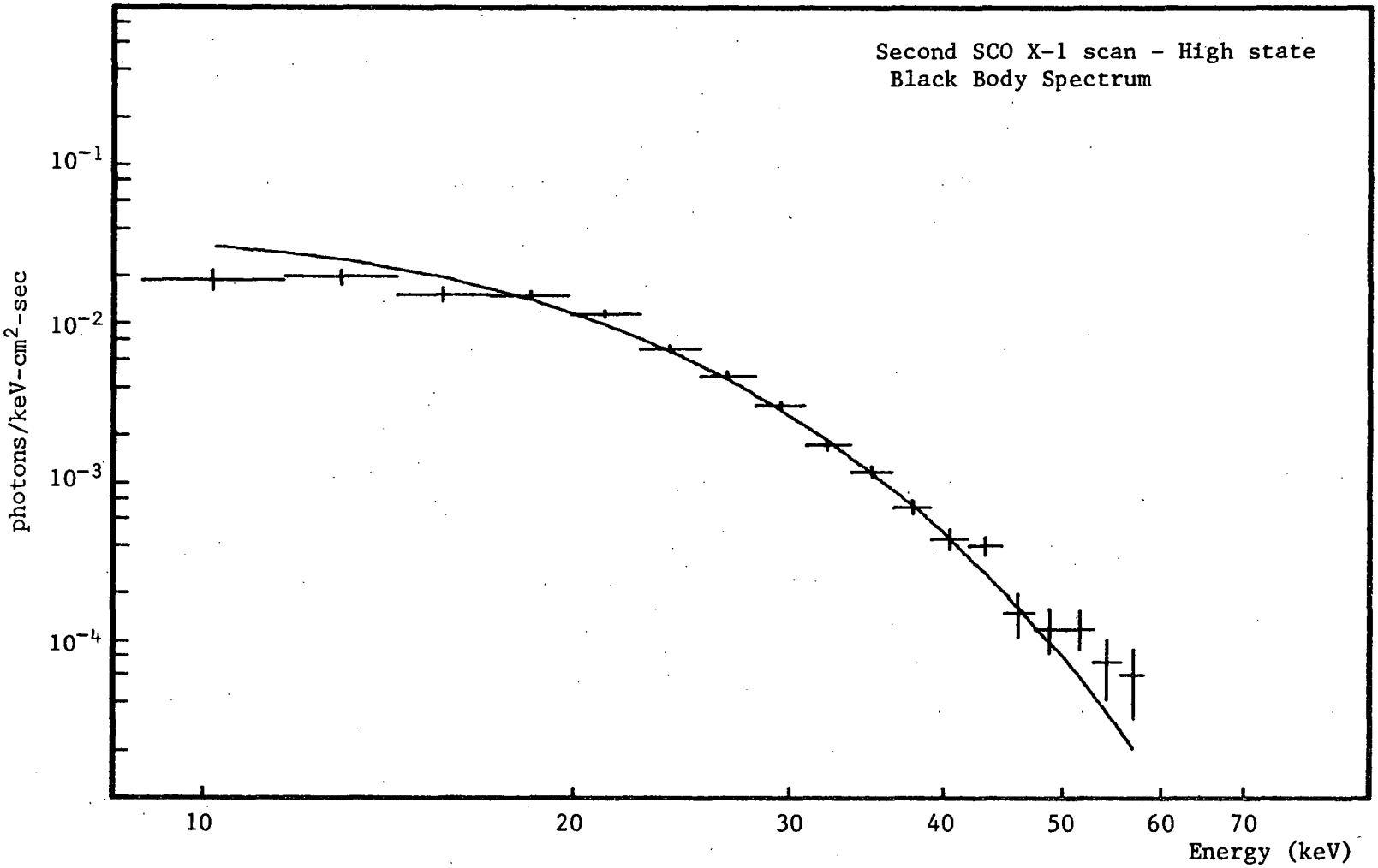
Second SCO X-1 scan - High state
Black Body Spectrum
photons/keV-cm^2-sec
10^{-1}
10^{-2}
10^{-3}
10^{-4}
10
20
30
40
50
60
70
Energy (keV)

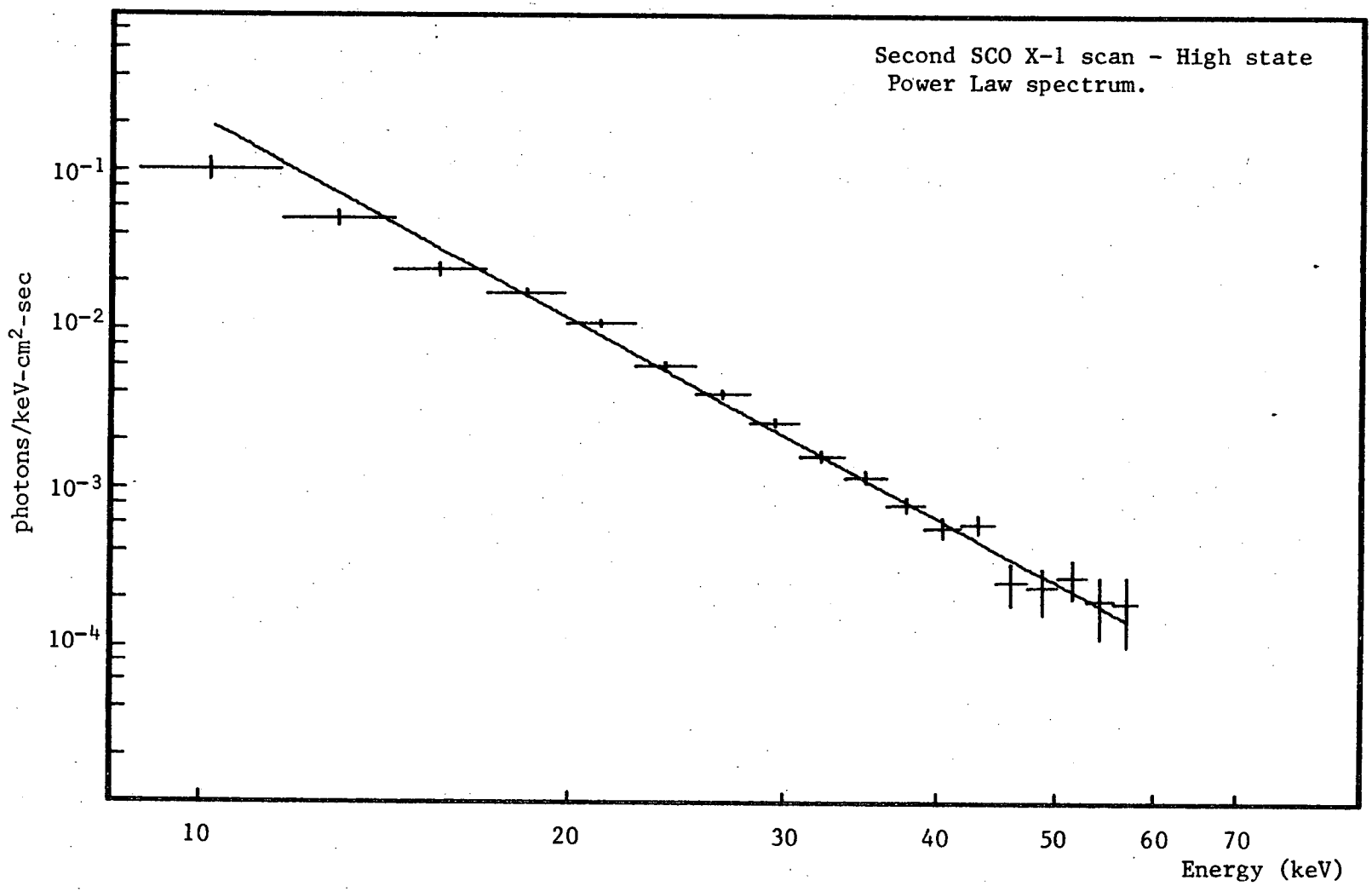
Second SCO X-1 scan - High state
Power Law spectrum.
photons/keV-cm^2-sec
10^{-1}
10^{-2}
10^{-3}
10^{-4}
10
20
30
40
50
60
70
Energy (keV)

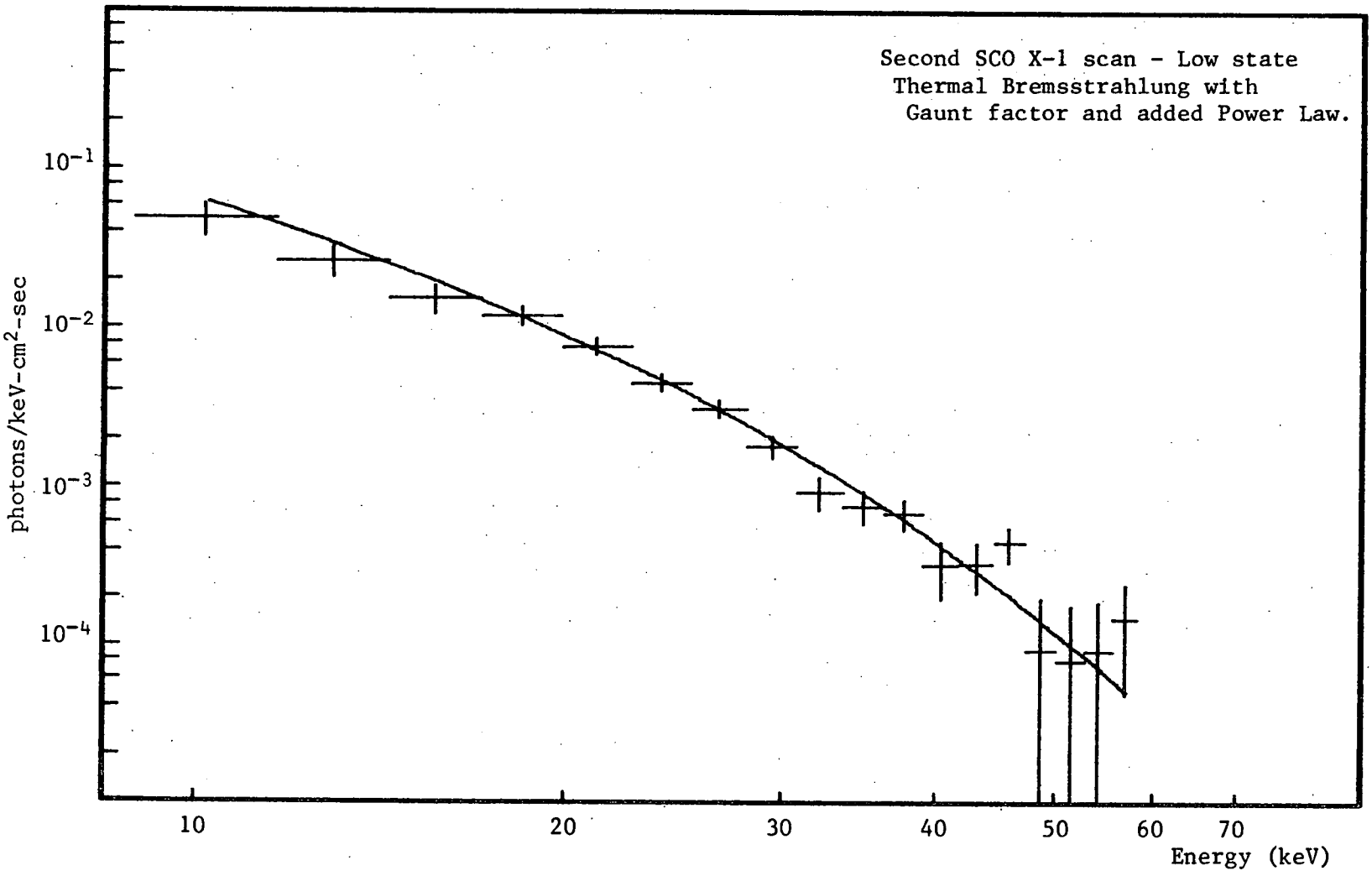
Second SCO X-1 scan - Low state
Thermal Bremsstrahlung with
Gaunt factor and added Power Law.
photons/keV-cm^2-sec
10^{-1}
10^{-2}
10^{-3}
10^{-4}
10
20
30
40
50
60
70
Energy (keV)

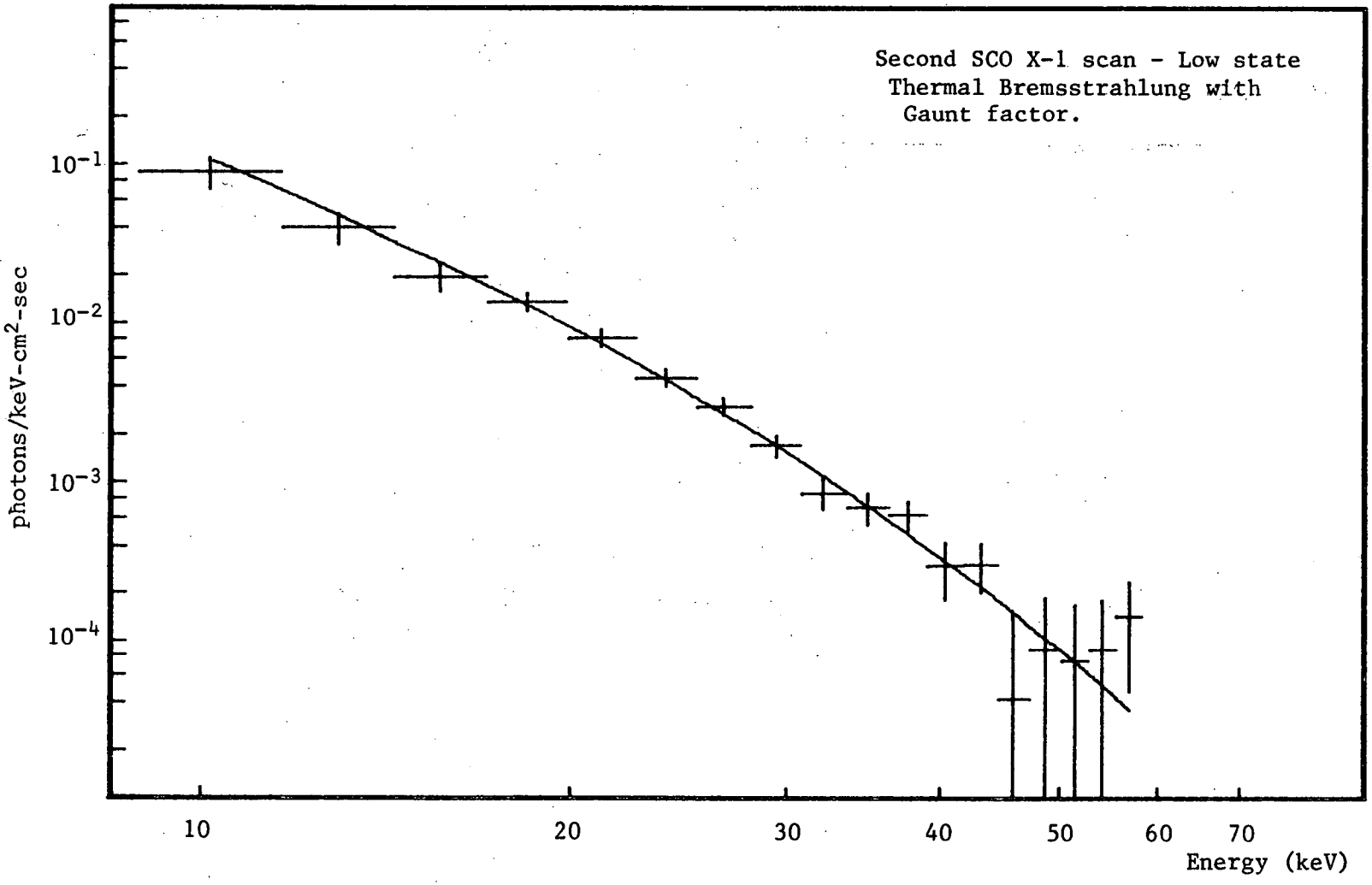
Second SCO X-1 scan - Low state
Thermal Bremsstrahlung with
Gaunt factor.
photons/keV-cm²-sec
10⁻¹
10⁻²
10⁻³
10⁻⁴
10
20
30
40
50
60
70
Energy (keV)

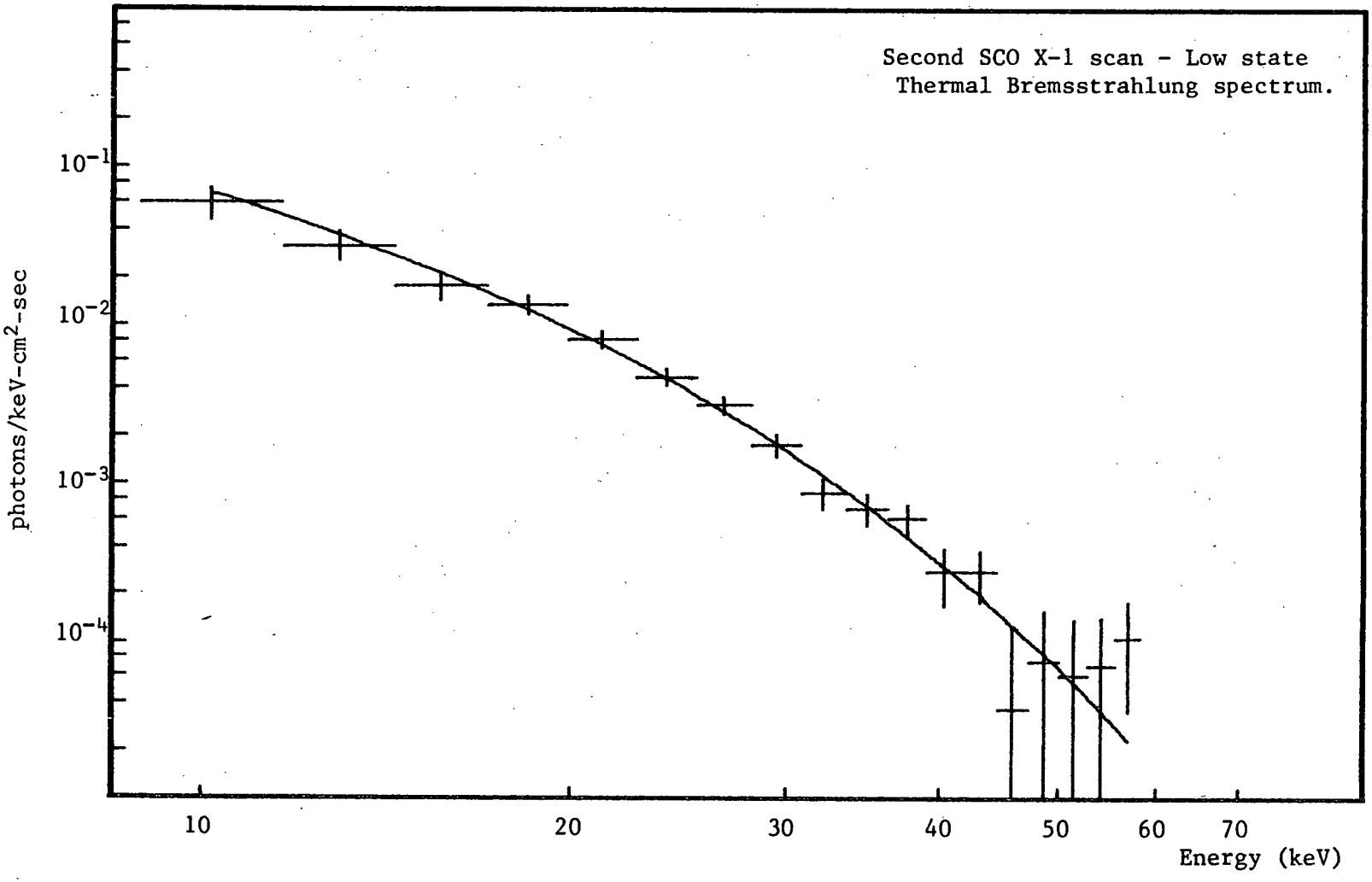
Second SCO X-1 scan - Low state
Thermal Bremsstrahlung spectrum.
photons/keV-cm^2-sec
10^{-1}
10^{-2}
10^{-3}
10^{-4}
10
20
30
40
50
60
70
Energy (keV)

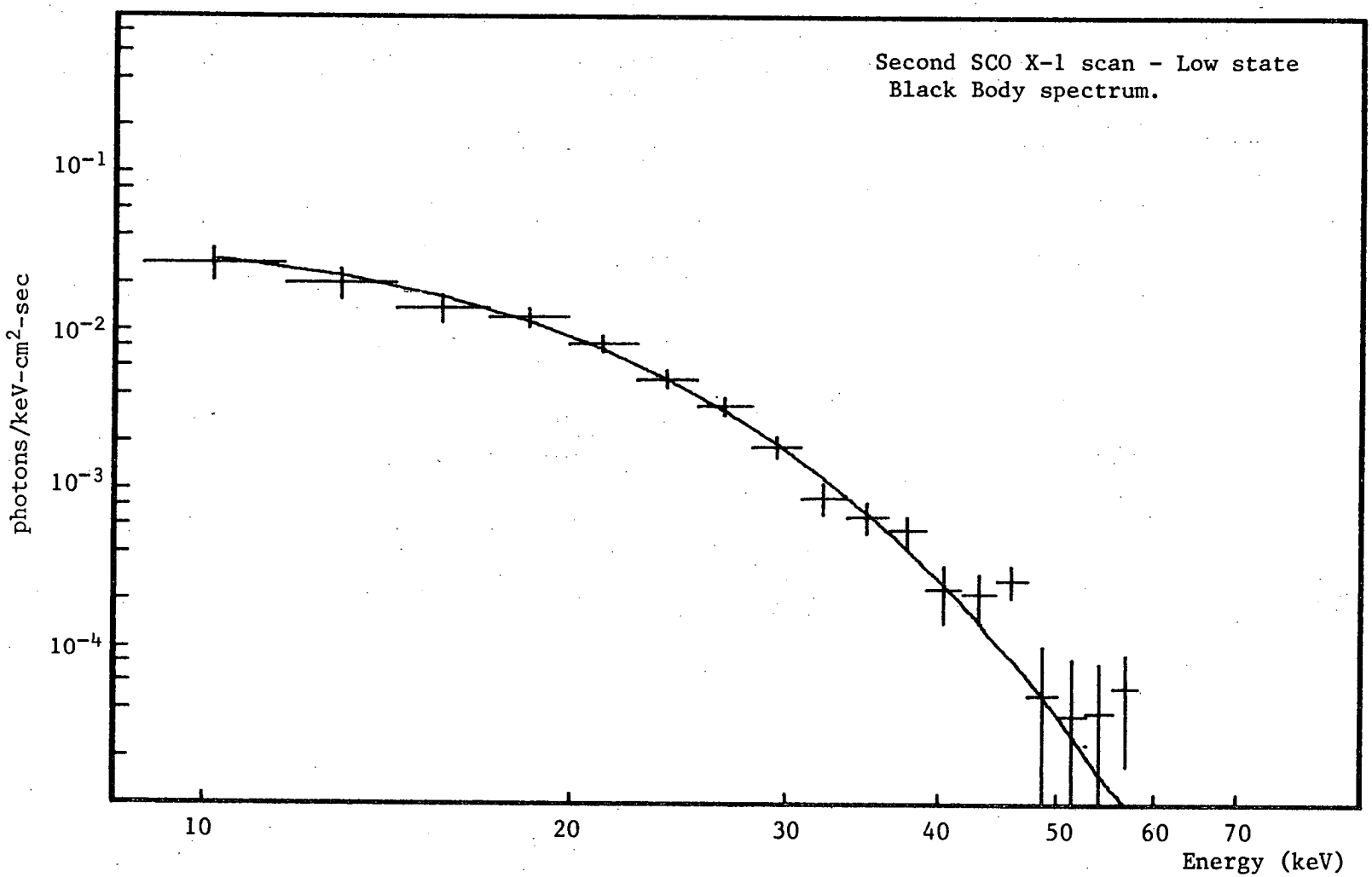
Second SCO X-1 scan - Low state
Black Body spectrum.
photons/keV-cm^2-sec
10^{-1}
10^{-2}
10^{-3}
10^{-4}
10
20
30
40
50
60
70
Energy (keV)

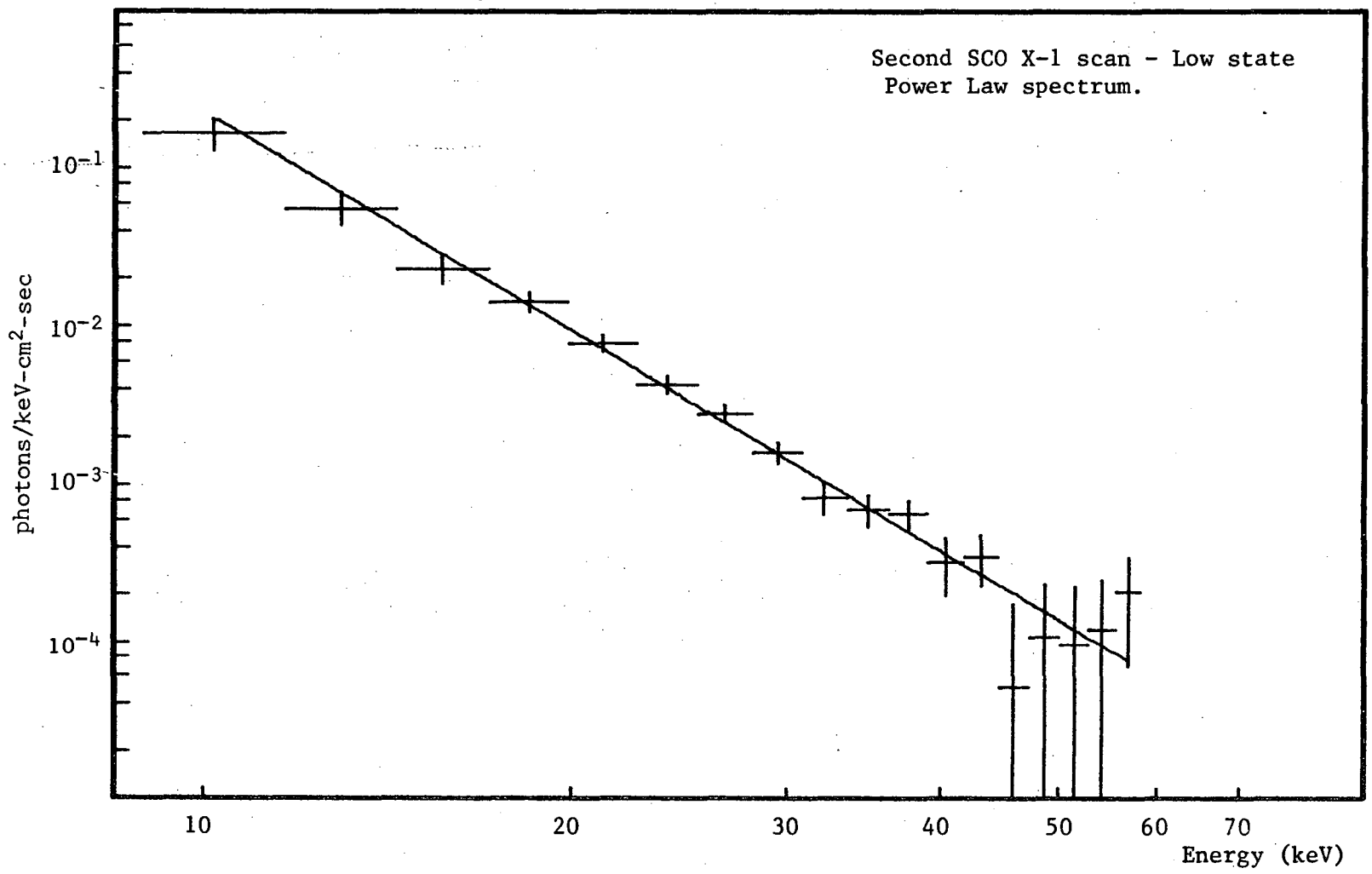
Second SCO X-1 scan - Low state
Power Law spectrum.
photons/keV-cm^2-sec
10^{-1}
10^{-2}
10^{-3}
10^{-4}
10
20
30
40
50
60
70
Energy (keV)

APPENDIX D

90% χ^2 CONFIDENCE CONTOURS OF THE SPECTRAL FITS

The solid curves apply to the "best" fit counter parameter solutions and the fitted minimum χ^2_ν is shown by the dot. The broken curves apply to the "calibration" fit counter parameter solutions with the fitted minimum χ^2_ν shown by a cross.

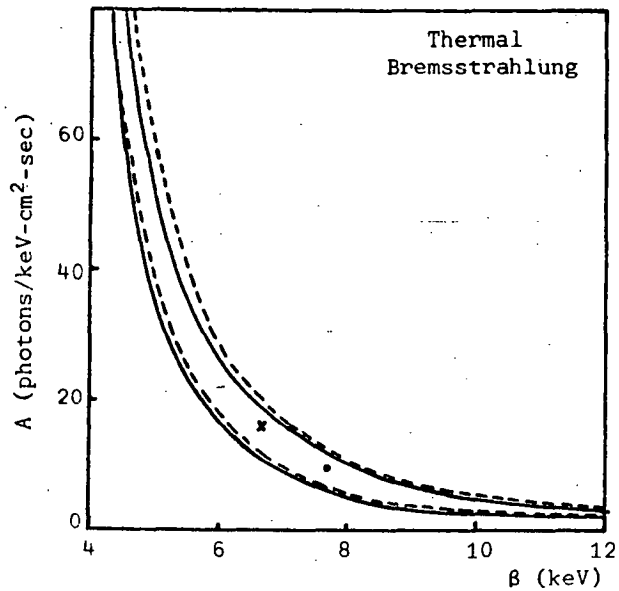

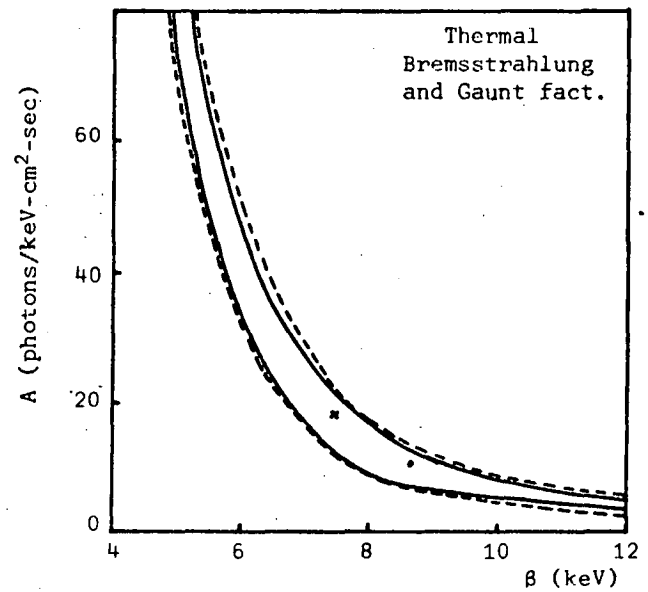

90% X^2 Confidence Contours
First SCO X-1 Scan
Low State

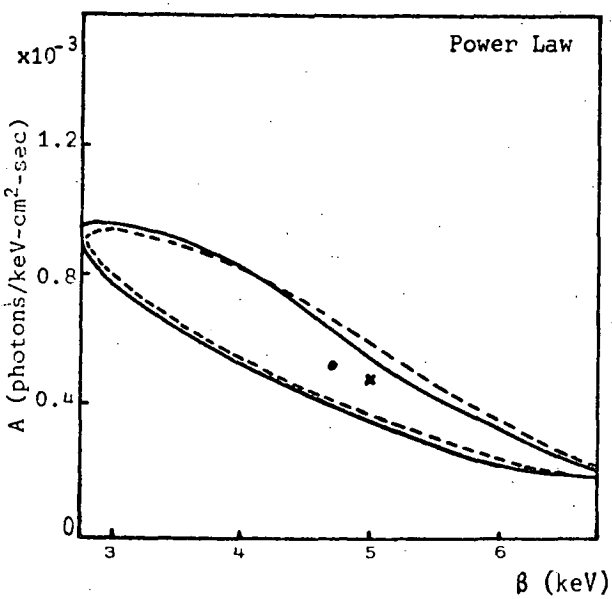

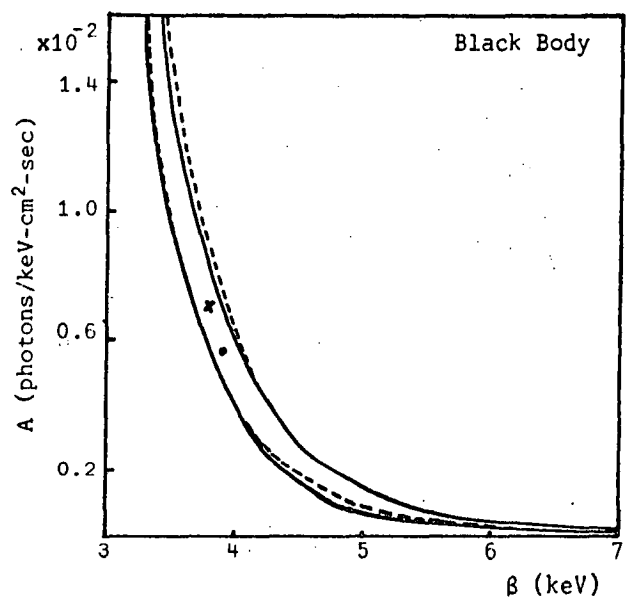

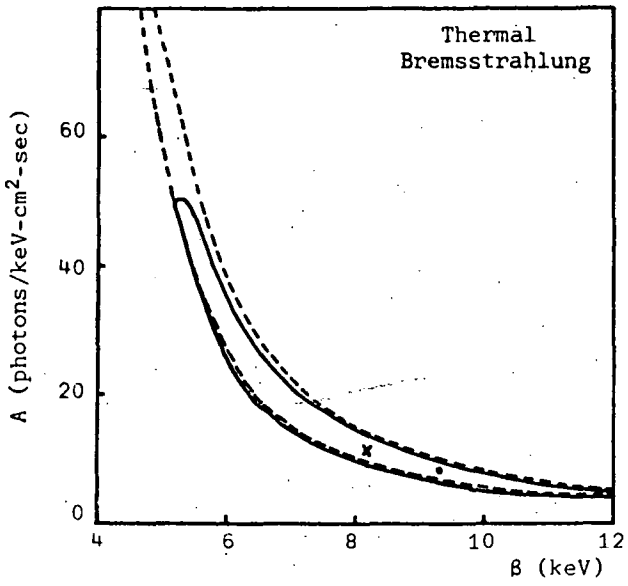

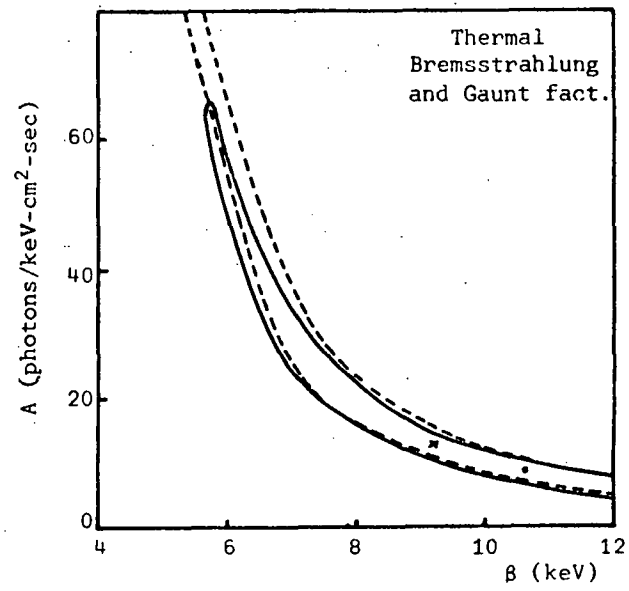

90% X^2 Confidence

Contours

First SCO X-1 Scan

High State

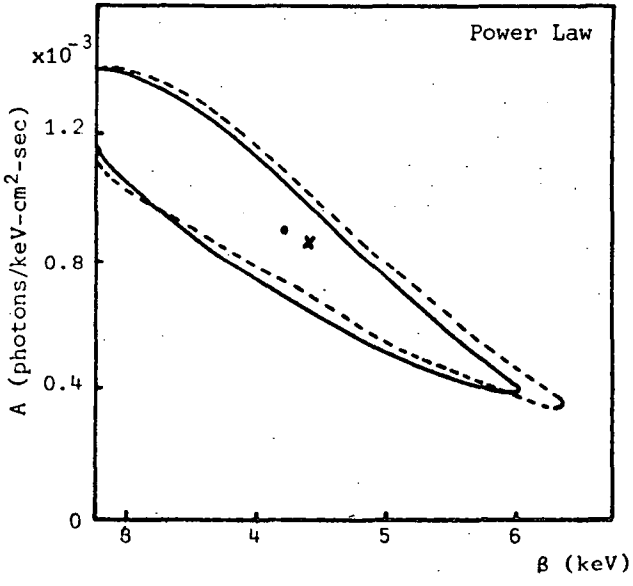

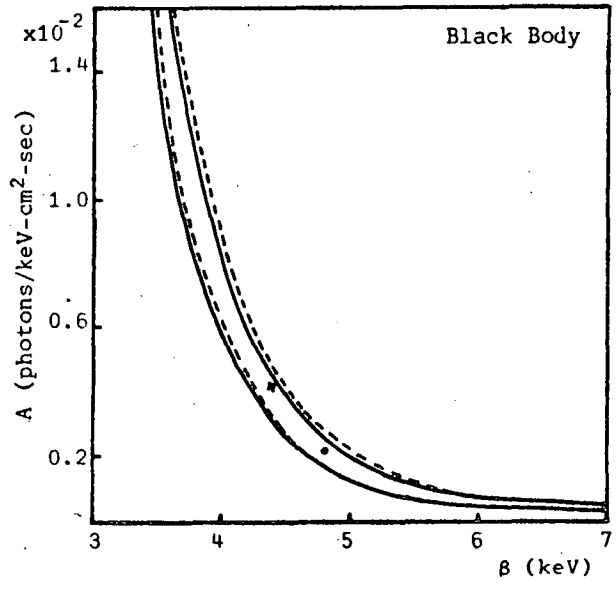

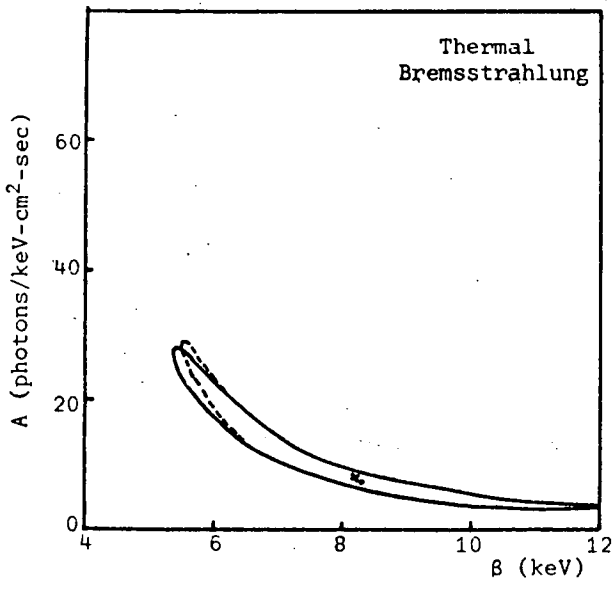

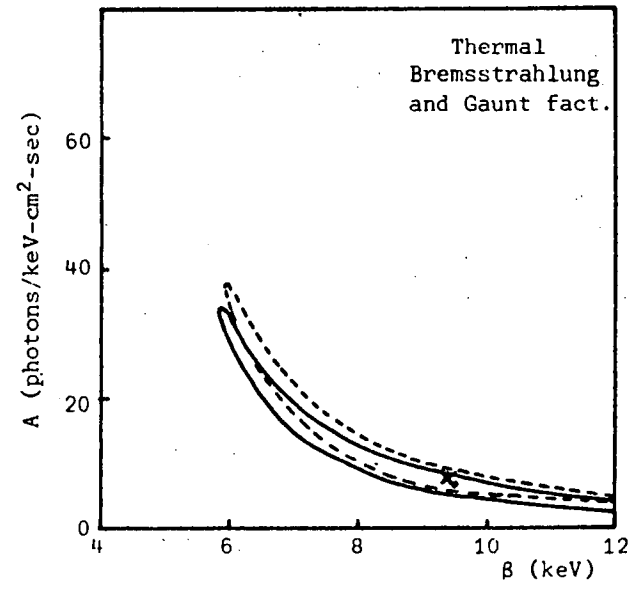

90% X^2 Confidence

Contours

Second SCO X-1 Scan

Both States

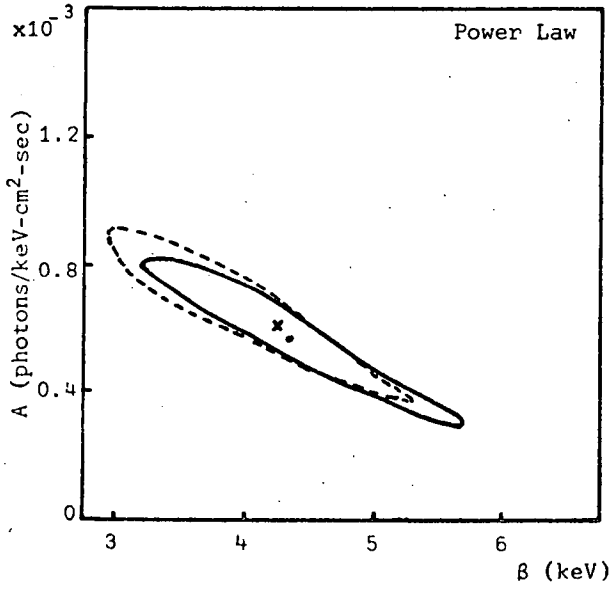

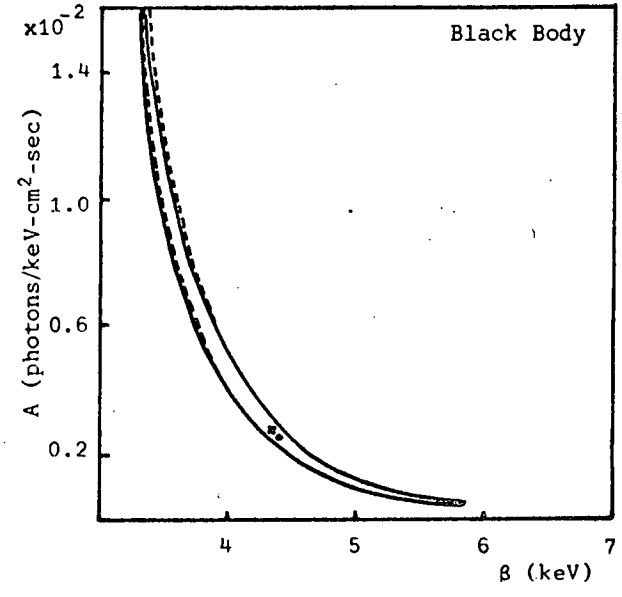

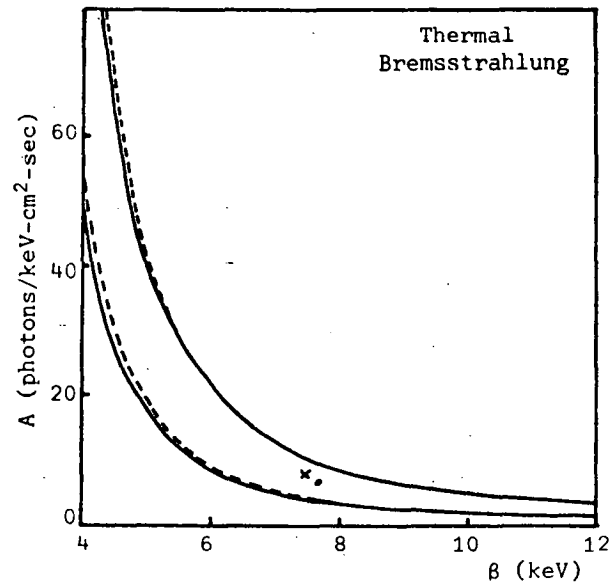

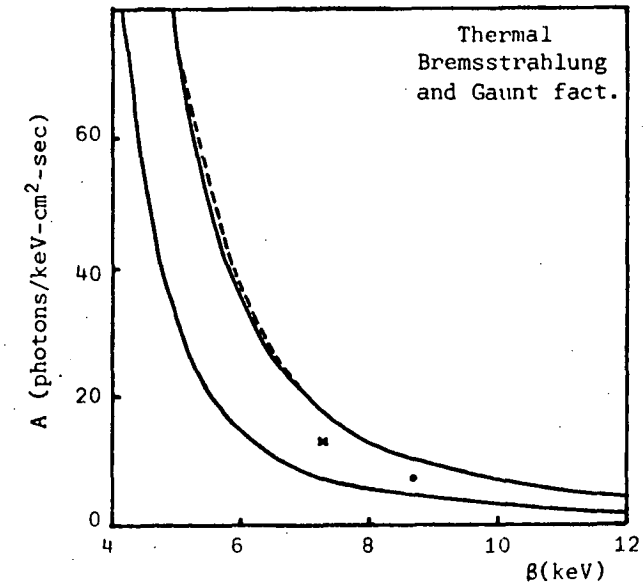

90% X^2 Confidence

Contours

Second SCO X-1 Scan

Low State

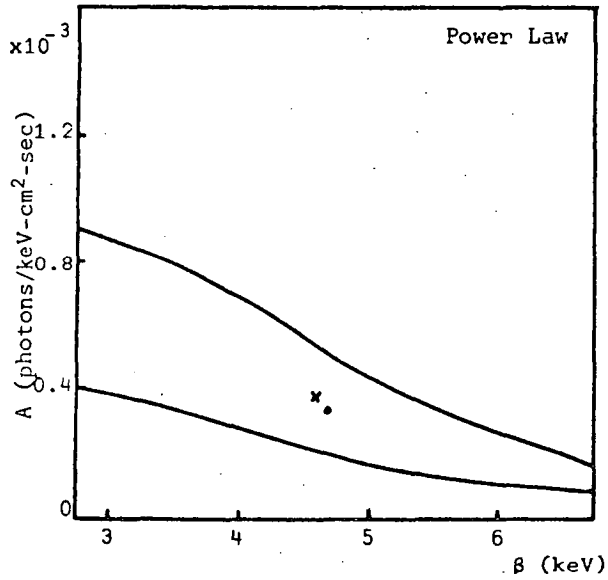

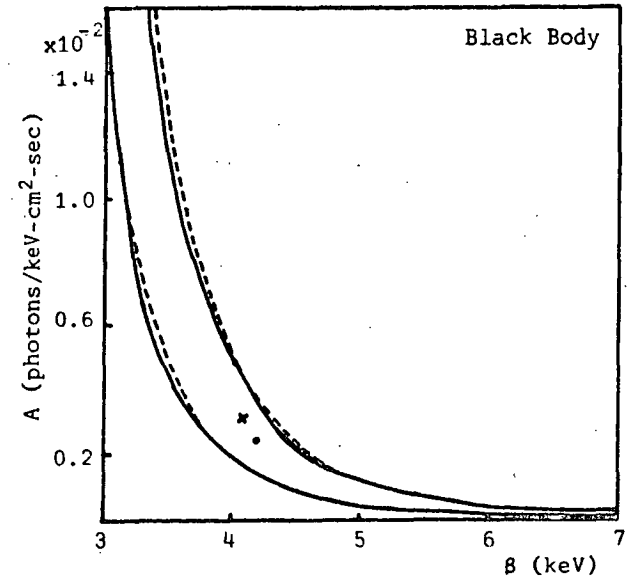

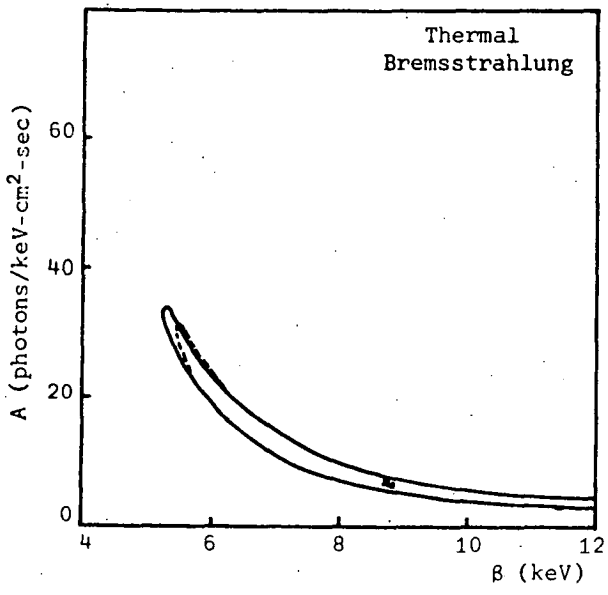

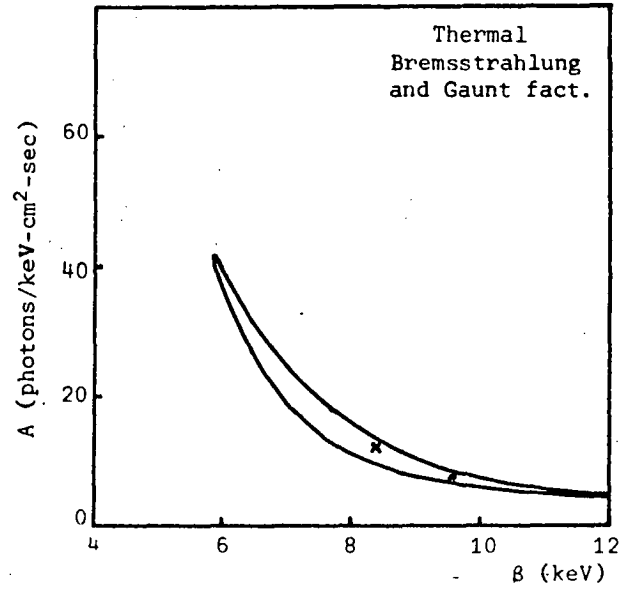

90% X^2 Confidence

Contours

Second SCO X-1 Scan

High State

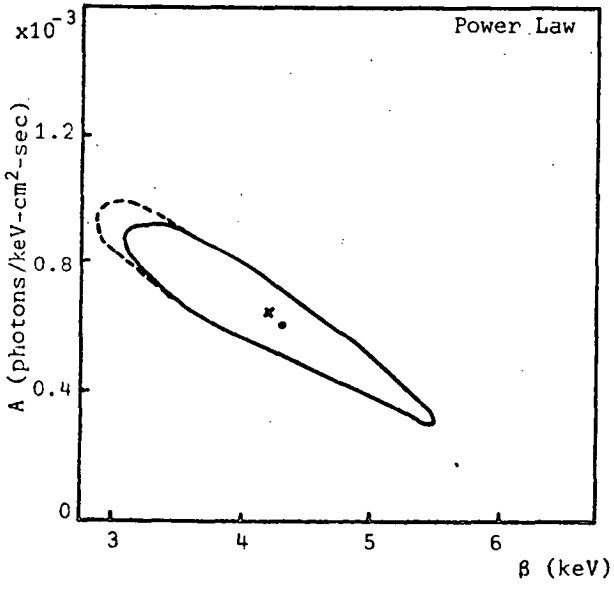

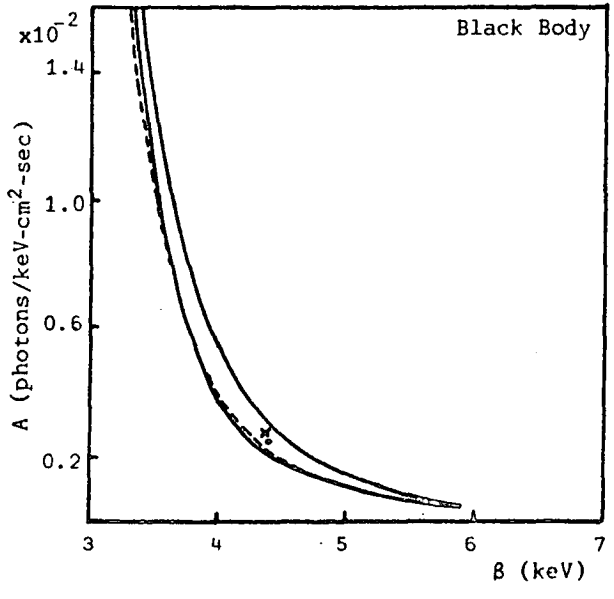

APPENDIX E

POWER SPECTRA

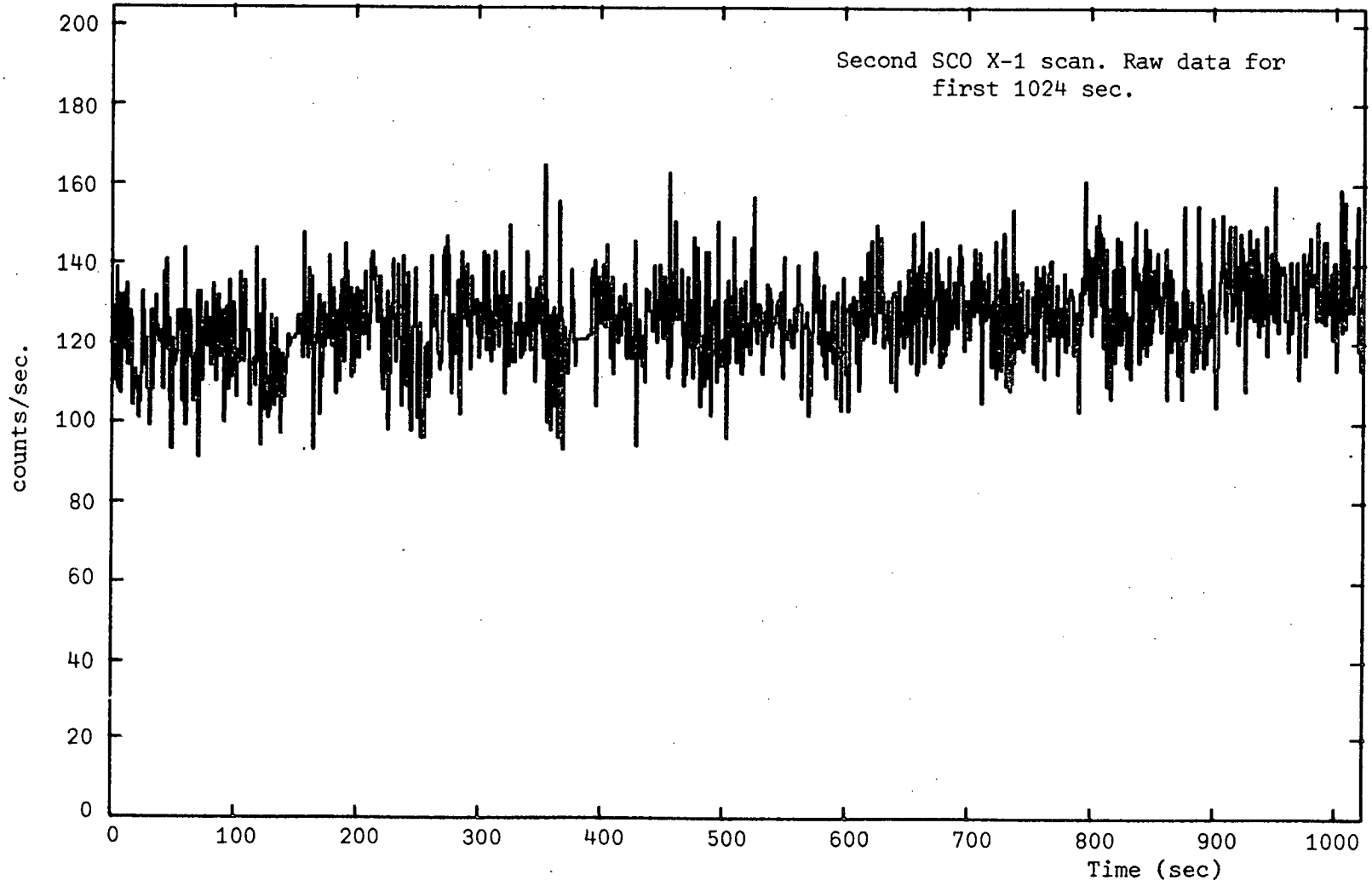
Second SCO X-1 scan. Raw data for
first 1024 sec.
counts/sec.
Time (sec)
0
20
40
60
80
100
120
140
160
180
200
0
100
200
300
400
500
600
700
800
900
1000

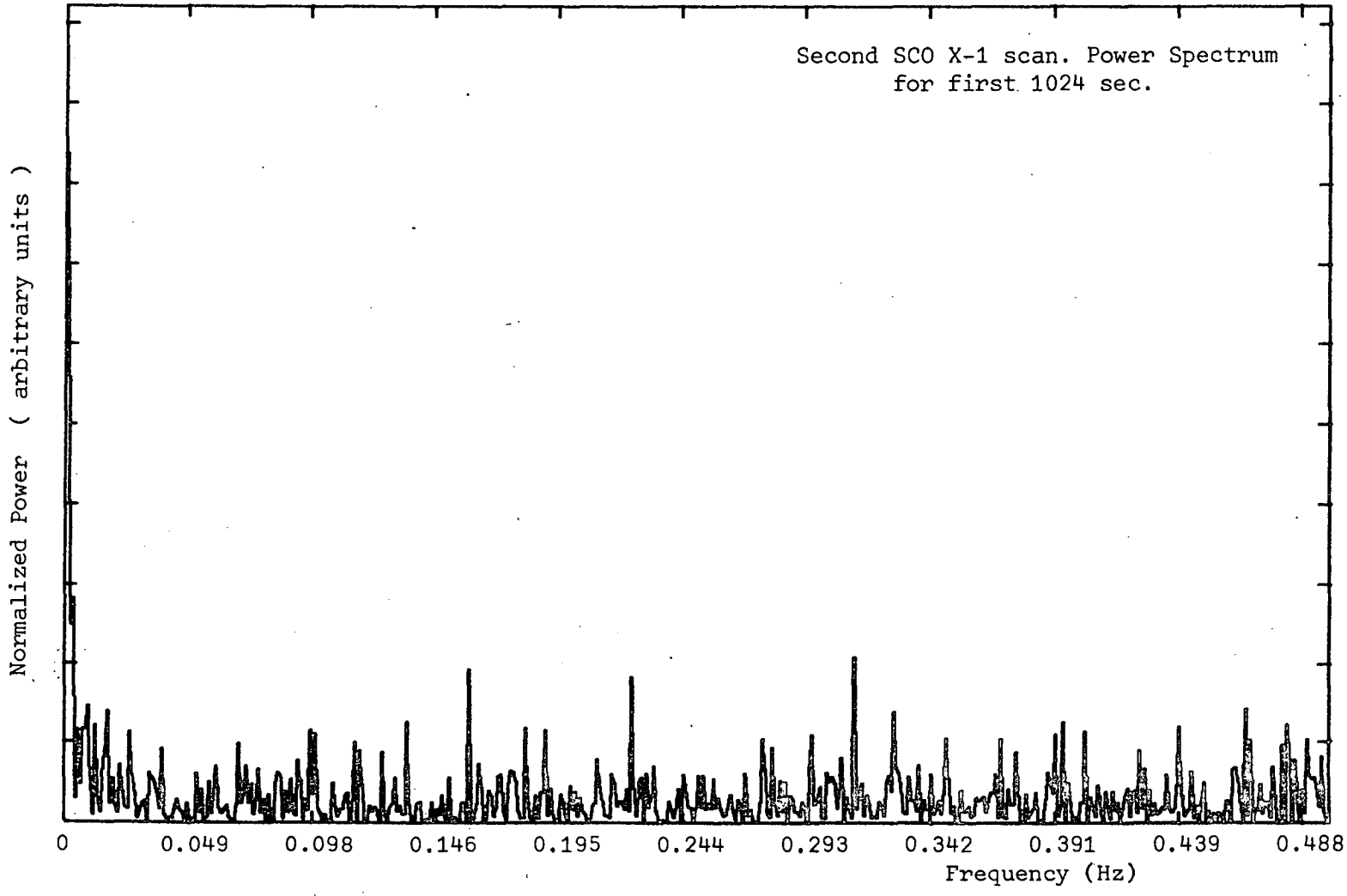
Second SCO X-1 scan. Power Spectrum
for first 1024 sec.
Normalized Power (arbitrary units)
0
0.049
0.098
0.146
0.195
0.244
0.293
0.342
0.391
0.439
0.488
Frequency (Hz)

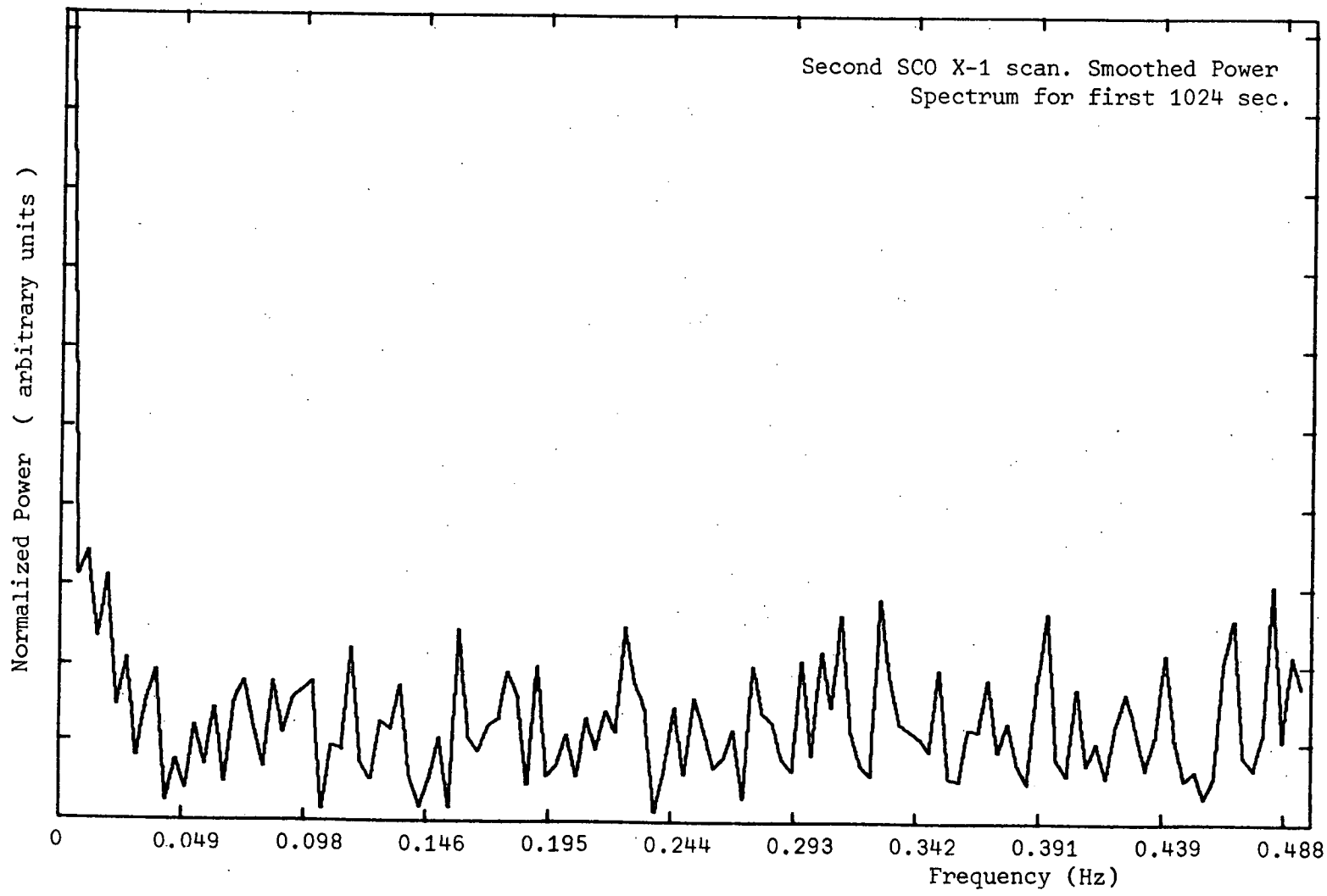
Second SCO X-1 scan. Smoothed Power
Spectrum for first 1024 sec.
Normalized Power (arbitrary units)
0
0.049
0.098
0.146
0.195
0.244
0.293
0.342
0.391
0.439
0.488
Frequency (Hz)

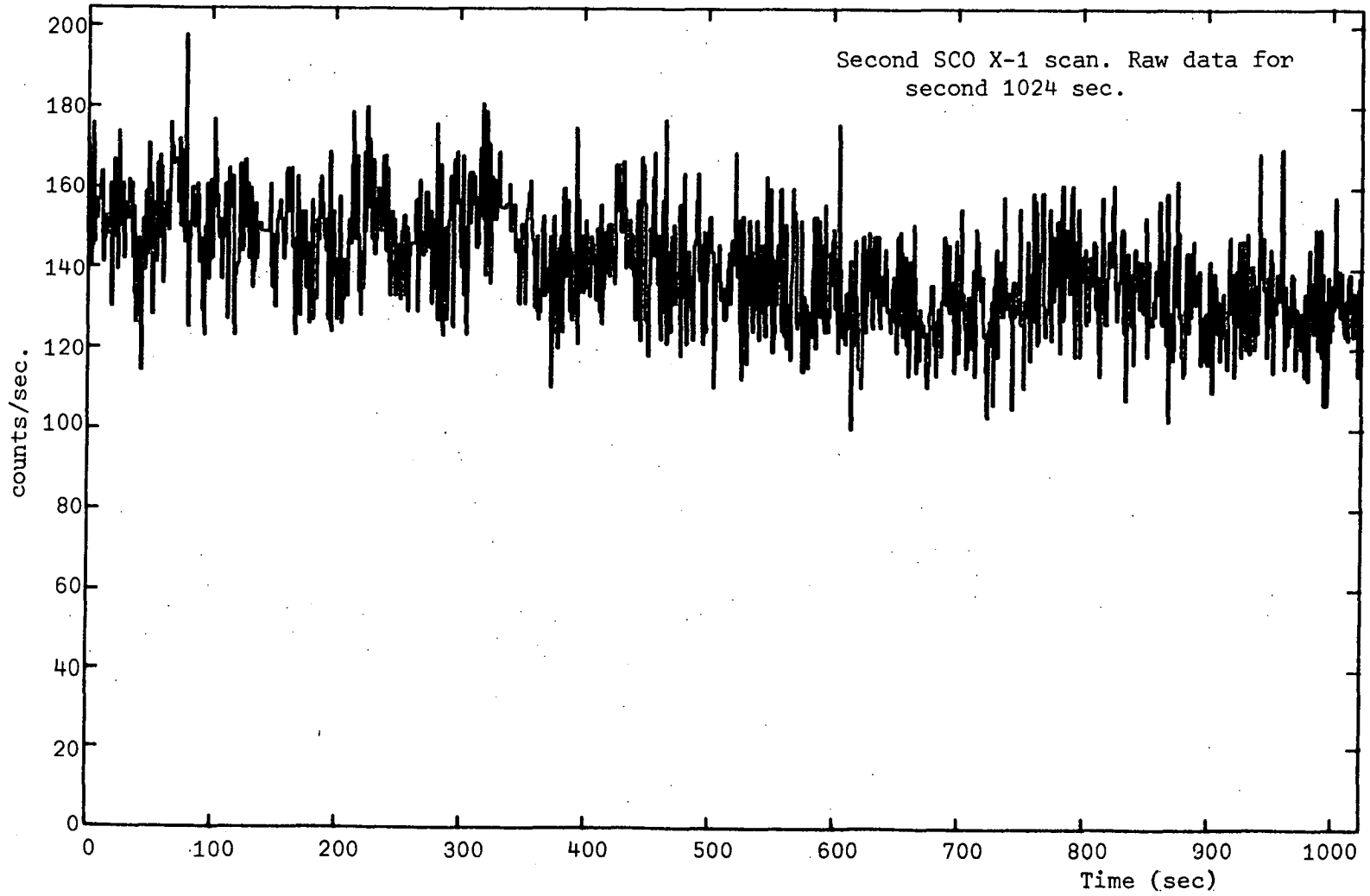
Second SCO X-1 scan. Raw data for
second 1024 sec.
counts/sec.
Time (sec)
0
20
40
60
80
100
120
140
160
180
200
0
100
200
300
400
500
600
700
800
900
1000

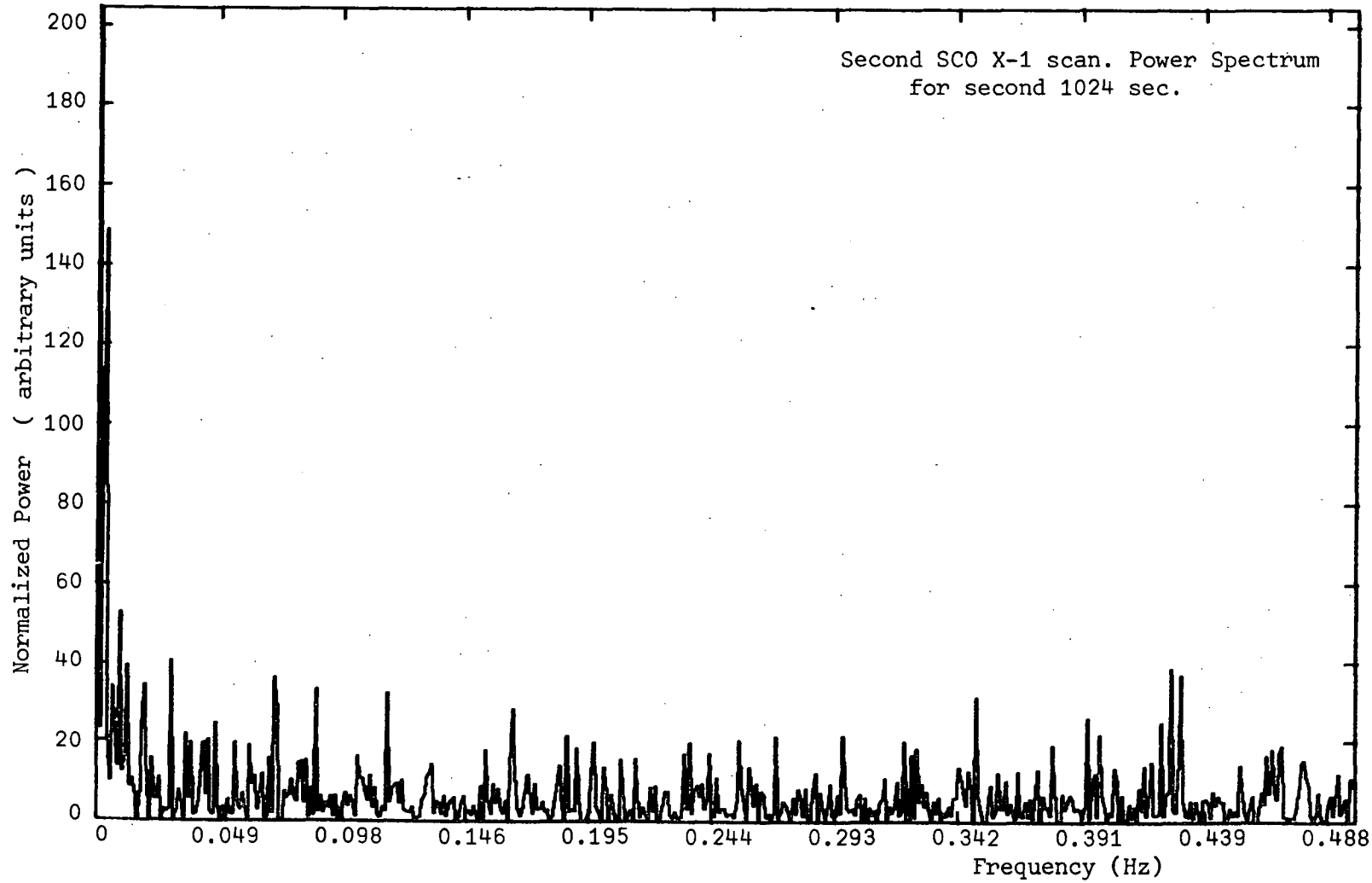
Second SCO X-1 scan. Power Spectrum
for second 1024 sec.
Normalized Power (arbitrary units)
200
180
160
140
120
100
80
60
40
20
0
0
0.049
0.098
0.146
0.195
0.244
0.293
0.342
0.391
0.439
0.488
Frequency (Hz)

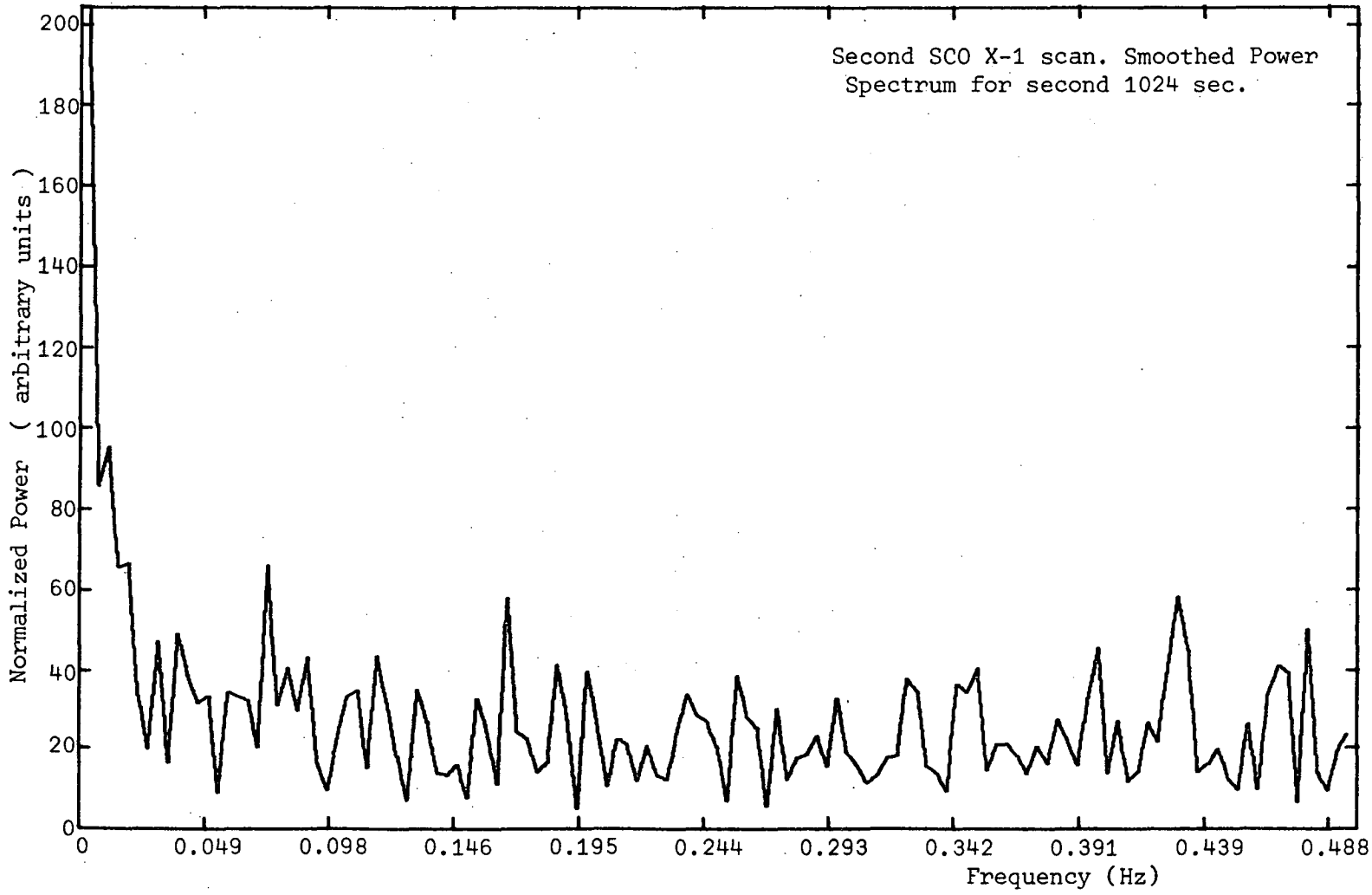
Second SCO X-1 scan. Smoothed Power Spectrum for second 1024 sec.
Normalized Power (arbitrary units)
200
180
160
140
120
100
80
60
40
20
0
0
0.049
0.098
0.146
0.195
0.244
0.293
0.342
0.391
0.439
0.488
Frequency (Hz)

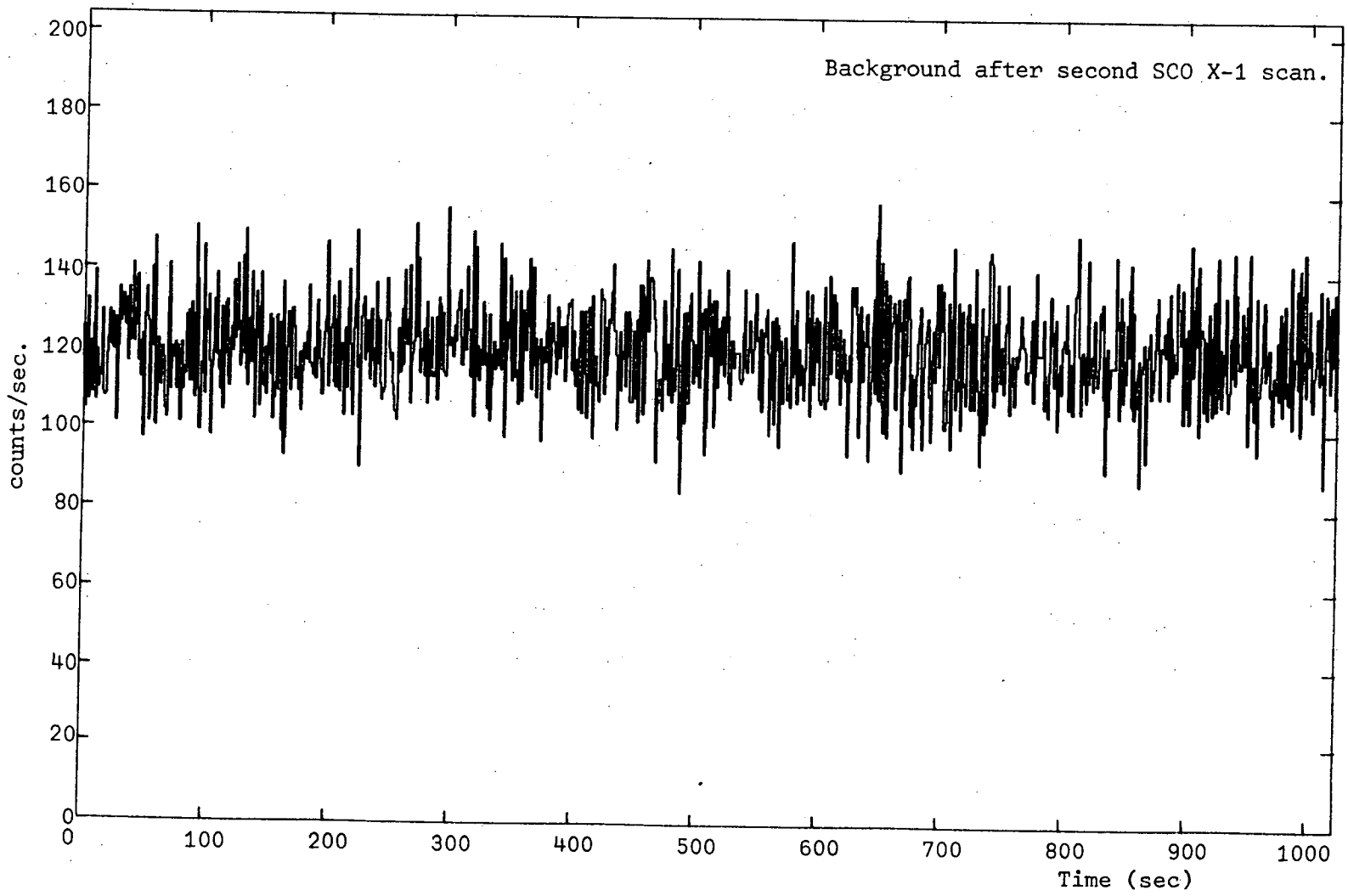
Background after second SCO X-1 scan.
counts/sec.
0
20
40
60
80
100
120
140
160
180
200
0
100
200
300
400
500
600
700
800
900
1000
Time (sec)

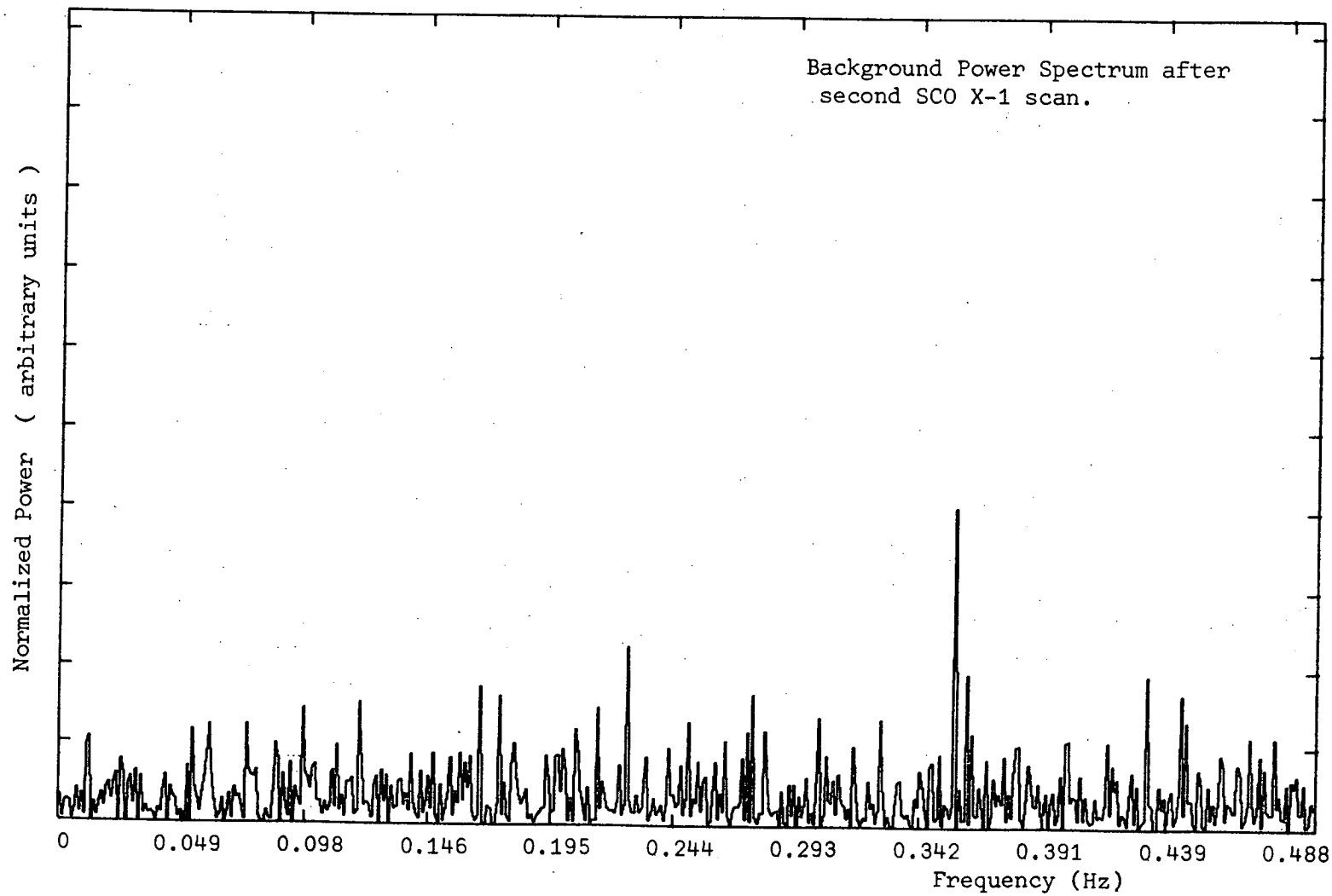
Background Power Spectrum after
second SCO X-1 scan.
Normalized Power (arbitrary units)
0
0.049
0.098
0.146
0.195
0.244
0.293
0.342
0.391
0.439
0.488
Frequency (Hz)

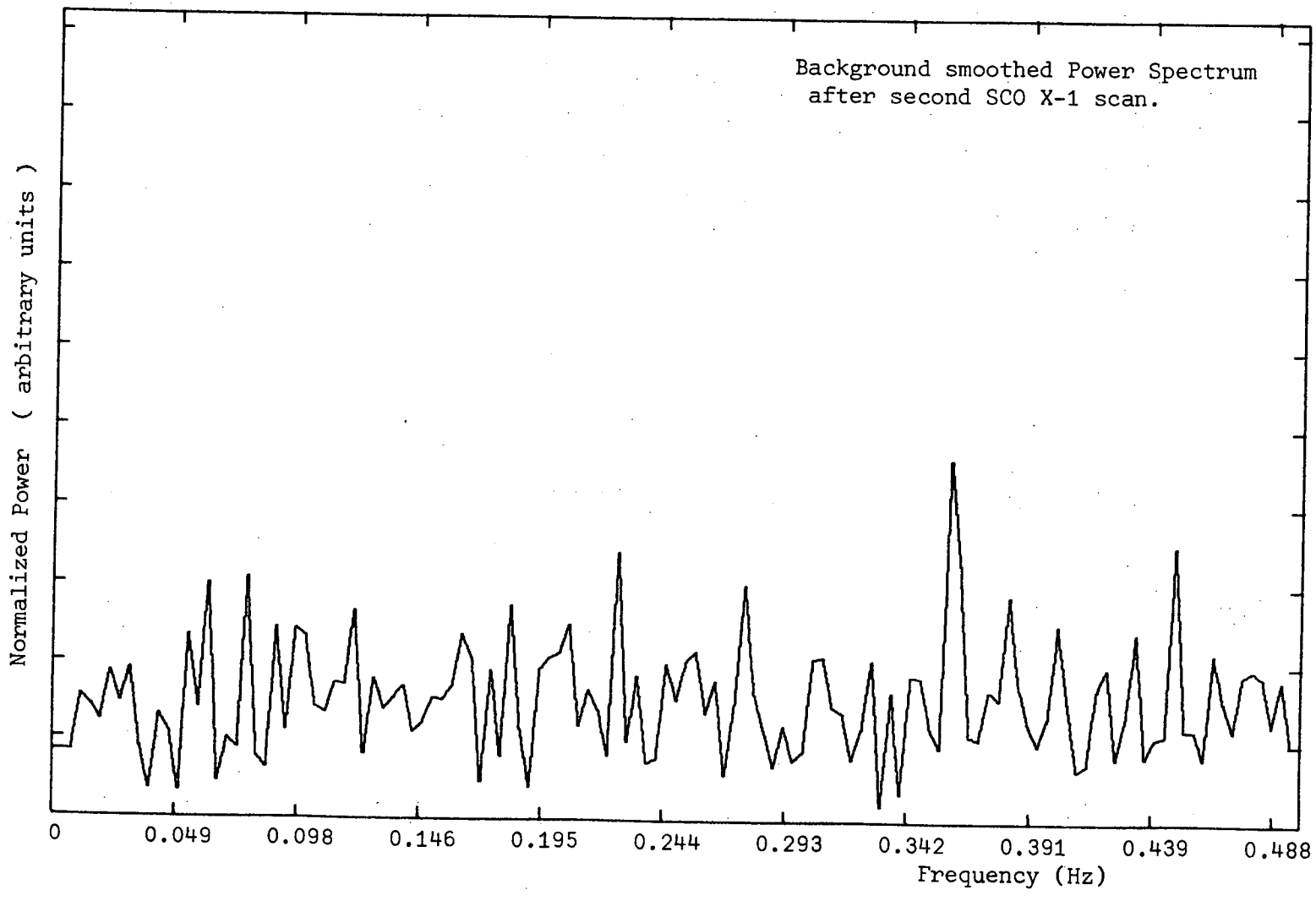
Background smoothed Power Spectrum
after second SCO X-1 scan.
Normalized Power (arbitrary units)
0
0.049
0.098
0.146
0.195
0.244
0.293
0.342
0.391
0.439
0.488
Frequency (Hz)

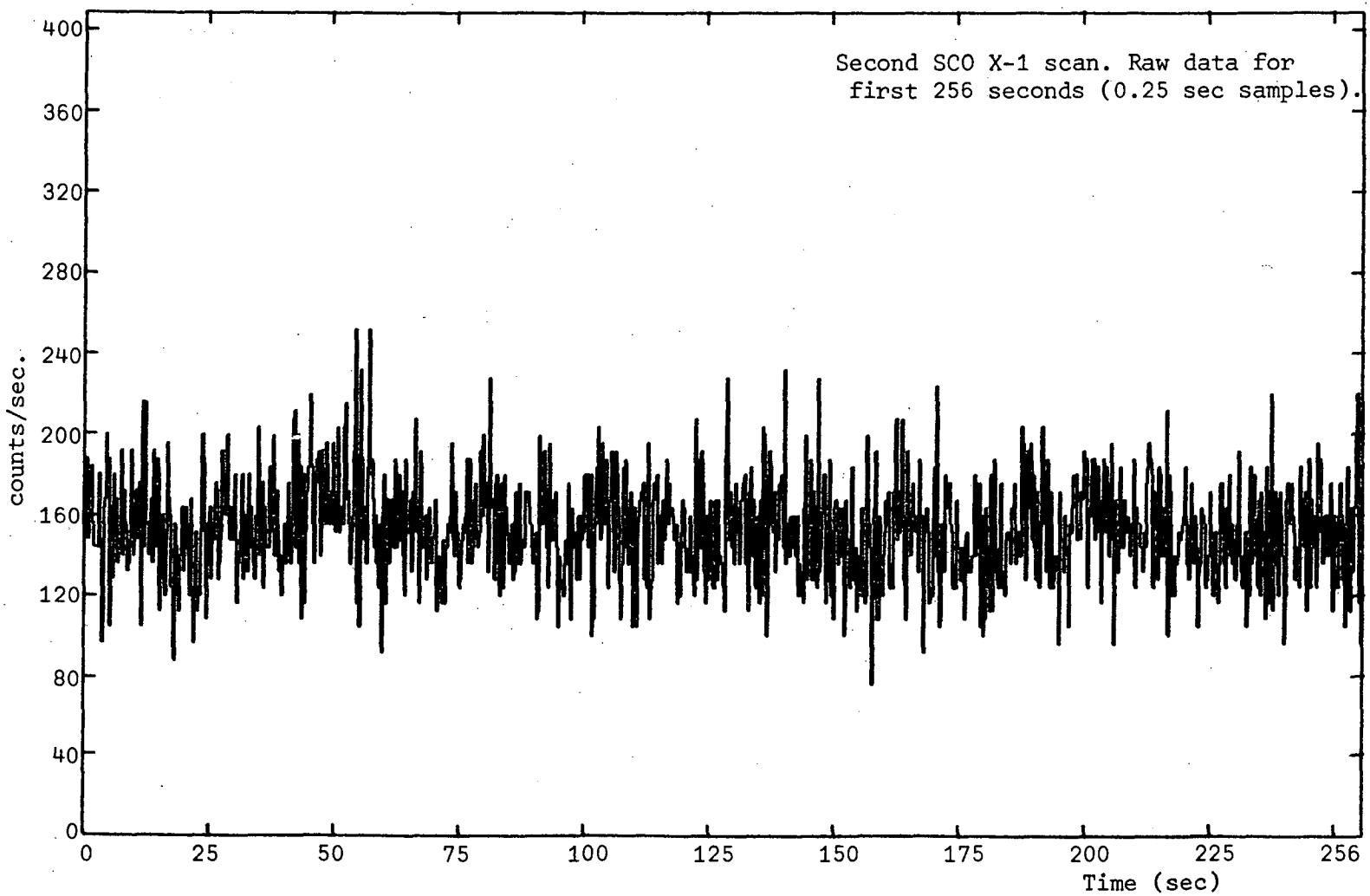
Second SCO X-1 scan. Raw data for
first 256 seconds (0.25 sec samples).
counts/sec.
400
360
320
280
240
200
160
120
80
40
0
0
25
50
75
100
125
150
175
200
225
256
Time (sec)

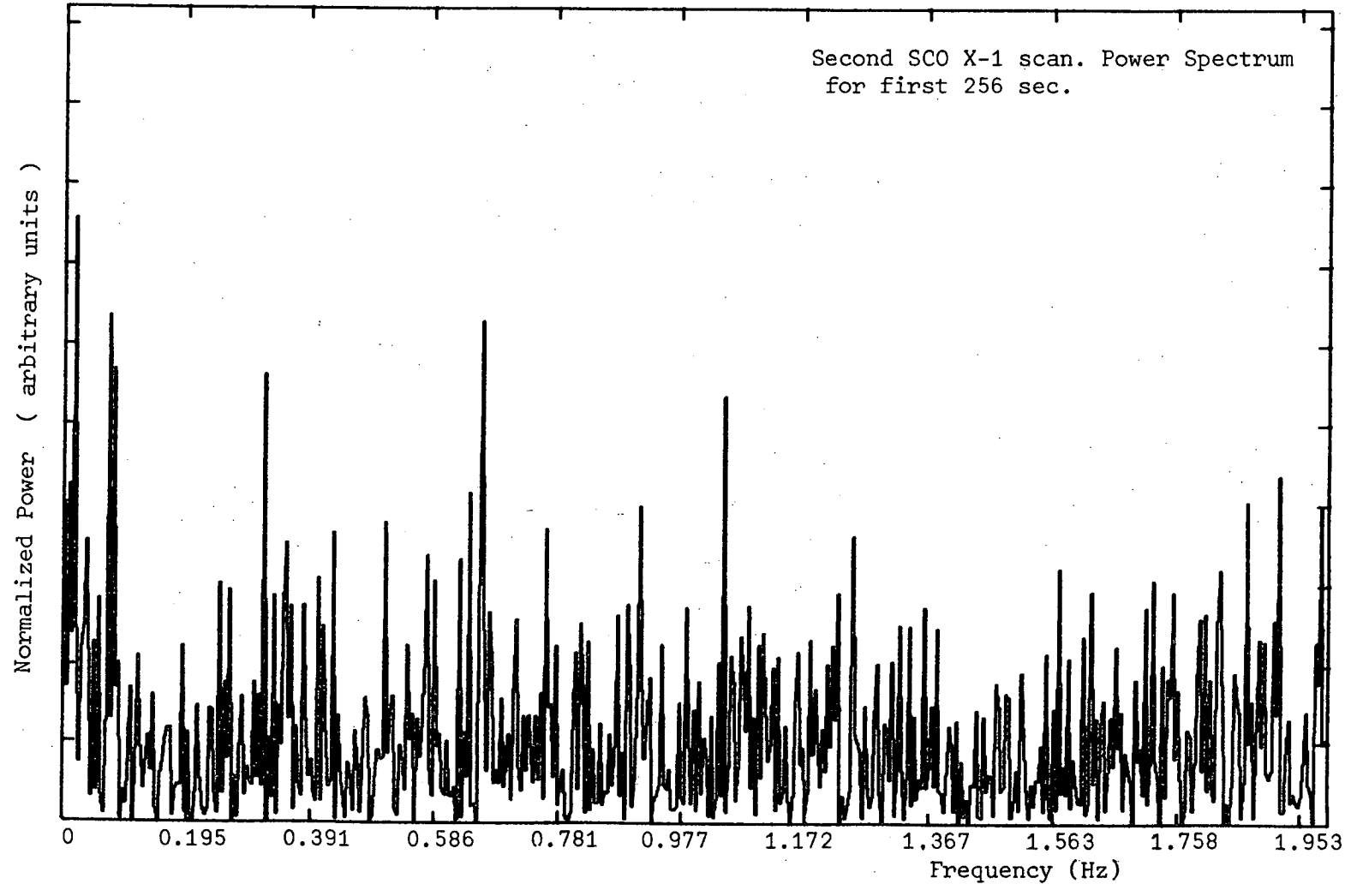
Second SCO X-1 scan. Power Spectrum
for first 256 sec.
Normalized Power (arbitrary units)
0
0.195
0.391
0.586
0.781
0.977
1.172
1.367
1.563
1.758
1.953
Frequency (Hz)

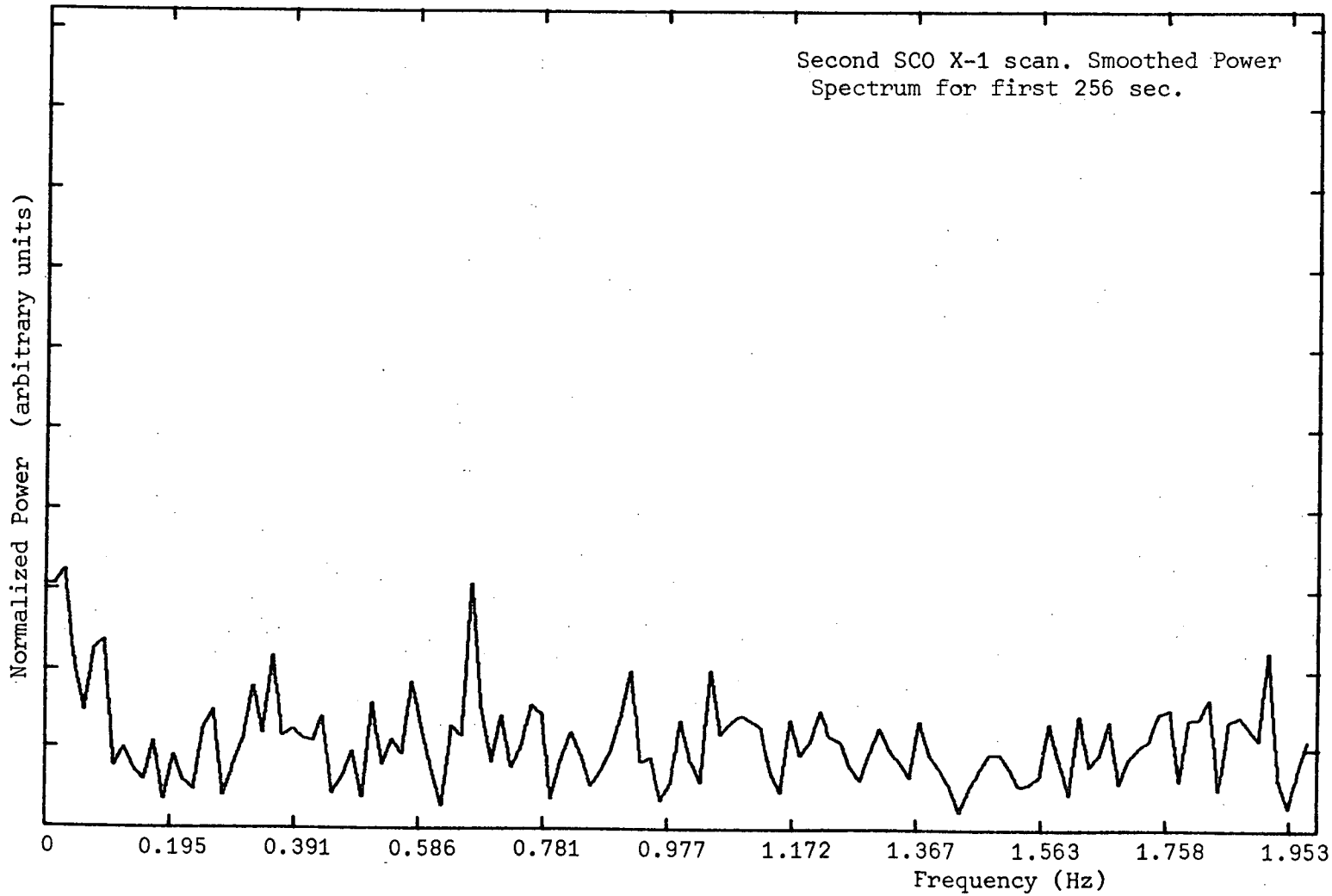
Second SCO X-1 scan. Smoothed Power
Spectrum for first 256 sec.
Normalized Power (arbitrary units)
0
0.195
0.391
0.586
0.781
0.977
1.172
1.367
1.563
1.758
1.953
Frequency (Hz)

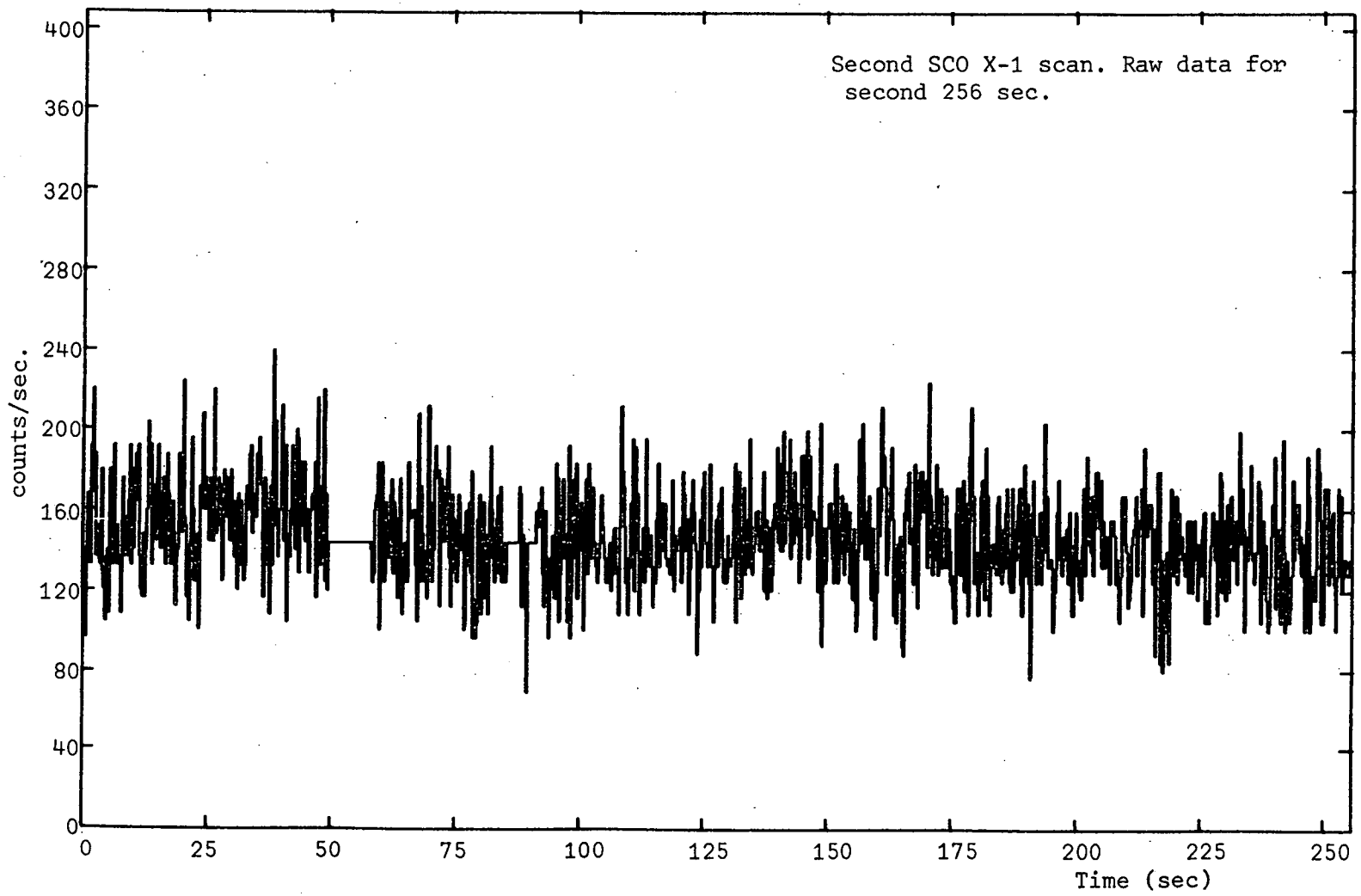
Second SCO X-1 scan. Raw data for second 256 sec.
counts/sec.
400
360
320
280
240
200
160
120
80
40
0
0
25
50
75
100
125
150
175
200
225
250
Time (sec)

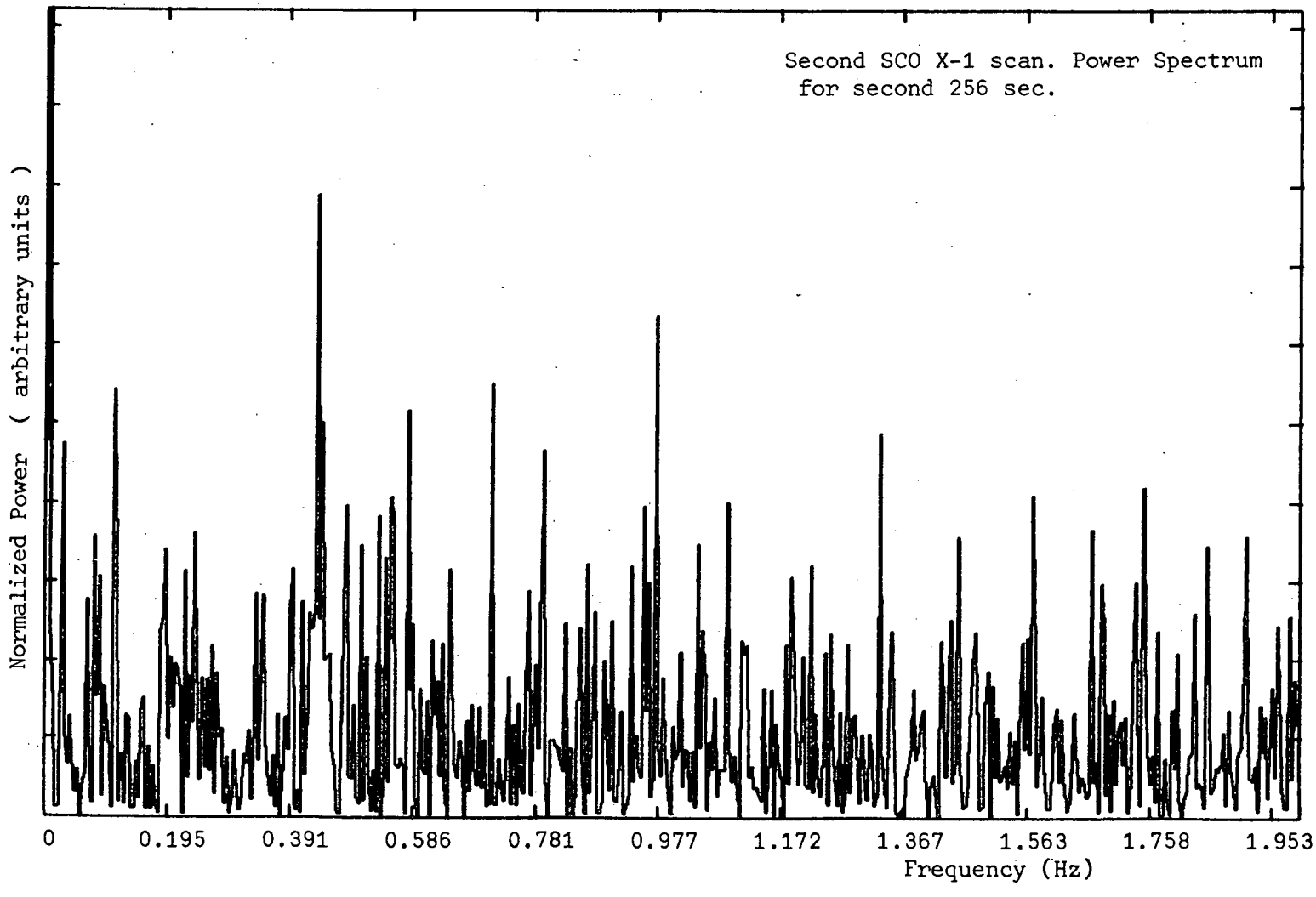
Second SCO X-1 scan. Power Spectrum
for second 256 sec.
Normalized Power (arbitrary units)
0
0.195
0.391
0.586
0.781
0.977
1.172
1.367
1.563
1.758
1.953
Frequency (Hz)

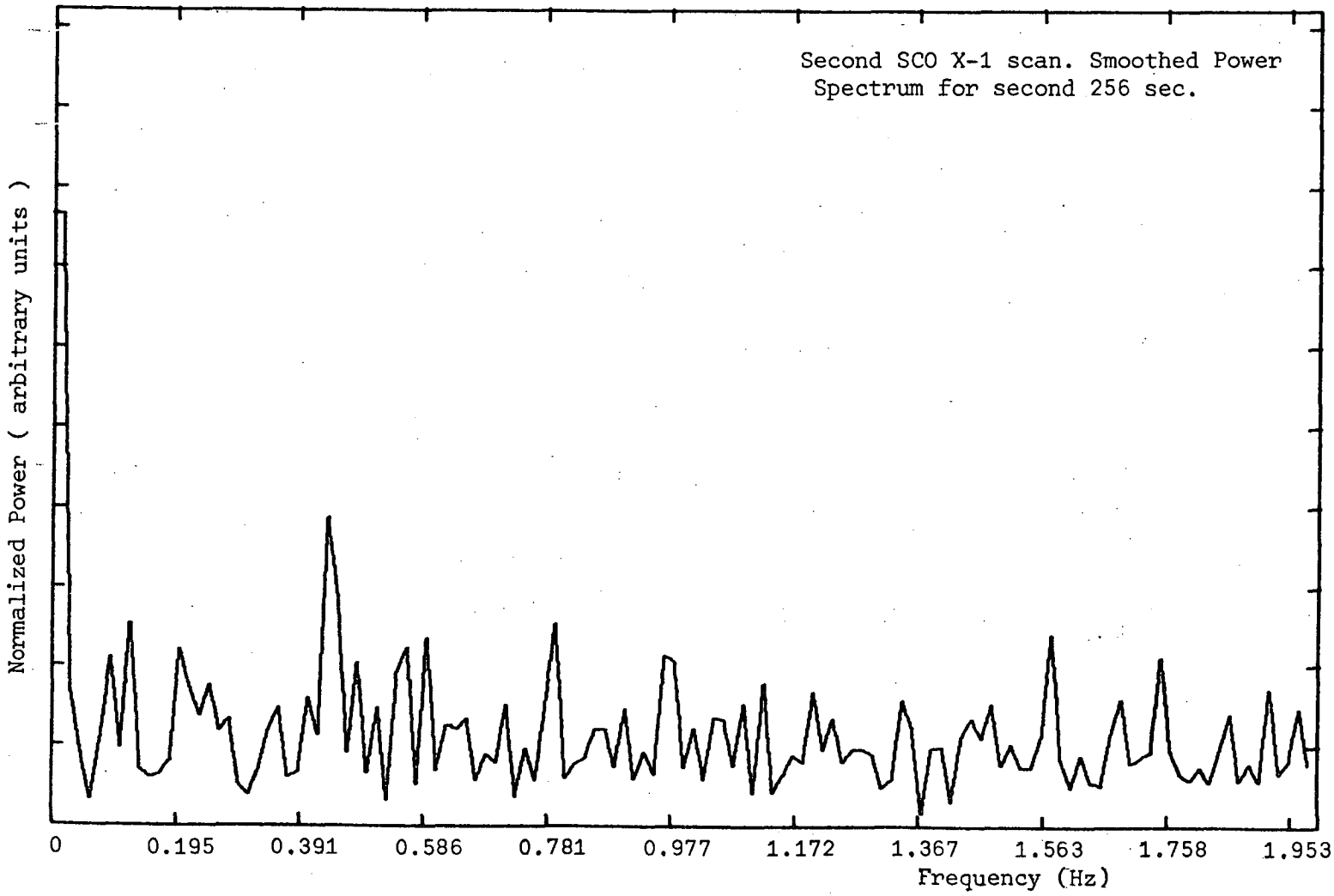
Second SCO X-1 scan. Smoothed Power
Spectrum for second 256 sec.
Normalized Power (arbitrary units)
0
0.195
0.391
0.586
0.781
0.977
1.172
1.367
1.563
1.758
1.953
Frequency (Hz)

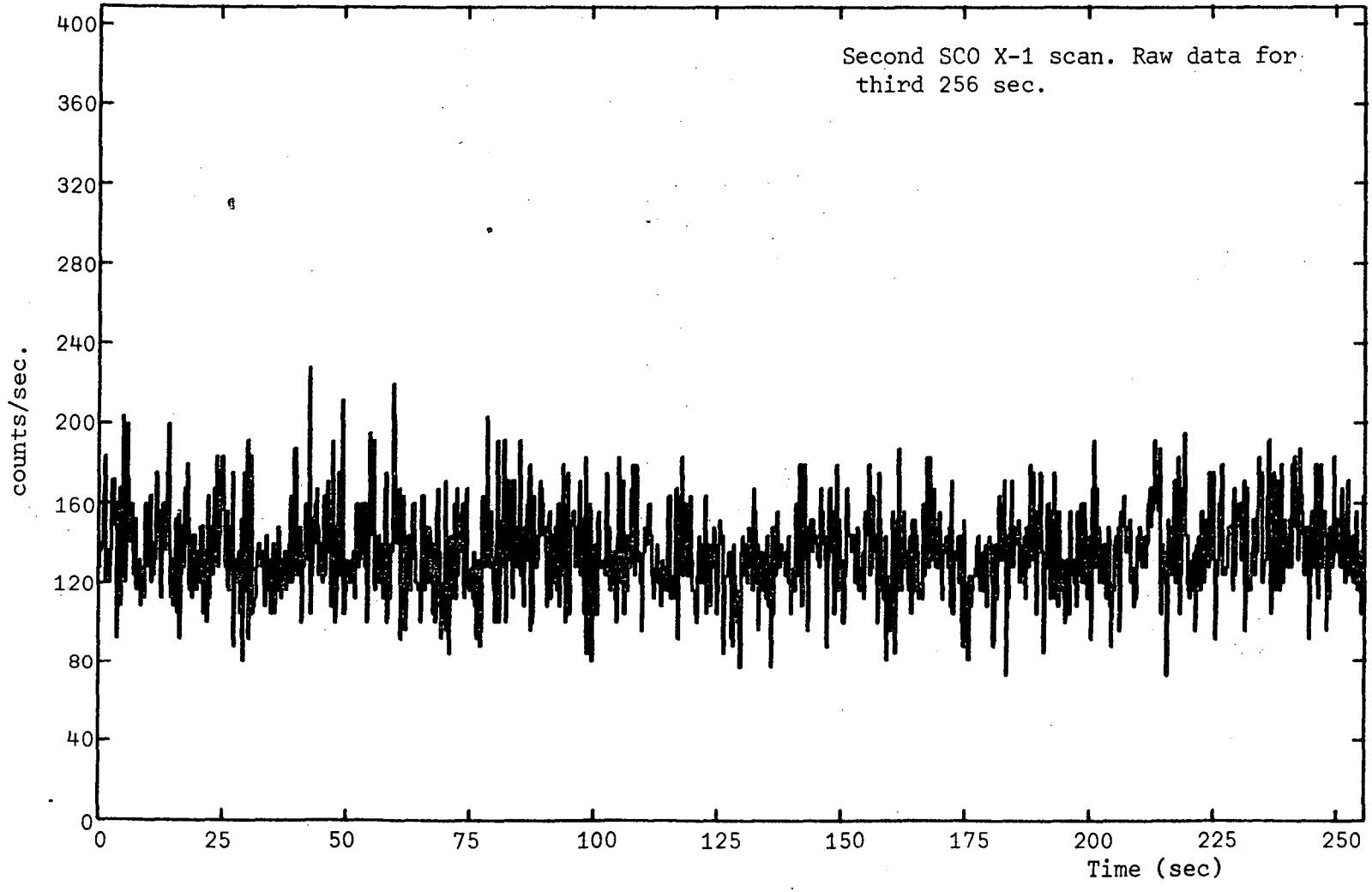
Second SCO X-1 scan. Raw data for third 256 sec.
counts/sec.
400
360
320
280
240
200
160
120
80
40
0
0
25
50
75
100
125
150
175
200
225
250
Time (sec)

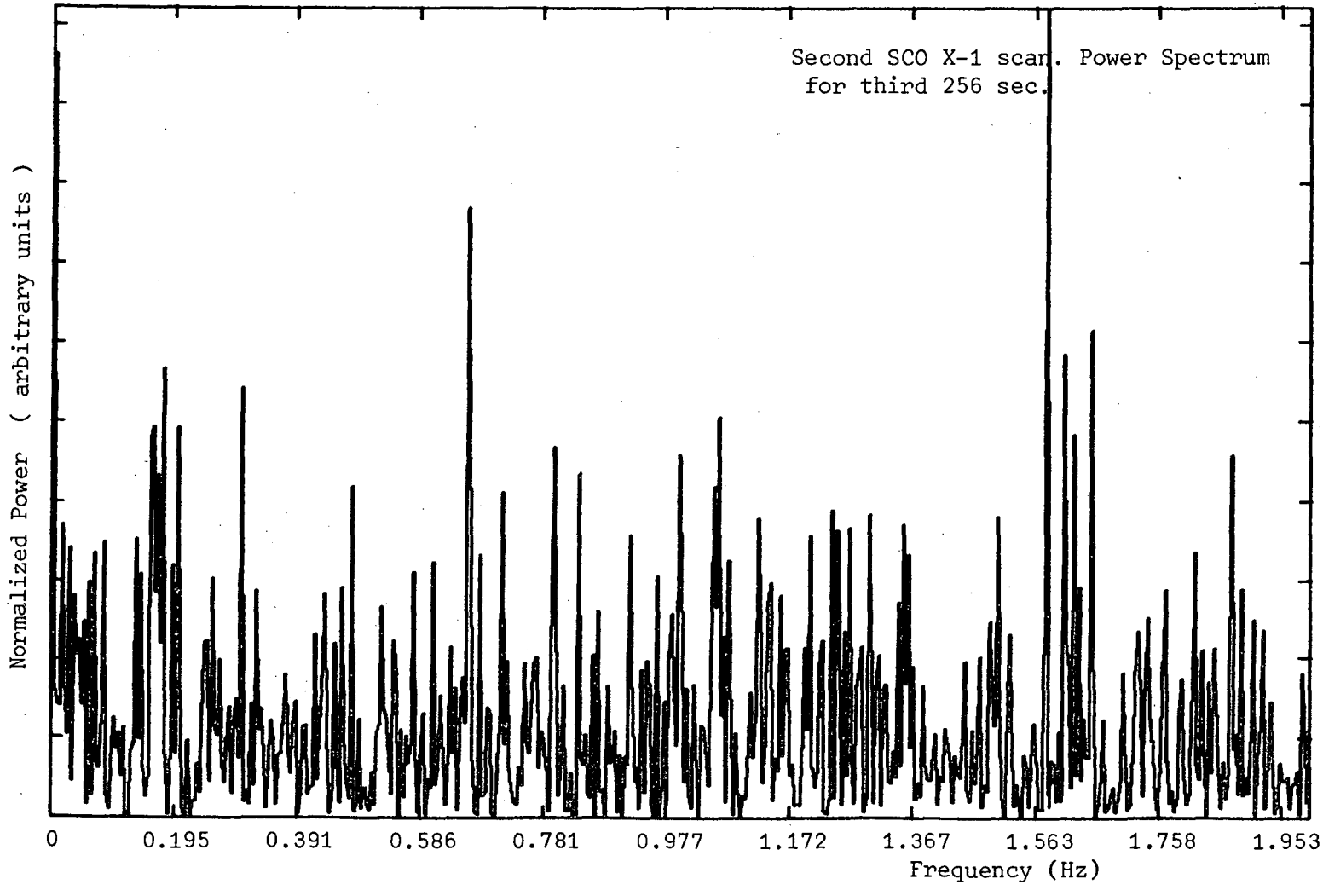
Second SCO X-1 scan. Power Spectrum
for third 256 sec.
Normalized Power (arbitrary units)
0
0.195
0.391
0.586
0.781
0.977
1.172
1.367
1.563
1.758
1.953
Frequency (Hz)

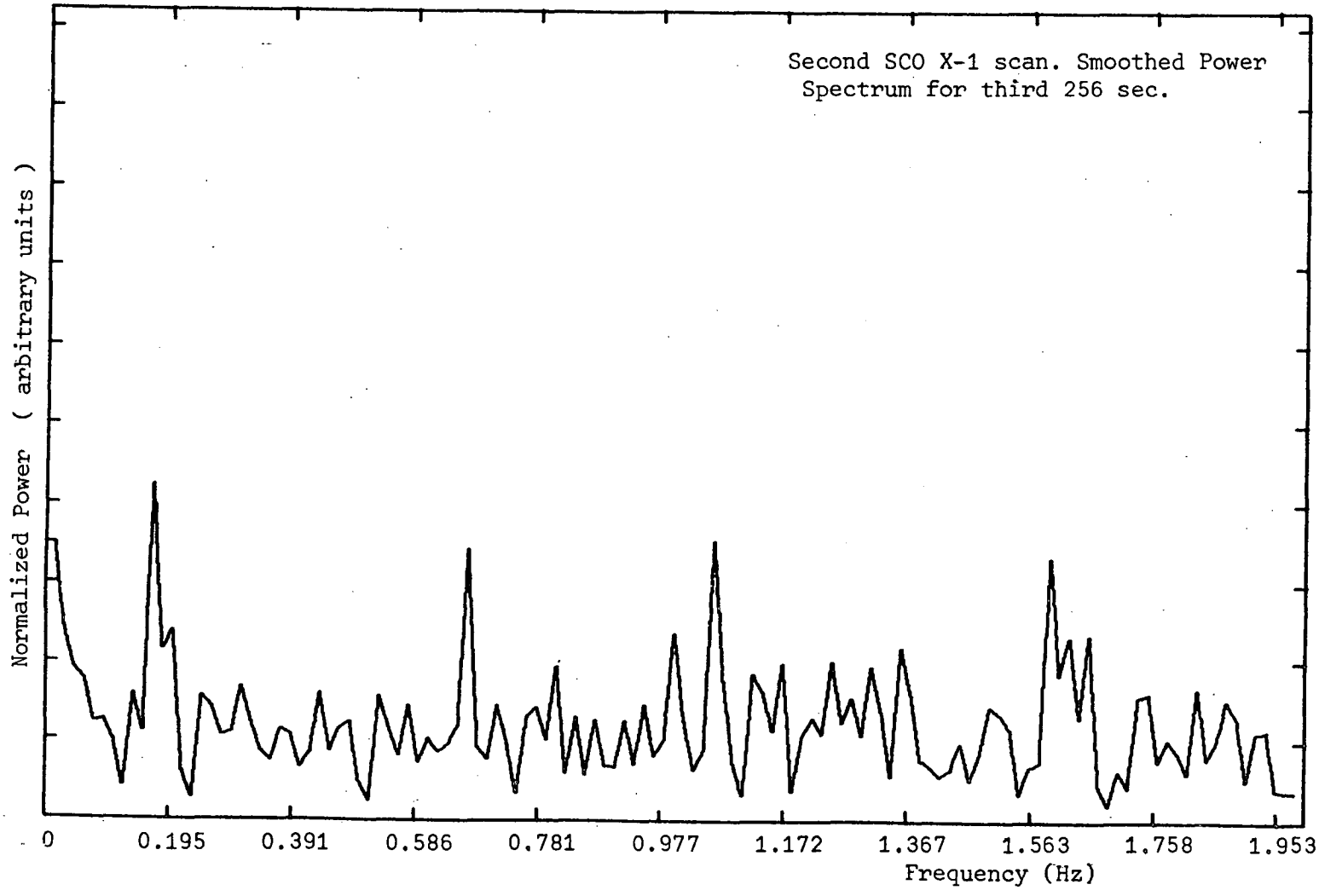
Second SCO X-1 scan. Smoothed Power Spectrum for third 256 sec.
Normalized Power (arbitrary units)
0
0.195
0.391
0.586
0.781
0.977
1.172
1.367
1.563
1.758
1.953
Frequency (Hz)

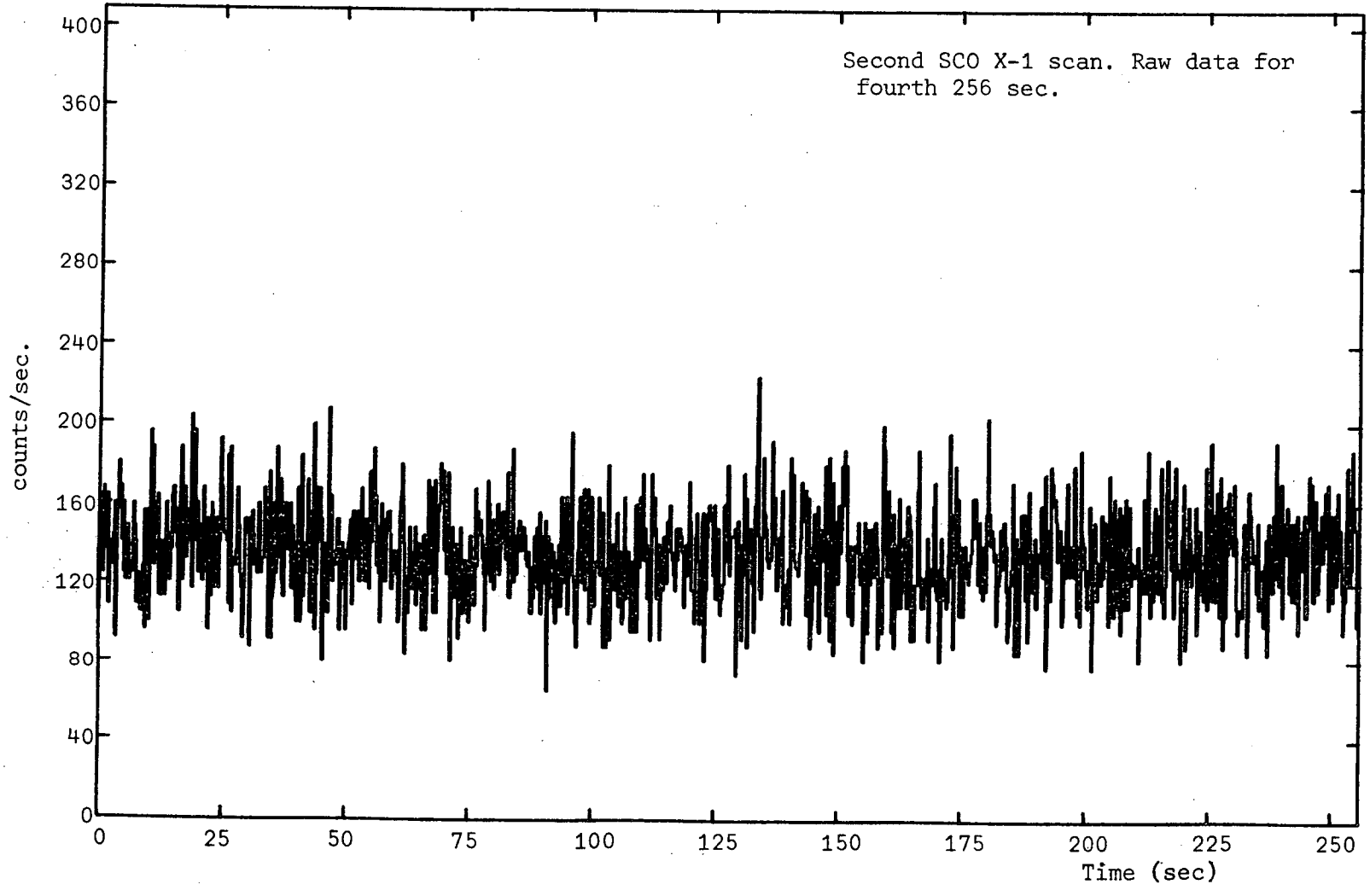
Second SCO X-1 scan. Raw data for
fourth 256 sec.
counts/sec.
400
360
320
280
240
200
160
120
80
40
0
0
25
50
75
100
125
150
175
200
225
250
Time (sec)

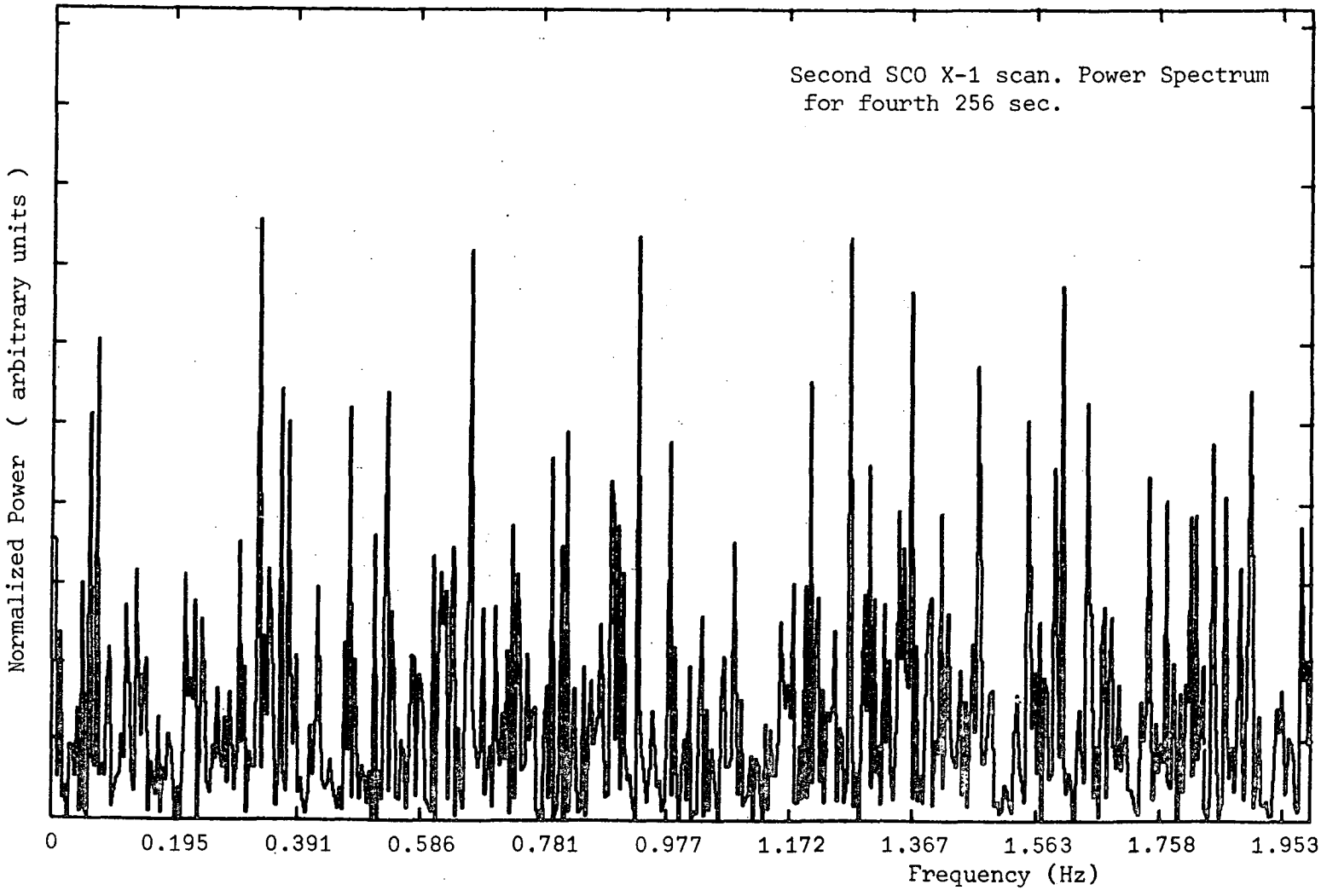
Second SCO X-1 scan. Power Spectrum
for fourth 256 sec.
Normalized Power (arbitrary units)
0
0.195
0.391
0.586
0.781
0.977
1.172
1.367
1.563
1.758
1.953
Frequency (Hz)

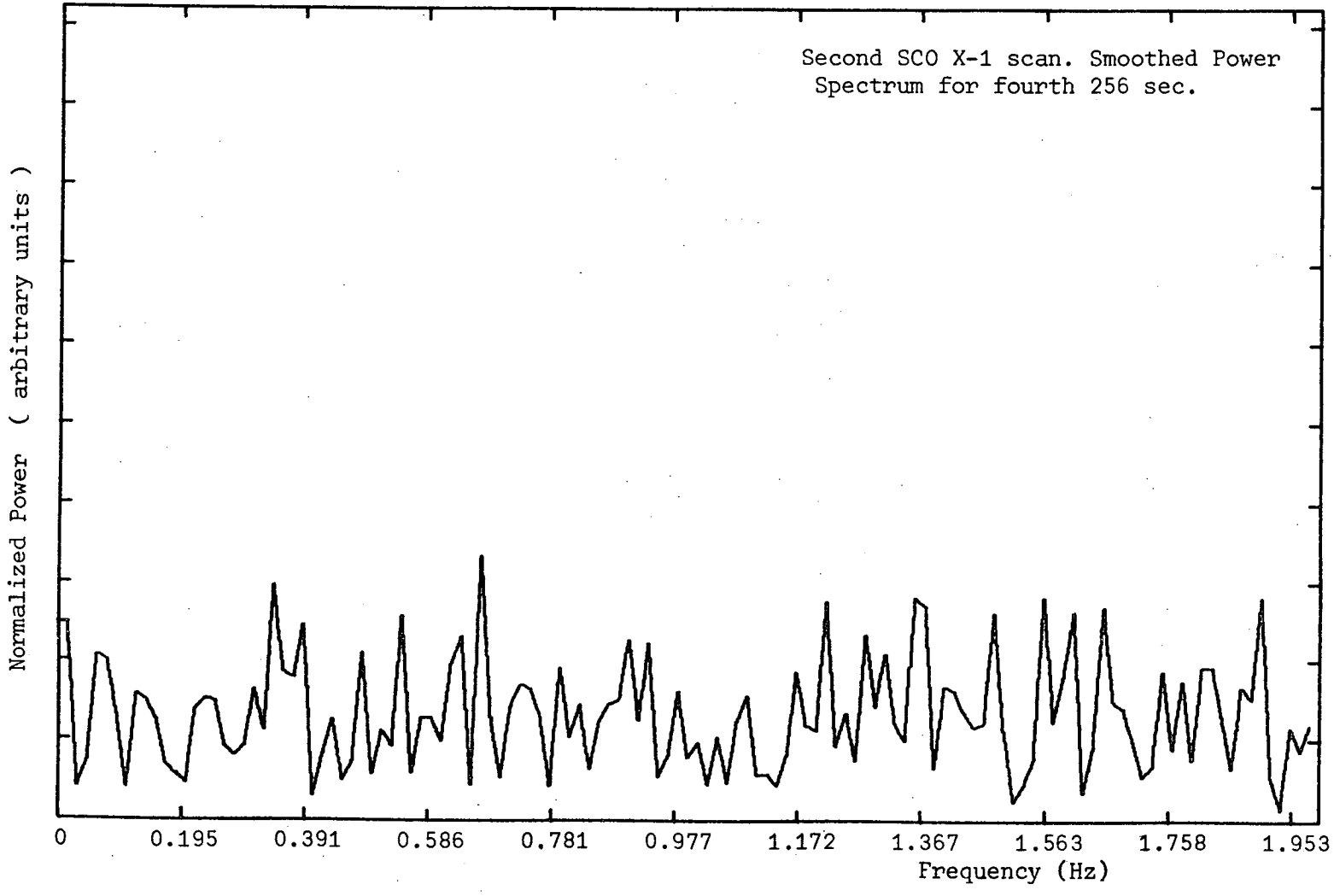
Second SCO X-1 scan. Smoothed Power
Spectrum for fourth 256 sec.
Normalized Power (arbitrary units)
0
0.195
0.391
0.586
0.781
0.977
1.172
1.367
1.563
1.758
1.953
Frequency (Hz)